

**Complex optical systems in space:  
numerical modelling of the heterodyne  
interferometry of LISA Pathfinder and LISA**

Der Fakultät für Mathematik und Physik der  
Gottfried Wilhelm Leibniz Universität Hannover  
zur Erlangung des Grades

Doktorin der Naturwissenschaften  
- Dr. rer. nat -  
genehmigte Dissertation

von  
Dipl.-Phys. Gudrun Wanner, geb. Diederichs  
geboren am 20. Januar 1981 in Dresden

2010

Referent: Prof. Karsten Danzmann (Universität Hannover)  
Korreferent: Dr. Andreas Freise (Senior Lecturer, University of Birmingham)  
Tag der Promotion: 15. Dezember 2010



# Abstract

This thesis is written in the context of the space mission LISA and its technology demonstration mission LISA Pathfinder. The Laser Interferometer Space Antenna (LISA) is a gravitational wave detector to be launched at the end of this decade. It aims to detect gravitational waves in the frequency range of 0.1 to 100 mHz by measuring pathlength changes in its 5 million km arms. The aim of LISA Pathfinder is to demonstrate critical technology, in particular the interferometric readout of an arm length to picometer precision in space.

In the scope of this thesis, a computer simulation was written which imitates the alignment and bonding procedure of LISA Pathfinder's interferometer, the assembly of the spacecraft, as well as the in-flight autonomous alignment procedure of the test masses, and computes the resulting interferometer signals. This computer simulation generates thereby realistic models of LISA Pathfinder's so called optical metrology system (OMS) which were then used to extract the values of calibration factors, cross coupling in the interferometer signals, resulting noise in the pathlength signal and the expected alignment of the test mass and interferometer in flight. The computed coupling factors were compared to measured values, wherever experimental results were available. These comparisons show good agreement.

The pathlength noise due to test mass angular jitter was known to violate the corresponding requirement such that a noise subtraction technique called DWS correction was planned and experimentally validated. This experiment could however only prove that the subtraction reduces the noise sufficiently for the engineering model of the optical bench which was used in the experiment. Therefore, simulations were performed with the flight model design of the optical bench, which showed that the resulting noise is sufficiently small as well.

Finally, simulation of the in-flight alignment showed that several requirements were violated, which had not been expected previously. Several alignment procedures as well as a signal calibration were investigated to improve the in-flight alignment of the test masses. As a result of the investigation it was decided to use the suggested signal calibration to optimize the in-flight alignment.

When the single element InGaAs-photodiodes which were meant to be used for amplitude stabilization of LISA Pathfinder's measurement and reference beam failed, it was decided to replace them by spare quadrant photodiodes. In this scope, the question arose how to optimally align the beam to these quadrant photodiodes. Simulations were performed and showed that the most stable position is to align the beam to one single quadrant. Furthermore it was shown, that the resulting noise in the relative power readout fulfills its requirement. Based on these simulations as well as for technical reasons, it was decided to align the beams in this way.

## *Abstract*

In LISA Pathfinder, cross coupling of angular jitter into the longitudinal pathlength readout is a significant noise source. This cross coupling shall be suppressed in LISA by using an especially designed optical imaging system. This lens system could potentially make the noise subtraction used in LISA Pathfinder unnecessary. In a first step it was shown that so called pupil plane imaging systems provide the required decoupling. In a second step, two systems which fulfill all constraints for the LISA optical bench were investigated. Both systems were shown to provide sufficient decoupling. However, tolerance analyses showed, that alignment precisions beyond experimental capability are required for both lens systems if noise subtraction is to be totally abandoned.

Keywords: gravitational waves, interferometry, LISA Pathfinder

# Zusammenfassung

Diese Arbeit wurde im Kontext der Weltraummission LISA und ihrer Technologie-Demonstrations-Mission LISA Pathfinder angefertigt. LISA (Laser Interferometer Space Antenna) ist ein Gravitationswellendetektor, der gegen Ende dieses Jahrzehntes starten soll. Sein Ziel ist es, Gravitationswellen im Frequenzbereich zwischen 0.1 und 100 mHz zu messen, indem es Weglängenunterschiede in seinen 5 Millionen km langen Armen detektiert. LISA Pathfinder dagegen testet Bauelemente und neue Technologie-Konzepte für LISA, insbesondere das interferometrische Auslesen einer Armlänge auf Pikometer-Genauigkeit im Weltall.

Als Teil dieser Dissertation wurde eine Computersimulation geschrieben, welche die Fertigungsverfahren der Optischen Bank von LISA Pathfinder, die darauf folgende Satelliten-Montage sowie die im Weltall stattfindende autonome Ausrichtung der Testmassen schrittweise nachstellt und anschließend die resultierenden Interferometer-Signale berechnet. Dadurch wurden realistische Modelle des sogenannten ‘Optical Metrology System’ (OMS) erstellt, die anschließend genutzt wurden um Kalibrierungsfaktoren, Kreuzkopplung in den Interferometer-Signalen, resultierendes Rauschen in Pfadlängen-Signalen und zu erwartende Fehlstellungen der Testmassen und des Interferometers zu bestimmen. Die berechneten Kalibrierungs-Faktoren wurden mit experimentellen Ergebnissen verglichen, soweit diese bereits vorhanden waren. Diese Vergleiche zeigten gute Übereinstimmung.

Bereits zu Beginn dieser Arbeit war bekannt, dass das Pfadlängen-Rauschen resultierend aus der Kreuzkopplung des Winkelrauschens der Testmassen den erlaubten Grenzwert nicht im gesamten Frequenzband einhalten können würde. Aus diesem Grund wurde eine Rausch-Subtraktion vorgeschlagen und experimentell bereits bestätigt. Für dieses Experiment wurde das Engineering-Modell der Optischen Bank verwendet, da das Flugmodell noch nicht zur Verfügung stand. Somit konnte nicht geprüft werden, ob diese sogenannte DWS-Korrektur auch für das leicht veränderte Flugmodell der Optischen Bank ausreichend die Kreuzkopplung unterdrücken würde. Im Rahmen dieser Arbeit wurden daher Simulationen mit dem Layout des Flugmodells durchgeführt, die zeigten, dass das resultierende Rauschen ausreichend gering ist um eine DWS-Korrektur durchzuführen.

Ein weiteres Ergebnis der Computer-Simulation war, dass die erzeugten Interferometer Fehlstellungen aufwiesen, die größer als die gesetzten Grenzwerte waren. Aus diesem Grund wurden mehrere alternative Fertigungsverfahren für die Optische Bank sowie eine Kalibrierung untersucht. Als Ergebnis dieser Studie wurde entschieden, die DWS-Signale von LISA Pathfinder zu kalibrieren, um dadurch die Fehlstellungen der Testmassen zu minimieren.

Als die Einzel-Element InGaAs-Photodioden, die für die Amplituden-Stabilisierung der LISA Pathfinder Laser verwendet werden sollten, technisch versagten, wurde ent-

schieden, Ersatz-Quadrantendioden zu verwenden. Dabei musste entschieden werden, wie die Dioden gegen den Laserstrahl ausgerichtet werden sollten, um eine möglichst stabile Leistungsmessung zu garantieren. Dazu wurden im Rahmen dieser Arbeit Simulationen durchgeführt, die zeigten, dass der Strahl zentriert auf einen einzelnen Quadranten ausgerichtet sein sollte. Weiterhin wurde gezeigt, dass das resultierende relative Leistungsrauschen unter dem gegebenen Grenzwert liegt. Aufgrund dieser Ergebnisse sowie technischen Kriterien wurden die InGaAs-Quadranten-Dioden auf die vorgeschlagene Art ausgerichtet.

Bei LISA Pathfinder ist die Kreuzkopplung von Testmassen Winkelrauschen in das longitudinale Pfadlängensignal eine wichtige Störquelle. Diese Kreuzkopplung soll bei LISA durch ein speziell entworfenes Linsensystem unterdrückt werden. Dieses Linsensystem könnte potentiell die DWS-Korrektur unnötig machen, die in LISA Pathfinder verwendet werden muss. In einem ersten Schritt wurde gezeigt, dass sogenannte Pupillen-Abbildungs-Systeme die Kreuzkopplung ausreichend unterdrücken. In einem zweiten Schritt wurden zwei unterschiedliche Pupillen-Abbildungs-Systeme untersucht, die alle notwendigen Randbedingungen erfüllen. Diese zeigten beide eine ausreichende Unterdrückung der Kreuzkopplung. Eine Toleranzanalyse offenbarte jedoch, dass die Präzision mit der die einzelnen Komponenten gegeneinander ausgerichtet werden müssen um DWS-Korrektur unnötig zu machen, die heutigen technischen Möglichkeiten überschreiten.

Schlüsselwörter: Gravitationswellen, Interferometrie, LISA Pathfinder

# Contents

<b>Abstract</b>	<b>i</b>
<b>Zusammenfassung</b>	<b>iii</b>
<b>1. Introduction</b>	<b>1</b>
1.1. Gravitational wave astronomy . . . . .	1
1.2. Gravitational wave detectors in space . . . . .	4
1.3. This thesis . . . . .	6
<b>I. Heterodyne interferometry</b>	<b>9</b>
<b>2. Detection principle and signal definition</b>	<b>11</b>
2.1. Detecting gravitational waves with homodyne interferometry . . . . .	11
2.2. Heterodyne interferometry . . . . .	13
2.2.1. Power readout in heterodyne interferometers . . . . .	15
2.3. Heterodyne signals . . . . .	18
<b>3. Phase demodulation at LISA Pathfinder</b>	<b>23</b>
3.1. Experimental phase demodulation at LISA Pathfinder . . . . .	23
3.2. Simulation of the LISA Pathfinder phase demodulation . . . . .	26
3.2.1. Gaussian beams . . . . .	26
3.2.2. Computing photocurrents of a QPD . . . . .	29
3.2.3. Computing heterodyne signals . . . . .	31
<b>4. Example interferometers and their signals</b>	<b>35</b>
4.1. Experimental setups versus setups in simulations . . . . .	35
4.2. Example: longitudinal beam shift . . . . .	37
4.3. Example: beam tilt . . . . .	38
4.4. Example: a system with zero phase and DWS response . . . . .	41
4.4.1. Simulation results . . . . .	42
4.5. Coupling factors . . . . .	43
4.6. Analytical computation of DC signals . . . . .	43
4.6.1. DC signal for one beam . . . . .	44
4.6.2. DC signal in an interferometer . . . . .	47

<b>II. LISA Pathfinder interferometry</b>	<b>51</b>
<b>5. Introduction to LISA Pathfinder</b>	<b>53</b>
5.1. The mission . . . . .	53
5.2. Interferometry aboard LISA Pathfinder . . . . .	58
5.2.1. Description of the four interferometers . . . . .	58
5.3. Optical metrology system: from manufacturing to space . . . . .	60
5.3.1. OBI alignment techniques . . . . .	61
5.3.2. Bonding procedure of the LTP OBI . . . . .	64
5.3.3. The route of the optical bench: from Glasgow to space . . . . .	66
5.4. Coordinate frames . . . . .	67
<b>6. The LTP-OBI-Alignment Simulation</b>	<b>71</b>
6.1. Context and structure of the simulation . . . . .	71
6.2. The nominal OBI . . . . .	73
6.2.1. Coupling factors of the nominal OBI . . . . .	74
6.3. Realistically misaligned OB in eight steps . . . . .	75
<b>7. Results obtained by the LTP-OBI-Alignment Simulation</b>	<b>81</b>
7.1. LTP coupling factors for realistically aligned OBI . . . . .	81
7.1.1. Coupling factors for pathlength readout . . . . .	83
7.1.2. DWS coupling factors . . . . .	87
7.1.3. DC coupling factors . . . . .	87
7.1.4. Application of coupling factors . . . . .	89
7.2. LTP noise spectra . . . . .	89
7.2.1. Estimates of spacecraft and test mass jitter . . . . .	90
7.2.2. Requirements . . . . .	91
7.2.3. Showing linearity . . . . .	91
7.2.4. Pathlength noise due to Spacecraft jitter . . . . .	93
7.3. Expected alignment of the OBI in science mode . . . . .	96
7.3.1. Nominal alignment strategy. . . . .	97
7.3.2. Alternative 1: DWS calibration . . . . .	100
7.3.3. Alternative 2: Hovered BS3 . . . . .	102
7.3.4. Alternative 3: generating a dummy test mass cavity . . . . .	104
7.3.5. Combining alternative 3 and 1 . . . . .	105
7.3.6. Combining alternative 3 and 2 . . . . .	106
7.3.7. Conclusions of OBI alignment in flight . . . . .	106
<b>8. QPDs to monitor amplitude stability</b>	<b>109</b>
8.1. Beam power measured by a QPD . . . . .	109
8.1.1. Methods and assumptions . . . . .	111
8.1.2. Result: measured power for different configurations . . . . .	112
8.2. Relative power fluctuations . . . . .	113
8.2.1. Relation of relative power noise and beam pointing jitter . . . . .	114
8.2.2. Relative power noise derived from a DWS-requirement . . . . .	115
8.2.3. Relative power noise derived from measured DC spectra . . . . .	117
8.3. Conclusion . . . . .	120

<b>III. LISA interferometry</b>	<b>123</b>
<b>9. LISA interferometry concepts</b>	<b>125</b>
<b>10. Imaging optics</b>	<b>131</b>
10.1. Objective . . . . .	131
10.2. Design criteria and constraints . . . . .	132
10.3. Simulating a pupil plane imaging system . . . . .	137
10.3.1. Setting lens parameters for a simulation . . . . .	137
10.3.2. Setting up a simulation for pupil plane imaging . . . . .	138
10.3.3. Results: pupil plane imaging . . . . .	140
10.3.4. Adaptibility of Setup D for the test mass interferometer . . . . .	144
10.3.5. Conclusions on pupil plane imaging . . . . .	145
10.4. New beam compressors: ASD-4L and AEI-D003 . . . . .	145
10.4.1. Nominal signals . . . . .	148
10.4.2. Tolerance analyses . . . . .	148
10.4.3. Cause of critical QPD alignment value . . . . .	153
10.4.4. Performance of D003 with experimentally realized beam parameters	154
<b>Appendix</b>	<b>161</b>
<b>A. Background information</b>	<b>163</b>
A.1. Strain caused by gravitational waves . . . . .	163
A.2. Science requirements for LISA and LISA Pathfinder . . . . .	167
A.3. LPF noise break down . . . . .	170
A.4. Implementation of tolerances in the LTP-OBI-Alignment Simulation . . . . .	172
A.5. Labeling of QPD-quadrants in LTP . . . . .	174
A.6. Design Criteria for the LISA OB . . . . .	175
<b>B. Proofs and validations</b>	<b>177</b>
B.1. Equivalent representations of the electric field . . . . .	177
B.2. Confirmation of power loss due to the insensitive slit . . . . .	178
B.3. Confirmation of computed power for a 3 mm SEPD . . . . .	179
B.4. Imaged waist position . . . . .	180
<b>C. Settings of the various simulations</b>	<b>181</b>
<b>D. Coupling factors and figures accompanying section 10.4.2</b>	<b>183</b>
<b>Glossary</b>	<b>197</b>
<b>Complete list of publications</b>	<b>229</b>
<b>Project Documents</b>	<b>231</b>
<b>Curriculum Vitae</b>	<b>235</b>





# 1. Introduction

## 1.1. Gravitational wave astronomy

Astronomy has changed our world-view promoted by science pioneers like Nicolaus Copernicus, Galileo Galilei and Johannes Kepler who fought for the acceptance of their heliocentric model of the solar system. Since then our comprehension of the universe and our place in it have vigorously changed and evolved. In the time of Copernicus, people believed Earth to be the center of the universe and the stars fixed to spheres that enclosed the Earth. By now, we know we live on a small planet, in one of approximately 200 billion solar systems of our Galaxy: the Milky Way - which is only one of  $10^{11}$  galaxies in the universe. We know about extraordinary stellar objects like pulsars, and black holes, observe supernovae and investigate dark matter and the big bang. All of this knowledge was gained through astronomy. Today astronomy splits into a wide range of branches: Radio astronomy, infrared, optical, and ultraviolet astronomy, X-ray and Gamma-ray astronomy. Nevertheless, all these fields have one thing in common: they observe electromagnetic waves. This fact alone limits the scope of future discoveries.

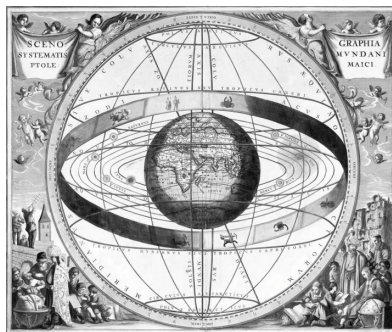


**Figure 1.1.:** Ptolemy's geocentric model, showing the knowledge about the universe from the Ancient Greece to the Middle Ages.



**Figure 1.2.:** Mice Galaxies, an example of merging galaxies and the knowledge we have today about the universe. Credit: ESA, NASA

The mean free path of electromagnetic radiation in the early universe was so small that the universe was opaque. That means we cannot observe any electromagnetic waves from the first 380 thousand years of the universe, and the big bang lies in the dark. A similar problem exists with the direct observation of black holes as these singularities do not, by definition, radiate directly. Observation of black holes will thus be always indirect, for example by tracking orbiting stars or measuring X-rays emitted by an accretion disc. Furthermore, neutron stars and also pulsars which radiate not in the direction of our solar system cannot be observed by electromagnetic astronomy. Finally, the absorption of electromagnetic waves by interstellar matter limits the prospects of astronomy today.

## 1. Introduction

At present, a new field of astronomy is about to evolve: gravitational wave astronomy. Instead of electromagnetic radiation, gravitational waves will be observed to study the universe. These waves have hardly any interaction with matter which means they are neither scattered nor absorbed by, for instance, interstellar matter. Gravitational waves reach us therefore effectively unperturbed from every part of the universe. They are emitted for example by spinning or orbiting neutron stars, pulsars, and black holes. Gravitational wave detectors will be able to sense large events in the center of galaxies and investigate the evolution of the universe back to its very beginning: the big bang.

But what are gravitational waves and why is gravitational wave astronomy new? Gravitational waves are a consequence of general relativity as postulated by Albert Einstein. These waves are disturbances in the four dimensional space time that are expected to travel with the speed of light through the universe. They are emitted by every accelerated massive object and carry large amounts of energy like  $10^{28}$  Watt for binary solar mass neutron star coalescences which is 100 times the energy radiated by our Sun, and yet their effect is small. Large cosmic events are expected to emit gravitational waves with amplitudes of the order of  $10^{-21}$ . These very strong gravitational waves would change the distance of Earth to the Sun by the diameter of an atom. This is the reason why Einstein himself thought gravitational waves could never be measured. However, state of the art technology enables us today to build detectors that are already capable of detecting gravitational waves even though their effect is so small.

In the past decades, detectors for gravitational waves were built all over the world. In general, there are three methods to be distinguished for gravitational wave research: resonant mass detectors, pulsar timing, and interferometric detectors. Resonant mass detectors like, for example, AURIGA [Conti2004] are large masses oscillating in resonance with gravitational waves of specific frequencies. They were the first type of detector, and were first built by Weber in the 1960s.

The second rather new type of gravitational wave detection is pulsar timing. This method compares the arrival time of pulses received from pulsars with an arrival time predicted by models. The residual difference between these arrival times is compared with residuals of other pulsars. Correlation indicates the presence of gravitational waves.

Interferometric detectors use the phase shift of light in large interferometers to detect gravitational waves. Today, there are several detectors operating all over the world: LIGO (USA), GEO600 (Germany British collaboration), VIRGO (Italy), TAMA300 and CLIO (Japan), and several more are in preparation: AIGO (Australia), LCGT (Japan) and ET (Europe). Furthermore, spaceborne missions are being prepared like LISA and LISA Pathfinder (ESA and NASA), DECIGO, and DECIGO Pathfinder (JAXA), and BBO<sup>[1]</sup>. This thesis investigates alignment issues for LISA and LISA Pathfinder and will therefore focus on interferometric gravitational wave detectors.

Up to now, no detector has measured a gravitational wave. Still, there is no doubt that they exist and their indirect observation by Hulse and Taylor was awarded the Nobel

---

<sup>[1]</sup>Please see the glossary on p. 197 ff. for a short explanation of these abbreviations and projects.



**Figure 1.3.:** Interferometric gravitational wave detectors all over the world.

prize in 1993. In the past decades, detectors were built and novel technology invented to ever increase the sensitivity of the detectors by decreasing the disturbing noise levels. By now, the interferometric detectors have an all-sky coverage of tens of megaparsecs, such that, for instance, the inspiral of any neutron star - neutron star (NS-NS) pair in the local group (the group of galaxies surrounding the Milky Way) could be observed. However, these events are rare, and detection rates of the order of two per century are currently estimated. [Abadie2010] That means detectors today are sensitive enough to detect gravitational waves, but due to the limited coverage and the low event rate no gravitational waves were detected yet. Still, in 2010, the interferometric detectors will go offline to be upgraded to the second generation.<sup>[2]</sup> These second generation detectors are expected to start operation in 2015 and, for example, advanced LIGO is expected to reach a sky coverage of over 150 Mpc [Leonor2009]. Thereby its detection rate for neutron star - neutron star (NS-NS) inspirals will become 40 per year<sup>[3]</sup> [Abadie2010] and the window to gravitational wave astronomy will be opened.

A question often asked is whether the variety of detectors indicates competition. This is not the case. Having several detectors in operation simultaneously in a similar frequency range and different location reduces the false alarm rate and allows localizing the source of a gravitational wave rather than just detecting the wave. Furthermore, each detector type is limited to a specific frequency band. Pulsar timing is sensitive in the nano-Hertz regime, LISA will cover the range of about 0.1 mHz and 0.1 Hz while DECIGO is planned to bridge the gap between LISA and earth-bound interferometric detectors which are most sensitive in the range of 10 to 1000 Hz. Finally, bar detectors like AURIGA are narrow banded detectors in the kHz regime. This means that the different detector types are sensitive to different events.

<sup>[2]</sup>More information about future generations of ground detectors including discussions of the various noise sources can be found for instance in [Punturo2010].

<sup>[3]</sup>Detection rate estimates depend on source types, e.g. NS-NS or neutron star - black hole (NS-BH) inspirals and the underlying models. The stated values are realistic values. Low estimates deviate by a factor of 100, high estimates by a factor of 10 with respect to the realistic value.

## 1.2. Gravitational wave detectors in space

Interferometric gravitational wave detectors on Earth are kilometer scale Michelson interferometers that are so sensitive that they can detect gravitational waves from any NS-NS, NS-BH or BH-BH inspiral within our local group. But they also sense Earth quakes all over the world as well as the surge of the oceans, planes and trains passing by and much more. This seismic background noise as well as gravity gradient noise, the noise originating from changes in the Earth's gravitational field, dominate the sub 1 Hz regime and make detection of gravitational waves with frequencies below approximately 1 Hz extremely challenging on Earth. Building detectors underground like CLIO and LCGT and using complicated seismic attenuation systems reduces seismic noise, but these techniques are not capable to filter it entirely. This is the main reason why space detectors are being built.

Probably the best known space detector is the Laser Interferometer Space Antenna: LISA which was first proposed in its present form in 1993 [Danzmann1993]. It is a joint effort between ESA and NASA such that industry and Universities from all over Europe and the USA contribute to this mission. The launch date is by now expected for the end of this decade, possibly the beginning of the next decade depending mainly on funding.

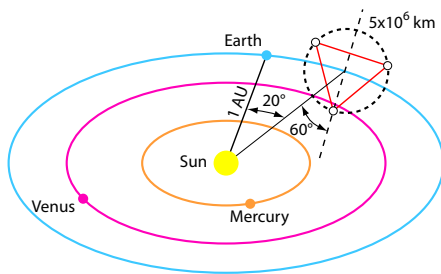


**Figure 1.4.:** LISA orbit (not to scale).  
Credit: NASA.

The LISA constellation is the well known equilateral triangle trailing Earth at a distance of 50 million kilometers, which is about  $20^\circ$  in the Earth orbit (cf. figure 1.4). Even though floating 5 million kilometers apart, the three spacecraft forming the triangle will be linked by laser beams. Like in earth-bound gravitational wave detectors these laser beams are used for the sensitive readout of the arm length, that means the distance between a test

mass aboard one spacecraft to a test mass on a remote spacecraft. This distance needs to be measured to sub-nanometer level at frequencies between 0.1 mHz and 0.1 Hz.

In contrast to the currently operating earth bound detectors, LISA has a large number of guaranteed sources: about 10 Million mainly white dwarf binaries of the total  $10^{12}$  binary systems in the Milky Way produce gravitational waves in the LISA frequency band. These will all be measured simultaneously by LISA, such that this signal type effectively acts as noise for other gravitational wave signals [Hughes2007]. Furthermore, LISA will measure several to a few hundred binaries of super massive black holes (SMBH) [Haehnelt1998]. This means that LISA will detect the merger of galaxies, the inspiral of smaller bodies into massive black holes (so called extreme mass ratio inspirals: EMRIs) and any white dwarf binary system within our galaxy that has an orbital period of less than 2 years.

With its three spacecraft and extreme stability requirements LISA is a comprehensive and expensive mission which comprises a substantial amount of new technology and stability requirements that were not yet shown in any other space mission. Therefore a

## 1.2. Gravitational wave detectors in space

technology test mission called LISA Pathfinder was scheduled in order to demonstrate new technologies and the achievability of critical stability requirements for LISA.

LISA Pathfinder (LPF) consists of only one satellite (cf figure 1.5) which is planned to be launched in 2013. Its final orbit will be around the Lagrangian point L1 which is located between Sun and Earth. With this soon approaching launch, LISA Pathfinder is now in a state where most flight hardware is already manufactured and is now successively tested.

Aboard LISA Pathfinder are two instruments: the European LISA Technology Package (LTP) and NASA's Disturbance Reduction System (DRS). The key element for both instruments are the two free floating test masses of LTP which are located in the center of the LISA Pathfinder spacecraft approximately 35 cm apart. The positions and attitudes of these test masses are monitored by an interferometric (LTP) and a capacitive readout (LTP and also used by DRS). LISA Pathfinder will thereby test the interferometry concept for LISA by shrinking one LISA interferometer arm from 5 million km to 35 cm. This short arm length makes LISA Pathfinder a pure technology test mission and does not allow detection of gravitational waves. Examples for critical technology to be tested are: achieving free floating test masses with a residual acceleration requirement relaxed by only a factor of ten with respect to the LISA requirement; spacecraft control with micro-Newton thrusters as the only propulsion mechanism to counteract any residual test mass acceleration; the sensitive caging mechanism which secures the test masses during launch and releases them in space into free fall. The requirements and main technology of LPF will be introduced in more detail in the LISA Pathfinder introduction, chapter 5.

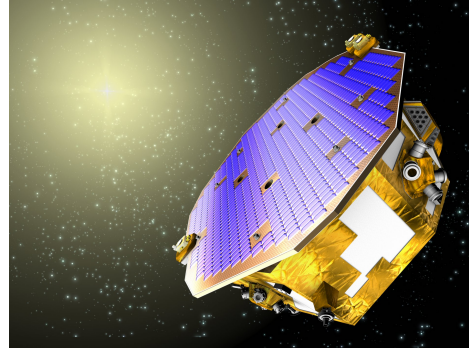


**Figure 1.5.:** LISA Pathfinder Satellite. Source:[3]

Besides LISA and LISA Pathfinder, another mission called the Big Bang Observer (BBO) is being planned for the further future. Unlike LISA and LISA Pathfinder, BBO is only in a study phase and hardware is not yet being developed. It is planned as an observatory for gravitational waves originating from the very beginning of the universe: the big bang. It could consist of four LISA constellations evenly distributed along the Earth's

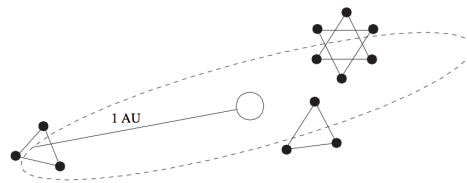


**Figure 1.6.:** BBO shall consist of 4 LISA-like triangular constellations (two overlapping to form a Star of David) at a distance of one astronomical unit (1 AU) to the Sun.

orbit, two of them overlapping and thereby forming a Star of David (figure 1.6). BBO would be so sensitive that the numerous gravitational waves of mainly neutron star - neutron star mergers will form a noise source that hides the desired primordial gravitational waves. Strategies for subtracting these gravitational waves are therefore needed to allow observation of the big bang [Harms2008, Cutler2006]. However, the technical

## 1. Introduction

requirements, like the 300 Watt laser beam or launching mirrors with a diameter of 3.5 m are not yet achievable.

The latest proposed mission is the Japanese gravitational wave antenna called DECIGO, the “Deci-hertz Interferometer Gravitational Wave Observatory”. DECIGO will consist of 12 satellites in the BBO constellation (cf. figure 1.6 with an arm length of 1000 km). Key components are the Fabry-Pérot arm cavities, frequency doubled Nd:YAG laser beams with a power of 10 Watt and 100 kg mirrors with a diameter of 1 m. The launch of DECIGO is currently planned for 2024 [Sato2009]. As for LISA, a technology demonstration mission DECIGO Pathfinder (DPF) is planned. Since LPF and DPF are related missions fighting with similar requirements and technical difficulties, DPF and its technology resemble the LPF mission and its technology. Unlike in the LISA and LPF mission, there is an intermediate stage for DECIGO planned: Pre-DECIGO is to be launched in 2018 and will be sensitive to gravitational waves.

### 1.3. This thesis

All interferometric gravitational wave detectors use the same working principle. Laser light is reflected from test masses such that the longitudinal pathlength signal of the interferometer senses changes in the light travel time between test masses, that means changes in the interferometer arm lengths. Yet, there are numerous effects that cross couple into the pathlength signal, such that, for example, laser frequency fluctuations or angular jitter of the test mass, or beam walk on the photodiode appear as fake armlength changes. As part of this thesis, the interferometer signals of LISA Pathfinder were investigated for cross coupling, and lens systems were examined for LISA which suppress one major type of cross coupling: the coupling of test mass angular jitter.

In general, this thesis splits into three parts: A fundamental part giving the physical and mathematical background, a part regarding the work performed for LISA Pathfinder and finally one part regarding the most recent work for LISA.

The first part: ‘Heterodyne interferometry’ lays the foundation of interferometric gravitational wave detection and introduces the interferometer output signals (chapter 2). The computation of the signals implemented in the LTP hardware is sketched and the similar implementation in the software QPD.c is described in detail (chapter 3). Finally, chapter 4 illustrates the meaning of the signals by means of a few selected examples.

The second part covers the work performed for LISA Pathfinder. Therefore, an overview of the mission and its technology are given in chapter 5. Special attention is given to the description of the bonding techniques and procedure as performed by UGL. As part of this thesis, this procedure was mimicked by a computer simulation, the LTP-OBI-Alignment Simulation which is described in chapter 6. The results obtained with this simulation concern coupling factors and cross coupling, noise spectrum estimates and the expected alignment of the LISA Pathfinder test masses in flight. These results are shown and discussed in chapter 7. Finally in chapter 8 it was investigated how a quadrant photodiode is optimally aligned to the laser beam in LTP if its signal needs to be used for amplitude stabilization of the impinging laser beam.

The third part considers the LISA mission, and after an introduction (chapter 9),



the search for a lens system is described that decouples the longitudinal pathlength readout from test mass angular jitter (chapter 10).

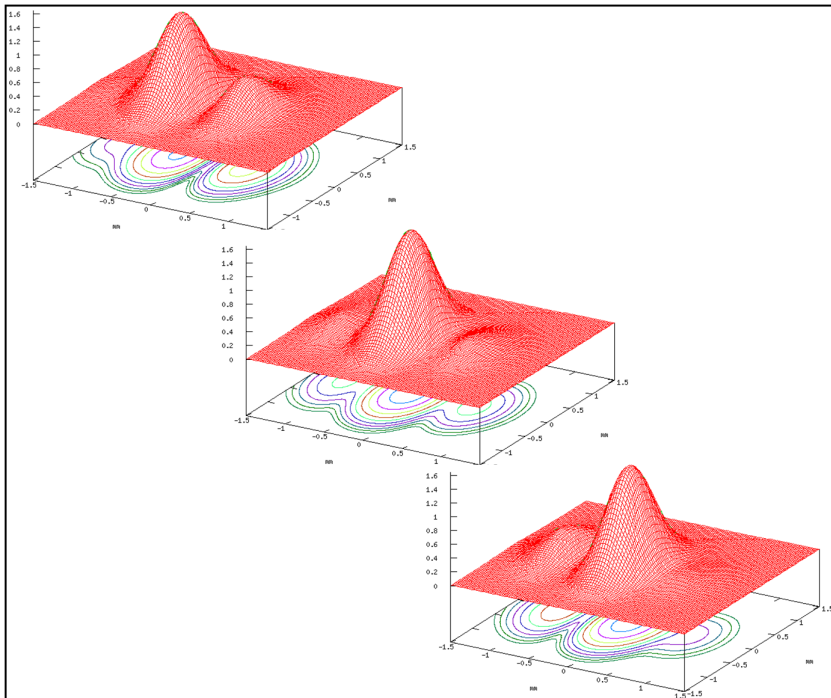
**This thesis is meant to be self-standing, such that any technical term used in this thesis is at least briefly explained and no additional literature is needed to understand the work performed.** For this purpose, a glossary in form of a miniature lexicon is prepared in the appendix. However, this thesis does not aim for completeness since the currently existing literature regarding the two missions LISA and LISA Pathfinder would cover a medium sized library. It is therefore not possible to completely describe either mission and their techniques in all detail in the scope of a thesis. For this reason bibliographic references are stated for the interested reader. Finally, a respectable amount of acronyms is used in the LISA and LISA Pathfinder community such that reading project documents can be like decrypting a secret code to a person new in the community. For better comprehensibility the use of these acronyms was reduced in this work. Nevertheless the commonly used acronyms are introduced in the text and briefly explained in the glossary, since they are needed to understand corresponding or deepening literature.





## Part I.

# Heterodyne interferometry





## 2. Detection principle and signal definition

*This chapter discusses the basics of interferometric gravitational wave detection. In the first section (section 2.1) the working principle of interferometric gravitational wave detectors is explained with the example of homodyne interferometers and simplified equations. In the second section (section 2.2) heterodyne interferometers and their time varying interference patterns are introduced. The time dependencies are computed and compared to the homodyne counterparts. Finally in section 2.3 heterodyne signals and the phase demodulation principle used in LISA Pathfinder are introduced.*

### 2.1. Detecting gravitational waves with homodyne interferometry

Gravitational waves cause an oscillating strain of the four dimensional space time orthogonal to their direction of propagation. This results in a change of the observed distances between masses, as shown in figure 2.1 for the end mirrors of a Michelson interferometer. The amplitude of the length change  $\Delta L$  caused by a gravitational wave of amplitude  $h$  on a distance  $L$  between two masses is

$$\Delta L = \frac{h \cdot L}{2} . \quad (2.1)$$

A derivation of this equation including the factor of 2 is shown in appendix A.1. In order to probe such a gravitational wave, at least two masses are needed whose distance  $\Delta L$  is monitored. These masses are called test masses (TMs) in analogy to electrodynamics, where test charges are used to probe electrical fields. The most precise readout method for distances is an interferometric readout. Therefore, test masses in earth-bound detectors are end mirrors of the corresponding laser interferometers. In case of LISA and LISA Pathfinder the test masses are small gold-platinum cubes from which the laser beams are reflected.

Assume a rather strong gravitational wave with an amplitude of the order of  $h \approx 10^{-21}$ . Using eq. (2.1), this would alter the distance  $L$  between Sun and Earth – which is approximately  $1.5 \cdot 10^8$  km – by roughly  $10^{-10}$  m, which is the diameter of an hydrogen atom. Likewise, such a gravitational wave would cause the geometrical arm length to change by  $\Delta L$  of:

$2.5 \cdot 10^{-12}$ m	in a LISA arm
$2 \cdot 10^{-18}$ m	in a LIGO arm
$3 \cdot 10^{-19}$ m	in a GEO600 arm
$1.5 \cdot 10^{-22}$ m	between LISA Pathfinder test masses.

## 2. Detection principle and signal definition

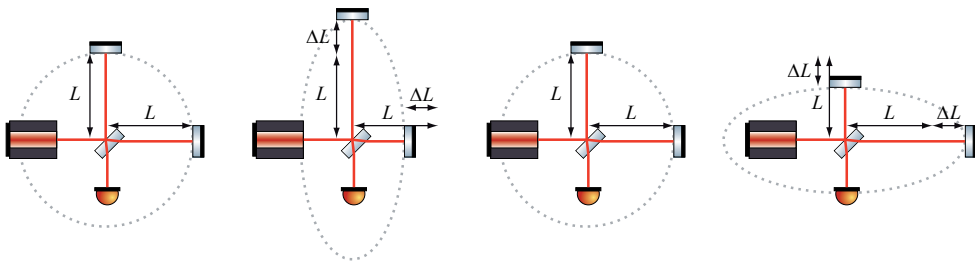


**Figure 2.1.:** Arm length changes in a simple Michelson interferometer if a gravitational wave impinges orthogonally to the shown plane.

This gives an impression why gravitational wave detectors are kilometer scale interferometers. It is also the reason why the arm length of LISA is even as long as 5 million km and why LISA Pathfinder – even though it has only a factor of 10 release in its noise budget – cannot measure gravitational waves.

Classical interferometers like the Michelson interferometer that was used in 1887 by Michelson and Morley in their investigation of the luminiferous ether are homodyne, that means the superimposing beams have the same frequency.

The detection principle in an interferometer is well known. The laser beam propagating through the interferometer arms accumulates a phase shift  $\phi$  over a distance  $s$ , the pathlength, by:

$$\phi = k \cdot s := \frac{2\pi}{\lambda} s . \quad (2.2)$$

The pathlength can then be related to the interferometer arm length  $L$ . In case of a Michelson interferometer, this relation is simply a factor of 2,  $s = 2 \cdot L$ , since the light propagates twice through the arms: from the beam splitter to the end mirror and back again. This phase is read from the detected power:

$$P = \bar{P}[1 + c \cdot \cos(\phi_0)] , \quad (2.3)$$

where  $\bar{P}$  is the mean detected power and  $c$  the measured contrast (see section 2.2.1). This phase  $\phi_0$  is a constant value that accounts for the different arm lengths. If both interferometer arms are exactly of the same length,  $\phi_0$  is zero. If the arm length changes, an additional phase  $\Delta\phi$  which is generally time dependent, is detected:

$$P = \bar{P}[1 + c \cdot \cos(\phi_0 + \Delta\phi)] . \quad (2.4)$$

From this measured phase shift it is then concluded that the interferometer arms changed by

$$\Delta L_m = 0.5 \Delta s_m = \frac{\lambda}{4\pi} \Delta\phi \quad (2.5)$$

The interpretation of a phase change as a length change is the working principle of every interferometer. However, one should carefully distinguish between the real length change  $\Delta L$  and the deduced measured length change  $\Delta L_m$ . An ideal detector provides

$\Delta L_m \equiv \Delta L$  at any time. In real detectors  $\Delta L_m$  contains  $\Delta L$  but also parts induced by the curvature of the interfering beams, their angle and shift with respect to each other, the location of the waists, frequency fluctuations and much more. This will be discussed more deeply in the following sections.

Interferometric gravitational wave detectors on Earth are today advanced homodyne Michelson interferometers. The detection scheme used in these detectors is slightly different than introduced above:

An ideal interferometer ( $\Delta L_m \equiv \Delta L$ ) with equal arm lengths and therefore  $\phi = 0$ , has according to eq. (2.3) a maximal power readout. It is then said to be locked to a bright fringe. If a gravitational wave passes such an interferometer, it induces a very small phase change which couples only in second order into the length measurement:

$$P = \bar{P}[1 + c \cdot \cos(\Delta\phi)] \quad (2.3)$$

$$\approx \bar{P} \left[ 1 + c \cdot \left( 1 - \frac{(\Delta\phi)^2}{2} \right) \right]. \quad (2.6)$$

Such a detection scheme with second order phase readout is not suitable for a gravitational wave detector, because of the extremely small length changes the detector aims to measure. Therefore, the arm lengths of the interferometer are intentionally shifted by half a fringe such that in absence of any noise or signal the interferometer does not sense any power, the interferometer is locked to a dark fringe. Special modulation techniques are then applied to extract the phase from the interferometer readout. The interested reader can find more information about such phase demodulation techniques for example starting with the key word Schnupp modulation [[Schnupp1988](#)] which is for instance described in [[Heinzel1999](#)]. The simplified equations stated above indicate the major requirement or disadvantage of homodyne detection: the absolute arm length of the interferometer needs to be stable to a high degree. Feedback loops control earth-bound gravitational wave detectors and keep the arm length stable, i.e. the detectors are locked to a dark fringe. Major seismic events cause phase drifts that cannot be corrected by the phase lock loops, the detector falls out of lock and needs to be locked again, often by human intervention.

The arm length stability achievable on ground cannot be ensured in space. LISA for example has an average arm length variation of approximately 15 m/s which is a variation of over ten million wavelengths per second. This cannot be implemented as a homodyne detection scheme. LISA and LISA pathfinder are therefore heterodyne.

## 2.2. Heterodyne interferometry

LISA and LISA Pathfinder will use heterodyne interferometry, that means the two superimposing beams are frequency shifted with respect to each other. In LISA, the frequency shifts originate from doppler shifts due to the relative motion of the spacecraft. In LISA Pathfinder the laser beams need to be actively frequency shifted. This can most easily be implemented in a Mach Zehnder interferometer (cf. figure 2.2) by shifting the laser frequency with acousto-optical modulators (AOM) in each arm. In LISA Pathfinder, the measurement beam is shifted by approximately 80 MHz + 0.5 kHz,

## 2. Detection principle and signal definition

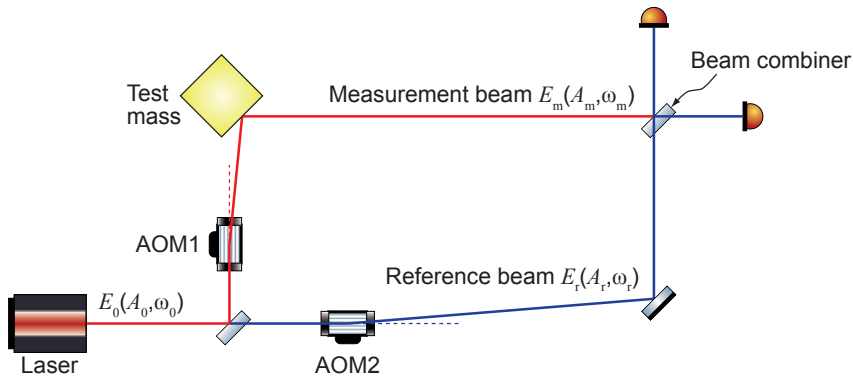


**Figure 2.2.:** Scheme of a heterodyne Mach Zehnder interferometer. The initial beam  $E_0$  is split into two beams. Each beam is frequency shifted by an AOM. The measurement beam ( $E_M$  with amplitude  $A_M$  and frequency  $\omega_M$ ) reflects on a moveable test mass, the reference beam ( $E_R$  with amplitude  $A_R$  and frequency  $\omega_R$ ) reflects from a fixed mirror. Both beams are recombined on a beam splitter labeled beam combiner.

the reference beam by  $80 \text{ MHz} - 0.5 \text{ kHz}$ . The beat frequency of the two laser beams is called the heterodyne frequency  $f_{\text{het}}$

$$f_{\text{het}} := f_M - f_R \quad (2.7)$$

and equivalently expressed for angular frequencies with  $\omega = 2\pi f$ :

$$\omega_{\text{het}} := \omega_M - \omega_R . \quad (2.8)$$

In LISA the heterodyne frequency is between 2 MHz and 20 MHz, for LISA Pathfinder it has a value of approximately 1 kHz:

$$f_{\text{het}}^{\text{LPF}} \approx (f_0 + 80 \text{ MHz} + 0.5 \text{ kHz}) - (f_0 + 80 \text{ MHz} - 0.5 \text{ kHz}) \quad (2.9)$$

$$\approx 1 \text{ kHz} , \quad (2.10)$$

where  $f_0$  is the initial laser frequency which can be computed from the wavelength  $\lambda = 1064 \text{ nm}$  of the Nd:YAG laser used in LISA and LISA Pathfinder and the vacuum speed of light  $c_0$  by

$$f_0 = \frac{c_0}{\lambda} \approx 281 \text{ GHz} . \quad (2.11)$$

Actually, the measurement and reference beam in a heterodyne interferometer have different wavelengths:

$$\lambda_{M,R} = \frac{c_0}{f_{M,R}} . \quad (2.12)$$

However, the frequency shift of  $\approx 1 \text{ kHz}$  in the case of LISA Pathfinder, or  $\approx 2..20 \text{ MHz}$  in case of LISA, is small compared to the initial laser frequency  $f_0$  such that  $\lambda_M = \lambda_R = \lambda$  can be generally assumed.

### 2.2.1. Power readout in heterodyne interferometers

For any heterodyne interferometer, the intensity on the photodiode can be expressed by the superposition of two fields of amplitude  $A_{M/R}$  that have different frequencies  $\omega_{M/R}$  and phases  $\Phi_{M/R}$ :

$$I = \|A_M \exp(i\omega_M t + i\Phi_M) + A_R \exp(i\omega_R t + i\Phi_R)\|^2. \quad (2.13)$$

Please see section 3.2.1 for a derivation and the precise definitions of  $A_{M,R}$  and  $\Phi_{M,R}$ . This intensity can be evaluated and rearranged

$$I = A_M^2 + A_R^2 + 2A_M A_R \cos([\omega_M - \omega_R]t + [\Phi_M - \Phi_R]) \quad (2.14)$$

$$= (A_M^2 + A_R^2) \left( 1 + \frac{2A_M A_R}{A_M^2 + A_R^2} \cos(\omega_{\text{het}} t + \Delta\Phi) \right), \quad (2.15)$$

whereas in the last step eq. (2.8) and the phase difference

$$\Delta\Phi := \Phi_M - \Phi_R \quad (2.16)$$

were used. The interference pattern (rings or fringes) of a homodyne interferometer

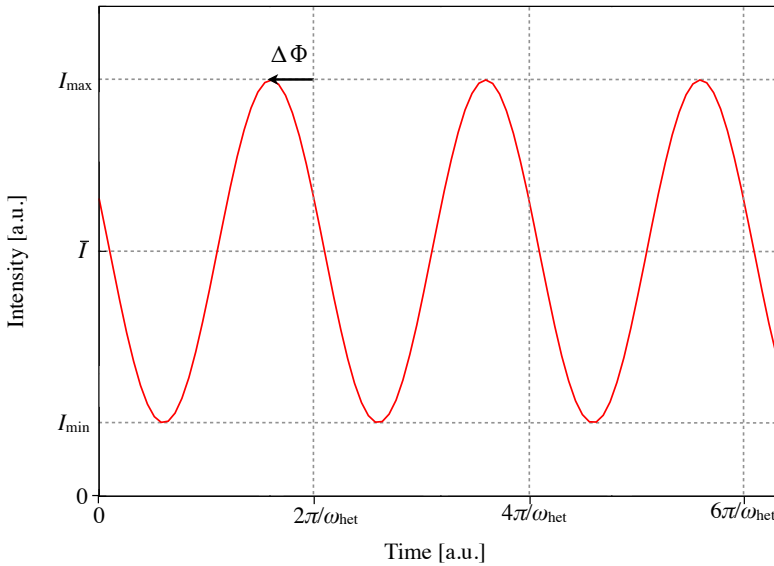


**Figure 2.3.:** Time variant intensity of an heterodyne interferometer. Shown is the mean Intensity  $\bar{I}$  the phase  $\Phi$  which carries information about variations in the interferometer arm lengths and the minimal and maximal intensity  $I_{\min}$ ,  $I_{\max}$  from which the contrast is defined.

is static and varies only with differential arm length changes of the interferometer. Equation (2.15) shows that this is different in a heterodyne interferometer:

In heterodyne interferometers the interference pattern oscillates with time, even if the arm lengths are constant.

## 2. Detection principle and signal definition

This is illustrated in figure 2.3. The maximum value  $I_{\max}$  is reached if the cosine in eq. (2.14) equals 1, and a minimum value  $I_{\min}$  if the cosine is  $-1$ :

$$I_{\max} = A_M^2 + A_R^2 + 2A_M A_R = (A_M + A_R)^2 \quad (2.17)$$

$$I_{\min} = A_M^2 + A_R^2 - 2A_M A_R = (A_M - A_R)^2. \quad (2.18)$$

The average intensity  $\bar{I}$  can be computed from  $I_{\max}$  and  $I_{\min}$  due to the sinusoidal shape of the intensity curve by:

$$\bar{I} = \frac{1}{2}(I_{\max} + I_{\min}) \quad (2.19)$$

$$= A_M^2 + A_R^2. \quad (2.20)$$

Finally, the contrast  $c_I$  of the intensity is defined as the ratio of the difference and sum of the maximum and minimum intensity, such that its value is

$$c_I = \frac{I_{\max} - I_{\min}}{I_{\max} + I_{\min}} \quad (2.21)$$

$$= \frac{2A_M A_R}{A_M^2 + A_R^2}. \quad (2.22)$$

Hence, eq. (2.15) can be rearranged using the average intensity  $\bar{I}$ , eq. (2.20), and the contrast  $c_I$ , eq. (2.22):

$$I = \bar{I}(1 + c_I \cos(\omega_{\text{het}} t + \Delta\Phi)). \quad (2.23)$$

$I$  in eq. (2.23) is an intensity, that is the power per area and depends not only on the time but also on the location. Alternatively,  $I$  can be interpreted as the power of an infinitesimal small detector or detector segment which is as such not directly measurable. If this is assumed, the power as measured by a detector (e.g. photodiode) can be computed from the intensity eq. (2.23) by integrating over the detector surface  $S$ :

$$P = \int_S d^2r I. \quad (2.24)$$

The intensity is in general not constant over the detector surface (as it is the well known interference pattern) and the mean intensity  $\bar{I}$ , contrast  $c_I$ , and phase difference  $\Delta\Phi$  vary over the detector surface, such that

$$P = \int_S d^2r \bar{I}(\vec{r}) [1 + c_I(\vec{r}) \cos(\omega_{\text{het}} t + \Delta\Phi(\vec{r}))]. \quad (2.25)$$

Even though this cannot be computed analytically for arbitrary fields and detector surfaces, the shape of the power function can be derived. The surface integral over the mean intensity is the mean power  $\bar{P}$  as measured by the detector

$$\int_S d^2r \bar{I}(\vec{r}) = \bar{P}. \quad (2.26)$$



Furthermore, it is known that the superposition of arbitrary harmonic oscillations is another harmonic oscillation [Bronstein]:

$$\sum_i a_i \cos(\omega t + \alpha_i) = a \cos(\omega t + \alpha) . \quad (2.27)$$

Generalizing this to integrals leads to

$$P = \int_S d^2 r \bar{I}(\vec{r}) [1 + c_I(\vec{r}) \cos(\omega_{\text{het}} t + \Delta\Phi(\vec{r}))] \quad (2.28)$$

$$= \bar{P} + a \cos(\omega_{\text{het}} t + \phi) , \quad (2.29)$$

where  $a$  is an unknown constant that depends on size and shape of the detector surface as well as on the properties of the impinging beams. The resulting contrast  $c$  for the detected power is defined analogous to the contrast  $c_I$  of the intensity (cf. eq. (2.21)):

$$c := \frac{P_{\max} - P_{\min}}{P_{\max} + P_{\min}} \quad (2.30)$$

$$= \frac{(\bar{P} + a) - (\bar{P} - a)}{(\bar{P} + a) + (\bar{P} - a)} \quad (2.31)$$

$$= \frac{a}{\bar{P}} . \quad (2.32)$$

Using the contrast, the power function gains a widely known form:

$$P = \bar{P}(1 + c \cos(\omega_{\text{het}} t + \phi)) . \quad (2.33)$$

Thus, the detected power in a heterodyne interferometer is a harmonic oscillation with time, plus a constant offset, such that  $P \geq 0$ .

A homodyne interferometer is actually a special form of a heterodyne interferometer with  $\omega_{\text{het}} = 0$ . Hence, eq. (2.3) results from eq. (2.33) if  $\omega_{\text{het}} = 0$ . Furthermore, the heterodyne power eq. (2.33) resembles in its form the heterodyne intensity, eq. (2.23). Nonetheless, the symbols for contrast and phase in both equations were intentionally chosen differently. The mean intensity, contrast and phase have generally a different value on any point or segment of a detector, such that

$$\bar{I} = \bar{I}(\vec{r}) \neq \bar{P} \quad (2.34)$$

$$c_i = c_i(\vec{r}) \neq c \quad (2.35)$$

$$\Delta\Phi = \Delta\Phi(\vec{r}) \neq \phi . \quad (2.36)$$

The detected mean power  $\bar{P}$ , contrast  $c$  and phase  $\phi$  depend on the detector shape (e.g. a circular quadrant photodiode with slit detects different values for  $\bar{P}$ ,  $c$  and  $\phi$  than a square single element photodiode). Nonetheless, it is always possible to convert the phase into a length – independent of the size and shape of the detector:

$$\phi = k \cdot \Delta s_{\text{m}} \quad (2.5)$$

$$= \frac{2\pi}{\lambda} \Delta s_{\text{m}} , \quad (2.5)$$

## 2. Detection principle and signal definition

also for an infinitesimal small detector:

$$\Delta\Phi = k \cdot \Delta s_m \quad (2.37)$$

$$= \frac{2\pi}{\lambda} \Delta s_m . \quad (2.38)$$

This measured pathlength change  $\Delta s_m$  therefore depends on the detector size and shape.

All equations given so far are simplified. Unfortunately, it is not possible to analytically compute the power in a homodyne or heterodyne interferometer for interfering Gaussian beams. Yet, it is possible to do it numerically. How this is done is shown in section 3.2. In that section the full equations are shown and a comparison to the simplified equations stated here is given.

### 2.3. Heterodyne signals

The term “heterodyne signals” is commonly used in the LISA Pathfinder community as a generic term for the interferometer signals to distinguish them from the signals of the various other modules like those of the capacitive sensors, star trackers, temperature sensors and charge sensors and many more. These signals are defined in the subsequent section explicitly for heterodyne interferometers. However, they can just as well be defined for any interferometer that allows for phase readout – i.e. in particular all signals can be defined for homodyne interferometers.

The only signal measured by a single element photodiode in a heterodyne interferometer is the time varying power  $P$  - or more accurately: the oscillating photocurrent which is proportional to  $P$ . A quadrant photodiode provides four of these photocurrents, one for each quadrant. Each photocurrent has the shape of eq. (2.33). From each photocurrent the average power  $\bar{P}$ , contrast  $c$ , and phase  $\phi$  can be computed. Furthermore, the photocurrents of all quadrants can be added which gives another set of  $\bar{P}$ ,  $c$  and  $\phi$ . From these 15 signals, six heterodyne signals are derived: the phase signal, the horizontal and vertical DC signals, the horizontal and vertical DWS signals and the overall contrast.

One possibility to generate the phase readout and to compute heterodyne signals is shown in the subsequent section. Examples of interferometers and their heterodyne signals are given in section 4.

#### Pathlength signal

Extracting the phase  $\phi$  from a photocurrent (often called phase demodulation) is an important part of every interferometric gravitational wave detector, since  $\phi$  contains the information about changes in the interferometer arm length. Therefore, the phase carries the information about passing gravitational waves. The phase  $\phi$  is thus the main science signal and phasemeters are specially designed for each detector to guarantee optimal phase readout.

The principle of phase demodulation used in LTP is a single-bin discrete Fourier transform (SBDFT) which is an implementation of the following few equations:

$$\phi = -\arctan\left(\frac{\text{int2}}{\text{int1}}\right), \quad (2.39)$$

where int1 and int2 are defined as

$$\text{int1} := \int_0^{2\pi} d(\omega_{\text{het}}t) \cos(\omega_{\text{het}}t) \cdot P(\omega_{\text{het}}t) = \bar{P}c\pi \cos(\phi) \quad (2.40)$$

$$\text{int2} := \int_0^{2\pi} d(\omega_{\text{het}}t) \sin(\omega_{\text{het}}t) \cdot P(\omega_{\text{het}}t) = -\bar{P}c\pi \sin(\phi). \quad (2.41)$$

Here,  $P$  is the detected power which is a function of the angular heterodyne frequency  $\omega_{\text{het}}$  and time  $t$  as shown in eq. (2.33). Thus multiplying the detected power by a cosine or a sine function respectively, integrating these signals over one period of the oscillation and calculating the arctangent from the quotient of these two signals gives the desired phase. It is convenient to convert the phase signal into a length according to eq. (2.5):

$$\Delta s_{\text{m}} = \frac{\phi}{k}. \quad (2.5a)$$

The thereby computed or measured length is generally referred to as the pathlength signal or the pathlength readout.

### Contrast

The contrast can be computed from eq. (2.40) and eq. (2.41) by

$$c = \frac{\sqrt{(\text{int1})^2 + (\text{int2})^2}}{\bar{P}\pi}, \quad (2.42)$$

which means that the mean power  $\bar{P}$  needs to be computed. This is done by integrating over one period of the oscillation, this time without the multiplication of a sine or cosine:

$$\bar{P} = \frac{1}{2\pi} \int_0^{2\pi} d(\omega_{\text{het}}t) P. \quad (2.43)$$

These three signals – the phase  $\phi$ , contrast  $c$  and mean power  $\bar{P}$  – is all that can be extracted from the photocurrent of one so-called single element photodiode (SEPD). To gain information of the incident angle and spot position of the measured beam, quadrant photodiodes (QPDs) are used instead of SEPDs. These QPDs consists of four segments (quadrants) separated by insensitive slits and provide phase, contrast and power signals for each quadrant. Thereby QPDs provide a spatial distribution of the beam power and phase. These signals can then be used to align the beam, test mass or spacecraft.

In LISA Pathfinder the QPDs are circular shaped with a diameter of 5 mm and the insensitive slit of 45  $\mu\text{m}$  width.

### DC signal

Comparing the mean power from different segments gives information about the position of the beam centroid and thus allows for fine alignment of the beam axes. There are two such alignment signals used for LISA and LISA Pathfinder: the horizontal and vertical DC signals

$$\text{DC}_h := \frac{\bar{P}_{\text{left}} - \bar{P}_{\text{right}}}{\bar{P}_{\text{left}} + \bar{P}_{\text{right}}} \quad (2.44)$$

$$\text{DC}_v := \frac{\bar{P}_{\text{top}} - \bar{P}_{\text{bottom}}}{\bar{P}_{\text{top}} + \bar{P}_{\text{bottom}}} . \quad (2.45)$$

The DC signal thus measures the position of the beam centroid relative to the photodiode. In LTP, this beam centroid position is (in a fairly wide range) proportional to the test mass angle. Thus, the DC signal is used in LTP for an initial angular alignment of the two test masses. This is described in more detail in section 5.3.3.

The term ‘‘DC’’ is taken from the known abbreviation for direct current and refers to the time constance of this signal. Nevertheless, the mean power on a quadrant can vary with time due to beam jitter and laser amplitude noise. Thus, it is possible to define a seemingly contradictory term: ‘‘DC-spectrum’’. More details on this subject will follow in section 8.2.3.

### DWS signal

The phase signals of the quadrants can be compared just as it is done with the mean power to generate the DC signals. The resulting signals are called *differential wave front sensing signals*, better known under the acronym DWS. It is generally defined either for the horizontal  $\text{DWS}_h$  or vertical  $\text{DWS}_v$  direction:

$$\text{DWS}_h = \phi_{\text{left}} - \phi_{\text{right}} \quad (2.46)$$

$$\text{DWS}_v = \phi_{\text{top}} - \phi_{\text{bottom}} . \quad (2.47)$$

Such a DWS signal measures the relative angle between two wavefronts and has, due to its definition, the unit ‘rad’. The underlying working principle is sketched in figure 2.4: if the incident beams are tilted with respect to each other, a phase difference on the left and right or top and bottom halves of the QPD occurs. Subtracting thus the phases for example on the left and right half of the QPD, results in a signal which depends on the relative angle  $\alpha$  between the wavefronts of the two interfering beams. In a small range, the DWS signal is proportional to this relative angle. If the angle is generated by tilting a component like a test mass, then the DWS signal is in a small range also proportional to the in-plane angle  $\varphi$  or out of plane tilt  $\eta$  of the component:

$$\text{DWS}_h = k_\varphi^{\text{DWS}} \varphi \quad (2.48)$$

$$\text{DWS}_v = k_\eta^{\text{DWS}} \eta . \quad (2.49)$$

The factor of proportionality called coupling factor is usually of the order of a few thousand, which makes the DWS signals optimal for measuring small angular changes. Therefore, the DWS signals will be used in the LISA and LISA Pathfinder missions for

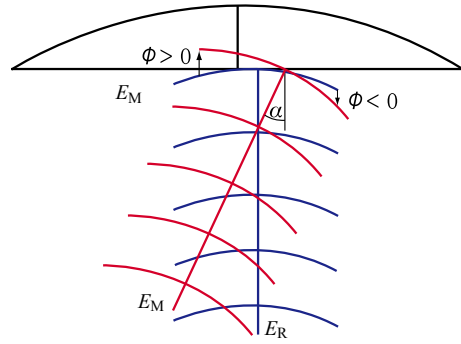


**Figure 2.4:** Working principle of differential wave front sensing (DWS). If one beam is tilted in plane with respect to the other, the phases on the left and right halves of a QPD differ. Subtracting the phase signals of the left and right quadrants results in a signal which is sensitive to an in-plane tilt of the beams. The same is true for out of plane rotations and the top and bottom segments of the QPD.

test mass angular readout and control. The DWS technique was originally developed for Fabry-Pérot cavities with Pound-Drever-Hall modulation and readout [[Morrison1994-1](#), [Morrison1994-2](#)].



## 3. Phase demodulation at LISA Pathfinder

The first section (section 3.1) sketches the technical implementation of the phase readout (often called phase demodulation) and signal generation in LISA Pathfinder as far as it is needed to understand the present thesis. The interested reader can find more detailed information on this topic e.g. in references [Wand2007] and [Heinzel2004]. Section 3.2 shows how this signal generation is imitated by QPD.c and IfoCad, the software tools used throughout this thesis for simulations. This section is thus the third and final step of introducing heterodyne signals: the first basic step were simplified equations for homodyne interferometers (section 2.1) which were then generalized to simplified heterodyne equations in section 2.2. Finally section 3.2 introduces non-simplified equations, which can only be evaluated numerically.

### 3.1. Experimental phase demodulation at LISA Pathfinder

The generation of heterodyne signals in LISA Pathfinder is done by the phasemeter and the data management unit (DMU) following the principle sketched in figure 3.1. The photocurrent of each quadrant is fed to the phasemeter, where it is converted to a voltage by a transimpedance amplifier and digitized by an analog to digital converter (ADC) with a sampling frequency  $f_{\text{samp}}$ . Ideally (i.e. noise free), the result is a discrete series of voltages of the form

$$V_n^i := C_1 \cdot \bar{P}_i \left[ 1 + c_i \cos \left( \omega_{\text{het}} \frac{n}{f_{\text{samp}}} + \phi_i \right) \right], \quad (3.1)$$

where  $i$  labels the quadrants of the QPD and  $C_1$  is the factor of proportionality between photovoltage and beam power. However, this constant cancels in the computation of the heterodyne signals. The measured voltage is multiplied by discrete values of a cosine or sine function respectively (taken from a look up table), and subsequently summed over  $N$  measurement points:

$$\Re(\tilde{V}^i) = \sum_{n=0}^{N-1} V_n^i \cdot \cos \left( \omega_{\text{het}} \frac{n}{f_{\text{samp}}} \right) \quad (2.40a)$$

$$\Im(\tilde{V}^i) = \sum_{n=0}^{N-1} V_n^i \cdot \sin \left( \omega_{\text{het}} \frac{n}{f_{\text{samp}}} \right). \quad (2.41a)$$

The labeling  $\Re$  and  $\Im$  indicate that the stated equations correspond to the real and imaginary part of a single-bin discrete Fourier transform (SBDFFT) which is the

### 3. Phase demodulation at LISA Pathfinder

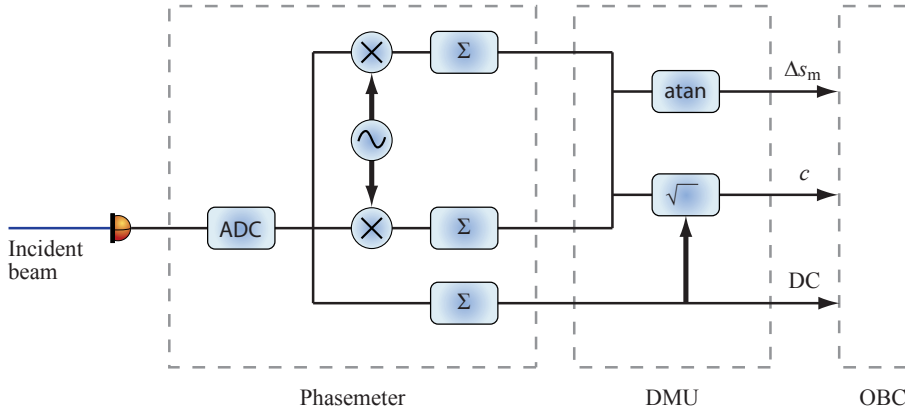


**Figure 3.1.:** Simplified sketch of phase demodulation used in LISA Pathfinder. The photocurrent provided by the QPD is fed to an analog to digital converter (ADC). The resulting voltage is multiplied (X symbol) by values of a sine or cosine respectively ( $\sim$  symbol) and summed ( $\Sigma$  symbol). The resulting signals are passed to the data management unit (DMU) which finally computes the heterodyne signals. These are passed to the on board computer (OBC) which passes then signals to the inertial sensors and thrusters to counteract sensed motion.

implementation of the integrals given in eq. (2.40)-(2.41). A third channel adds the originally digitized signal up and thereby computes the mean power on quadrant  $i$  according to eq. (2.43):

$$\bar{P}^i = \frac{1}{2\pi} \frac{1}{C_1 \bar{n}_p} \sum_{n=0}^{N-1} V_n^i. \quad (2.43a)$$

Unlike in the continuous form shown in eq. (2.43), the summation is not over one but over several periods, which reduces noise. The number of periods  $\bar{n}_p$  is given by

$$\bar{n}_p = \Delta t \cdot f_{\text{het}} \quad (3.2)$$

$$= \frac{N}{f_{\text{samp}}} \cdot f_{\text{het}}, \quad (3.3)$$

where  $\Delta t$  is the integration time. The following numbers apply for the LTP phasemeter and the AEI laboratory phasemeter PM3 (see figure 3.2):

$$N = \begin{cases} 20000 & \text{for PM3} \\ 500..1000 & \text{for LTP} \end{cases} \quad f_{\text{samp}} = \begin{cases} 800 \text{ kHz} & \text{for PM3} \\ 50..100 \text{ kHz} & \text{for LTP} \end{cases}.$$

For a heterodyne frequency of  $f_{\text{het}} = 1$  kHz, this implies an averaging over approximately  $\bar{n}_p = 60$  periods in case of the LTP phasemeter and  $\bar{n}_p = 150$  periods in case of the phasemeter PM3. In QPD.c this averaging is not implemented, since there is no need for noise reduction.

The signals of the three channels (eq. (2.40a), (2.41a) and (2.43a)) are passed to the



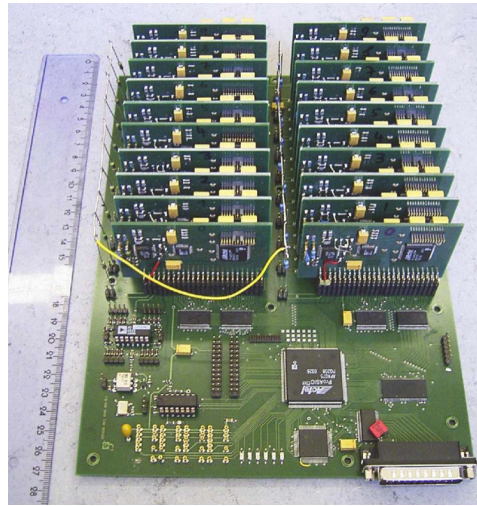


**Figure 3.2:** Photograph of the AEI phasemeter PM3 which was developed to provide phase demodulation for LTP related experiments.

DMU which computes the phase signal by

$$\phi = -\arctan\left(\frac{\Im(\tilde{V})}{\Re(\tilde{V})}\right), \quad (2.39a)$$

and the DWS, DC and contrast with equations similar to those shown in the previous section (eq. (2.39), (2.42), (2.44) – (2.47)). These signals are then passed to the on board computer (OBC) which sends signals to the thrusters and capacitive sensors. This will be further discussed in section 5.3.3.

The exact implementation in the LTP phasemeter and DMU is more complicated than shown here. For instance, the following algorithms are implemented:

- Phase tracking: removes phase jumps by adding an integer multiple of  $2\pi$ . Due to this phase tracking algorithm the test mass position can be monitored over many fringes.
- For each QPD in LTP there is a redundant QPD. The signals of these redundant QPDs are averaged by adding up the phasemeter signals before applying the arctan in the DMU to extract the phase.
- On the OBI of LTP there exist four interferometers: the x1-, x12-, frequency- and reference interferometer, which will be described in more detail in section 5.2. The phase signals of the reference interferometer is subtracted from the x1- and x12-phase signals in order to provide a phase reference.
- Failure detection isolation and recovery (FDIR) is implemented which defines the signal processing in the case of failure of single quadrants.

Further details on this phasemeter can be found for example in references [Wand2007, Heinzel2004, Steier2008].

## 3.2. Simulation of the LISA Pathfinder phase demodulation

In section 2.2.1 the heterodyne power was introduced using simplified equations for the electric field. Unfortunately, there is no way to compute the heterodyne power analytically for Gaussian beams in the general case when both beam parameters and beam axis differ. Nonetheless, it is possible to compute the time-varying heterodyne power numerically and deduce the heterodyne signals from this power. The following section (section 3.2.1) shows the full equations of the electric field and gives a comparison to the simplified equations of section 2.2.1 and section 2.1.

In section 3.2.2 it is shown how the heterodyne power, which is proportional to the photocurrent of a photodiode in a heterodyne interferometer, can be computed numerically. The stated equations are implemented in a script-based software called QPD.c and were recently (winter 2009) also implemented in a ray tracing and interferometer optimization tool called IfoCad. Both programs are written by Gerhard Heinzl.

Unlike IfoCad, which is a self standing program, QPD.c needs the input of a set of Gaussian beam parameters which are typically computed by OptoCad, a script-based Fortran program by Roland Schilling that ray-traces Gaussian beams through two dimensional optical setups. Both IfoCad and QPD.c compute in a first step the time-varying photocurrent as described in section 3.2.2. In a second step, they imitate the procedures of the LTP phasemeter and data management unit (DMU) to compute the heterodyne signals. This second step of computing heterodyne signals from a given photocurrent is described in section 3.2.3.

QPD.c was extensively used for all simulations done throughout this thesis. IfoCad was used mainly for the design of the LISA Imaging Optics, described in section 10.

### 3.2.1. Gaussian beams

The electric field of a Gaussian beam has the shape shown in figure 3.3. Let  $z$  be the direction of propagation of the beam. The radius  $w(z)$ , also called spot size, of a Gaussian beam is defined as the value where the intensity drops to  $1/e^2$  of the axial value. The value  $z$  is the distance from the minimum beam spot size, the waist  $w_0$ , such that

$$w(z = 0) = w_0 . \quad (3.4)$$

At the so-called Rayleigh range  $z_0$  the spot size is increased by  $\sqrt{2}$  with respect to the waist size:

$$w(z_0) = \sqrt{2}w_0 . \quad (3.5)$$

Generally, the spot size is computed from the Rayleigh range  $z_0$ , and the waist size  $w_0$ , by

$$w(z) = w_0 \sqrt{1 + \left(\frac{z}{z_0}\right)^2} . \quad (3.6)$$

This equation was used to plot the red lines which represent the beam size in figure 3.3. The Rayleigh range and the waist size of a beam with wavelength  $\lambda$  are related by:

$$w_0 = \sqrt{\frac{z_0 \cdot \lambda}{\pi}} . \quad (3.7)$$

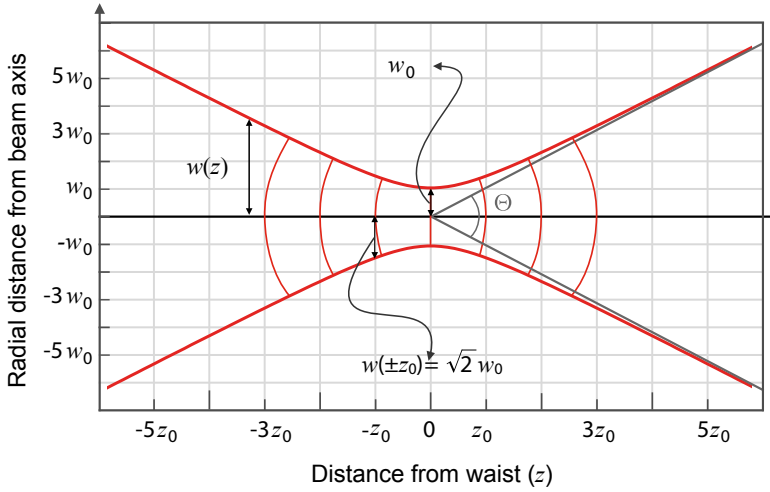


**Figure 3.3.:** Gaussian beam properties. Shown are the waist  $w_0$ , spot size  $w(z)$  and the meaning of the Rayleigh range  $z_0$ . Furthermore the divergence  $\theta_{\text{div}}$  of the beam is half of the opening angle  $\theta_{\text{div}} = \frac{\Theta}{2}$ .

The red arcs of circles in figure 3.3 indicate the wavefronts of the Gaussian beam, that means all points with the same phase  $\phi$ . These wavefronts have locally the shape of spheres which can be fully represented by their radius: the radius of curvature  $R(z)$ . This can be computed from the Rayleigh range  $z_0$  and the distance  $z$  from the waist:

$$R(z) = z \left[ 1 + \left( \frac{z_0}{z} \right)^2 \right]. \quad (3.8)$$

Its shape is illustrated in figure 3.4.

A Gaussian beam collects an additional phase shift of  $\pi$  when it passes its waist. This additional phase is called Gouy phase  $\zeta(z)$  and has a value of

$$\zeta(z) := \arctan(z/z_0). \quad (3.9)$$

This is illustrated again in figure 3.4. Finally, the complex beam parameter  $q(z)$  is defined as

$$q(z) := z + iz_0, \quad (3.10)$$

and the wavenumber  $k$  is

$$k = 2\pi/\lambda. \quad (3.11)$$

A Gaussian beam is symmetric with respect to the axis of propagation – the beam axis. Thus, cylindrical coordinates are used:  $(r, z) = (\sqrt{x^2 + y^2}, z)$ . Using all given definitions and setting the electric constant  $\epsilon_0$ , and the magnetic constant  $\mu_0$ , to one, the electric field of a Gaussian beam can be written in the standard form:

$$E(r, z, t) = E(r, z) \cdot \exp(i\omega t) \quad (3.12)$$

### 3. Phase demodulation at LISA Pathfinder

with

$$E(r, z) = E_0 \frac{w_0}{w(z)} \exp\left(-\frac{ikr^2}{2q(z)} + i\zeta(z) - iks\right) \quad (3.13)$$

according to references [Yariv] or [Saleh]

$$E(r, z) = E_0 \frac{w_0}{w(z)} \exp\left(\frac{-r^2}{w(z)^2}\right) \cdot \exp\left(-\frac{ikr^2}{2R(z)} + i\zeta(z) - iks\right), \quad (3.14)$$

where  $s$  is the optical pathlength. It takes into account the phase accumulated by the beam since its initial definition point, which might be the position of the laser or the end of a fiber injector. The variables  $s$  and  $z$  differ thus only by an offset in their origin.

Both representations of the electric field (eq. (3.13) and eq. (3.14)) are equivalent. This is shown in appendix B.1. The representation of the electrical field  $E(r, z)$  shown in eq. (3.14) allows easy computation of the beam power  $P_b$ , which is the surface integral of the absolute square of  $E(r, z)$ :

$$P_b = \int d^2r \|E(r, z)\|^2 \quad (3.15)$$

$$= 2\pi \int_0^\infty dr r \|E(r, z)\|^2 \quad (3.16)$$

$$= 2\pi E_0^2 \frac{w_0^2}{w(z)^2} \int_0^\infty dr r \exp\left(\frac{-2r^2}{w(z)^2}\right) \quad (3.17)$$

$$= 2\pi E_0^2 \frac{w_0^2}{w(z)^2} \cdot \frac{w(z)^2}{4} \quad (3.18)$$

$$= \frac{w_0^2 \pi E_0^2}{2}. \quad (3.19)$$

Since the power  $P$  is directly observable in contrast to the amplitude  $E_0$ , eq. (3.19) is solved for  $E_0$ :

$$E_0 = \sqrt{\frac{2P_b}{\pi w_0^2}}, \quad (3.20)$$

and used to replace  $E_0$  in the electric field which then gives the form

$$E(x, y, z) = \sqrt{\frac{2P_b}{\pi w(z)^2}} \exp\left[-\frac{ikr^2}{2q(z)} + i\zeta(z) - iks\right] \quad (3.13a)$$

or

$$E(r, z) = \sqrt{\frac{2P_b}{\pi w(z)^2}} \exp\left(\frac{-r^2}{w(z)^2}\right) \cdot \exp\left[-\frac{ikr^2}{2R(z)} + i\zeta(z) - iks\right]. \quad (3.14a)$$

A comparison of eq. (3.14a) and eq. (3.12) with eq. (2.13) shows that the amplitudes  $A_M$  and  $A_R$  have Gaussian profile:

$$A_{M,R} = \sqrt{\frac{2P_b}{\pi w(z)^2}} \exp\left(\frac{-r^2}{w(z)^2}\right). \quad (3.21)$$

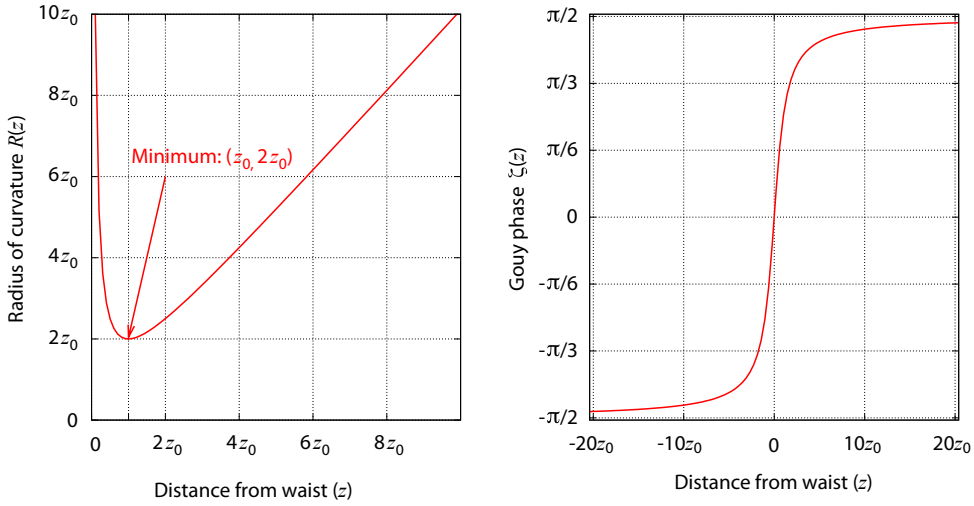


**Figure 3.4.:** Radius of curvature  $R(z)$  (left graph) and Gouy phase  $\zeta(z)$  (right graph) of a Gaussian beam.

The phase  $\Phi$ , of each beam in eq. (2.13) is then

$$\Phi = -\frac{kr^2}{2R(z)} + \zeta(z) - ks, \quad (3.22)$$

and is thus a function of  $r$ ,  $z$  and  $s$ . The phase difference  $\Delta\Phi$  consequently is a function of the pathlength difference accumulated since the beam waist:  $\Phi = k(s_M - s_R) = k\Delta s$ , but also of the relative displacement and tilts with respect to each other, their radii of curvature and Gouy phases.

### 3.2.2. Computing photocurrents of a QPD

In order to simulate the signal processing in the phasemeter and DMU, it is necessary to simulate the photocurrent which is fed to the phasemeter. This photocurrent is proportional to the detected beam power but the constant of proportionality is not known. However, this constant is not needed, since it cancels from the definitions of the heterodyne signals.

On the photodiode, there are two impinging beams. The first one is the measurement beam (labeled with an underscore “M” and is generally drawn in red), the second one is the reference beam (labeled with an underscore “R” and generally drawn in blue). The latter one is often called local oscillator. The equations for the electric field are generally given in the coordinate system of the beam, where the  $z$ -axis is the beam axis which shows the direction of propagation and  $r$  is the radial distance from the beam axis. For a computation of the beam intensity at any location on the detector surface, a coordinate transformation is needed that transforms beam coordinates into detector-surface coordinates.

### 3. Phase demodulation at LISA Pathfinder

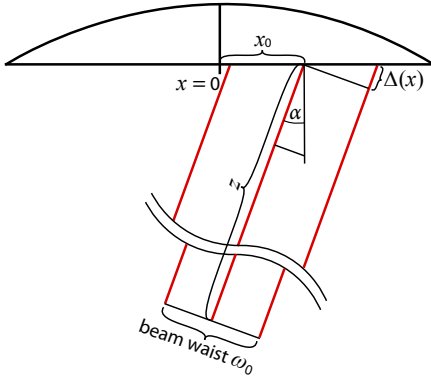


**Figure 3.5:** Incident beam on a QPD. Shown is one beam with incident angle  $\alpha$  and horizontal offset  $x_0$  from the center of the QPD. This figure shows that a beam segment at position  $x$  propagates an additional pathlength of  $\sin(\varphi) + (x - x_0)$  with respect to the beam centroid located at  $x_0$ . This additional pathlength is accounted for in the coordinate transformation of eq. (3.23) and eq. (3.25).

The coordinate system of a photodiode throughout this work is:

- $x$ -axis: horizontal axis (in plane of the photodiode's active surface)
- $y$ -axis: vertical axis (in plane of the photodiode's active surface)
- $z$ -axis: orthogonal to the surface of the photodiode .

For simplicity, it is assumed that both beams can only be misaligned in the horizontal plane, such that each beam impinges on the photodiode with a distinctive angle  $\varphi_{M,R}$  and a horizontal offset  $x_{0M,R}$  of the beam centroid to the center of the QPD. This leads to an effective longitudinal shift  $\Delta_{M,R}(x)$  of the beam depending on the distance  $(x - x_{0M,R})$  of a beam segment to the centroid position (cf. figure 3.5):

$$z_{M,R} \rightarrow z_{M,R} + \sin(\varphi_{M,R})(x - x_{0M,R}) \quad (3.23)$$

$$=: z_i + \Delta_{M,R}(x) . \quad (3.24)$$

Since  $z$  and  $s$  differ only in their origin, the same substitution is also valid for the optical pathlength  $s$ :

$$s_{M,R} \rightarrow s_{M,R} + \Delta_{M,R}(x) . \quad (3.25)$$

The radial distance  $r$  underlies likewise a coordinate transformation which can be deduced from cf. figure 3.5:

$$r = \sqrt{x^2 + y^2} \rightarrow r_{M,R} = \sqrt{\cos^2(\varphi_{M,R}) \cdot (x - x_{0M,R})^2 + y^2} . \quad (3.26)$$

This coordinate transformation affects only  $x$ , not  $y$ , because the beam is never vertically tilted. This stems from the interaction of QPD.c with OptoCad, which will be explained in more detail in chapter 6. OptoCad is a 2D program and cannot handle vertical tilts. Hence, there is no need to transform the  $y$  coordinate.

Combining all equations given so far, the spatial part of the electric field obtains the following form

$$E_{M,R}(x, y, z_{M,R}) = \frac{\sqrt{2P_{M,R}}}{\sqrt{\pi}w_{M,R}} \exp \left[ -ik\Delta_{M,R} + i\zeta_{M,R} - i\frac{kr_{M,R}^2}{2q_{M,R}} \right] \cdot \exp[-iks_{M,R}] . \quad (3.27)$$

At this point, the phase  $ks_{M,R}$  is split off to avoid numerical problems. These might occur since  $s_{M,R}$  is the distance of the waist to the photodiode which is in LISA Pathfinder of the order of tens of centimeters. The phase shifts of interest result from misalignments which are of the order of a few microns and need to be computed to picometer precision.

In order to allow clearer arrangements, the complex amplitudes  $a_{M,R}$  are defined:

$$a_{M,R} := \frac{\sqrt{2P_{M,R}}}{\sqrt{\pi}w_{M,R}} \exp \left[ -ik\Delta_{M,R} + i\zeta_{M,R} - i\frac{kr_{M,R}^2}{2q_{M,R}} \right] \quad (3.28)$$

and the electric field takes the form

$$E_{M,R}(x, y, z_{M,R}, t) = a_{M,R} \cdot \exp[-iks_{M,R} + i\omega_{M,R}t] . \quad (3.29)$$

From this, the power on a surface  $S$  at a time  $t$  can be computed by

$$P^S = \int_S d^2r \|E_M + E_R\|^2 \quad (3.30)$$

$$= \int_S d^2r \|a_M \exp[-iks_M + i\omega_M t] + a_R \exp[-iks_R + i\omega_R t]\|^2 \quad (3.31)$$

$$= \int_S d^2r \|a_M + a_R \cdot \exp[ik(s_M - s_R) + i\omega_{het}t]\|^2 . \quad (3.32)$$

Evaluating this integral over the surfaces of the quadrants of a QPD leads to the time-varying power detected by the QPD quadrants. That means, at this point the photocurrent is computed except for a factor of proportionality.

As input for the computation, the following parameters are needed for each beam:

- $z$  distance propagated from waist to detector surface
- $z_0$  Rayleigh range
- $x_0$  offset of beam to center of the detector in horizontal direction
- $\alpha$  incident angle on detector relative to the normal vector on the surface
- $s$  total pathlength propagated
- $P$  beam power .

These values are called beam parameters, because they fully describe a laser beam in its fundamental mode.

### 3.2.3. Computing heterodyne signals

As it is done in the phasemeter, the photocurrent needs to be digitized, i.e. discretized. The straight forward method of implementation would be a substitution of the form

$$t \rightarrow \frac{n}{f_{\text{samp}}} . \quad (3.33)$$

This is not done because of two reasons. The first one is that there are no noise sources implemented in the simulation, such that there is no need to average over

### 3. Phase demodulation at LISA Pathfinder

several periods as it is implemented in the phasemeters. Therefore, a substitution of the following form could be implemented in order to use the formalism of Surrel [Surrel2000]:

$$\int_0^{2\pi} d(\omega t) F(\omega t) \rightarrow \sum_{n=0}^{N-1} \delta \cdot F(\delta n), \quad (3.34)$$

where  $\delta$  is given by

$$\delta = \frac{2\pi}{N}. \quad (3.35)$$

An implementation of this form would likely lead to numerical evaluation problems, since the phase decomposes in a macroscopic and a microscopic part. The macroscopic part is accumulated when the beam travels the distance from the waist position to the QPD which is in case of LISA Pathfinder of the order of centimeters. The microscopic part is the phase of interest. It results from test mass misalignment, is of the order of micrometers and needs to be computed to picometer precision. To allow separation of these two phases in the computation and thus avoid numerical problems, the macroscopic phase is subtracted from the discretized power on each surface  $s$  by substituting

$$k(s_M - s_R) + \omega_{het} t \rightarrow n\delta, \quad (3.36)$$

such that the power on a surface  $S$  at a specific phase  $n$  (referring to a specific time) is

$$P_n^S = \int \int_S dx dy \|a_M + a_R \cdot \exp[in\delta]\|^2. \quad (3.37)$$

The equations given in this section can be implemented in any software, like e.g. MATLAB or Mathematica. For the present thesis, the implementation in a C program was used. The implementation of the surface integral was accomplished by an adaptive 2D integrator [Berntsen1991]. This integrator computes 2D square integrals only, which means QPD.c evaluates by default signals for square shaped QPDs. There is no simple way to change the integrator to compute the signals of circular QPDs. Therefore, whenever it is necessary to compute signals of circular photodiodes, the electric field is multiplied by a mask-function of the correct shape before the integration is performed.

Finally, the phase is extracted with the discretized form of eq. (2.39)-(2.41):

$$\phi_{\text{micro}} = -\arctan\left(\frac{\text{sum2}}{\text{sum1}}\right), \quad (2.39b)$$

where sum1 and sum2 are computed by

$$\text{sum1} := \delta \sum_{s=q1}^{q4} \sum_{n=0}^{N-1} \cos(n\delta) \cdot P_n^s \quad (2.40b)$$

$$\text{sum2} := \delta \sum_{s=q1}^{q4} \sum_{n=0}^{N-1} \sin(n\delta) \cdot P_n^s \quad (2.41b)$$

using quadrant labeling according to figure 3.6(a). The labeling was intentionally not



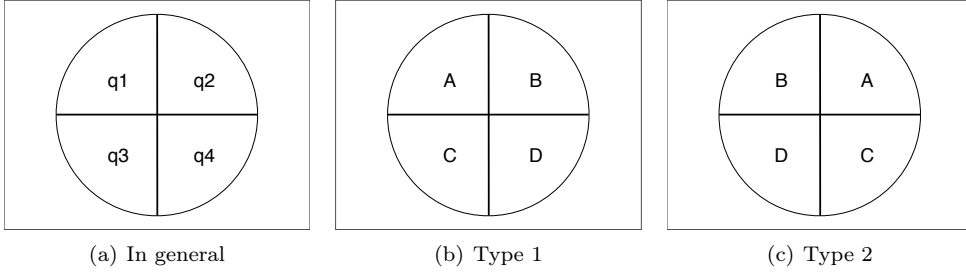


**Figure 3.6.:** Labeling of the quadrants of a quadrant photodiode (QPD). In LTP QPDs are labeled either according to Type 1 or Type 2 in order to account for the opposing beam walk on redundant counterparts caused by beam tilts (see appendix A.5 and figure A.5 for an illustration). In QPD.c there is no differentiation between these types of QPDs, therefore the equations given here use a general form shown in (a).

chosen in the widely used form shown in figure 3.6(b), to differ it from the also used inverted form shown in figure 3.6(c). These different types of labeling QPDs is briefly discussed in appendix A.5.

Since no noise is implemented,  $N$  could be as small a number as 4. By default  $N = 16$  is used in QPD.c for consistency and error check. Due to the phase shift of  $-k(s_R - s_M)$  inserted in eq. (3.36), the phase evaluated here is only the microscopic phase  $\phi_{\text{micro}}$  to which the macroscopic phase has to be added:

$$\phi = \phi_{\text{micro}} + k(s_R - s_M). \quad (3.38)$$

The total pathlength propagated is a value that ray tracing tools like OptoCad compute. In case of QPD.c, this value is taken directly as input from OptoCad and defines the macroscopic phase. For the DWS signal, only the microscopic phases on the left, right, upper and lower halves of a QPD are needed. However, the macroscopic phase is constant over all segments of a QPD and thus cancels in the definition of the DWS signals:

$$\text{DWS}_h = \phi_{\text{left}} - \phi_{\text{right}} \quad (2.46)$$

$$\text{DWS}_v = \phi_{\text{top}} - \phi_{\text{bottom}}, \quad (2.47)$$

with

$$\phi_{\text{left}} = -\arctan\left(\frac{\sum_{n=0}^{N-1} \sin(n\delta) \cdot (P_n^{q1} + P_n^{q3})}{\sum_{n=0}^{N-1} \cos(n\delta) \cdot (P_n^{q1} + P_n^{q3})}\right) \quad (3.39)$$

$$\phi_{\text{right}} = -\arctan\left(\frac{\sum_{n=0}^{N-1} \sin(n\delta) \cdot (P_n^{q2} + P_n^{q4})}{\sum_{n=0}^{N-1} \cos(n\delta) \cdot (P_n^{q2} + P_n^{q4})}\right) \quad (3.40)$$

$$\phi_{\text{top}} = -\arctan\left(\frac{\sum_{n=0}^{N-1} \sin(n\delta) \cdot (P_n^{q1} + P_n^{q2})}{\sum_{n=0}^{N-1} \cos(n\delta) \cdot (P_n^{q1} + P_n^{q2})}\right) \quad (3.41)$$

$$\phi_{\text{bottom}} = -\arctan\left(\frac{\sum_{n=0}^{N-1} \sin(n\delta) \cdot (P_n^{q3} + P_n^{q4})}{\sum_{n=0}^{N-1} \cos(n\delta) \cdot (P_n^{q3} + P_n^{q4})}\right). \quad (3.42)$$

### 3. Phase demodulation at LISA Pathfinder

The DC signals are defined as

$$\text{DC}_h = \frac{\bar{P}_{\text{left}} - \bar{P}_{\text{right}}}{\bar{P}_{\text{left}} + \bar{P}_{\text{right}}} \quad (2.44)$$

$$\text{DC}_v = \frac{\bar{P}_{\text{top}} - \bar{P}_{\text{bottom}}}{\bar{P}_{\text{bottom}} + \bar{P}_{\text{bottom}}}, \quad (2.45)$$

where the average power on the halves of a QPD is computed by

$$\bar{P}_{\text{left}} = \frac{1}{N} \sum_{n=0}^{N-1} (P_n^{q1} + P_n^{q3}) \quad \bar{P}_{\text{right}} = \frac{1}{N} \sum_{n=0}^{N-1} (P_n^{q2} + P_n^{q4}) \quad (3.43)$$

$$\bar{P}_{\text{top}} = \frac{1}{N} \sum_{n=0}^{N-1} (P_n^{q1} + P_n^{q2}) \quad \bar{P}_{\text{bottom}} = \frac{1}{N} \sum_{n=0}^{N-1} (P_n^{q3} + P_n^{q4}). \quad (3.44)$$

Finally, the contrast is computed by

$$c = \frac{\sqrt{(\text{sum1})^2 + (\text{sum2})^2}}{\bar{P}\pi} \quad (3.45)$$

using the mean power  $\bar{P}$  detected by the whole QPD which is computed by

$$\bar{P} = \frac{1}{M} \sum_{s=q1}^{q4} \sum_{n=0}^{M-1} P_n^s. \quad (3.46)$$

## 4. Example interferometers and their signals

For all simulations, interferometer setups have to be implemented in the software tools (*OptoCad* or *IfoCad*). These implementations are far more simple, than a corresponding experimental setup. This difference is discussed in section 4.1.

In general, the phase and DWS signal cannot be computed analytically. Therefore, it is hard to validate the results given by *QPD.c* or *IfoCad*. Nevertheless, a few systems exist with qualitatively predictable phase and DWS response. Two of these systems are discussed in section 4.2, section 4.3 and section 4.4. These examples show

- that the pathlength signal provides an accurate measure of arm length changes in an interferometer but generally suffers under cross-coupling of beam tilts
- that the DWS signal can be used to monitor the angle of a test mass
- a system which has neither a pathlength nor DWS response to beam tilts.

The DC signal in general is analytically computable. How this is done is shown in section 4.6. The result is used to validate the numerically computed DC signals of section 4.3 and section 4.4.

### 4.1. Experimental setups versus setups in simulations

The experimental realization of a heterodyne interferometer is shown in figure 4.1. The setup is usually split into two parts:

- The modulation bench carries the initial beam splitter and the unstable components such as the acousto-optical modulators (AOM). Thus, the modulation bench prepares the frequency shifted beams for the optical bench.
- The optical bench carries the beam combiners, mirrors, beam splitters and the photodiodes. In most experiments but especially in LISA and LISA Pathfinder, all components are bonded to the optical bench using the stable bonding technique hydroxide-catalysis bonding. If there is no real test mass (like in LISA or LISA Pathfinder) available, it might also contain a piezoelectric driven mirror which is then called test mass for convenience.

On the optical bench, there are at least two interferometers: the measurement interferometer which contains a reflection off a test mass and the reference interferometer. The signals of the reference interferometer are then subtracted from those of the measurement interferometer. This procedure cancels the common mode path length noise which originates from jitter on the modulation bench and length changes of the optical fibers.

#### 4. Example interferometers and their signals

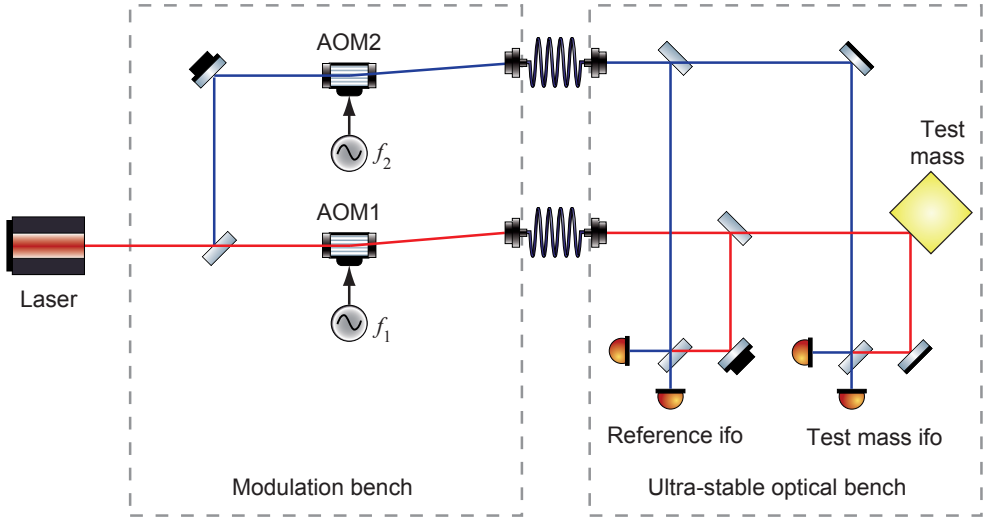


**Figure 4.1.:** Experimental setup of a simple heterodyne interferometer with a test mass. The labels ‘reference ifo’ and ‘test mass ifo’ indicate the position of the reference and test mass interferometer. The test mass is drawn here as yellow cube, in analogy to the LISA and LISA Pathfinder test masses. In a laboratory implementation, the test mass is generally a dummy in form of a piezo mounted mirror.

For simplicity, the laser, modulation bench, and optical fibers will be neglected in all figures from now on. Thus, only the optical bench with its components will be shown. To further simplify the setup shown in figure 4.1, the reference interferometer can also be neglected such that a setup in the form of figure 4.2(a) should fully represent an experimental setup in the form of figure 4.1.

The interferometer shown is a simple non-polarizing interferometer with a test mass. An alternative setup with identical properties from a simulation point of view is the corresponding polarizing interferometer, shown in figure 4.2(b).

In either case, an implementation of the experimental setup into a simulation can be very simple: it is sufficient to define two beams at the location of the test mass which are propagated to a photodiode. Test mass tilt or displacement is then implemented as rotation or shift of the measurement beam with respect to the reference beam (see figure 4.3(a) for an illustration). Thus, the test mass and the beam combiners are neglected. However, if a test mass tilt is implemented in a simulation and the test mass itself is omitted it has to be taken into account that the measurement beam angle is twice as large as the misalignment angle of the test mass in the corresponding interferometer:

$$\varphi_{\text{beam}} = 2 \cdot \varphi_{\text{TM}} . \quad (4.1)$$

The factor of two results from beam angle doubling during reflection as shown in figure 4.3(b).

Only if tolerances are the subject of the investigation, which means the impact of misalignment of one or several components are to be estimated, the complete optical bench is implemented in the simulation.

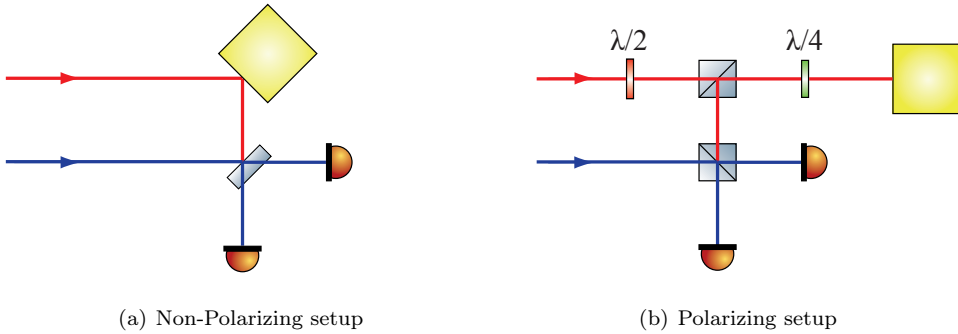


**Figure 4.2.:** Experimental setup of a system described in section 4.4 and figure 4.6, with neglected reference interferometer and omitted modulation bench. The system can be arranged either as a non-polarizing (a) or a polarizing interferometer (b). The most simple implementation of these two setups into a simulation is shown in figure 4.3(a).

## 4.2. Example: longitudinal beam shift

As a first very simple example, a system consisting of two mode-matched beams impinging on a QPD is assumed, which means that the two beams have identical beam parameters on the QPD. One of the beams – the measurement beam – is now shifted in the direction of propagation (cf. figure 4.3(c)). The heterodyne signals of such a system were computed with OptoCad and QPD.c. The resulting graphs are shown in figure 4.4.

**Pathlength signal** The pathlength signal computed by OptoCad and QPD.c is shown in figure 4.4(a). This figure shows an identity (straight line with slope one) between pathlength readout and induced beam shift. This result is anticipated, because shifting one beam with respect to the other in the longitudinal direction changes the macroscopic phase  $k(s_M - s_R)$ . Changes in the microscopic phase are negligible in comparison to the macroscopic phase change, such that the pathlength readout is effectively equal to the induced pathlength change.

**DWS signal** The two beams are shifted longitudinally with respect to each other, but not tilted and both beams impinge at the very center of the QPD. The resulting wavefronts are both circularly symmetric with respect to the normal through the center of the QPD (cf figure 4.3(d)). Therefore, the phase difference, and thus phase signal, on the left and right side of the QPD are identical. Hence, the DWS signal is zero (cf. figure 4.4(b)).

**DC signal** The DC signal effectively measures the position of the beam centroid. Both beams impinge at the very center of the QPD. The measurement beam is shifted only longitudinally and thus there is no beam walk on the surface of the QPD. Therefore, the DC signal is zero for all values of the longitudinal beam shift (cf. figure 4.4(c)).

#### 4. Example interferometers and their signals

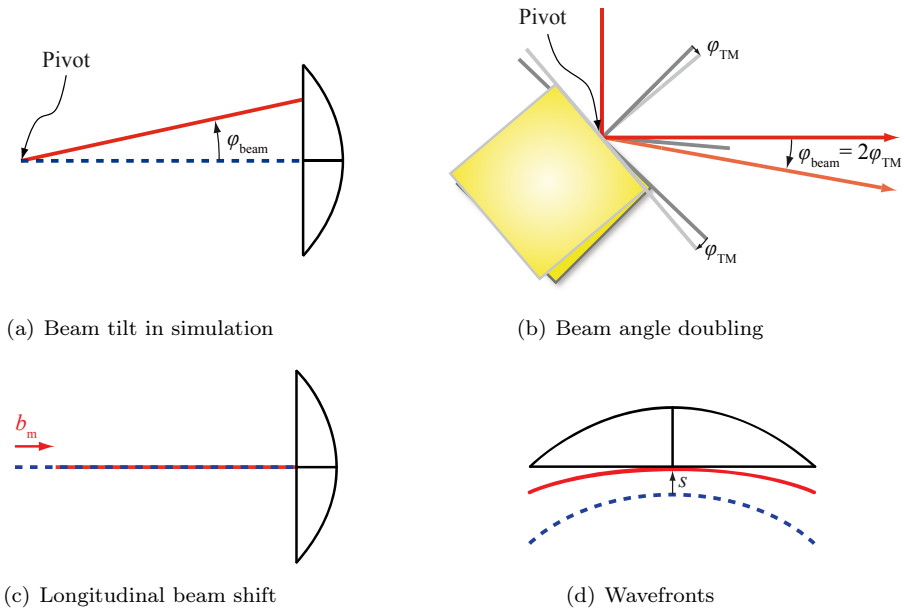


**Figure 4.3.:** Simplified interferometer as implemented in a simulation. Only two beams and a QPD are defined. Nevertheless, this system has the properties of a perfectly aligned interferometer shown in figure 4.1, figure 4.2(a) or figure 4.2(b). In this simplified setup, beam doubling due to reflection needs to be considered as shown in (b).

(c) Setup for the first simulation and sketch of corresponding wavefronts. The measurement beam  $b_m$  (red) is shifted longitudinally with respect to the reference beam. The corresponding wavefronts are shown in subfigure (d). The phase mismatch is symmetrical such that the DWS signal is zero.

**Contrast** The longitudinal beam shift in the example was a small fraction of the Rayleigh range: a beam shift of  $\pm 1$  mm was computed while the Rayleigh range was  $z_0 = 250$  mm. Thus, both beams are almost mode-matched, and impinge with identical angles at the same point on the QPD. Hence, the contrast is approximately 1 for all values of the longitudinal beam shift (cf. figure 4.4(d)).

### 4.3. Example: beam tilt

The same system as in the previous section can be used for another example. Keeping all settings but tilting the measurement beam instead of shifting it, leads to the results shown in figure 4.5.

**Pathlength signal** The upper left graph in figure 4.5 shows that the phase signal senses the rotation. The shape of this pathlength signal depends on the properties of the photodiode. It is thus a sensor property.

**DWS signal** The upper right graph figure 4.5 shows that the DWS signal is proportional to the beam angle. This proportionality of the DWS signal to beam tilts

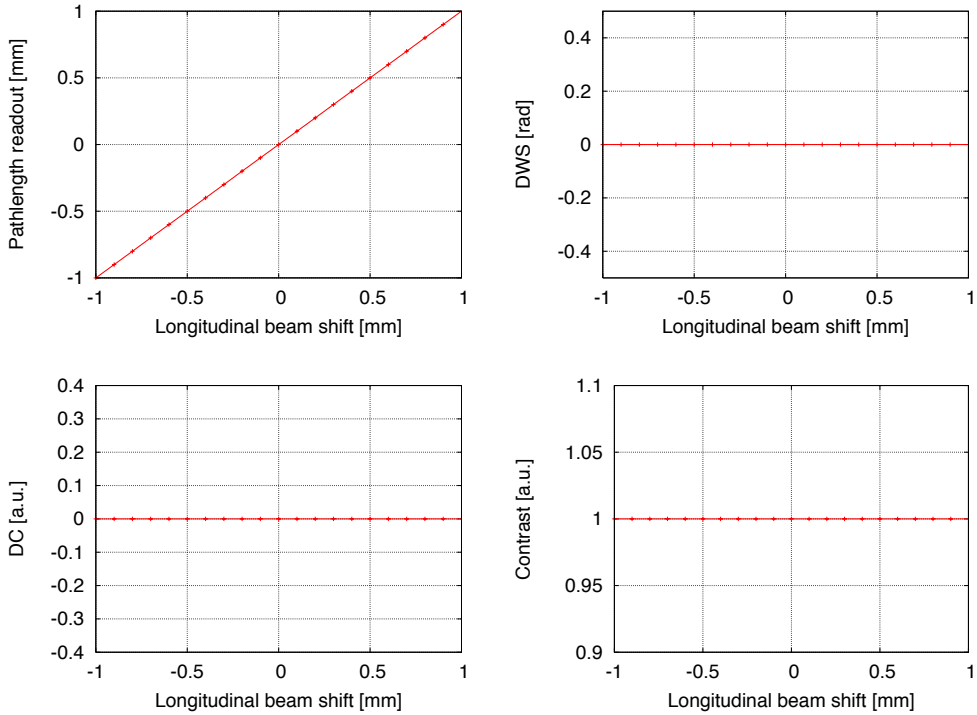


**Figure 4.4.:** Signals of a system with longitudinal shift of the measurement beam with respect to the reference beam (cf. figure 4.3(c)). All settings of the simulation are listed in table C.2.

makes the DWS signal the optimal sensor for beam or component rotations. The proportionality factor in the given example is  $-7727$ . The unit of a DWS signal is rad, since a DWS signal is simply a phase difference. The beam tilt is naturally also measured in rad, such that the coupling factor has unit 1. However, in this form it cannot directly be seen how the coupling factor is to be used: from the number itself it is not clear, whether it transfers from angle to DWS or vice versa. It is therefore beneficial to express the unit directly as  $\text{rad}^{\text{DWS}}/\text{rad}$ , in this case  $-7727 \text{ rad}^{\text{DWS}}/\text{rad}$ . Here it can be seen from the units, that multiplying the coupling factor with an angle results in a DWS-signal.

**DC signal** As discussed in section 2.3 the DC signal measures the position of the beam centroid. The beam tilt causes a beam walk on the QPD, since the pivot is 0.5 m away from the QPD and no imaging optics is used (cf. figure 4.3(a)). Therefore, beam rotation couples in this example into the DC signal.

**Contrast** If the test mass is tilted, the measurement beam tilts and shifts with respect to the reference beam. Thus, the contrast decreases with increasing beam angle.

#### 4. Example interferometers and their signals

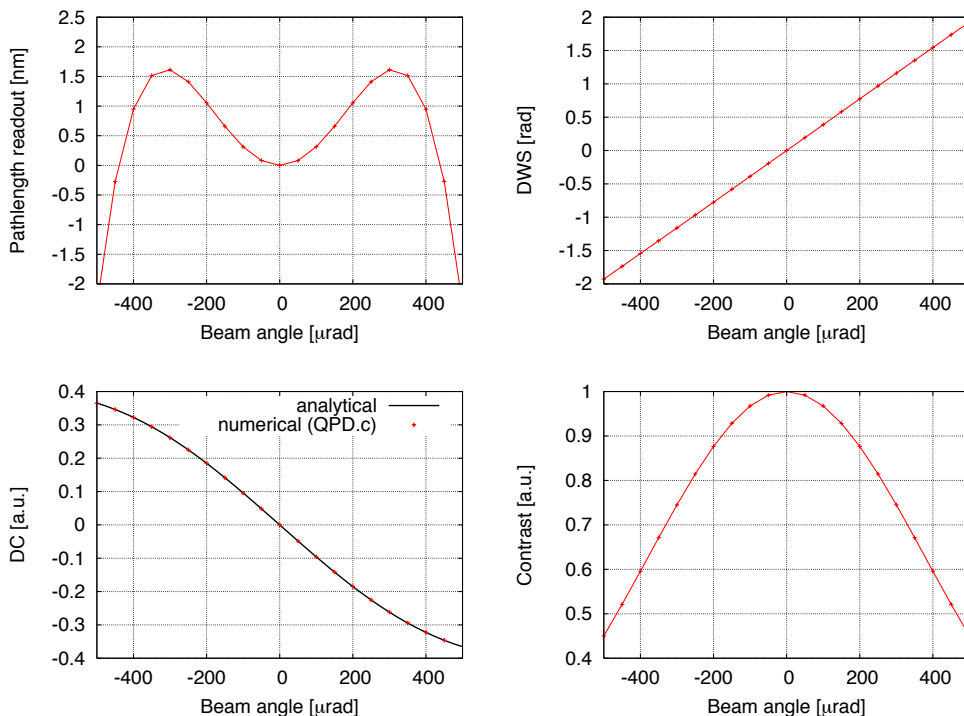


**Figure 4.5.:** Signals of example 3 computed numerically by OptoCad and QPD.c. The same settings were used as for figure 4.4 (settings are listed in table C.2). For the DC signal an analytical result is plotted as well as the numerical result of QPD.c. This will be discussed in detail in section 4.6.

#### Discussion

Ideally, the phase signal senses longitudinal beam shifts, the DWS signal senses beam tilts, the DC signal senses beam walk on the QPD and the contrast is used to assure validity of the signals: if the contrast is too low, than the interferometer is misaligned too much to trust the other three signals.

Unfortunately, there is usually crosstalk between all channels just like in this example. A pure beam rotation causes a phase response which usually cannot be distinguished from a longitudinal beam shift in the experiment. An example is the x1-interferometer of LISA Pathfinder. Here, angular jitter of the test mass causes a phase signal which is then interpreted as a longitudinal jitter of the test mass. This problem will be further discussed in section 7.2.4 and has an impact on the design of the LISA optical bench, discussed in section 10.

Furthermore, the beam tilt causes a beam walk on the QPD and thus a DC-response. This is generally indistinguishable from an orthogonal beam shift. Thus, the given example is a typical example of crosstalk in the various heterodyne signals.



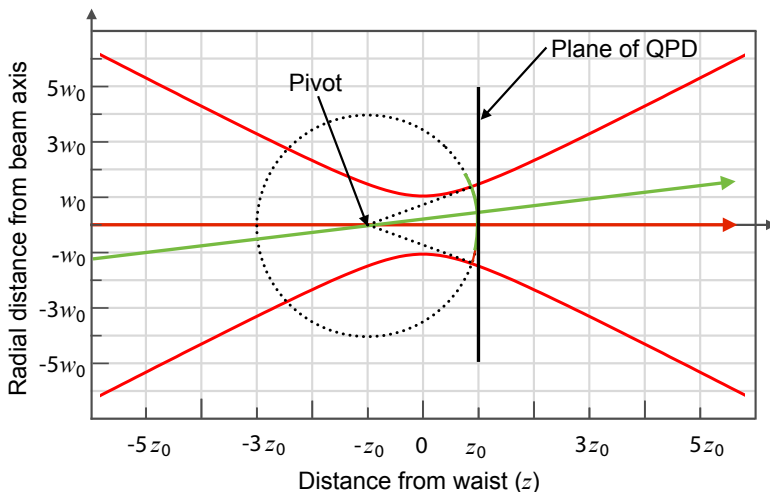


**Figure 4.6.:** Gaussian beam shape in example 1. The dotted circle indicates the sphere which represents locally at  $z = z_0$  the wavefront of both the nominal (red) and the tilted (green) beam. A QPD at this location does not sense a phase or DWS response to the shown beam tilt.

#### 4.4. Example: a system with zero phase and DWS response

In the last example, the cross-coupling of beam tilt into the phase signal was shown, which is a problem in most interferometer setups. This example will show a system where beam tilt does not couple into the phase signal. Unfortunately, the DWS signal in this system does also not sense the beam tilt.

The wavefront of a Gaussian beam can locally be described by the section of a sphere which is fully defined by its radius of curvature. If the pivot of the beam tilt is the center of this sphere, then the beam rotation maps a spherical wavefront upon itself. In that case, the beam tilt will not cause a phase shift on any quadrant of the QPD. Thus, the phase signal and the DWS signal will not sense the rotation.

**Implementation** The radius of curvature (cf. eq. (3.8)) of a Gaussian beam at the Rayleigh range  $z_0$  equals twice the Rayleigh range:

$$R(z_0) = 2z_0 . \quad (4.2)$$

This means, that at the Rayleigh range  $z = +z_0$  the beam has locally the shape of a sphere with radius  $2z_0$ . The center of this sphere is located at  $z = -z_0$  (cf. figure 4.6). Therefore, the setup is implemented in the following form: The distance between pivot (or test mass) and QPD is twice the Rayleigh range. The beam waist is positioned in the center between test mass and QPD.

### 4.4.1. Simulation results

The resulting signals are shown in figure 4.7. The y-range of the phase and DWS-graphs are set to typical responses. As expected, both the phase and DWS curves show zero response to a test mass or beam tilt at the pivot. The settings used to compute the signals in figure 4.7 are listed in table C.1 in appendix C.

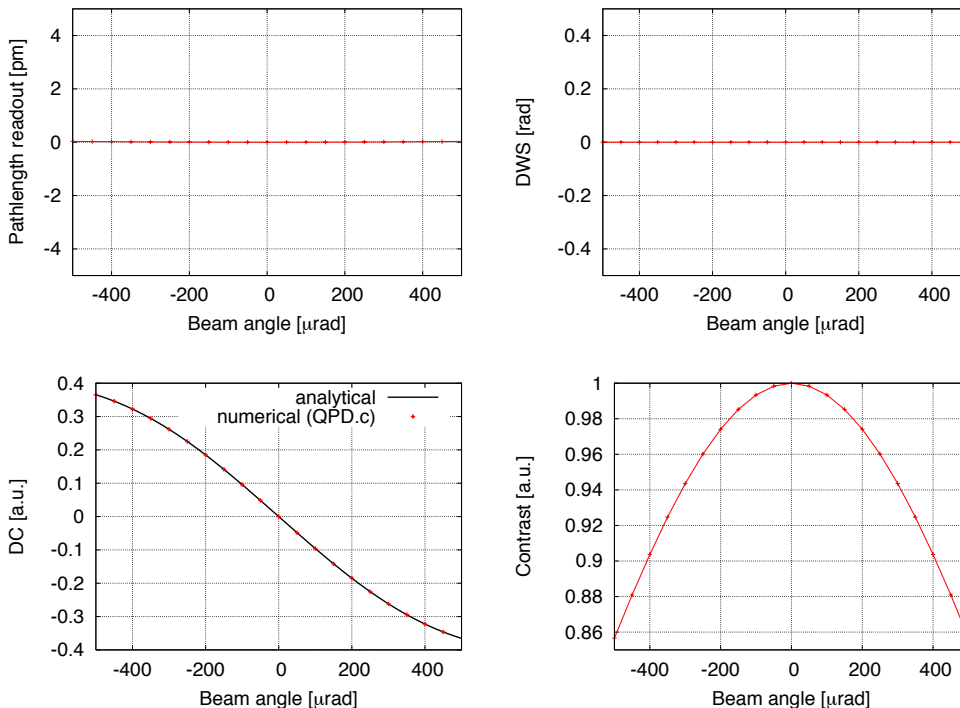


**Figure 4.7.:** Signals of example 1. All signals show the expected shapes. The system shows no coupling of a beam rotation at the pivot into the longitudinal phase or DWS signal. The settings used to compute these values are listed in table C.1 in appendix C.

**Discussion** The system described here is very useful as a sanity test of the tools used. The phase response of a system can in general not be computed analytically. Therefore, this system can, and should, be used to test any new software that computes heterodyne signals, like IfoCad and QPD.c.

Nevertheless, this system is not a sensible choice for an interferometer aboard LISA Pathfinder or LISA, even though it decouples angular jitter from the phase readout. In both missions an interferometric readout of the angles of test masses or point ahead actuators is needed. The most sensitive angular readout known to the author is the DWS-readout. In the system described here, the DWS signal is insensitive to test mass rotation. Therefore, this system cannot be used on the LISA Pathfinder optical bench or in the test mass or PAAM-interferometer of LISA.

Furthermore, it is very hard to arrange such a system experimentally. Even though

components can be positioned with accuracies of the order of a few micrometers and a few tens of microradians, it is very hard to arrange beam parameters. Positioning a waist to an exactly specified point is experimentally not feasible. An uncertainty of the waist position of the order of roughly a tenth of a Rayleigh range needs to be assumed.

## 4.5. Coupling factors

Throughout this thesis, a coupling factor  $k$  is defined as the first derivative of a signal by a degree of freedom (DoF) of the interferometer:

$$k_{\text{DoF}}^{\text{signal}} := \frac{\partial \text{signal}}{\partial \text{DoF}}, \quad (4.3)$$

such that the signal near the operation point used in eq. (4.3) can in first order be computed from the product of the coupling factor and the degree of freedom:

$$\text{signal} \approx k_{\text{DoF}}^{\text{signal}} \cdot \text{DoF}. \quad (4.4)$$

A typical example is the coupling factor between test mass tilt and the corresponding DWS signal:

$$k_{\varphi}^{\text{DWS}} = \frac{\partial \text{DWS}}{\partial \varphi}. \quad (4.5)$$

In the example of section 4.3 this coupling factor had a value of  $k_{\varphi}^{\text{DWS}} = -7727/2 \approx 3863$ , where the factor of 2 was used to convert from beam angle to test mass angle, such that normal incidence on the test mass and therefore a polarizing interferometer was assumed.

Coupling factors can be used to characterize an interferometer without plotting the signal response as a function of a parameter. One curve (signal response) is represented by the slope at one point: the coupling factor. Certainly, the coupling factor provides limited knowledge about the signal response, but it allows a quick and easy characterization of the interferometer without plotting all corresponding curves.

## 4.6. Analytical computation of DC signals

In the previous section, the phase and DWS signal were discussed. This section will show how to compute analytically the DC signal shown in figure 4.7(c).

As shown in section 2.3, the horizontal DC signal is a normalized difference of the time-averaged power sensed on the left and right hand side of a QPD:

$$\text{DC}_h = \frac{\bar{P}_{\text{left}} - \bar{P}_{\text{right}}}{\bar{P}_{\text{left}} + \bar{P}_{\text{right}}}. \quad (2.44)$$

This signal can be used to align either one single beam on a QPD or just as well the beam centroid of two (or more) superimposing beams in an interferometer. The special case of a DC signal caused by a single beam on a QPD is analytically computable.

### 4.6.1. DC signal for one beam

For computing a beam power, it is convenient to use the representation of the electric field that contains the radius of curvature:

$$E(r, z) = \sqrt{\frac{2P_b}{\pi w(z)^2}} \exp\left(\frac{-r^2}{w(z)^2}\right) \cdot \exp\left(-\frac{ikr^2}{2R(z)} + i\zeta(z) - iks\right). \quad (3.14a)$$

The local intensity can then be easily read from this representation of the electric field:

$$I(r, z) = \|E(r, z)\|^2 \quad (4.6)$$

$$= \frac{2P_b}{\pi w(z)^2} \exp\left(\frac{-2r^2}{w(z)^2}\right). \quad (4.7)$$

For shifting and tilting the beam, the same coordinate transformations are needed as in section 3.2.2. For simplicity, only horizontal beam shifts and tilts are assumed:

$$r = \sqrt{x^2 + y^2} \quad \rightarrow \quad r = \sqrt{\cos^2(\varphi) \cdot (x - x_0)^2 + y^2}. \quad (3.26a)$$

For a square QPD with half width  $r_{\text{QPD}}$  and total width of the slit that separates the quadrants  $d_{\text{Slit}}$ , the sensed power on the left or right side of the QPD is the respective surface integral over the local intensity:

$$P_{\text{left}} = \int_{-r_{\text{QPD}}}^{-d_{\text{Slit}}/2} dx \int_{-r_{\text{QPD}}}^{r_{\text{QPD}}} dy I(x, y, z) \quad (4.8)$$

$$P_{\text{right}} = \int_{d_{\text{Slit}}/2}^{r_{\text{QPD}}} dx \int_{-r_{\text{QPD}}}^{r_{\text{QPD}}} dy I(x, y, z). \quad (4.9)$$

**Analytical solution for an infinitely large QPD without slit** The resulting DC signal for an infinite QPD ( $r_{\text{QPD}} \rightarrow \infty$ ) without slit ( $d_{\text{Slit}} = 0$ ) is

$$\text{DC}_{1 \text{ beam}} = -\text{erf}\left[x_0 \sqrt{\frac{1 + \cos(2\varphi)}{w(z)^2}}\right] \quad (4.10)$$

or arranged in a slightly different form:

$$\text{DC}_{1 \text{ beam}} = -\text{erf}\left[x_0 \frac{\sqrt{2} \|\cos(\varphi)\|}{w(z)}\right], \quad (4.11)$$

where erf is the error function. Figure 4.8 shows the resulting signal shape for a beam radius on the QPD of  $w(z) = 411 \mu\text{m}$  and various incident angles  $\varphi$ , when the beam is shifted over the surface of an infinitely large QPD without slits. For normal incidence, the graph shows that the DC signal is one if the beam points to the left side of the QPD. That means, all power is sensed by the left side of the QPD. If the beam is gradually shifted to the right side, the DC signal has a linear range and passes through zero, when the beam is centered on the QPD – that means when both sides of the

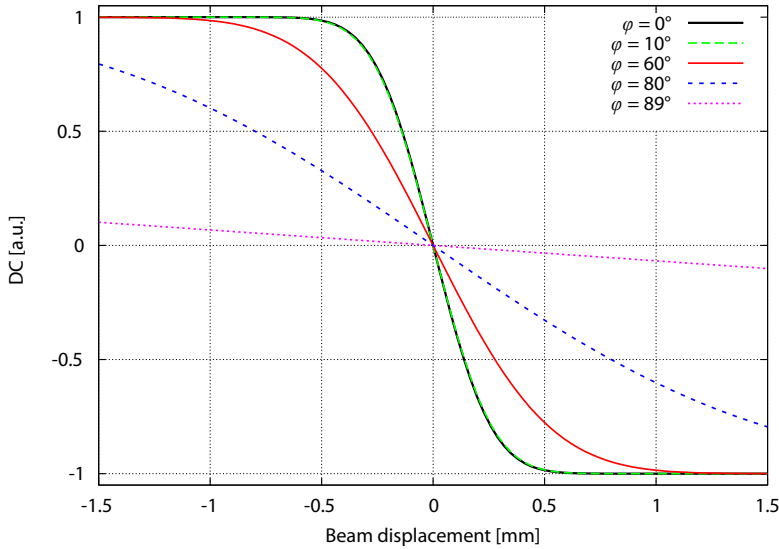


**Figure 4.8.:** DC signal of one beam with radius  $w(z) = 411 \mu\text{m}$  on the QPD for various beam angles, when shifted over the surface of a QPD of infinite size without slits.

QPD sense the same amount of power. Shifting the beam further to the right results in a negative DC signal until the beam is completely on the right side of the QPD and the DC signal reaches -1.

The linearized DC signal at  $x_0 = 0$  is

$$\text{DC}_{1 \text{ beam}}(x_0 \approx 0) = -\frac{2\sqrt{2} \|\cos(\varphi)\|}{\sqrt{\pi}w(z)}x_0 + O(x_0^2) \quad (4.12)$$

and consequently for normal incidence ( $\varphi = 0$ ):

$$\text{DC}_{1 \text{ beam}}(x_0 \approx 0) = -\frac{2\sqrt{2}}{\sqrt{\pi}w(z)}x_0 + O(x_0^2). \quad (4.13)$$

Especially the linearized DC signal for normal incidence therefore only depends on the beam radius on the QPD and is thus easily predictable.

Equation (4.12) shows that in first order the DC signal is proportional to beam shifts on the QPD. Therefore, the DC signal is generally used to align beams to the center of a QPD. Furthermore, the DC signal depends only in higher order on the incident angle of the beam, such that in most cases it is sufficient to assume normal incidence. Nevertheless, in most optical systems a rotation of an optical component results in a beam walk on the respective QPD. For small angles, the angle of the component is proportional to the resulting beam shift and thus to the DC signal. This is used in LISA Pathfinder for a rough initial angular alignment of the test masses when LISA Pathfinder has reached its final orbit and the test masses are released into free fall. This alignment procedure is described in section 5.3.3.

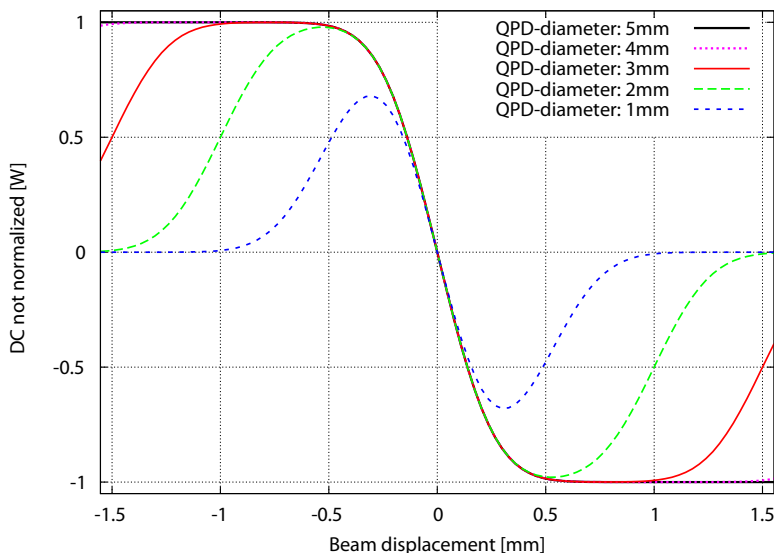


**Figure 4.9.:** DC signal of one beam with radius  $w(z) = 411 \mu\text{m}$  on finite QPDs with various diameters, when shifted over the surface of a the QPD with a  $20 \mu\text{m}$  slit.

**Analytical solution for a finite QPD with slits** The power on the left and right side of a finite QPD with slits can also be computed analytically using eq. (4.8) and eq. (4.9). Nevertheless, for large beam shifts the beam is shifted off the photodiode such that the total power sensed by the QPD ( $P_{\text{left}} + P_{\text{right}}$ ) is zero. Normalizing the DC signal would then lead to a division by zero. To avoid this problem a unnormalized DC signal is computed but the total beam power can be set to one Watt for convenience:

$$\text{DC}_{nn} := P_{\text{left}} - P_{\text{right}} \quad (4.14)$$

$$= \frac{P}{2} \cdot \text{erf}\left(\frac{\sqrt{2}r_{\text{QPD}}}{w(z)}\right) \cdot \left[ \text{erf}\left(\frac{d_{\text{slit}} - 2x_0}{\sqrt{2}w(z)}\right) - \text{erf}\left(\frac{d_{\text{slit}} + 2x_0}{\sqrt{2}w(z)}\right) \right] \quad (4.15)$$

$$+ \text{erf}\left(\frac{\sqrt{2}(x_0 - r_{\text{QPD}})}{w(z)}\right) + \text{erf}\left(\frac{\sqrt{2}(x_0 + r_{\text{QPD}})}{w(z)}\right) \quad (4.16)$$

The resulting graphs for a 1 Watt input beam with a radius of  $w(z) = 411 \mu\text{m}$  on finite QPDs with various diameters are shown in figure 4.9. This graph shows the effect of beam clipping on the outer edges of the QPD. If the QPD is large, there are large plateaus where all beam power is either on the left or right side of the QPD (corresponding to  $\text{DC} = \pm 1$ ). The smaller the QPD, the smaller are these plateaus because large shifts move the beam off the QPD. If the size of the QPD is of the order of the beam size, the clipping is so large, that there is no position of the beam, where one side of the QPD can sense total beam power. Therefore, the non-normalized DC signal does not reach the value of the total beam power of 1 Watt in figure 4.9 if the QPD has a diameter of 2 mm or less.

Generally, photodiodes are chosen to have a radius of at least 3 times the beam radius in order to minimize beam clipping.

### 4.6.2. DC signal in an interferometer

Computing the power in an interferometer analytically without simplifications is currently not possible. Nevertheless, it is possible to analytically predict, for example, the DC signal for the system in section 4.4 by making a few simplifications.

Generally, the intensity of an interference pattern can be computed by

$$I = \|E_M + E_R\|^2 \quad (4.17)$$

$$= \|E_M\|^2 + \|E_R\|^2 + 2\Re(E_M \cdot E_R^*) \quad (4.18)$$

$$= I_M + I_R + 2I_M^{\frac{1}{2}}I_R^{\frac{1}{2}}\cos(\Phi) . \quad (2.14a)$$

Using eq. (3.14a) and assuming that the beams are mode-matched (that is, they have the same beam parameters) and have the same power  $P_M = P_R = P$  the intensity  $I$  is

$$I = \frac{2P_b}{\pi w(z)^2} \left[ \exp\left(\frac{-2r_M^2}{w(z)^2}\right) + \exp\left(\frac{-2r_R^2}{w(z)^2}\right) + 2 \exp\left(\frac{-(r_M^2 + r_R^2)}{w(z)^2}\right) \cos\left(\frac{k(r_M^2 - r_R^2)}{2R(z)}\right) \right]. \quad (4.19)$$

Here,  $r_M$  and  $r_R$  are not equal, because the beams might be shifted or tilted with respect to each other. The interference term

$$2I_M^{\frac{1}{2}}I_R^{\frac{1}{2}}\cos(\Phi) = 2 \exp\left(\frac{-(r_M^2 + r_R^2)}{w(z)^2}\right) \cos\left(\frac{k(r_M^2 - r_R^2)}{2R(z)}\right) \quad (4.20)$$

is hard to integrate analytically. Nevertheless, this term is not needed to compute the resulting DC signal. However, the interference term has a vanishing time average, such that it is sufficient to compute the power sensed by the quadrants of the QPD by integrating over the single intensities, thereby ignoring that the beams interfere (for example, for a square QPD):

$$P_{\text{left}} = \int_{-r_{\text{QPD}}}^{-d_{\text{slit}}/2} dx \int_{-r_{\text{QPD}}}^{r_{\text{QPD}}} dy \left[ I_M(x, y, z) + I_R(x, y, z) \right] \quad (4.21)$$

$$P_{\text{right}} = \int_{d_{\text{slit}}/2}^{r_{\text{QPD}}} dx \int_{-r_{\text{QPD}}}^{r_{\text{QPD}}} dy \left[ I_M(x, y, z) + I_R(x, y, z) \right]. \quad (4.22)$$

In section 4.4 there was one reference beam, pointing to the center of the QPD, while the measurement beam was effectively shifted over the QPD surface. Therefore, the following substitutions are required:

$$r_M^2 \rightarrow (x - x_0)^2 + y^2 \quad (4.23)$$

$$r_R^2 \rightarrow x^2 + y^2 . \quad (4.24)$$

#### 4. Example interferometers and their signals

The power on the left or right side of the square QPD is then:

$$P_{\text{left}}(x_0, r_{\text{QPD}}) = \frac{P}{2} \operatorname{erf}\left(\frac{\sqrt{2} r_{\text{QPD}}}{w(z)}\right) \cdot \left[ -\operatorname{erf}\left(\frac{d_{\text{Slit}}}{\sqrt{2} w(z)}\right) - \operatorname{erf}\left(\frac{d_{\text{Slit}} + 2x_0}{\sqrt{2} w(z)}\right) + \operatorname{erf}\left(\frac{\sqrt{2} r_{\text{QPD}}}{w(z)}\right) + \operatorname{erf}\left(\frac{\sqrt{2}(x_0 + r_{\text{QPD}})}{w(z)}\right) \right] \quad (4.25)$$

$$P_{\text{right}}(x_0, r_{\text{QPD}}) = \frac{P}{2} \operatorname{erf}\left(\frac{\sqrt{2} r_{\text{QPD}}}{w(z)}\right) \cdot \left[ -\operatorname{erf}\left(\frac{d_{\text{Slit}}}{\sqrt{2} w(z)}\right) - \operatorname{erf}\left(\frac{d_{\text{Slit}} - 2x_0}{\sqrt{2} w(z)}\right) + \operatorname{erf}\left(\frac{\sqrt{2} r_{\text{QPD}}}{w(z)}\right) - \operatorname{erf}\left(\frac{\sqrt{2}(x_0 - r_{\text{QPD}})}{w(z)}\right) \right]. \quad (4.26)$$

The resulting analytical DC signal is a function of the beam shift  $x_0$ . To compare it to the result shown in figure 4.7(c), it is easiest to plot the result of QPD.c in figure 4.7(c) not against the test mass angle, but the resulting beam shift on the QPD. The dependency of the test mass angle  $\varphi_{\text{TM}}$  (which is twice the beam angle  $\varphi_{\text{beam}}$ ) and the beam shift is given by

$$\tan(2\varphi_{\text{TM}}) = \tan(\varphi_{\text{beam}}) = \frac{x_0}{l}, \quad (4.27)$$

where  $l$  is the lever arm, that means the distance between test mass and QPD. It has a value of  $l = 2z_0 = 0.5$  m. Since the test mass angle is small, it is sufficient to use the first order of a Taylor series:

$$2\varphi \approx \frac{x_0}{l} \quad (4.28)$$

$$\rightarrow \varphi \approx \frac{x_0}{1 \text{ m}}. \quad (4.29)$$

Thus, in this special example the test mass angle  $\varphi$  (with unit “rad”) is exchangeable for a beam shift  $x_0$  in meters.

The resulting graph matches perfectly with the analytical result (cf. figure 4.10) – even though the interference term was neglected in the analytical computation, while the numerical computation in QPD.c computed all terms.

**Understanding figure 4.10:** The DC signal for the interfering beams is similar to the unnormalized DC signal for the 1 mm QPD for one beam shown in figure 4.9. Nonetheless, they are not the same, even though the same beam parameters and QPDs were used. This is reasonable.

The difference between both graphs is the power bias given by the reference beam. This bias allows the normalization of the DC signal in the interferometer even if the measurement beam is shifted off the QPD. This can be seen in figure 4.10 in the curves for the power on the left (solid red curve) or right side (dashed green curve) of the QPD and the total power sensed (dashed blue). The left and right side of the QPD sense almost 0.5 Watt when both beams point to the center of the QPD. This



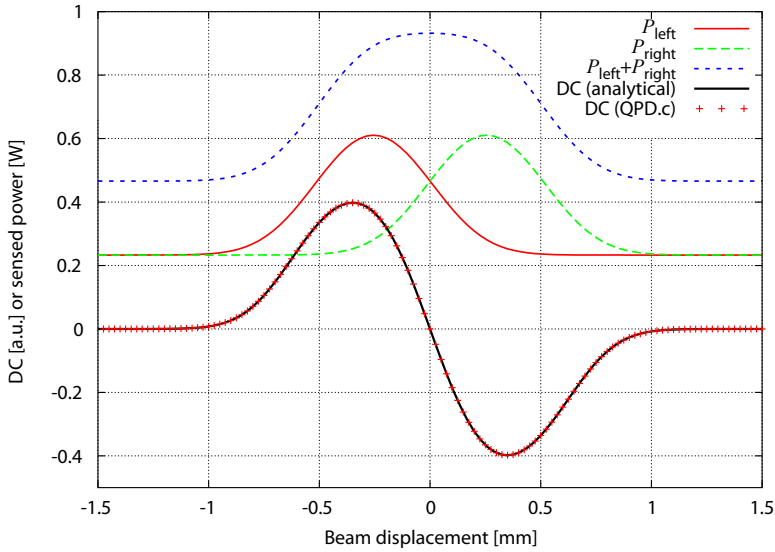


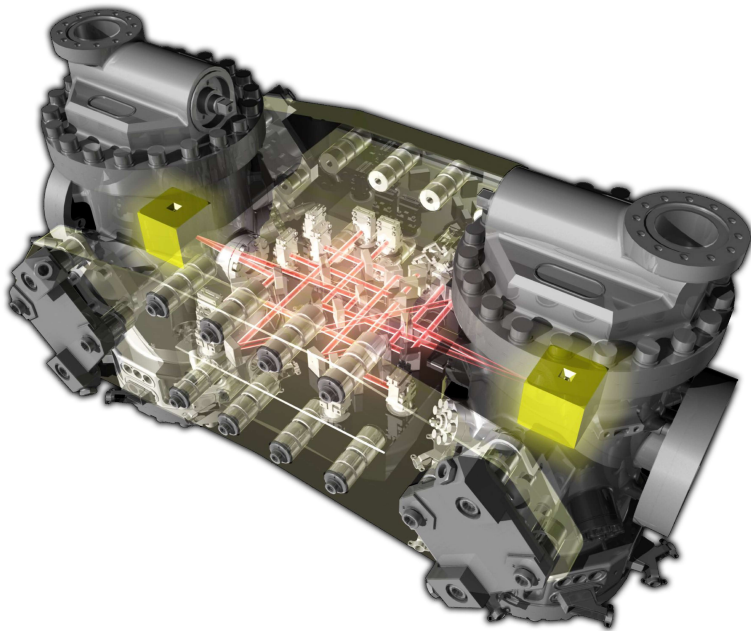
**Figure 4.10.:** Comparison between the analytically computed DC signal (black) and the numerically computed DC signal computed by QPD.c. For better comprehensibility the beam power on the left (red solid line) and right side (green dashed line) of the QPD as well as the total power detected (dashed blue line) are shown as well.

value increases when the measurement beam shifts further to the side and reaches a maximum before it decreases due to clipping on the outer borders of the QPD. When the measurement beam is shifted off the QPD, each side of the QPD still senses a little less than 0.25 Watt, which is half the power of the reference beam.



Part II.

# LISA Pathfinder interferometry





## 5. Introduction to LISA Pathfinder

*This chapter provides all necessary information on LISA Pathfinder needed for the subsequent chapters which describe the work performed for this mission. The first section (5.1) describes the general mission including the top-level science requirements and introduces the main technology. Section 5.2 introduces the optical bench interferometry (OBI). Finally, section 5.3 gives a detailed description of the alignment and bonding procedure of the OBI and its way to space. This section is the basis for section 6.3 and therefore all results presented in chapter 7.*

### 5.1. The mission

LISA Pathfinder (LPF) is a technology demonstration mission for LISA consisting of only one spacecraft (cf. figure 1.5). LPF is planned to be launched in 2013 by a VEGA rocket from Kourou, French Guiana and will reach its final 500,000 km by 800,000 km Halo orbit around the Lagrangian point L1 roughly 2 months later. [LISA-LPF-0002] [4] After reaching its final orbit, LISA Pathfinder will have an operational phase of six months.

On board LISA Pathfinder will be two instruments: the European LISA Technology Package (LTP) and NASA's Disturbance Reduction System (DRS). The operation time is divided into 90 days for LTP experiments, 60 days for DRS and 30 days for joint operation.[EST-5007] [4] During this operation time there will be approximately an 8 hour contact each day between ground control and LPF with average data rate of 10 to 20 kbit per second.

The aim of LISA Pathfinder is to demonstrate technical readiness for LISA and show free floating test masses with a residual acceleration noise of

$$S(a)^{\text{LPF}} \leq 3 \cdot 10^{-14} \frac{\text{ms}^{-2}}{\sqrt{\text{Hz}}} \sqrt{1 + \left(\frac{f}{3 \text{ mHz}}\right)^4} \quad (5.1)$$

over a frequency interval of 1–30 mHz, the so called measurement band [LISA-LPF-0002]. This top level science requirement is written in form of an amplitude spectral density and is referred to as top-level science requirement. It is a factor of 10 relaxed both in noise level and in frequency with respect to the LISA requirement ([Jennrich2009], cf. figure 5.1

$$S(a)^{\text{LISA}} \leq 3 \cdot 10^{-15} \frac{\text{ms}^{-2}}{\sqrt{\text{Hz}}} \sqrt{1 + \left(\frac{f}{2.8 \text{ mHz}}\right)^4} \quad (5.2)$$

over a frequency band of 0.1 – 100 mHz. For this purpose, LTP contains two test masses whose relative distance is measured by an interferometric readout. Thereby, LTP comprises one of the LISA interferometer arms shrunk from 5 million km to approximately 35 cm. Each test mass is located in an electrode housing (cf. figure 5.2(b)),

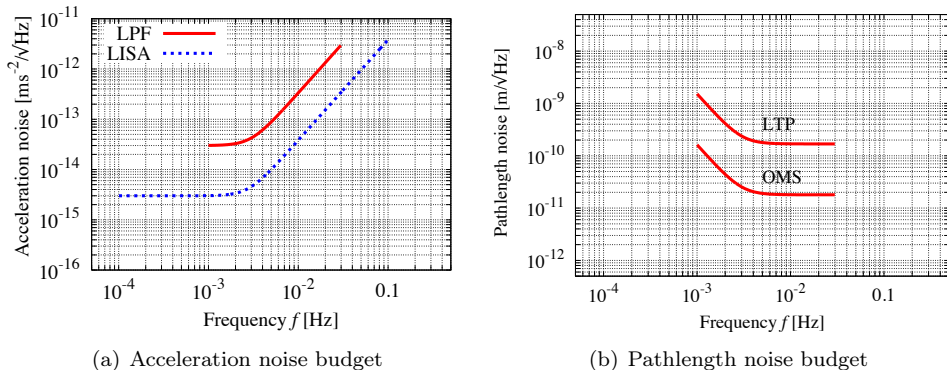


**Figure 5.1.:** (a) LISA and LISA Pathfinder acceleration noise budget. These are top-level science requirements for both missions. (b) Pathlength noise budget for LISA Pathfinder for instance LTP as well as the budget for the optical metrology system (OMS).

which is embedded in a vacuum enclosure to maintain a clean environment, mainly during launch. Furthermore, the vacuum chamber houses a caging mechanism for the test mass, which secures it during launch. After reaching the final orbit the caging mechanism releases the test mass into free fall. Even though caging is used in a variety of missions, the caging mechanism of LTP has requirements on residual motion after release, that were never realized before. Therefore, the caging mechanism is one example of critical new technology to be tested by LISA Pathfinder for the LISA mission.

The assembly consisting mainly of test mass, electrode housing, caging mechanism and vacuum chamber is generally referred to as an inertial sensor or gravitational reference sensor (GRS, cf. figure 5.3), since the electrode housing provides a capacitive readout of the position and attitude of the enclosed test mass.

The inertial sensors are located symmetrically around the center of the spacecraft as part of the LTP core assembly (LCA) as shown in figure 5.2. Located between the inertial sensors is the optical bench (OB) which hosts the interferometers (cf. figure 5.4) that read out the test masses attitude and position. For this interferometric readout of the test masses, some infrastructure is needed: the laser assembly which provides the laser beams, laser modulators that frequency shift the laser beams for the heterodyne interferometry, the optical bench including all components that form the interferometers, as well as the phasemeter assembly, consisting of photodiodes and phasemeter unit. This assembly of components that are needed for the interferometric readout of the test mass' positions and attitudes is the optical metrology system (OMS).

Ideally, both test masses would remain undisturbed while the distance between both is measured. However, there exist residual forces acting on the spacecraft or the test masses, which originate from a variety of sources like solar radiation pressure, residual magnetic fields, static gravity imbalance or temperature fluctuations. These residual forces would eventually cause the test masses to crash into the surrounding structure, the electrode housing. In order to prevent this but keep one test mass

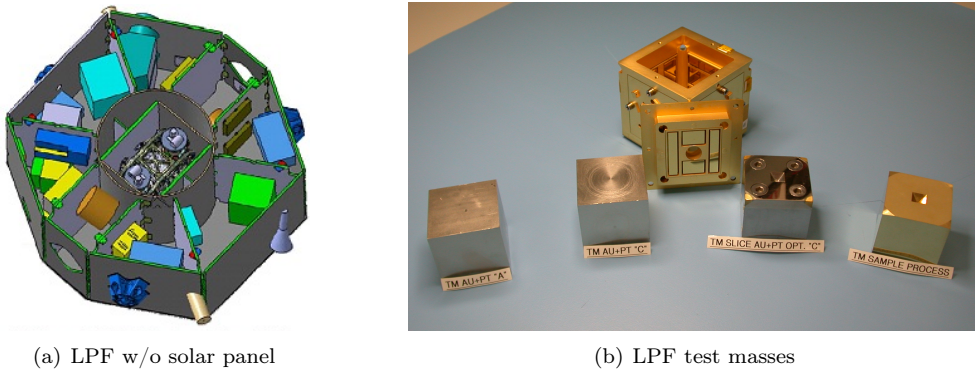


**Figure 5.2.:** (a) CAD view of the LISA Pathfinder satellite with removed solar panel. Located in the center of the satellite is the LTP Core Assembly (LCA) which was shown on p. 51. Source: EADS Astrium.

(b) LISA Pathfinder test masses (front) and electrode housing (behind). Credit: ESA.

drag-free, the satellite is accelerated to keep the test mass at its nominal position by the so-called Drag Free Attitude and Control System (DFACS). For this fine control of the spacecraft, micro-Newton thrusters are needed. These thrusters are another example of critical new technology to be tested by LISA Pathfinder. DFACS makes the thrusters part of the science experiment, such that payload and spacecraft (S/C) are no longer distinguishable. This is unlike traditional spacecraft and therefore the generic term sciencecraft was introduced.

A displacement of the spacecraft to counteract the displacement of the first test mass results in a displacement of the second test mass with respect to its surrounding structure. In order to correct this displacement and again prevent the second test mass from touching its surrounding structure, the second test mass needs to be controlled as well. This control is performed by the electrostatic actuators at frequencies below the LTP measurement band and is therefore called the low frequency suspension.

This thesis investigates mainly the interferometric readout provided by the optical metrology system (OMS). It provides a more accurate measurement of the test mass position and attitude than the capacitive sensors such that the interferometer signals are used in the various control loops to align the test masses and spacecraft with respect to each other. As described in section 2.3 the primary interferometer signal is the pathlength signal, since it carries the information about arm length changes and will therefore in the LISA mission carry the information about passing gravitational waves. It is therefore convenient to express the requirements in terms of residual pathlength noise. The conversion from acceleration noise to pathlength noise as well as a discussion of the different requirements appearing in literature is shown in appendix A.2. The equivalent to eq. (5.1) in pathlength noise is:

$$S(\Delta s_m)^{\text{LPF}} \leq 170 \frac{\text{pm}}{\sqrt{\text{Hz}}} \sqrt{1 + \left( \frac{3 \text{ mHz}}{f} \right)^2}. \quad (5.3)$$

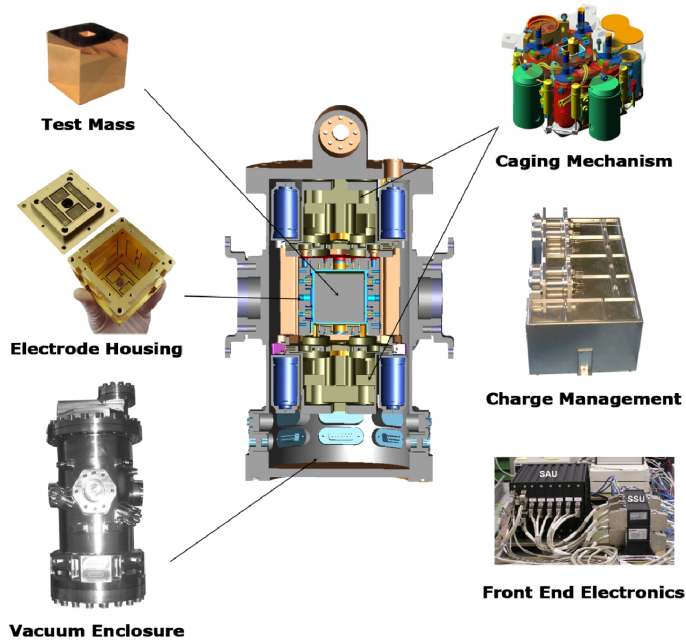


**Figure 5.3.:** One LTP inertial sensor and its components: the test mass and its electrode housing which provides a capacitive readout of the test mass attitude and applies forces to the test mass to position it. Furthermore, the caging mechanism is shown, which secures the test mass during launch and releases it into free fall in space. Furthermore the charge management unit is shown, which shines ultra violet light onto the test mass to clear it from charges. Naturally front end electronics is needed to control the various techniques. Finally, the vacuum chamber which encloses the various subsystems is shown. Credit: ESA.

Both instruments aboard LISA Pathfinder (LTP and DRS) aim to show this stability requirement for the differential pathlength readout between both test masses. This total pathlength noise is apportioned to the various noise sources in LTP. The OMS as one contributor has an allocation of  $9 \text{ pm}/\sqrt{\text{Hz}}$  for position noise and thus  $18 \text{ pm}/\sqrt{\text{Hz}}$  for pathlength noise (cf. figure 5.1(b)). Originally, it was assumed that each contributing noise source has a budget of

$$S(\Delta x_m)^{\text{OMS contr.}} \leq \frac{1 \text{ pm}}{\sqrt{\text{Hz}}} \sqrt{1 + \left(\frac{3 \text{ mHz}}{f}\right)^4}. \quad (5.4)$$

Later on, a detailed break-down of the top-level science requirement to all contributors was performed by ASD, which is described in [ASD-3036].



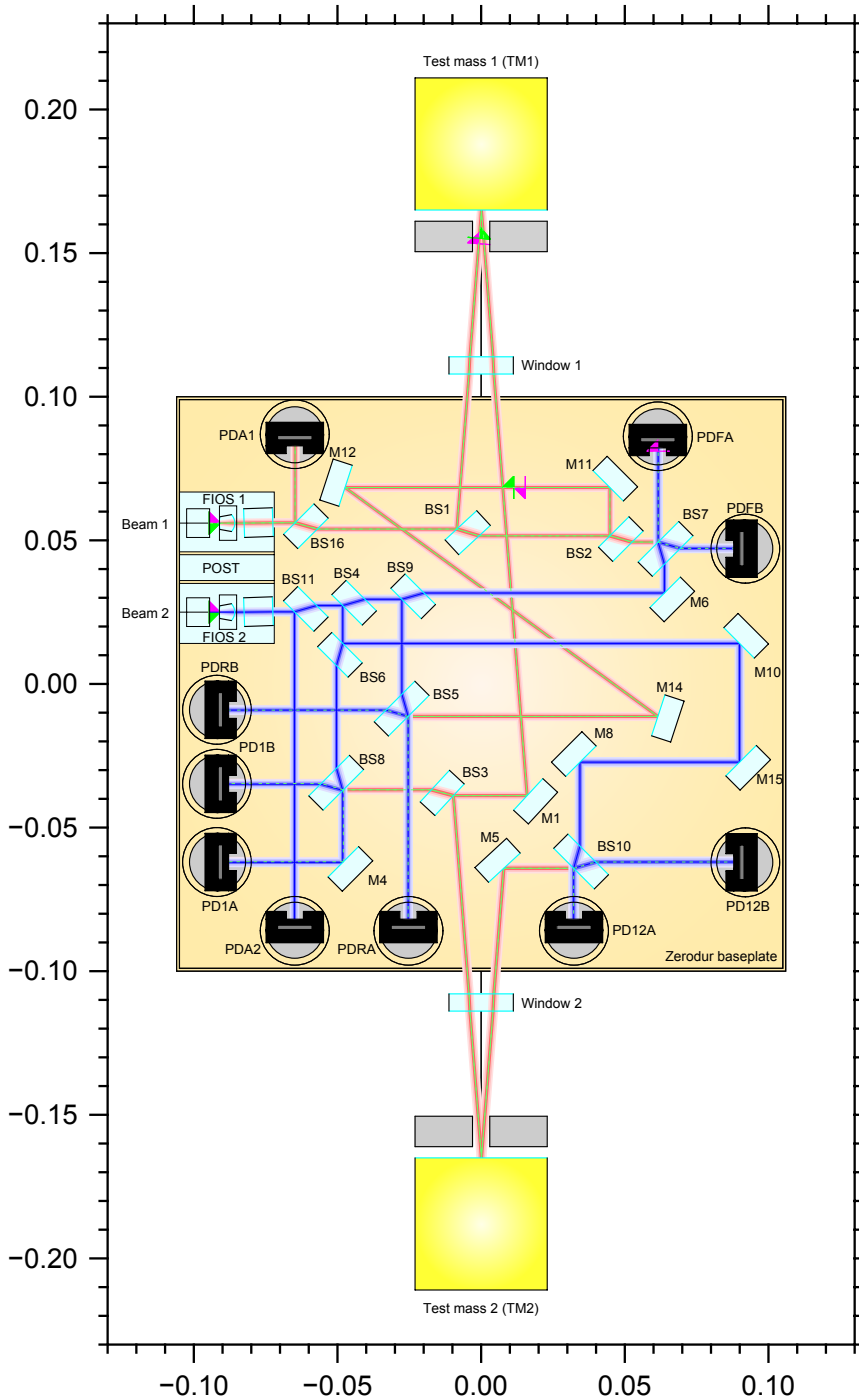


**Figure 5.4.:** Flight model of the LTP optical bench interferometer (OBI) including test masses, pinholes in electrode housing and optical windows in the vacuum chambers. Dimensions are in meters.

## 5.2. Interferometry aboard LISA Pathfinder

The optical metrology system (OMS) provides the interferometric readout of the test mass' positions and attitudes. One major part of the OMS is the optical bench interferometer (OBI), which consists of a Zerodur baseplate, and a variety of mirrors and beam splitters (BS) which form four Mach Zehnder interferometers: the x1-, x12-, reference and frequency interferometer as shown in figure 5.4. This figure shows the design of the flight model (FM) of the optical bench as well as the test masses and pinholes in the electrode housings. Furthermore, the optical windows in the vacuum valve are shown. The components labeled FIOS are the fiber injector optical subassemblies. These are the custom made quasi-monolithic fiber injectors developed by UGL which deliver the measurement (red with green trace) and reference beam (blue) from the modulation bench.

There are three optical benches manufactured to this design: a qualification model which is planned to be tested in Hannover, a flight model which will actually be implemented in LTP and a flight spare model. Apriori it is not clear, which bench will be the flight model and which the flight spare model. Therefore both benches are referred to as proto flight models. These proto flight models are labeled 2OB and 3OB. By today (autumn 2010), 3OB is complete and first calibration measurements were performed [UGL-3039], while 2OB is fully bonded but without photodiodes. Most simulations for LISA Pathfinder performed as part of this thesis regard the flight model of the optical bench. However, a few tests were also performed for the engineering model (EM) of the OBI which has the same dimensions and optical layout with only a few minor differences in the arrangement of the optical components (cf. figure A.5 in appendix A.5), and has commercial fiber injectors.

### 5.2.1. Description of the four interferometers

In the x1-interferometer the measurement beam (beam 1) is reflected off test mass 1 (TM1) but not off TM2. That means that the x1-interferometer monitors the position and angle of TM1 with respect to the optical bench. The optical bench is rigidly connected to the surrounding support structure and thereby to the spacecraft. Acceleration noise caused by the thrusters as part of the DFACS is thus equivalently transferred to an acceleration of the optical bench with respect to the free floating test mass. Therefore, the x1-interferometer pathlength readout is expected to be dominated by thruster noise. Figure 5.5 shows an obvious optical pathlength difference for the two beams. Since the pathlength difference in both interferometers needs to be as small as possible in order to reduce pathlength noise originating from frequency fluctuations, the

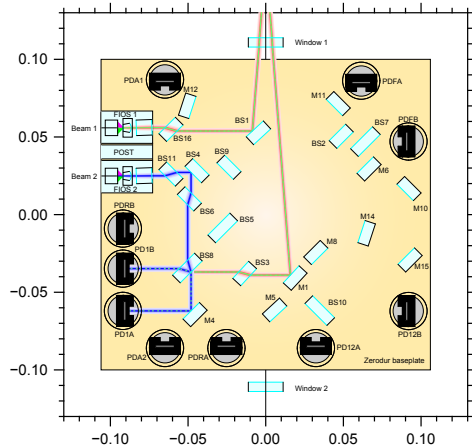
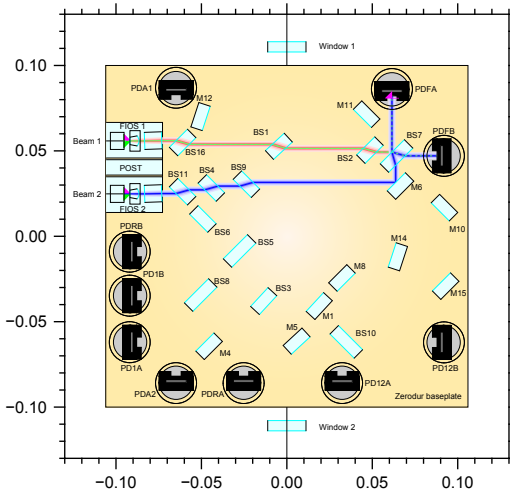


Figure 5.5.: The x1-interferometer of LTP.



ometers.



**Figure 5.8.:** The frequency interferometer.

difference (here 38 cm) and  $\delta t$  the time difference for two photons propagating through the arms. Then,  $\delta L_{xy}$  and  $\delta t$  are related by

$$\delta t = \frac{\delta L_{xy}}{c_0} . \quad (5.5)$$

Since frequency fluctuations and phase fluctuations are related by

$$\delta \phi = \delta t \delta f \quad (5.6)$$

it can be seen that the frequency fluctuations couple linearly into the phase readout of an unequal arm interferometer:

$$\delta \phi = \frac{\delta L_{xy}}{c_0} \delta f . \quad (5.7)$$

The phase or pathlength signal of the frequency interferometer measures therefore laser frequency fluctuations.

Besides these four interferometers with two redundant quadrant photodiodes each, two single element photodiodes (SEPD) are located on the optical bench (OB): PDA1 and PDA2 measure the beam power and thereby the amplitude stability of the beams provided by the FIOS'. Their signals are therefore used to stabilize the beam amplitudes.

### 5.3. Optical metrology system: from manufacturing to space

The subsequent chapters (chapter 6 and chapter 7) regard the work performed for LISA Pathfinder as well as the obtained results. In order to understand the assumptions

Besides the measurement interferometers, the LTP optical bench comprises a frequency interferometer, whose signal is used in a feed-back loop to stabilize the laser frequency. For this purpose, the frequency interferometer needs unequal arm lengths. Since the optical fibers for the measurement and reference beam have a length difference of approximately 38 cm, the optical pathlength difference (OPD) on the optical bench is chosen to be approximately the same for this interferometer, as shown in figure 5.8. Therefore, the frequency interferometer has unequal arms. The working principle of the frequency interferometer is explained with a few simple equations. Let  $\delta L_{xy}$  be the armlength

used in these chapters, it is necessary to have some background knowledge about the bonding procedure of the optical bench, as well as the assembly of LTP and the in-flight alignment procedure of the test masses. For this reason, the techniques and the bonding procedure are discussed in the subsequent section and key points of spacecraft assembly, launch and finally the in-flight alignment of the test mass are briefly introduced.

### 5.3.1. OBI alignment techniques

The components on the optical bench are bonded to the Zerodur baseplate by hydroxide-catalysis bonding [Ellife2005]. For convenience hydroxide-catalysis bonding is referred to as bonding throughout this thesis. There exists a variety of techniques used for the alignment of the components during this bonding procedure which are, for instance, described in references [Fitzsimons2010] and [Bogenstahl2010] and are briefly introduced below.

**CMM** The coordinate measurement machine (CMM) shown in figure 5.11(c) measures positions with micrometer precision.

**Templates** The fastest and least complicated procedure used to align components on the LTP OBI is using unique brass templates for each alignment step. These are manufactured with cut-outs called pockets for the components that are already bonded

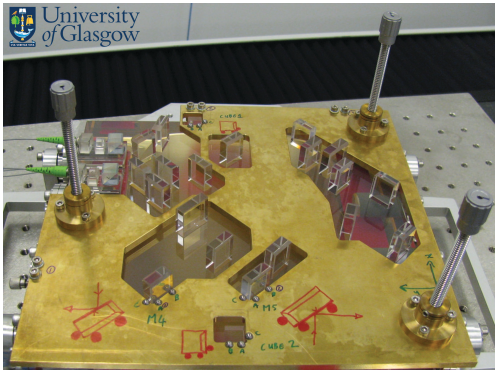


**Figure 5.9.:** Brass templates used during the alignment and bonding of the LTP optical bench. Credit: UGL.

and those to be bonded with the template (cf. figure 5.9). The sides of the pockets house three ball-bearings which define the position and angle of the components to be bonded. The alignment of the template with respect to the optical baseplate is achieved by using a coordinate measurement machine (CMM, cf. figure 5.11(c)). The precision reached with this technique is of the order of  $100\ \mu\text{m}$  and  $2\ \text{mrad}$  [UGL-3009]. Any component that needs to be aligned to a higher precision than this cannot be aligned with a template and is rated as critical.

**Critical components** A precision alignment is needed for any component whose misalignment cannot be compensated by another component in a later bonding session. This is true for beam combiners, components that direct the beam towards a test mass and pathlength compensators. This is discussed in detail in section 5.3.2.

**Aligning to CQP signals** A calibrated quadrant photodiode pair (CQP) is a device that allows precision measurement of beam angle and location. It consists at least of one beam splitter and two photodiodes (cf. figure 5.11(b)). The incident beam is

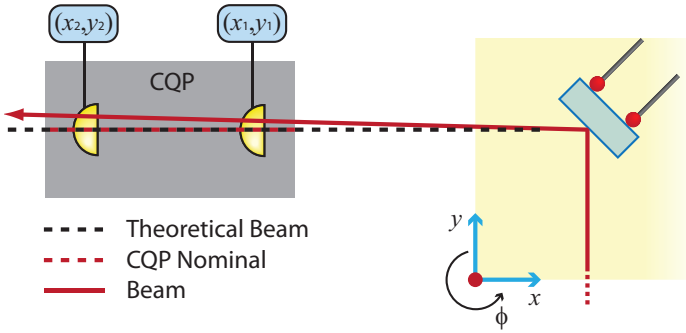


**Figure 5.10:** Working principle of a CQP. The beam hits both QPDs of the CQP centered, only if its beam is coaligned to the CQP. Source and credit: [Fitzsimons2010].

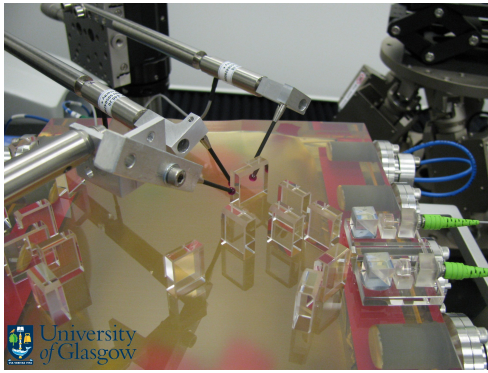
split at the beam splitter. Each beam segment propagates towards a photodiode, but the pathlength between the photodiodes is intentionally set unequal. In the device at UGL, one beam travels approximately 2 cm, the other one about 48 cm. If the beam is then aligned to the center of one QPD, it hits the center of the other QPD only if the beam angle is aligned to the CQP, as illustrated in figure 5.10. In other words, if the beam hits simultaneously both QPDs centered, its vector (direction of propagation) is determined. Therefore, a CQP allows the measurement of the beam position and angle. The achievable precision of the CQP at UGL is approximately  $\pm 2.5 \mu\text{m}$  lateral and  $\pm 20 \mu\text{rad}$  angular. The calibration process of a CQP is for example described in reference [Fitzsimons2010] and [Bogenstahl2010], the latter is the source of the numbers stated in this paragraph. The CQP can generally be used for two different tasks: either it is aligned to a fixed beam to measure its direction of propagation and position, or it is positioned in a predefined location, while a component on the optical bench is shifted and tilted until the beam reflecting from this component hits both QPDs of the CQP centered. The beam is then in the correct location and has the intended direction, which means that also the component is at its optimal position and orientation.

The components aligned and bonded with templates to CQP signals are the FIOS post, BS2, BS4, BS6, BS7, BS9, BS11, BS16, M4, M5, M10, M11, M12, and M15 as shown in figure 5.12.

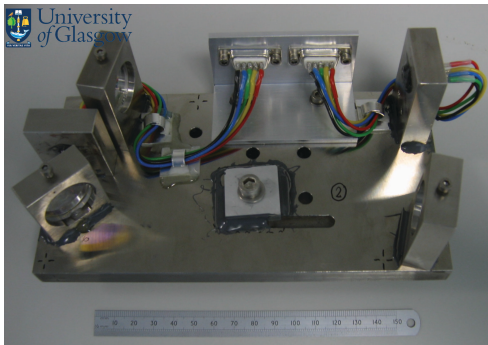
**Adjuster aided bonding** All critical components are positioned three piezo-driven probes in direct contact with the component as shown in figure 5.11(a). These probes are referred to as adjusters. The adjuster aided bonding procedure is often called adjustable bonding. The components bonded with this technique to CQP signals are BS1, BS3, M1, M8 and M14.

**Adjuster aided bonding to heterodyne signals** If the CQP is aligned to one beam, the vertical and horizontal DC signals, the total beam power and the contrast of the four quadrants can be used for alignment. When beam combiners or photodiodes are to be aligned, two interfering beams are injected in the interferometer. For these two interfering beams, heterodyne signals can be measured, which means a phasemeter and computer plus software are additionally needed. However, this provides additionally the horizontal and vertical DWS signals which accurately measure the relative angular





(a) Alignment with adjusters



(b) UGL CQP



(c) AEI CMM

**Figure 5.11.:** (a) Precision bonding with piezo manipulators called adjusters. Shown is a bonding session of one of 2OB, the optical bench which is currently designated for flight. Credit: University of Glasgow (UGL). (b) Photograph of the UGL calibrated quadrant photodiode pair (CQP). Credit: UGL. (c) Photograph of the coordinate measurement machine (CMM) at the AEI. This CMM is a twin of the machine at UGL that was used for the alignment of the engineering model (EM) and flight model (FM) of the LTP OBI.

alignment of the interfering beams. The alignment procedure, for instance of a beam combiner, is then to place the CQP at a predefined position and the beam combiner at its nominal position. The beam combiner is then shifted and tilted until the horizontal DC and DWS signals are zero. That means the beam centroid of the interfering beams is centered on the QPD, and the relative angle between both beams is minimal. The vertical alignment signals are not used, because the vertical beam position and direction are initially set by the FIOS and cannot be altered by any other component on the optical bench.

Due to the precision of adjusters and CMM, the alignment precision for the beam combiners was estimated to  $\pm 55 \mu\text{rad}$ , a value for which one adjuster needs to be moved by  $0.55 \mu\text{m}$  [UGL-3009, p. 9]. The components bonded with adjusters to heterodyne signals were BS5, BS8, BS10 and M6 (cf. figure 5.12).

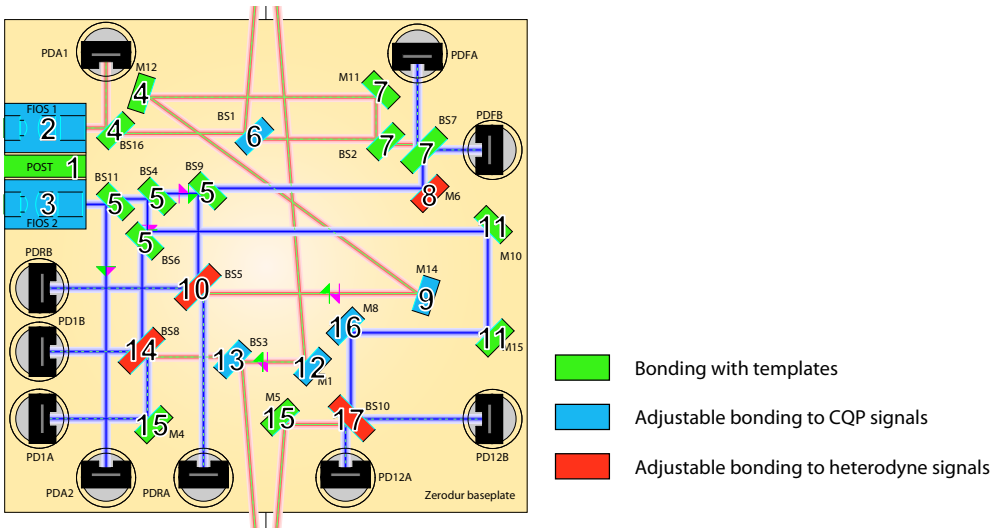


**Figure 5.12.:** Bonding procedure of the LTP OBI as performed in Glasgow. The colors indicate which type of procedure is performed. Green: templates are used; blue: adjuster aided bonding to CQP signals is performed; red: adjuster aided bonding to heterodyne signals is performed. The same colors and numbers are chosen as in the original document describing the alignment plan of the LTP OB in Glasgow: [UGL-3002]

### 5.3.2. Bonding procedure of the LTP OBI

The alignment procedure planned and performed by UGL is described below, based on [UGL-3002]. This procedure consists of 17 bonding sessions. However, the alignment of the fiber injector optical subassemblies (FIOS) is done in a separate session prior to the bonding of the optical bench (OB). The 17 bonding sessions are described below and illustrated in figure 5.12. The color of the components in this figure indicate the bonding technique: Components bonded with templates are green, those bonded with adjusters to CQP signals are blue, and finally components that are bonded with adjusters to heterodyne signals are shown in red.

- 1–3. The first component to be bonded is the FIOS post, a fused silica cuboid to which then in the second and third step the pre-built FIOS are bonded with adjusters to CQP signals. The vertical alignment of the FIOS is rated as critical, because no other component on the optical bench can compensate a beam tilt  $\theta$  in vertical direction.
4. M12 and BS16 are bonded with templates. Both are rated uncritical, because PDA1 and M14 can compensate the caused misalignment.
5. BS11, BS4, BS8 and BS9 are bonded with templates. Again any misalignment of the beams caused in this step can be compensated by components bonded in later sessions.
6. It is required that the reflection point on the test mass has an error cube of  $\pm 20 \mu\text{m}$  with respect to nominal [ASD-3020, iss 3, table 5.4]. BS1 is the



component that directs the measurement beam to the (dummy) test mass. It is therefore a critical item and bonded with adjuster aided bonding to CQP signals. Therefore, the CQP is placed in the nominal test mass position and BS3 was aligned with the adjusters until the measurement beam hits both QPDs of the CQP centered. After this step, a mirror is positioned to the nominal position of test mass 1 (TM1) which acts as a dummy test mass (DTM). This mirror is therefore referred to as dummy test mass 1 (DTM1). The position of DTM1 is measured with the coordinate measurement machine.

7. BS2, BS7 and M11 are bonded with a template, such that the bonding of all components that direct the measurement beam in the frequency interferometer is finished.
8. M6, the final component of the frequency interferometer is bonded. Since the beam combiner of this interferometer is bonded prior to M6, the alignment of M6 sets the angular alignment between measurement and reference beam of this interferometer. It is therefore a critical item and bonded with adjusters to heterodyne signals. A resulting contrast of 80% is required [UGL-3001, LTP-PFM-OBI-3401].
9. M14, the mirror that directs the measurement beam towards the reference interferometer, is bonded. Since M14 is the pathlength compensator for the reference interferometer it is rated as critical and therefore aligned with adjusters and bonding to CQP signals.
10. BS5, the beam combiner of the reference interferometer is bonded using adjuster aided bonding to heterodyne signals in order to achieve optimal alignment of both beams. Since BS5 is the component that finally aligns measurement and reference beam with respect to each other, it is a critical component.
11. M10 and M15 are bonded with templates. The resulting misalignment of the beam can be compensated by the pathlength compensator M8 in step 16.
12. M1 is bonded. Since M1 is the pathlength compensator of the x1-interferometer, it is aligned and bonded with adjusters to CQP signals.
13. BS3, the component that directs the measurement beam towards TM2, is bonded. The requirement is the same as for TM1, to position the reflection point within  $\pm 20 \mu\text{m}$  with respect to nominal [ASD-3020, iss 3, table 5.4]. Therefore, the same technique is used as for BS1. Once BS1 is bonded, dummy test mass 2 (DTM2) is positioned to the nominal position of the test mass.
14. BS8, the beam combiner of the x1-interferometer is adjustable bonded to heterodyne signals, just like the beam combiner BS5 in step 10. This is a critical step in the bonding procedure, since BS1 is the final component of the x1-interferometer and no component on the optical bench can compensate for its misalignment. The only component which could compensate the resulting angular misalignment of the interfering beams is test mass 1. It would thereby pick up a rather large misalignment in comparison to the requirements. With the conventional in-flight

alignment procedure of the test masses, this would be the case. This is discussed in detail in section 7.3.

15. M4 and M5 are bonded. M4 is a non-critical component, since it directs the beatnote of the x1-measurement and reference beam to PD1A. M5 is also a non-critical component, because its misalignment can be compensated by BS10, the beam combiner of the x12-interferometer. Therefore, M4 and M5 are bonded with templates.
16. M8, the pathlength compensator of the x12-interferometer is bonded. Like the other pathlength compensators (M4 and M14), it is rated as a critical component and therefore bonded with adjuster aided bonding to CQP signals.
17. BS10, the beam combiner of the x12-interferometer is bonded. Like the other beam combiner, BS10 is bonded with adjuster aided bonding to heterodyne signals. The angular alignment of BS10 is as critical as the angular alignment of the beam combiner BS8 for the same reasons. Apart from the photodiodes, BS10 is the final component to be bonded to the optical bench. Therefore, there is no component on the optical bench, which could compensate for the angular misalignment of BS10. Like test mass 1 could compensate the angular misalignment of BS8, test mass 2 could compensate the angular misalignment of BS10. This would have the same effect as described in bonding session 14. For further information, please read section 7.3.

Once these 17 bonding sessions are performed, the photodiodes provided by the University of Birmingham (UBI) are mounted and aligned to the various beams. Here, a lateral displacement of the beam centroid with respect to the center of the QPD of less than  $33\ \mu\text{m}$  is required, which was derived in [UGL-3001, requirement LTP-PFM-OBI-4403]. Afterwards, the optical bench is complete and ready to be shipped to ASD and later AEI for on ground testing.

### 5.3.3. The route of the optical bench: from Glasgow to space

Once all on-ground tests are successfully performed, LTP is assembled. During the assembly, the inertial sensors need to be aligned with respect to the optical bench (OB). This means in particular that the electrode housing inside the vacuum enclosure is positioned, which defines the alignment of the electrical null inside the electrode housing with respect to the optical bench. Electrical null refers to the position which the test mass takes when the capacitive sensor measures zero. This is the position, to which the DFACS will shift the test masses in flight.

Once the LTP core assembly (LCA) construction is complete, it is mounted inside the satellite. Finally, when the assembly of LISA Pathfinder is finished, it will be shipped to Kourou in French Guiana for launch. During launch, the test masses need to be firmly caged to prevent them from damaging the surrounding electrode housing. Approximately two months after launch, LISA Pathfinder will reach its final orbit and can go into operation. One of the first steps then is to carefully release the test masses from the caging. This is a critical point in the lifetime of LISA Pathfinder, since the harsh forces that act on the test masses during launch may not lead to

cold welding. Furthermore, the release of the test masses needs to be extraordinarily smooth. Residual motion of the test masses must be small enough to prevent the test masses from touching the surrounding electrode housing. The caging mechanism (shown in figure 5.3) and the proof of successful de-caging is an important technology to be tested for LISA.

Once the test masses are successfully de-caged and free floating, they will not be optimally aligned with respect to the optical bench. That means in particular, that the photodiodes are likely hit only by the reference beam, and not by the measurement beam. An autonomous alignment procedure [Marin2007, Marin2006] is planned to align both test masses successively. This procedure will be referred to as in-flight alignment of the test masses and consists of three steps. The first one is a scanning procedure in which one test mass is moved along an expanding spiral until a certain amount of light power is detected by the corresponding QPD. The next step is aligning the test mass to the DC signal of the x1- or x12-interferometer respectively. Once the DC-alignment goal is reached and the centroid of the interfering beam hits the QPD centered, the DWS-alignment starts. The conventional alignment procedure was to rotate the test mass until the horizontal and vertical DWS signal of the corresponding interferometer is zero. After this step, the measurement and reference beam are optimally aligned on the photodiodes. In section 7.3 it is shown, that this does not necessarily mean, that the test masses are also optimally aligned. Instead it is likely that the test masses are then neither parallel to the optical bench nor to each other with angular misalignments in the order of  $100 \mu\text{rad}$ . Alignment strategies are therefore discussed in section 7.3.

After the in-flight alignment procedure is performed, the interferometer is optimally aligned and LTP is ready to start experiments. There is a large variety of experiments planned for the mission time of LTP, which are described and defined in the experimental master plan (cf. for instance [EST-5007]).

## 5.4. Coordinate frames

In general, the coordinate frame shown in figure 5.13(a) is used throughout LTP. The  $x$ -axis directs from test mass 2 (TM2) to test mass 1 (TM1). The  $y$ -axis lies in the plane of the optical bench and is of course orthogonal to the  $x$ -axis, the  $z$ -axis is orthogonal to both the  $x$ - and  $y$ -axis. This simple definition is useful for a general overview. However, it is not very precise. It does not state, which test masses are used for the definition: dummy test masses, test masses at their nominal position, free-falling test masses aligned to DWS zero, free-falling test masses aligned to a pre-defined DWS offset, and so on.

Throughout this thesis, several coordinate frames are used. These coordinate frames are defined in the subsequent paragraphs. The labels of these coordinate frames are chosen analogue to those in [ASD-3020, iss 3] and [ASD-3020, iss 6].

**OCF: OptoCad frame** In the LTP-OBI-Alignment Simulation there are no vertical misalignments implemented, such that all interferometer beams lie in one plane. This plane is by definition the  $x - y$ -plane. The OptoCad frame (OCF) is the natural coordinate frame of this thesis, since it is the coordinate frame used in OptoCad for the

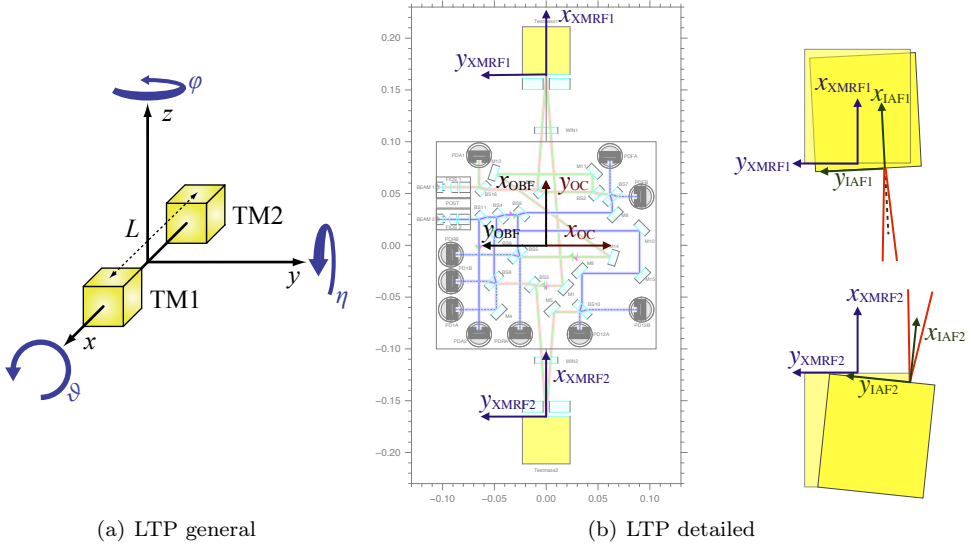


**Figure 5.13.:** Coordinate frames. (a) general coordinate frame used for LTP: the  $x$ -axis is the connecting axis between both test masses. The  $x - y$ -plane is the plane of the OBI. A rotation around the vertical  $z$ -axis is labeled  $\varphi$ .

(b) On the left side are the definitions of the OCF, OBF and XMRF, which are all defined with respect to the nominal interferometer setup in OptoCad. The figure to the right shows the relation between XMRF and IAF. The transparent light yellow cubes show the nominally aligned test masses which define the OBF, while the solid yellow cubes indicate the position and alignment of the free-floating test masses after DWS zero-correction and shifting to the electrical null.

definition of the LTP-OBI. Figures showing the LTP-OBI, like for instance figure 5.4 show coordinates in the OCF. The origin of the OCF is the center of the square that indicates the size of the optical bench or baseplate. The  $y$ -axis goes from this center of the baseplate in direction of the nominal TM1 position. The  $x$ -axis is the axis which is orthogonal to the  $y$ -axis and in the plane of the interferometer. If expanded to the third direction, the  $z$ -axis points out of the paper plane and thus off the baseplate.

**OBF: optical bench frame** The optical bench frame (OBF) in [ASD-3020, iss 6] is defined by the geometry of the built flight model of the optical bench. Throughout this work, the OBF is a  $90^\circ$  rotated OCF, that means

$$x_{\text{OBF}} = y_{\text{OC}} \quad (5.8)$$

$$y_{\text{OBF}} = -x_{\text{OC}} \quad (5.9)$$

$$z_{\text{OBF}} = z_{\text{OC}} \quad (5.10)$$

An illustration is shown in figure 5.13(b). The  $x$ -direction of the OBF is the connecting line between the nominal positions of the test masses. The  $y$ -axis is in the plane of the interferometer and orthogonal to the  $x$ -axis. The  $z$ -axis points out of the drawn optical bench plane.

**IAF: interferometer axis frame** The interferometer axis frame (IAF) is defined by the reflection points on the free-floating test masses, that is after aligning the test masses to the electrical null and DWS zero. The IAF1 is defined by the reflection point on TM1, IAF2 by the reflection point on TM2. The center of each IAF is the reflection point. The  $x$ -axis is orthogonal to the reflecting surface and thus the bisecting line between the incident and reflected beam. The direction of the  $x$ -axis is roughly the direction of the OBF- $x$ -axis, such that the IAF1- $x$ -axis points into TM1, while the IAF2- $x$ -axis points out of TM2. The  $y$ -axis is the axis which is orthogonal to the  $x$ -axis and (roughly) in the plane of the optical bench. The  $z$ -axis is then constructed by the vector product  $\vec{z} = \vec{x} \times \vec{y}$ . In the nominal setup of the OBI, the IAF is identical to the OBF except of a shift of the origin in  $x$ -direction by  $\pm 16.5$  cm.

**XMRF: Reference frame of the nominal reflection point in flight** The XMRF is the reference frame of the reflecting surfaces of the test masses aligned in-flight, that means each test mass is located in its electrical null. The center of the XMRF is the center of the reflecting surface. The  $x$ -axis is orthogonal to the TM-surface and points into TM1 for XMRF1 and out of TM2 for XMRF2. The  $y$ - and  $z$ -axes are defined analogue to  $y$  and  $z$  in the IAF. Thereby, the XMRF defines the nominal reflection point for the in-flight aligned test masses. A comparison XMRF/IAF  $\Delta y$  gives thus the displacement of the reflection point in flight with respect to the center of the reflecting test mass surface.



## 6. The LTP-OBI-Alignment Simulation

*In this chapter, the LTP-OBI-Alignment Simulation is introduced, a software tool that interfaces between OptoCad and QPD.c and uses both programs to imitate the alignment procedure of the LTP optical metrology system (OMS) on ground as well as in flight. The interface part of this software was used for any simulation performed for this thesis. The first section (section 6.1) comprises the general structure and aim of this software, and gives information about implemented statistics. Since any variation is based upon a nominal model, section 6.2 introduces the nominal model of the engineering and flight model (EM, FM) of the LTP optical bench interferometer (OBI). The heterodyne signals for these interferometers were computed and the resulting coupling factors are compared to experimental results. Finally, section 6.3 gives a detailed description of the implemented alignment procedure of the LTP OBI, which is based upon the procedures described in section 5.3.2.*

### 6.1. Context and structure of the simulation

The performance of LISA Pathfinder is affected by the alignment of the OBI. Misalignment couples into the various interferometer channels, causes static misalignment of the test masses in flight which then results in additional noise. These effects cannot be fully investigated experimentally on ground before the mission. Therefore, simulations were needed to

- predict the amount of cross-coupling between the heterodyne signals,
- find critical components that are the main contributors to resulting noise,
- compute the final static alignment of the test masses in flight.

The simulation was programmed to imitate the alignment procedure, assembly and in-flight alignment of the test masses as described in section 5.3 by taking into account the alignment tolerances in each step. It thereby generates step by step a realistically misaligned OBI. For each investigation a large number of possible realistic OBIs was computed to give statistics for the investigated problem.

The LTP-OBI-Alignment Simulation is based upon OptoCad and QPD.c. OptoCad is a two dimensional raytracing program which also computes gaussian beam parameters, while QPD.c is a program that computes heterodyne signals from a set of beam parameters using the equations derived in section 3.2. The LTP-OBI-Alignment Simulation splits therefore into two parts: an interface between OptoCad and QPD.c and a logical part, containing the alignment procedure of LTP.

## 6. The LTP-OBI-Alignment Simulation

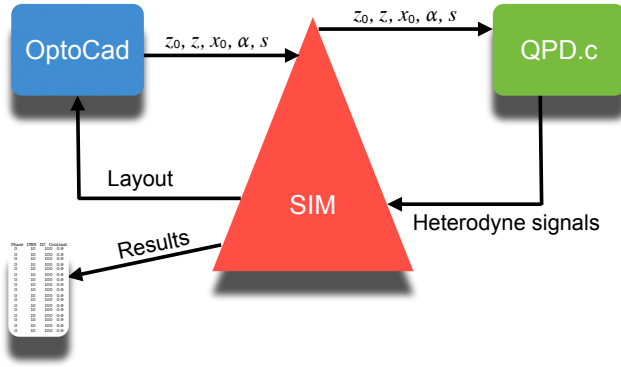


**Figure 6.1.:** Interface part of the LTP-OBI-Alignment Simulation (abbreviated here as SIM). The simulation generates an optical setup and passes it to OptoCad, which traces the defined beams through the setup and computes beam parameters  $(z_0, z, x_0, \alpha, s)$  for each beam. The simulation passes these parameters on to QPD.c after arranging them in the correct input format for QPD.c. Finally, the simulation reads the heterodyne signals computed by QPD.c and further processes these to coupling factors or uses them for realignment of components.

**Interface** In this part of the simulation, an interferometer setup is built, following the working principle sketched in figure 6.1. Positions and angles of all components are defined and the setup is passed to OptoCad. OptoCad traces the defined beams through the optical setup and gives back beam parameters at requested positions which are usually the active surfaces of photodiodes. The simulation reads the beam parameters, rearranges them and calls QPD.c. As described in section 3.2.2 and section 3.2.3 QPD.c computes the heterodyne signals and passes these back to the simulation. By changing the value of a variable, and thereby shifting or rotating a component, the simulation computes how this variable affects the heterodyne signals.

The interface part is thus independent of LTP and can be used for any arbitrary interferometer. It was used for any simulation result throughout this thesis, for instance for the example interferometers of chapter 4 and the investigation of imaging optics for LISA (cf. chapter 10) but it is also used today in the AEI prototype group.

**Alignment Simulation** This part of the simulation consists of functions that imitate the alignment procedure of the OBI from stepwise bonding the OBI over LPF assembly to the final in-flight alignment of the test masses, as described in section 5.3. In each step of the procedure, the corresponding tolerances are taken into account. The detailed procedure is presented and discussed in section 6.3.

**Implementation of tolerances** For the implementation of the alignment procedure, statistics of tolerances need to be defined. For example, a mirror that shall be bonded to the baseplate at a specific angle  $\varphi$  will indeed have an angle of  $\varphi \pm \Delta\varphi$  with  $\Delta\varphi \leq \varphi_T$  due to tolerances in the bonding procedure (these define  $\varphi_T$ ). However, the statistics are not known, that means, it is not known whether an angle in close proximity to the nominal value  $\varphi$  is more likely than an angle with large deviation (close to  $\varphi \pm \varphi_T$ ) or



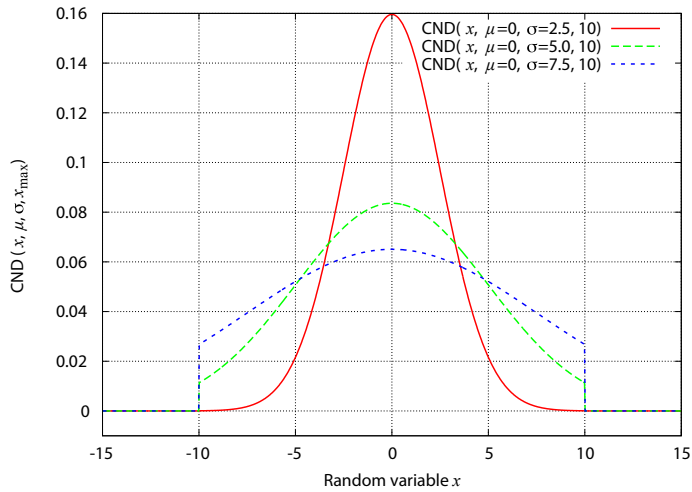


**Figure 6.2.:** Probability density function of a clipped normal distribution of a random variable  $x$  for different standard deviations  $\sigma$ , mean value of  $\mu = 0$ , clipped at  $x = 10$ . This type of distribution was chosen for the random variables used in the implementation of alignment tolerances in the LTP-OBI-Alignment Simulation. Further information is given in appendix A.4.

if so by how much. Therefore, assumptions had to be made. The assumed distribution for all statistically distributed variables is a clipped normal distribution (CND) as shown in figure 6.2. A detailed description why this distribution was chosen and an overview of the assumptions are given in appendix A.4.

## 6.2. The nominal OBI

The basis of any simulation regarding the LTP optical bench is the nominal OBI setup, which is implemented in the interface part of the simulation. This nominal OBI setup is an hypothetical implementation of the LTP OBI which was optimized to an experimentally unreachable high accuracy of alignment. For instance, the nominal flight model has the following alignment:

- the beam centroids are centered to less than 3 pm on PD1B and PD12B,
- the angle between both impinging beams on a QPD is less than 0.3 prad,
- the incident beam on each test mass is centered to less than 3 fm .

This layout was generated before optimization routines were implemented in the simulation. It was rated as sufficiently well aligned, since it is well beyond alignment capabilities and reasonably close to a perfect model. This nominal OBI thus has contrasts  $c$ , very close to 1, and DWS and DC signals of approximately zero, as listed in table 6.1.

## 6. The LTP-OBI-Alignment Simulation

signal	PD1B	PD12B
DWS	< 8.1 prad	< 5.3 nrad
DC	< $1.3 \cdot 10^{-12}$	< $4 \cdot 10^{-9}$
contrast	> 99.994 %	> 99.9992 %

**Table 6.1.:** Signals of the nominal LTP-OBI as implemented in OptoCad and evaluated with QPD.c

### 6.2.1. Coupling factors of the nominal OBI

In section 4.5 coupling factors were introduced. These coupling factors were computed with the interface part of the simulation and are now used to characterize the nominal OBI. Therefore, the DWS coupling factors were computed for the engineering model (EM) as well as for the flight model (FM). The resulting values are listed in table 6.2. The coupling factors for the engineering model were already measured during the functional and performance tests of the EM [AEI-3017] when this investigation was performed. These measured values are also listed in table 6.2. This table shows a general agreement between numerically computed and measured coupling factors for a tilt of test mass 1 ( $k_{\varphi_1}^{\text{DWS1}}$ ,  $k_{\varphi_1}^{\text{DWS12}}$ ). However, the coupling factor of a tilt of test mass 2 to the x12-DWS signal ( $k_{\varphi_2}^{\text{DWS12}}$ ) shows a rather high deviation of 24% (5453 vs. 7263). This deviation can be explained by the beam parameters: if the beam parameters used in the simulation do not match the beam parameters of the real EM, the computed DWS coupling factors deviate from the measured coupling factors. This is likely to be the case in the EM since the beam parameters on this bench are up to now unknown and not measured, due to technical difficulties: the space on the fully bonded optical bench is too limited to measure the beam parameters without risking to damage components.

The coupling factors for the flight model (FM) are also stated in table 6.2. When this investigation was performed (in 2007), the FM of the OB did not exist yet and measured results for the coupling factors were not yet available. Nevertheless, it was important to ensure that the changes between EM and FM did not result in small DWS coupling factors. The DWS coupling factors are assumed to be sufficiently high if they have a value of the order of a few thousand. This guarantees optimal readout of the test mass angles. The results in table 6.2 thus show that the FM DWS coupling factors are comparable to the EM DWS coupling factors. The last but one column of table 6.2 shows results obtained at the University of Glasgow (UGL). These values were computed with MATLAB and the LightPipes toolbox. Since completely different formalisms were used for the computation it is to be expected that deviations in the results occur. These deviations are comparably small which gives confidence in the stated values as well as in the reliability of the used tools.

By today (autumn 2010), the proto flight model 3OB is fully bonded and DWS coupling factors were measured by UGL. The values obtained during the 3OB characterization are shown in the last column of table 6.2. These measured coupling factors show only a small deviation of less than 10% to the computed values of the nominal OBI. This will be further investigated in section 7.1.2.

	QPD.c nom. EM	measured real EM	QPD.c nom. FM	UGL sim. nom. FM	meas.real FM
$k_{\varphi_1}^{\text{DWS}_1}$	5276	5441	4901	4800	4985
$k_{\varphi_1}^{\text{DWS}_{12}}$	4836	5365	4355	4500	4529
$k_{\varphi_2}^{\text{DWS}_{12}}$	5853	7263	5619	5700	5155

**Table 6.2.:** Absolute values of DWS coupling factors of the nominal setup of the engineering model (EM) and flight model (FM) of the LTP-OBI in comparison to measurement results. The first column shows values computed with OptoCad and QPD.c for the EM, the second column shows corresponding laboratory results according to [AEI-3017]. The third column shows computed results for the FM design and the second-last column states corresponding results from UGL [UGL-3019]. Finally, the last column shows recent results measured at UGL for the built PFM 3OB [UGL-3039].

### 6.3. Realistically misaligned OB in eight steps

The LTP-OBI-Alignment Simulation was written and mainly used between 2005 and 2008. Accordingly, the tolerances and requirements that were implemented in the simulation use values from documents from this time period.

One major problem of the LTP-OBI-Alignment simulation was a rather high runtime. Each call of OptoCad and QPD.c usually costs only a fraction of a second on a typical computer. However, imitating the alignment procedure of the OBI results in a high number of these calls. Therefore, the implemented alignment procedure is shortened to the key points of the actual procedure. The resulting runtime was still of the order of 8 to 12 hours for a set of 1000 realistic OBIs.

In LTP, the reference interferometer provides a phase reference. The subtraction of its phase signal from the phase signals of the x1- and x12-interferometer cancels any common mode fluctuation resulting for example from pathlength variations in the fiber or variations caused on the modulation bench which are caused for example by temperature fluctuations. However, these are fluctuations that are not implemented in the simulation and the reference interferometer would provide constant signals. Therefore, it was decided to neglect the reference interferometer. Instead, the phase reference of each interferometer is the signal computed on PD1B or PD12B respectively, after a realistic OBI is generated, that means after step 8 is completed.

**Step 1: Setting mirrors and beam splitters** In the first step of the simulation, several sessions of the experimental bonding procedure are merged: all reflective components that are part of the x1 or x12-interferometer are set at the same time. The only exception are the beam combiners BS8 and BS10, which are set in step 5. In the engineering model these components are BS1, BS3, BS4, BS6, M1, M4, M5, M8 and M10. For the flight model design BS1, BS3, BS4, BS6, M1, M5, M8, M10 and M15 are positioned as shown in figure 6.3. Furthermore, the angle of the FIOS is varied. For all components the tolerances of adjustable bonding are used such that each position and angle is drawn from a CND clipped at  $\pm 10 \mu\text{m}$  or  $\pm 50 \mu\text{rad}$  respectively around its nominal value. In this step components that are bonded with templates are not distinguished from those



all beam parameters and the propagated path length of each beam are kept constant. For instance, the position of the beam waist is shown in figure 6.3 and 6.4 by the green and pink triangles. Even though the FIOS is removed from figure 6.4, the beam waist is at the same position as in figure 6.3.

Once the FIOS is removed, the beam parameters are changed directly by shifting the waist position by  $\pm 10$  cm and altering the beam radius at the end of the FIOS by  $\pm 10\%$ . A more precise description of the implementation of these variations and an explanation why these values were chosen, can be found in section 2.3.2 of [PD9]. These variation ranges were not agreed with UGL. However, this is assumed as non-critical and was performed rather to get an impression of the influence of beam parameters.

**Step 3: Positioning of both dummy test masses** According to the bonding procedure, BS1 and BS3 are aligned in bonding session 6 and 13 to CQPs which are replaced afterwards by mirrors acting as dummy test masses (DTM). This procedure is simplified in the simulation by placing the dummy test masses with errors resembling the experimental precision and aligning the beam splitters to these positioned test masses. Therefore, the  $x$ - and  $y$ -positions of the test masses in the simulation are drawn from a CND that is clipped at  $\pm 20 \mu\text{m}$ . This results in an error box of the reflection point on each DTM by  $\pm 20 \mu\text{m}$ , which is the requirement taken from reference [ASD-3020, iss 3, table 5-4]. The angle of the DTMs are drawn from a CND clipped at  $\pm 30 \mu\text{rad}$ . This value is the sum of the precisions of CQP ( $\pm 20 \mu\text{rad}$ ) and the CMM ( $\pm 10 \mu\text{rad}$ ), which are used to align the dummy test masses and impinging beam.

**Step 4: Aligning BS1 and BS3 to the dummy TMs** In this step, beam splitter BS1 is rotated until the reflection point on dummy test mass DTM 1 coincides to numerical precision with the centre of the DTM reflecting surface. Once this optimal angle for BS1 is found, BS3 is aligned with the same procedure to DTM2.

It is assumed here that the misalignment of BS1 and BS3 is small compared to the positioning error of the DTMs. Therefore, both beam splitters stay aligned to their optimal angle and no further misalignment of the beams is implemented and the entire alignment error budget is allocated in step 3. The measurement beam is thus optimally aligned to both dummy test masses. However, this does not mean that later on, the real test masses are hit at the centers of their reflective surfaces. The alignment of the flight test masses is implemented in step 7, the LTP assembly step, with new tolerances.

**Step 5: setting the beam combiners BS8 and BS10** This is the final and critical step in the bonding procedure. All mirrors and beam splitters are fully bonded to the base plate, except of the beam combiners (BS8 and BS10, cf. figure 6.5) which are bonded in session 14 or 17 respectively. The resulting misalignment of both beams cannot be corrected by any other component. Likewise, BS8 and BS10 can correct most of the misalignment that resulted from misalignment of other components. This makes the alignment of BS8 and BS10 critical and important.

The bonding of BS8 and BS10 is implemented in the following way: the intersection point of the measurement and reference beam is computed as well as the bisecting angle. The computed values are the optimal positions and angles for BS8 and BS10. The real positions and angles are drawn from a CND (clipped at  $\pm 10 \mu\text{m}$  or  $\pm 65 \mu\text{rad}$  respectively) around these optimal values. The value of  $\pm 65 \mu\text{rad}$  was a cautious assumption given by UGL. It was later found that UGL had put a slightly more stringent estimate of  $\pm 55 \mu\text{rad}$  in [UGL-3009] (cf. also section 5.3.1). This more stringent value improves the alignment of the test masses in flight, which is discussed in section 7.3.1.

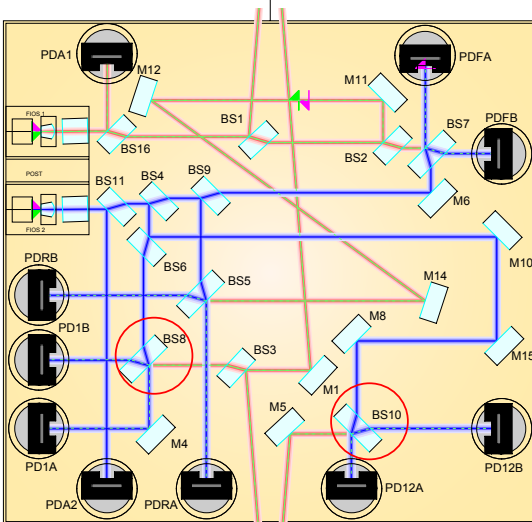


**Figure 6.5.:** Step five in the flight model design.

**Step 6: positioning of the photodiodes PD1B and PD12B** In this step, PD1B and PD12B are set orthogonally to the incident measurement beam. Subsequently, the optimal position is derived by shifting the photodiode orthogonally to the measurement beam until the DC signal is zero. The resulting position is the optimal PD position. The real position is drawn from a CND clipped at  $\pm 30 \mu\text{m}$  according to [UGL-3019, p. 17] (the requirement was later set to  $33 \mu\text{m}$  [UGL-3001, requirement LTP-PFM-OBI-4403]) around the previously derived optimal value. The longitudinal position of the photodiodes and their angle are not varied.

The specifications used for the photodiodes are those of the originally planned InGaAs-photodiodes: a diameter of 5 mm and a slit width of  $45 \mu\text{m}$ . The redundant counterparts PD1A and PD12A are per default not used in the simulation. At nominal position, redundant photodiodes provide identical signals. The effect of misalignment of the redundant QPDs was rated as a minor effect in comparison to the increased runtime if both photodiode signals were computed. Therefore, per default only PD1B and PD12B are implemented to compute the heterodyne signals.

After this step, the optical bench is complete and all components are bonded onto it.

**Step 7: LTP assembly, launch, TM in-flight positioning** During the assembly of LTP, the inertial sensors are aligned with respect to the optical bench. This means in particular, that the electrical null is positioned during the assembly phase. The position of this electrical null is completely independent from the interferometer and thus from the alignment of the dummy test masses. Its position is determined by the mechanical alignment precision of the inertial sensors with respect to the virtual nominal position of the test mass, as well as by the homogeneity of the test mass. The alignment of the electrical null is the only alignment during assembly, assumed

to affect the in-flight alignment of the test masses. Once LPF reaches its final orbit and after successful de-caging, the test masses are shifted by the capacitive sensors to exactly these electrical nulls of the inertial sensors. For the implementation in the simulation it is assumed that the tolerances stated for the electrical null define the tolerances of the in-flight position of the test masses. That means in particular, that a perfectly homogeneous cubic test mass is assumed. According to [ASD-3020, iss 3, table 3-2] the requirement for aligning of the electrical null in the sensitive longitudinal  $x$ -direction is  $\pm 100 \mu\text{m}$  with respect to its nominal position. Therefore, the  $x$ -position of the test masses are each drawn from a CND clipped at  $\pm 100 \mu\text{m}$  with respect to the nominal value.

The requirement for the insensitive  $y$ -axis is not defined with respect to the nominal position, but to the interferometer axis frame (IAF). It is required that the reflection point is shifted by less than  $50 \mu\text{m}$  with respect to the center of the test mass' reflecting surface:  $\text{XMRF}/\text{IAF} \leq \pm 50 \mu\text{m}$  (stated as  $42 + 8 \mu\text{m}$  [ASD-3020, iss 3, table 3-3]). From this value,  $\pm 8 \mu\text{m}$  need to be allocated for the misalignment of the sensitive axis, since a misalignment of  $\pm 100 \mu\text{m}$  in  $x$ -direction with an incident angle of  $4.5^\circ$  causes a beam shift in the insensitive  $y$ -direction of  $\delta y = 100 \mu\text{m} \cdot \tan(4.5^\circ) \approx 8 \mu\text{m}$ . Furthermore,  $\pm 20 \mu\text{m}$  need to be allocated for step 3, the misalignment of the dummy test masses. Therefore, the  $y$ -positions of the flight test masses are drawn from a CND clipped at  $\pm 22 \mu\text{m}$ . The TM angles are varied in the subsequent step.

**Step 8: angular in-flight alignment of the test masses** After successful uncaging, each test mass will have a certain angle with respect to the optical bench. This angle will be measured by the DWS signals of the x1- and x12-interferometer and will be driven to zero by a servo in the DFACS. This is implemented in the simulation by rotating first TM1 until the DWS signal of PD1B is zero, followed by rotating TM2 until the DWS signal of PD12B is zero (numerically implemented as 1 nrad).

All rotations done in this simulation are defined with respect to the centre of the reflecting surface, except of the rotation in this step. The in-flight angular alignment will be performed by rotating the test masses around the electrical zero, which will be approximately the same point as the centre of mass, which again is approximately the geometrical centre. Therefore, the test mass rotation implemented in this step is defined with respect to the geometrical centre of the TM.

Up to this step of the simulation, the test masses were always parallel. In this step they receive their non-nominal and unequal angles. This will be further discussed in section 7.3.1.

After these 8 steps are performed, one OBI with realistic alignment is generated. This realistic OBI can then be further investigated for resulting alignment, cross-coupling, noise or signal shape. The results obtained from these investigations are discussed in the next chapter.





## 7. Results obtained by the LTP-OBI-Alignment Simulation

*This chapter comprises the results obtained with the LTP-OBI-Alignment Simulation. These can be generally categorized into three parts: coupling factors (section 7.1), noise estimates (section 7.2) and resulting alignment (section 7.3). In the first section, selected lists of coupling factors are shown and discussed, since these values are important calibration factors of LTP. The second section shows how these coupling factors can be used to generate noise estimates. The resulting pathlength noise caused by spacecraft jitter is shown and compared to the corresponding requirements. Finally in section 7.3, the resulting alignment of the test masses and interferometer in flight are investigated. Since the conventional alignment procedure of the OMS results in a violation of a variety of alignment requirements (section 7.3.1), several alternative strategies are investigated for an improvement of the resulting alignment in flight. (section 7.3.2- section 7.3.6). Finally, section 7.3.7 summarizes the alignment conclusions and presents the resulting decisions made in the LTP community.*

### 7.1. LTP coupling factors for realistically aligned OBI

One major post-processing of the realistic OBI generated by the LTP-OBI-Alignment Simulation was the investigation of coupling factors for both test masses and the spacecraft. The coupling factors of the test masses are important calibration factors for the OMS and DFACS, since these coupling factors translate signals into equivalent test mass motion. For instance, the measured  $x$ -displacement of test mass 1 is computed from the coupling factor  $k_{\Delta s_{1m}}^{x_1}$  and measured pathlength changes in the x1-interferometer  $s_{1m}$  by

$$x_{1m} = k_{\Delta s_{1m}}^{x_1} \cdot \Delta s_{1m} \quad (7.1)$$

and the angle of test mass 1 by

$$\varphi_{1m} = k_{DWS}^{\varphi_1} \cdot DWS \quad (7.2)$$

These coupling factors are the inverse of the coupling factors stated throughout this theses, for instance:

$$k_{DWS}^{\varphi_1} = \frac{1}{k_{\varphi_1}^{DWS}} \quad (7.3)$$

The coupling factors for the spacecraft are needed for estimating the coupling of spacecraft jitter into the heterodyne signals. For instance spacecraft  $x$ -jitter should not couple into the x12-pathlength readout because it does not alter the distance between the test masses. However, misalignment of the OBI causes a residual coupling which

## 7. Results obtained by the LTP-OBI-Alignment Simulation

can be estimated with these coupling factors.

All coupling factors were computed numerically, that means:

$$k_{\text{DoF}}^{\text{signal}} := \frac{\partial \text{signal}}{\partial \text{DoF}} \quad (4.3)$$

$$= \frac{\text{signal}(\text{DoF} + \epsilon) - \text{signal}(\text{DoF} - \epsilon)}{2\epsilon}, \quad (7.4)$$

where DoF stands for a degree of freedom of either a test mass or the optical bench, which is very close to the spacecraft center of mass (CoM). The coupling factor of test mass longitudinal displacements  $x_1$  into the length measurement of the x1-interferometer  $\Delta s_{1m}$  for instance, were computed by shifting test mass 1 by  $\pm\epsilon$  respectively and computing the resulting pathlength signal  $\Delta s_{1m}$ . The resulting values were then used to compute the numerical derivative:

$$k_{x_1}^{\Delta s_{1m}} = \frac{\Delta s_{1m}(x_1 + \epsilon) - \Delta s_{1m}(x_1 - \epsilon)}{2\epsilon}. \quad (7.5)$$

The coupling factors for the spacecraft cannot be computed directly, since the spacecraft is not part of the LTP-OBI-Alignment Simulation. Yet, the optical bench is rigidly connected with the spacecraft. It is therefore assumed that any jitter of the spacecraft results in an equivalent amount of jitter of the optical bench with respect to the test masses. Furthermore, it is indistinguishable whether the optical bench shifts in a specific direction while both test masses are at rest, or both test masses simultaneously shift in the opposite direction while the optical bench stays at rest. This principle was used for the implementation of the spacecraft coupling factors: instead of shifting the optical bench and thus the spacecraft by  $\pm\epsilon$ , both test masses were shifted simultaneously by  $\mp\epsilon$  and the derivatives were computed analogously to eq. (7.4). The rotation of the spacecraft is implemented as a common mode rotation (in opposite direction) of the TMs around the geometrical centre of the optical bench.

In this section a selection of coupling factors computed by the LTP-OBI-Alignment Simulation is presented and discussed. The full set of coupling factors is shown in appendix D. These coupling factors were computed in three independent simulations:

- computation of test mass coupling factors with 1000 realistic setups with constant beam parameters,
- computation of test mass coupling factors with 1000 realistic setups including variation of beam parameters, that means including step 2 in section 6.3,
- computation of spacecraft coupling factors with over 4000 realistic setups and constant beam parameters.

It was shown in [PD7], that this is a sufficiently large number of setups to estimate the values of the coupling factors. In this document it was shown, that the RMS of  $k_{\varphi_1}^{\Delta s_1}$  varies by less than 2% if more than 1000 setups were used. If more than 2000 setups were used for the computation of the RMS, its variation was less than 0.5%. However, the settings used for the LTP-OBI-Alignment Simulation are slightly different than those described in section 6.3.

	BP	RMS $\frac{\mu\text{m}}{\mu\text{m}}$	$\sigma$ $\frac{\text{pm}}{\mu\text{m}}$	Min $\frac{\mu\text{m}}{\mu\text{m}}$	Max $\frac{\mu\text{m}}{\mu\text{m}}$
$k_{x_1}^{\Delta s1_m}$	var	1.99382	17.0891	1.99377	1.99387
$k_{x_1}^{\Delta s1_m}$	const	1.99382	17.3391	1.99377	1.99386
$k_{x_{OB}}^{\Delta s1_m}$	const	1.99382	17.5035	-1.99387	-1.99377
$k_{x_1}^{\Delta s12_m}$	var	1.99382	16.9015	1.99377	1.99387
$k_{x_1}^{\Delta s12_m}$	const	1.99382	17.2227	1.99377	1.99386
$k_{x_2}^{\Delta s12_m}$	var	1.99382	47.5934	-1.99393	-1.99367
$k_{x_2}^{\Delta s12_m}$	const	1.99382	47.5447	-1.99393	-1.99367
$k_{x_{OB}}^{\Delta s12_m}$	const	$63.4768 \cdot 10^{-6}$	63.4723	$-175.64 \cdot 10^{-6}$	$173.743 \cdot 10^{-6}$

**Table 7.1.:** Coupling factors for the interferometer length measurements  $\Delta s1_m$  and  $\Delta s12_m$ . The column 'BP' states whether beam parameters were varied. The column RMS states the root mean square,  $\sigma$  the standard deviation, max and min the maximum and minimum value of the computed set of coupling factors.

**Coupling factors for TM2-DoF to x1-signals** Since the x1-measurement beam does not reflect from test mass 2, variations of the attitude of TM2 do not affect the x1-interferometer, such that all coupling factors  $k_{\text{DoF}_{\text{TM2}}}^{\Delta s1}$ ,  $k_{\text{DoF}_{\text{TM2}}}^{\text{DWS1}}$ ,  $k_{\text{DoF}_{\text{TM2}}}^{\text{DC1}}$ ,  $k_{\text{DoF}_{\text{TM2}}}^{\text{C1}}$  are zero.

### 7.1.1. Coupling factors for pathlength readout

The resulting coupling factors for the pathlength readout are listed in table 7.1. The first column states whether a variation of the beam parameters was performed. The RMS value is 1.99382, independent of the beam parameter variation and identical for all coupling factors except  $k_{x_{OB}}^{\Delta s12_m}$ . This is discussed in the paragraphs below. These coupling factor have a small standard deviation  $\sigma$  of a few tens of micrometer per meter, compared to the RMS value. The pathlength readout is further investigated in section 7.2, where resulting pathlength noise is computed.

**RMS value of  $k_{x_1}^{\Delta s1}$ ,  $k_{x_1}^{\Delta s12}$  and  $k_{x_2}^{\Delta s12}$**  Noticeable is the value of the root mean square (RMS) of 1.99382. This value is nothing but the coupling factor between pathlength and armlength which was already introduced in section 2.1 to be 2 for normal incidence (cf. eq. (2.1)). Its value can be derived by analyzing the geometrical path length as shown in figure 7.1. The beam path of the x1-interferometer is folded by the M1-mirror. Unfolding this beam path leads to an effective position of PD1B (or PD1A respectively). As in its real position, the photodiode is orthogonal to the incident beam, but therefore not parallel to the test mass. A plane that is parallel to the photodiode in the effective position and intersects the nominal test mass reflection point needs to be constructed to define the additional path length  $\Delta s = l_1 + l_2$  which can be read from figure 7.1:

## 7. Results obtained by the LTP-OBI-Alignment Simulation

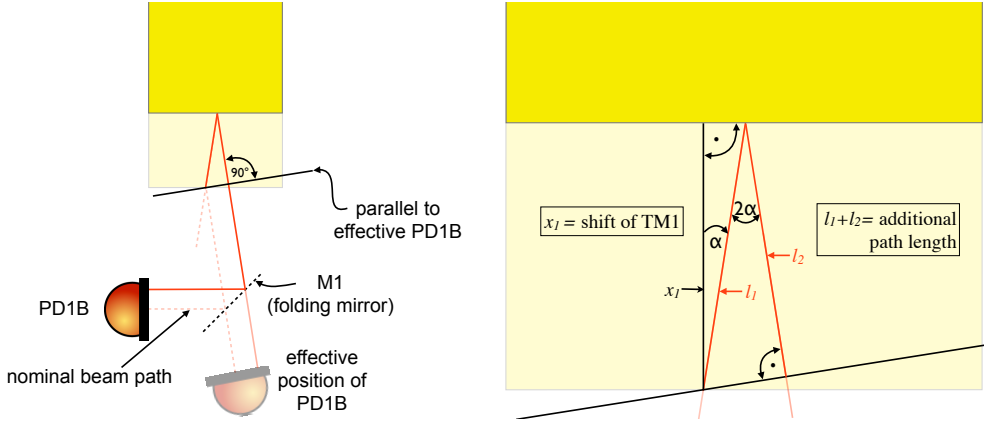


**Figure 7.1.:** Beam path if test mass 1 (TM1) is shifted in  $x$ -direction by  $x_1$ . The left figure shows the unfolding of the beam path and construction of the reference plain that defines the addition path length  $\Delta s$ . The right figure shows a zoom on the additional path length  $\Delta s = l_1 + l_2$ , the test mass shift  $x_1$  and the incident angle  $\alpha$  which is nominally  $4.5^\circ$ .

$$\Delta s = l_1 + l_2 = l_1 + l_1 \cdot \cos(2\alpha) = l_1[1 + \cos(2\alpha)] \quad (7.6)$$

$$= l_1[2(\cos(\alpha))^2] = \frac{x_1}{\cos(\alpha)}[2(\cos(\alpha))^2] \quad (7.7)$$

$$= 2x_1 \cos(\alpha) . \quad (7.8)$$

The incident angle  $\alpha$  on the test mass has a nominal value of  $4.5^\circ$ . The additional path length  $\Delta s$  is a real geometrical length change in the  $x_1$ - as well as in the  $x_{12}$ -interferometer, such that the coupling factors

$$k_{x_1}^{\Delta s 1} := \frac{\partial \Delta s 1}{\partial x_1} \quad \text{and} \quad k_{x_1}^{\Delta s 12} := \frac{\partial \Delta s 12}{\partial x_1} \quad (7.9)$$

have identical values:

$$k_{x_1}^{\Delta s 1} = k_{x_1}^{\Delta s 12} = 2 \cos(\alpha) \quad (7.10)$$

$$\stackrel{\text{nom.}}{=} 2 \cos(4.5^\circ) \approx 1.99383 . \quad (7.11)$$

In the LTP-OBI-alignment simulation, the angle of BS1, the beam splitter that reflects the measurement beam towards TM1 is adjusted. The incident angle  $\alpha$  is thus different for each realistic OBI. Therefore, the RMS of the coupling factor is not precisely the value  $2 \cos(4.5^\circ) \approx 1.99383$  but 1.99382.

This derivation is also valid for the coupling factor  $k_{x_2}^{\Delta s 12}$ . The only difference is that TM2 needs to be shifted in  $-x$ -direction to increase the optical path length, not in

$+x$ -direction like TM1. Therefore, the coupling factors are nominally (!) identical but with opposite sign:

$$k_{x_2}^{\Delta s12} \stackrel{\text{nom.}}{=} -k_{x_1}^{\Delta s12} . \quad (7.12)$$

This sign vanishes, of course, in the computation of an RMS-value. Generally, these coupling factors will not be identical, because the incident angles will not be precisely the same, such that

$$k_{x_1}^{\Delta s12} = 2 \cos(\alpha_1) , \quad (7.13)$$

$$k_{x_2}^{\Delta s12} = -2 \cos(\alpha_2) . \quad (7.14)$$

**RMS value of  $k_{x_{OB}}^{\Delta s1}$**  As already mentioned, the coupling factors for the optical bench are effectively computed by a simultaneous shift of both test masses. Since a shift of TM2 does not couple into the x1-signals, it is indistinguishable in the x1-signals whether TM1 was shifted in  $+x$ -direction or the whole optical bench was shifted in  $-x$ -direction. Hence, the coupling factors  $k_{x_1}^{\Delta s1}$  and  $k_{x_{OB}}^{\Delta s1}$  are identical except of the sign. This sign change can be seen in table 7.1 by comparing the maximum and minimum values of  $k_{x_1}^{\Delta s1}$  and  $k_{x_{OB}}^{\Delta s1}$ . Mathematically this can be expressed as:

$$k_{x_{OB}}^{\Delta s1} := \frac{\partial \Delta s1}{\partial x_{OB}} \quad (7.15)$$

$$= \frac{\Delta s1(x_1 - \epsilon, x_2 - \epsilon) - \Delta s1(x_1 + \epsilon, x_2 + \epsilon)}{2\epsilon} \quad (7.16)$$

$$= \frac{\Delta s1(x_1 - \epsilon, x_2) - \Delta s1(x_1 + \epsilon, x_2)}{2\epsilon} \quad (7.17)$$

$$= -\frac{\partial \Delta s1}{\partial x_1} \quad (7.18)$$

$$= -k_{x_1}^{\Delta s1} . \quad (7.19)$$

The step from eq. (7.16) to eq. (7.17) accounts for the fact, that the x1-interferometer does not sense changes in the attitude of test mass 2.

**RMS value of  $k_{x_{OB}}^{\Delta s2}$**  The value of this coupling factor can be deduced analogously to the value of  $k_{x_{OB}}^{\Delta s1}$ :

$$k_{x_{OB}}^{\Delta s12} := \frac{\partial \Delta s12}{\partial x_{OB}} \quad (7.20)$$

$$= \frac{\Delta s12(x_1 - \epsilon, x_2 - \epsilon) - \Delta s12(x_1 + \epsilon, x_2 + \epsilon)}{2\epsilon} \quad (7.21)$$

$$= -\left( \frac{\partial \Delta s12}{\partial x_1} + \frac{\partial \Delta s12}{\partial x_2} \right) \quad (7.22)$$

$$= -(k_{x_1}^{\Delta s12} + k_{x_2}^{\Delta s12}) , \quad (7.23)$$

assuming linearity in the step from eq. (7.21) to eq. (7.22). Therefore, the value of this coupling factor is nominally zero (eq. (7.12)), which is reasonable:

The x12-interferometer senses the differential motion of TM1 and TM2. Since any

## 7. Results obtained by the LTP-OBI-Alignment Simulation

motion of the spacecraft is considered to be identical to a common mode motion of the test masses, the spacecraft jitter should not couple into the x12-pathlength readout. However, misalignments of the OMS causes a residual coupling. The RMS-value of  $k_{x_{OB}}^{\Delta s12}$  was computed by the simulation to be approximately  $63 \frac{\text{pm}}{\mu\text{m}}$  as shown in table 7.1. RMS and the standard deviation  $\sigma$  are approximately the same

$$\text{RMS} (k_{x_{OB}}^{\Delta s12}) \approx \sigma (k_{x_{OB}}^{\Delta s12}) \quad (7.24)$$

which indicates that the mean value of this coupling factor is approximately zero.

**Comparison with Data Analysis** The objective of the x1-interferometer is the readout of longitudinal motion of TM1 with respect to the optical bench which is equivalent to a measurement of spacecraft jitter with respect to a resting test mass 1. while the x12-interferometer senses changes in the distance between TM1 and TM2. Therefore, it is convenient to scale the pathlength signals of these interferometers ( $\Delta s1$  and  $\Delta s12$ ) by their coupling factors to show equations for the measured relative position  $x_{1m}$  or distance  $x_{12m}$ . For the x1-interferometer this determined relative position is:

$$x_{1m} = \frac{\Delta s1}{(k_{x_1}^{\Delta s1})_{\text{nom.}}} \approx x_1 . \quad (7.25)$$

It is clear, that measurement values are generally not identical to the underlying physical cause due to limited measurement precision. It is therefore  $x_{1m} \approx x_1$ , accounting for example for cross-coupling which is but one contributor to measurement precision. The x12-interferometer measures a differential motion  $\Delta x := x_2 - x_1$  of the test masses:

$$\Delta s12 = k_{x_1}^{\Delta s12} x_1 + k_{x_2}^{\Delta s12} x_2 \quad (7.26)$$

$$= (k_{x_1}^{\Delta s12} + k_{x_2}^{\Delta s12}) x_1 + k_{x_2}^{\Delta s12} (x_2 - x_1) \quad (7.27)$$

$$= -k_{x_{OB}}^{\Delta s12} x_1 + k_{x_2}^{\Delta s12} \Delta x . \quad (7.28)$$

In a perfectly aligned interferometer,  $k_{x_{OB}}^{\Delta s12}$  is zero, such that the x12-interferometer measures solely changes in the separation of the two test masses. However,  $k_{x_{OB}}^{\Delta s12}$  does not vanish entirely such that the measured relative distance between the test masses

$$\Delta x_m = \frac{\Delta s12}{(k_{x_2}^{\Delta s12})_{\text{nom.}}} \quad (7.29)$$

$$\approx \frac{-k_{x_{OB}}^{\Delta s12}}{(k_{x_2}^{\Delta s12})_{\text{nom.}}} x_1 + \Delta x \quad (7.30)$$

$$=: \delta x_1 + \Delta x . \quad (7.31)$$

In LTP data analyses the measured relative distances  $x_{1m}$  and  $\Delta x_m$  are usually labeled  $o1$  and  $o_\Delta$  and the previous equations are combined in a matrix formalism:

$$\begin{pmatrix} o1 \\ o_\Delta \end{pmatrix} := \begin{pmatrix} x_{1m} \\ \Delta x_m \end{pmatrix} = \begin{pmatrix} S11 & S12 \\ S21 & S22 \end{pmatrix} \cdot \begin{pmatrix} x1 \\ \Delta x \end{pmatrix} \quad (7.32)$$

$$= \begin{pmatrix} 1 & 0 \\ \delta & 1 \end{pmatrix} \cdot \begin{pmatrix} x1 \\ \Delta x \end{pmatrix} . \quad (7.33)$$

The value of  $\delta$  can be read from eq. (7.31) and table 7.1 as

$$\delta \approx \pm \frac{1.75 \cdot 10^{-4}}{1.99382} \approx \pm 8.75 \cdot 10^{-5}. \quad (7.34)$$

This value is currently the best estimate of how much spacecraft jitter will couple into the longitudinal readout. It is therefore (rounded to  $10^{-4}$ ) used in the LISA Pathfinder mock data challenges [P5].

### 7.1.2. DWS coupling factors

The DWS coupling factors are listed in table 7.2 as root mean square (RMS), standard deviation  $\sigma$ , maximum and minimum of the set of results. Furthermore, the second last column shows the values for the nominal OptoCad OBI model as already shown in table 6.2. Finally, the last column states the corresponding experimental results as obtained in the 3OB characterization at UGL [UGL-3039]. Naturally, the RMS-values of the alignment simulation results are almost identical to the nominal values.

All lines in table 7.2 without beam parameter variation show insignificant spreading of the coupling factors: the standard deviation is of the order of 0.1% of the RMS values, but the experimental results are not between the minimum and maximum values of the simulated results. That means that the alignment of the OBI has little impact on the coupling factors and does not cause the experimentally achieved values.

The lines with the results that included beam parameter variations show a much larger standard deviation. The experimental results lie well between the minimum and maximum values of these simulation results. It can therefore be deduced:

- Beam parameter variations are the driving factor for the value of the DWS calibration factors.
- The values obtained in the 3OB characterization at UGL agree nicely with the results predicted with the LTP-OBI-Alignment Simulation.
- The beam waist position was varied in the simulation by  $\pm 10$  cm and the beam radius behind the FIOS by  $\pm 10\%$ . Since the measured coupling factors are well between the minimal and maximal values obtained by the simulation, the beam parameters on 3OB are expected to be within these tolerance values.

Additional information about the dependency of the DWS coupling factors  $k_{\varphi}^{\text{DWS}}$  on test mass displacement are given in [PD4]. This dependency is relevant for the on-ground calibration of the DWS signals. The error in the calibration depends on the precision to which the test masses can be placed to their optimal position.

### 7.1.3. DC coupling factors

The DC coupling factors for the flight model of the LTP-OBI are listed in table 7.3. These values are calibration factors needed for the autonomous in-flight alignment of

## 7. Results obtained by the LTP-OBI-Alignment Simulation

	BP	RMS	$\sigma$	Min	Max	nom.	3OB
$k_{\varphi_1}^{\text{DWS1}} \left[ \frac{\text{rad}}{\text{rad}} \right]$	var	4890.52	244.254	4167.26	5459.87	4901	4985
$k_{\varphi_1}^{\text{DWS1}} \left[ \frac{\text{rad}}{\text{rad}} \right]$	const	4903.45	3.56021	4900.14	4923.18	4901	4985
$k_{\varphi_{\text{OB}}}^{\text{DWS1}} \left[ \frac{\text{rad}}{\text{rad}} \right]$	const	4903.60	3.80308	4900.02	4925.39	—	—
$k_{\varphi_1}^{\text{DWS12}} \left[ \frac{\text{rad}}{\text{rad}} \right]$	var	4352.72	301.593	−5006.73	−3361.2	−4355	−4529
$k_{\varphi_1}^{\text{DWS12}} \left[ \frac{\text{rad}}{\text{rad}} \right]$	const	4358.21	3.95939	−4383.24	−4354.17	−4355	−4529
$k_{\varphi_2}^{\text{DWS12}} \left[ \frac{\text{rad}}{\text{rad}} \right]$	var	5616.14	183.881	4994.62	6105.5	5619	5155
$k_{\varphi_2}^{\text{DWS12}} \left[ \frac{\text{rad}}{\text{rad}} \right]$	const	5622.33	5.07279	5618.11	5655.24	5619	5155
$k_{\varphi_{\text{OB}}}^{\text{DWS12}} \left[ \frac{\text{rad}}{\text{rad}} \right]$	const	1264.19	1.23955	1262.17	1272.3	—	—

**Table 7.2.:** DWS coupling factors. Shown are the root mean square (RMS), standard deviation ( $\sigma$ ), the maximum (max) and minimum (min) value of the computed set of coupling factors. The second last column lists the computed coupling factors of the nominal FM-optical bench. Finally, the last column states results of the experimental FM-characterization taken from reference [UGL-3039]. The column ‘BP’ states whether beam parameters were varied, that means whether step 2 (cf. p. 76) was carried out in the LTP-OBI-alignment simulation.

the test masses, described in section 5.3.3. For an interpretation of these values, the analytical results from section 4.6 can be used. In that section it is shown that the DC signal is mainly driven by the spot size and the beam shift over the surface of the QPD. However, the spot sizes are approximately the same<sup>[1]</sup> in both interferometers and variations due to the rotation are negligible. The DC signals are therefore driven by beam walk on the photodiodes.

The lever arm for a TM1 rotation is smaller in the x1-interferometer than in the x12-interferometer, which can be seen for instance in figure 5.4 or by comparison of figure 5.5 and figure 5.6. A test mass tilt causes thus a smaller beam walk and smaller DC response on the photodiodes of the x1-interferometer (PD1A and PD1B) than on the photodiodes of the x12-interferometer (PD12A and PD12B). The RMS values of  $k_{\varphi_1}^{\text{DC1}} \approx 900$  and  $k_{\varphi_1}^{\text{DC12}} \approx 1400$  are thus reasonable. The same yields for the very short lever arm for a TM2 rotation. The coupling factor is thus also small:  $k_{\varphi_2}^{\text{DC12}} \approx 470$ .

It is also anticipated, that the variation of beam parameters has an impact on the coupling factors, since it alters the spot size on the photodiodes. The small fluctuations for constant beam parameters probably result from slightly varying pathlengths in the interferometer setups. These cause small deviations in the spot size on the photodiodes and thus deviations in the DC response.

<sup>[1]</sup>The beam specifications are regulated by requirement no LTP-PFM-OBI-4204 and LTP-PFM-OBI-4202 in reference [UGL-3001]. These state that the spot size has to be between 500 and 650 microns at any point on the optical bench and the spot size ratio on the photodiodes of the x1- and x12-interferometer may not be larger than 1.2. This has been verified for the qualification model and flight models of the LTP OBI as shown in [Bogenstahl2010].



	BP	RMS	$\sigma$	Min	Max
$k_{\varphi_1}^{\text{DC1}} \left[ \frac{1}{\text{rad}} \right]$	var	902.64	48.7365	-1072.42	-790.834
$k_{\varphi_1}^{\text{DC1}} \left[ \frac{1}{\text{rad}} \right]$	const	901.804	6.41945	-907.255	-868.046
$k_{\varphi_{\text{OB}}}^{\text{DC1}} \left[ \frac{1}{\text{rad}} \right]$	const	901.506	6.85116	-907.278	-856.94
$k_{\varphi_1}^{\text{DC12}} \left[ \frac{1}{\text{rad}} \right]$	var	1405.1	59.0319	1269.2	1588.09
$k_{\varphi_1}^{\text{DC12}} \left[ \frac{1}{\text{rad}} \right]$	const	1406.73	14.0027	1323.18	1418.12
$k_{\varphi_2}^{\text{DC12}} \left[ \frac{1}{\text{rad}} \right]$	var	466.139	19.5801	-526.961	-421.176
$k_{\varphi_2}^{\text{DC12}} \left[ \frac{1}{\text{rad}} \right]$	const	466.671	4.64693	-470.669	-438.953
$k_{\varphi_{\text{OB}}}^{\text{DC12}} \left[ \frac{1}{\text{rad}} \right]$	const	939.375	10.1018	871.841	947.71

**Table 7.3.:** DC coupling factors. Listed are the root mean square (RMS), standard deviation ( $\sigma$  the), the maximum (max) and minimum (min) value of the computed set of coupling factors. The column ‘BP’ states, whether beam parameters were varied during the computation.

### 7.1.4. Application of coupling factors

The computed coupling factors transfer test mass motion into optical readout signals. If the test mass motion is known, that means for given noise estimates in the various degrees of freedom, these coupling factors can be used to estimate the resulting interferometric readout noise. This is shown in the subsequent section.

Besides the test mass coupling factors shown in this thesis, it is also possible to compute coupling factors for each component on the optical bench. From these coupling factors it was investigated, how stress which results in optical bench deformation, affects the heterodyne signals. It is known that the struts, which connect the LTP core assembly (LCA) to the thermal shield cause stress in the OBI. In [PD5] and [PD8] it is investigated how thermal noise in the struts affects the heterodyne signals.

## 7.2. LTP noise spectra

The coupling factors presented in the previous section are effectively calibration factors for the LTP experiment. The tables listed in section 7.1 show the variance expected for these calibration factors and the impact of beam parameter variations. Furthermore, they give an impression of cross-coupling in the various channels and about the quality of the DWS-signal. However, they do not allow a direct estimate, whether the amount of crosstalk will fulfill all requirements. Therefore, these coupling factors are multiplied to existing noise spectra for the test mass’ degrees of freedom, a procedure only valid in case of linearity. The resulting noise spectra can then be compared to requirements. Naturally, the most significant noise spectra are those regarding the x12-pathlength signal, since this is the main science signal and showing that this signal fulfills the total allocated noise budget is part of the mission goal (cf. section 5.1 and eq. (5.3)). In this section, the pathlength noise originating from spacecraft (S/C) jitter is investigated.

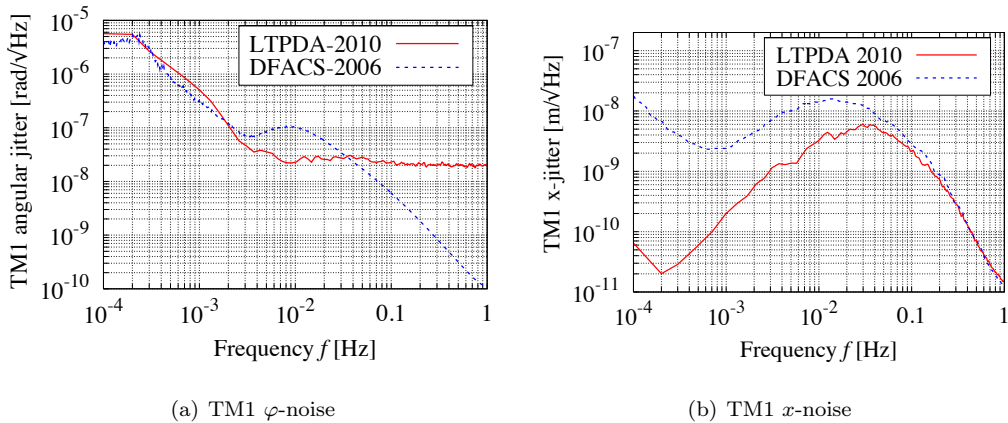


**Figure 7.2.:** Noise estimates for test mass 1 longitudinal jitter (a) and in plane angular jitter (b). Shown is a comparison of estimates of 2006 (taken from [ASD-2003]) and 2010, generated by LTPDA [12]. According to the new estimates, the angular jitter of TM1 is dominated by white OMS readout noise at high frequencies, which corresponds to the assumptions made for LTP’s total path-length noise (cf. figure 5.1(b)). Furthermore the thruster noise which caused the maximum in the 2006 angular jitter estimate is suppressed in probably by the new control loops. The estimates of  $x$ -jitter changed mainly for low frequencies, since the TM1- (or effectively spacecraft-) longitudinal control was changed from inertial sensors to OMS.

### 7.2.1. Estimates of spacecraft and test mass jitter

Since LISA Pathfinder is not yet in space, there do not exist any measured noise spectra with free floating test masses. However, it is important to estimate the noise in order to define requirements and find critical areas for optimization. Providing estimates of noise spectra is an iterative process, since any instrument aboard LISA Pathfinder contributes to the final measurement noise and changes of hardware or software can affect the resulting measurement noise. For an example figure 7.2 shows a comparison between test mass 1 jitter estimates from 2006 and 2010. The spectra of 2006 are taken from a DFACS analysis document [ASD-2003], while the spectra of 2010 are generated by LTPDA [12, Hewitson2009] (state space model, LSS V4.90, SCI1 M3 OPT). It can be seen that the noise estimates significantly changed in the past years. However, the new noise shapes do also depend on a variety of parameters, such that different choice of settings and assumptions changes these noise curves. Noise estimates should therefore generally be handled with care, since they come with some amount of uncertainty and will evolve until in-flight measurement results are available.

In order to investigate the amount of pathlength noise originating from spacecraft jitter, estimates for spacecraft noise are required. The x1-interferometer senses displacements between test mass 1 and the optical bench. Furthermore, the optical bench is rigidly connected to the spacecraft, such that any spacecraft jitter is equivalently measured by the x1-pathlength readout, as already discussed in section 5.2.1. It is therefore indistinguishable, whether the spacecraft jitters while TM1 is at rest, or vice versa. For this reason, noise curves for TM1  $x$ -jitter are used as spacecraft  $x$ -jitter estimates.

The attenuation and spacecraft control in  $y$ - and  $\varphi$ -direction is rather complicated such that it is not right away clear how to estimate these noise spectra. For simplicity the same assumption as in  $x$ -direction is made and test mass 1 lateral and angular noise curves are used as estimates of spacecraft lateral ( $y$ -) and angular ( $\varphi$ -) jitter.

### 7.2.2. Requirements

In order to evaluate the noise spectra, they need to be compared to corresponding requirements. Unfortunately, the according requirement specification document [ASD-3036] does not contain directly requirements for pathlength noise originating from spacecraft jitter in the various degrees of freedom. The required break down was performed by Nico Brand (ASD) and is shown in appendix A.3. The resulting requirements are listed in table 7.4.

		S/C $x$ -jitter	S/C $y$ -jitter	S/C $\varphi$ -jitter
$S(\Delta s_{12_m})$	$\frac{\text{pm}}{\sqrt{\text{Hz}}}$	1.50	0.96	6.14

**Table 7.4.:** Requirements for pathlength noise due to spacecraft jitter in its various degrees of freedom. The stated values are valid for high frequencies, the omitted frequency dependency is the same as for the top level science requirement in eq. (5.3). These requirements are derived by ASD as shown in appendix A.3, as a further break down of the 6.0 pm/ $\sqrt{\text{Hz}}$  requirement for TM and OB alignment in [ASD-3036, req. 42200].

### 7.2.3. Showing linearity

As mentioned, it is possible to generate noise spectra by multiplying coupling factors to an existing linear spectral density, for example the angular jitter spectrum of a test mass. This is called the ‘linear approach’ for convenience. However, this approach is valid only, if the system is indeed linear. This assumption is reasonable since the aim of LTP is to prove free floating test masses with a residual jitter in the picometer range. However, the signals of the x12-interferometer depend on the attitude and jitter of both test masses simultaneously and it is known, that the phase response to TM rotation is a non linear function. Furthermore, it is clear that a rotation of TM1 leads to a shift of the reflection point on TM2. Therefore, the x12 signal is expected to be a function of both TM angles including cross terms and higher order terms. It therefore needs to be shown that the cross terms and higher order terms are negligible for the amount of jitter expected for LTP.

To verify that the linear approach can be used for the pathlength readout of the x12-interferometer  $\Delta s_{12}$ , this pathlength noise was computed for independent jitter of both test masses. The runtime of the LTP-OBI-Alignment Simulation was too high to compute noise spectra directly, that means by jittering the test masses or optical bench respectively, and computing the amplitude spectral density from the resulting pathlength signals. Therefore, the following approach was taken instead:

1. The pathlength signal of the x12-interferometer was sampled on a rectangular grid of the in plane angles of both test masses ( $\varphi_1, \varphi_2$ ).

## 7. Results obtained by the LTP-OBI-Alignment Simulation

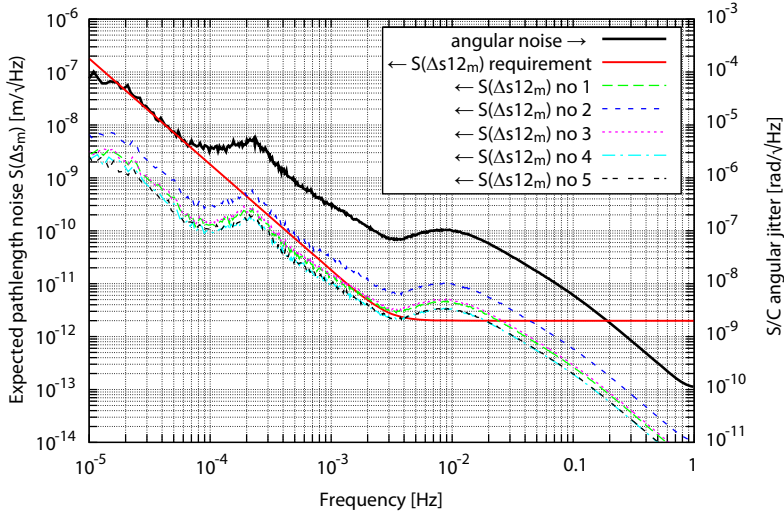


**Figure 7.3.:** Five results for pathlength readout noise, computed by the steps described in section 7.2.3. This figure shows, that the linear approach (multiplying a factor to an existing spectrum) can be used, since the resulting  $\Delta s_{12}$  spectra are in fact scaled angular jitter curves.

2. The data was fitted to obtain an interpolation function  $\Delta s_{12} = \Delta s_{12}(\varphi_1, \varphi_2)$ .
3. A random number generator [AEI-3034] was used to compute two independent time series for the test mass angles  $\varphi_1(t_i)$  and  $\varphi_2(t_i)$  with  $10^7$  values each. These time series have identical spectra, which are the test mass angular jitter estimates taken from [ASD-2003].
4. The generated time series  $\varphi_1(t_i), \varphi_2(t_i)$  for the TM angles were inserted in the function  $\Delta s_{12}(\varphi_1, \varphi_2)$  to generate a time series for  $\Delta s_{12}$ :  $\Delta s_{12}(t_i) = \Delta s_{12}(\varphi_1(t_i), \varphi_2(t_i))$ .
5. The time series  $\Delta s_{12}(t_i)$  was converted to a linear spectral density by LPSD, a program by Michael Tröbs and Gerhard Heinzel [Tröbs2009, Tröbs2006].

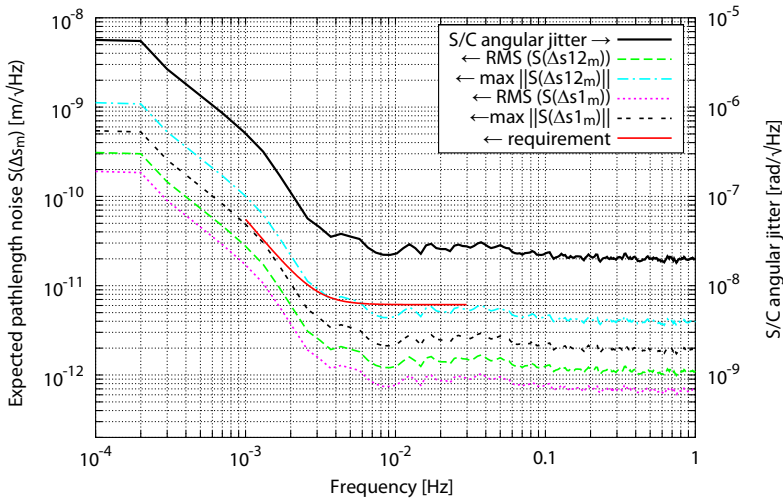
This was computed for five arbitrary results of the LTP-OBI-Alignment Simulation in spring 2007 and the resulting spectra are shown in figure 7.3. The settings of the simulation were not yet those described in this thesis and are described in detail in [PD7]. However, these changes do not affect the validity of the results:

Figure 7.3 shows clearly, that the resulting pathlength noise is linear with respect to the used test mass jitter spectrum. The factor of proportionality  $k$  between the angular spectrum and the pathlength spectrum was found to be a combination of the coupling factors:

$$S(\Delta s_{12}) = k \cdot S(\varphi) = \sqrt{(k_{\varphi_1}^{\Delta s_{12}})^2 + (k_{\varphi_2}^{\Delta s_{12}})^2} \cdot S(\varphi) . \quad (7.35)$$

This equation shows the typical summation of uncorrelated noise:

$$\text{total noise} = \sqrt{(\text{noise 1})^2 + (\text{noise 2})^2} , \quad (7.36)$$



**Figure 7.4.:** Expected pathlength noise in the x1- and x12-interferometer due to spacecraft (S/C) angular jitter. The S/C jitter curve upon which the estimates base is shown as solid black curve and refers to the right hand side axis. This jitter was generated by LTPDA and is actually an estimate of the jitter of test mass 1. The pathlength spectra refer to the left hand side axis. They were generated by multiplying the coupling factors from table 7.5 to the S/C angular jitter.

such that it can be deduced that all cross terms and higher order terms generated in the fit (step 2) are negligible. This was rated as sufficient evidence to use the linear approach.

#### 7.2.4. Pathlength noise due to Spacecraft jitter

In this section estimates of the x1- and x12-pathlength noise originating from spacecraft jitter are evaluated. These are derived by multiplying coupling factors to the spacecraft jitter estimates, generated with LTPDA. The uniqueness of this work is, that the coupling factors are generated by the LTP-OBI-Alignment Simulation. They result therefore from realistically misaligned optical benches with in-flight aligned test masses. More than 4000 of these realistic OBI's were generated and the resulting noise of these is now evaluated. For clarity, only the absolute maximal coupling (max) and the root mean square (RMS) coupling factors are used as representatives of the 4000 results. Thereby, RMS and maximal noise estimates are generated which are then compared to the corresponding requirements.

**S/C angular jitter and DWS correction** It is already known for several years in the LTP community, that angular jitter of the test masses or spacecraft respectively, couple intensely into the main science signal  $\Delta s_{12_m}$ , the pathlength readout between both test masses. The resulting pathlength noise is expected to exceed the requirement and it was suggested to subtract the longitudinal error signal from the measured pathlength

## 7. Results obtained by the LTP-OBI-Alignment Simulation

spectrum  $S(\Delta s_{12_m})$ :

$$S(\Delta s_{12_m}^{\text{residual}}) = S(\Delta s_{12_m}) - S(\Delta s_{12_e}) \quad (7.37)$$

$$= S(\Delta s_{12_m}) - k_{\varphi}^{\Delta s_m} \cdot (k_{\varphi}^{\text{DWS}})^{-1} S(\text{DWS}) . \quad (7.38)$$

This procedure was shown experimentally to reduce sufficiently the pathlength noise and thereby to fulfill the corresponding requirement [P7]. The experiments were performed using the engineering model of the OBI. The main question for the simulation was, whether this subtraction can also be used for noise reduction in the flight model of the OBI, which was not yet built at the time of the investigation.

**Spacecraft angular jitter** It is not possible to subtract an arbitrary amount of noise to recover a small underlying signal. Likewise, DWS correction can only be performed if the measured noise violates the requirement by a not too large amount. Factors of the order of up to 10 or 20 are assumed to be feasible. In the previous section it is shown that the noise spectra for the pathlength readout  $S(\Delta s_{12_m})$  can be generated by multiplying coupling factors to the existing angular noise spectrum. The coupling factors between spacecraft (S/C) angular jitter and the longitudinal pathlength readout are listed in table 7.5. These factors were multiplied to the angular jitter generated by LTPDA. The resulting pathlength noise curves are shown in figure 7.4.

	RMS	$\sigma$	Max	Min
$k_{\varphi_{OB}}^{\Delta s_{1_m}} \left[ \frac{\text{pm}}{\mu\text{rad}} \right]$	33.653	33.656	95.957	-89.265
$k_{\varphi_{OB}}^{\Delta s_{12_m}} \left[ \frac{\text{pm}}{\mu\text{rad}} \right]$	54.653	54.650	187.47	-198.04
$k_{y_{OB}}^{\Delta s_{1_m}} \left[ \frac{\text{pm}}{\mu\text{m}} \right]$	84.3175	84.3257	200.792	-207.392
$k_{y_{OB}}^{\Delta s_{12_m}} \left[ \frac{\text{pm}}{\mu\text{m}} \right]$	87.5974	87.6023	254.288	-239.332
$k_{x_{OB}}^{\Delta s_{1_m}} \left[ \frac{\mu\text{m}}{\mu\text{m}} \right]$	1.99382	$17.5035 \cdot 10^{-6}$	-1.99387	-1.99377
$k_{x_{OB}}^{\Delta s_{12_m}} \left[ \frac{\text{pm}}{\mu\text{m}} \right]$	63.4768	63.4723	-175.64	173.743

**Table 7.5.:** Coupling factors of optical bench – and thus spacecraft – tilt or displacement into the pathlength readout of the x1- and x12-interferometer. Beam parameters were not varied during the simulation. RMS is the root mean square,  $\sigma$  the standard deviation, max and min the maximum and minimum value of the coupling factors of the 4000 generated OBI.

The pathlength noise in the x1-interferometer entirely satisfies the required 6.12 pm requirement, while the maximal pathlength noise in the x12-interferometer violates the requirement at low frequencies by approximately a factor of 2. This is a small violation which can easily be mitigated by noise subtraction.

**Spacecraft longitudinal jitter** The resulting pathlength noise in the x1- and x12-interferometer caused by spacecraft  $x$ -jitter is shown in figure 7.5. Here, noise estimates generated with LTPDA, the coupling factors of table 7.5 and the requirement of table 7.4

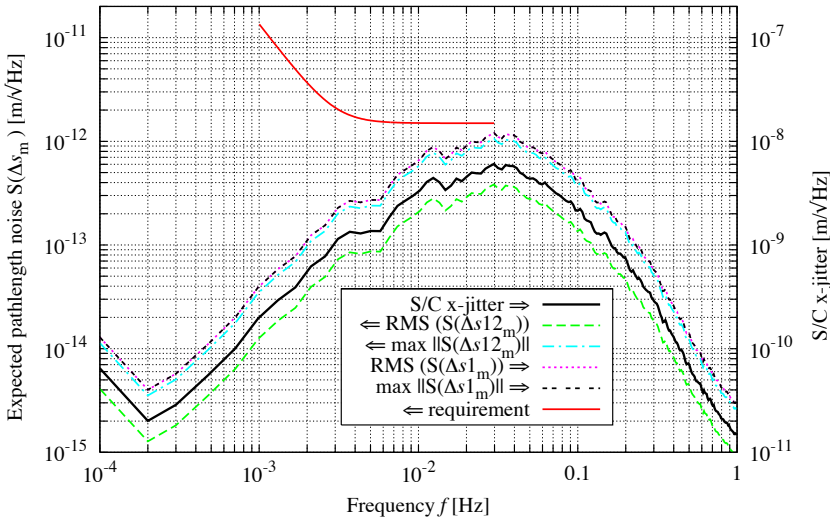


**Figure 7.5.:** Pathlength noise in the x1- and x12-interferometer caused by spacecraft  $x$ -jitter. The coupling factors from table 7.5 were multiplied by the TM1  $x$ -jitter (right hand side axis) and compared to the requirement taken from table 7.4. Due to the size of the coupling factor for PD1B, the x1-pathlength noise is plotted with respect to the right hand side axis, while the pathlength noise for PD12B is plotted with respect to the left hand side axis. The x12-pathlength noise due to spacecraft  $x$ -jitter entirely fulfills the requirement.

are combined.

The pathlength noise in the x1-interferometer is plotted with respect to the right hand side axis and does not fulfill the shown requirement, however, this is as expected and the requirement is not valid for the x1-pathlength. In section 7.1 it was discussed that spacecraft jitter is equivalent to a common mode jitter of both test masses when the optical bench is at rest. Since the x1-interferometer measures the displacement of test mass 1 with respect to the optical bench, it will measure the full amount of spacecraft  $x$ -jitter. The resulting pathlength noise is therefore twice the amount of spacecraft displacement noise (since  $k_x \Delta s \approx 2$ , cf. table 7.1).

The x12-interferometer measures the differential position of both test masses. As discussed in section 7.1.1, the distance between both test masses does not change due to spacecraft jitter, since this is assumed to be equivalent to a common mode jitter of the test masses. Ideally, the spacecraft jitter would thus not couple into the differential pathlength readout  $\Delta s_{12_m}$ . However, misalignment of the OBI causes a residual coupling, which can be expressed by the non-vanishing coupling factor  $k_{x_{OB}} \Delta s_{12_m}$ . The resulting pathlength noise however, does fulfill the current requirement, as shown in figure 7.5.

**Spacecraft lateral jitter** The pathlength noise in the x1- and x12- interferometer caused by spacecraft  $y$ -jitter is shown in figure 7.6. This graph was generated from an LTPDA noise estimate for TM1  $y$ -jitter, the coupling factors of optical bench  $y$ -jitter to pathlength signals listed in table 7.5 and the requirement taken from table 7.4. The



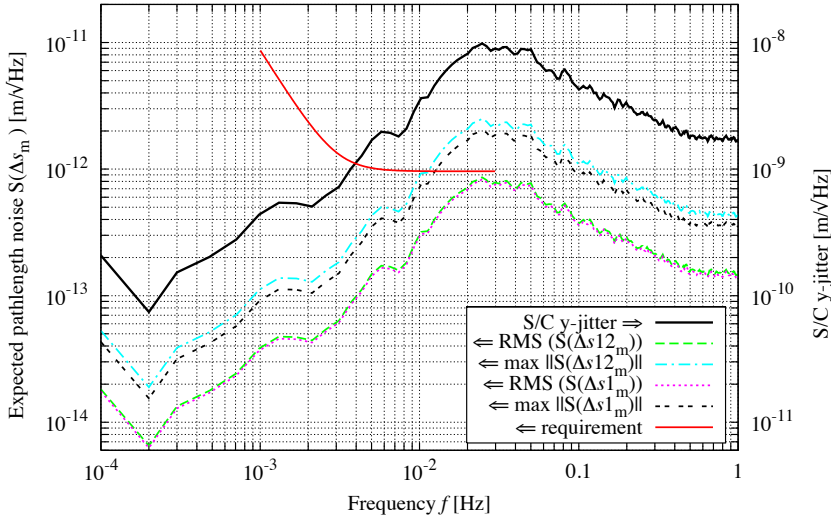


**Figure 7.6.:** Pathlength noise in the x1- and x12-interferometer originating from spacecraft lateral jitter. Used were LTPDA noise estimates as discussed in section 7.2.1 and the coupling factors  $k_{yOB}^{\Delta s_m}$  listed in table 7.5. The graph shows a pathlength noise of approximately  $2 \text{ pm}/\sqrt{\text{Hz}}$  at 30 mHz in both interferometers. This corresponds to a violation of the requirement by approximately a factor of two – a value which is highly dependent on the underlying assumptions.

pathlength noise in both interferometers shows a maximum of approximately  $2 \text{ pm}/\sqrt{\text{Hz}}$  at 30 mHz. The allocated noise budget at this frequency is currently approximately  $1 \text{ pm}/\sqrt{\text{Hz}}$ , such that the requirement is violated by a factor of two. A small change in the noise break down could remove this violation. This reallocation is assumed to be uncritical, since currently more than  $6 \text{ pm}/\sqrt{\text{Hz}}$  are allocated to pathlength noise originating from  $\varphi$ - and  $\eta$ -jitter each. Since DWS correction is planned for this noise type, it is assumed that this requirement can be set to a more stringent value. If a reallocation of the  $4.46 \text{ pm}/\sqrt{\text{Hz}}$  for displacement noise due to spacecraft jitter is not possible, it is still possible to reallocate some noise within the  $6.4 \text{ pm}$  OMS-alignment budget ([ASD-3036, req. 42000], cf. appendix A.3).

### 7.3. Expected alignment of the OBI in science mode

The LTP-OBI-Alignment Simulation generates step-by-step realistically misaligned optical bench interferometer (OBI), as discussed in section 6.3. Each OBI setup generated in the simulation is therefore a model which gives information about the misalignment status of the OBI in flight. In the previous sections it was shown that misalignment causes cross-coupling in the interferometer channels and therefore pathlength noise, a variety of stringent requirements was defined by ASD, mainly in [ASD-3020, iss 3]. In this section it is therefore investigated whether the requirements are expected to be fulfilled or, if not, how the alignment can be improved.



Conventional		RMS	$\sigma$	Max	Min	Req	above Req
XMRF1/nominal	$\Delta x$ [ $\mu\text{m}$ ]	52	52	100	-100	$\pm 100$	
	$\Delta y$ [ $\mu\text{m}$ ]	12	12	23	-24		
	$\Delta\varphi$ [ $\mu\text{rad}$ ]	42	42	104	-101	$\pm 50$	27%
XMRF2/nominal	$\Delta x$ [ $\mu\text{m}$ ]	52	52	100	-100	$\pm 100$	
	$\Delta y$ [ $\mu\text{m}$ ]	12	12	24	-24		
	$\Delta\varphi$ [ $\mu\text{rad}$ ]	51	51	143	-143	$\pm 50$	35%
XMRF1/IAF1	$\Delta y$ [ $\mu\text{m}$ ]	17	17	44	-49	$\pm 50$	
XMRF2/IAF2	$\Delta y$ [ $\mu\text{m}$ ]	34	34	100	-92	$\pm 50$	15%
IAF1/IAF2	$\Delta y$ [ $\mu\text{m}$ ]	38	38	119	-109	$\pm 50$	20%
IAF1/IAF2	$\Delta\varphi$ [ $\mu\text{rad}$ ]	44	44	128	-120	$\pm 50$	28%

**Table 7.6.:** Conventional alignment procedure. Shown is the static misalignment of the coordinate frames. The column “req” gives the required values according to [ASD-3020, iss 3] except of the angular requirements which are taken from [ASD-3065]. These values are the result of a simulation with default settings, constant beam parameters and more than 4000 generated OBI setups. The column “above Req” shows how many of the 4000 generated OBI could not satisfy the stated requirement.

### 7.3.1. Nominal alignment strategy.

The alignment procedure described in section 6.3 results in the alignment listed in table 7.6. To allow a comparison with the requirements in reference [ASD-3020, iss 3], the there used coordinate frames and labeling were adopted. These coordinate frames are those introduced in section 5.4.

Some of the results in table 7.6 show asymmetry, which indicates that the actual maximum or minimum value was not yet generated. The more statistics contribute to a result, the longer it takes to converge. The 4000 generated OBI were thus not always sufficient to find the actual maximal misalignment.

**Designed results** Some of the values listed in table 7.6 are in fact designed, that means the settings in the LTP-OBI-Alignment Simulation were chosen in a way such that these values had to be generated. Designed values are printed in green in table 7.6 to distinguish them from actual results of the simulation. The design values are:

- **XMRFi/nominal**  $\Delta x$ , (in the sensitive direction: the distance between nominal test mass position and in-flight position): The requirement for this value is  $\pm 100 \mu\text{m}$  [ASD-3020, iss 3, table 3-2]. Therefore, the test mass was positioned with a precision of  $\pm 100 \mu\text{m}$  in step 7 (cf. p. 78) of the LTP-OBI-Alignment Simulation. The final step 8 did effectively not alter the position of the test mass. Even though the test masses were rotated around their geometrical center, the resulting  $x$ -shift was well below one micron. Therefore, the resulting alignment of the test mass is designed to have a value of  $\pm 100 \mu\text{m}$ .
- **XMRF1/IAF1**  $\Delta y$  (in flight the displacement of the reflection point on test mass 1 with respect to the center of the reflecting surface): This value has a

## 7. Results obtained by the LTP-OBI-Alignment Simulation

requirement of  $\pm 50 \mu\text{m}$  (stated as  $42 + 8 \mu\text{m}$  [ASD-3020, iss 3, table 3-3]). Step 7 was specifically designed to build OBIs that fulfill this requirement.

- **XMRFi/nominal  $\Delta y$**  (in insensitive direction: displacement of each test mass in flight with respect to its nominal position): In order to fulfill the requirement for XMRFi/IAFi, each test mass was positioned in step 7 with a precision of  $\pm 22 \mu\text{m}$ . The in-flight rotation of the test masses in step 8 shifted each test mass in  $y$ -direction by  $r \cdot \sin(\varphi)$  which is at most  $\approx 23 \text{ mm} \cdot \sin(100 \mu\text{rad}) \approx 2 \mu\text{m}$ , where  $r$  is the half-width of the test mass.

**Non-designed results** All remaining values are not designed and are thus a result of the LTP-OBI-alignment simulation. These values are listed and discussed below.

- **XMRf1/nominal  $\Delta\varphi$**  (in-plane tilt of the in-flight aligned test mass with respect to the nominal angle and thus with respect to the optical bench (OBF)): It was found that this angle takes a value of roughly  $\pm 100 \mu\text{rad}$  and violates thereby the requirement by a factor of two. Furthermore, the alignment of 27% of the 4000 generated OBIs violated the requirement of  $\pm 50 \mu\text{rad}$  [ASD-3065]. This result is comprehensible:

The in-flight angle of TM1 mainly depends on the in-flight alignment procedure which rotates TM1 until the DWS signal on PD1A/B is zero. For this angle, the following things are known:

During the OB-alignment procedure, the step of bonding the recombination beam splitters is critical. There exists one position and angle of BS8, for which both beams perfectly overlap. If it was possible to bond BS8 to exactly that position and angle, the DWS signal would be zero. Therefore, the in-flight alignment would rotate the test masses back to exactly the angle which the dummy test masses had. Since a precision of  $\pm 30 \mu\text{rad}$  was assumed for the dummy test masses, the resulting alignment of the test masses would also be  $\pm 30 \mu\text{rad}$ . However, placing the beam combiners with a precision of  $\pm 65 \mu\text{rad}$  (cf. step 5), results in a DWS signal which is proportional to the relative angle of BS8:

$$\text{DWS1} = k_{\varphi_{\text{BS8}}}^{\text{DWS1}} \cdot \varphi_{\text{BS8}} . \quad (7.39)$$

Here,  $\varphi_{\text{BS8}}$  is the angular misalignment of BS8, that means the tilt with respect with respect to the angle which results in a perfect coalignment of the interfering beams. The in-flight alignment of TM1 compensates then the angular misalignment of BS8 by:

$$\varphi_1 = \frac{\text{DWS1}}{k_{\varphi_1}^{\text{DWS1}}} = \frac{k_{\varphi_{\text{BS8}}}^{\text{DWS1}}}{k_{\varphi_1}^{\text{DWS1}}} \cdot \varphi_{\text{BS8}} . \quad (7.40)$$

The reason why the resulting test mass angle  $\varphi$  is slightly higher than  $\pm 95 \mu\text{rad}$  – the sum of  $\pm 30 \mu\text{rad}$  and  $\pm 65 \mu\text{rad}$  – is that  $k_{\varphi_{\text{BS8}}}^{\text{DWS1}}$  is slightly larger than  $k_{\varphi_1}^{\text{DWS1}}$ . After this investigation was performed, it was found that UGL had placed a slightly more stringent estimate of  $\pm 55 \mu\text{rad}$  for the angular alignment precision of the beam combiners in [UGL-3009] (cf. also section 5.3.1 and step 5 in section 6.3). If an alignment of the beam combiners of  $\pm 55 \mu\text{rad}$  instead of

$\pm 65 \mu\text{rad}$  is achieved, the angular alignment of the TM1 would correspondingly improve by approximately  $\pm 10 \mu\text{rad}$ .

- **XMRF2/nominal  $\Delta\varphi$ :** The angular misalignment of test mass 2 showed values between  $\pm 143 \mu\text{rad}$  and thereby a violation of the requirement by roughly a factor three and every third generated OBI did not fulfill the required alignment. Even though the misalignment of TM2 is about 50% higher than TM1, the cause is again the in-flight alignment to  $\text{DWS} = 0$ .

After bonding BS8 (the beam combiner of the x1-interferometer) to the baseplate, the beam combiner of the x12 interferometer BS10 is bonded using the same dummy test masses at the same position. After assembly of LTP, launch and decaging, TM1 is rotated to  $\text{DWS} = 0$ . This causes a beam walk and tilt in the x12-interferometer. When TM2 is then rotated to  $\text{DWS}=0$  in the x12 interferometer, it corrects the angular misalignment between measurement and reference beam caused by the misalignment of the beam combiner BS10. Additionally, it corrects the angular misalignment between measurement and reference beam caused by the rotation of TM1. That means, TM2 picks up the angular misalignment of both beam combiners: BS8 and BS10. The total angle of TM2 results therefore from the angular misalignment of the dummy test mass, BS8 and BS10.

- **XMRF2/IAF2  $\Delta y$ :** The reflection point on test mass 2 was designed in the same way as the reflection point on test mass 1. Nonetheless, XMRF2/IAF2 showed twice the amount of variance as XMRF1/IAF1:  $-92 \dots 100 \mu\text{m}$ . This is caused by two effects: First of all,  $\pm 8 \mu\text{m}$  were allocated for beam walk caused by a test mass displacement of  $\pm 100 \mu\text{m}$ . This was allocated independently for TM1 and TM2. However, a displacement of TM1 causes roughly the same amount of beam walk on both test masses. Therefore,  $\pm 16 \mu\text{m}$  should be allocated for TM2 instead of  $\pm 8 \mu\text{m}$ . Secondly, the in-flight alignment procedure rotates TM1, which causes an additional beam walk on TM2.
- **IAF1/IAF2  $\Delta y$ :** the differential displacement of both test mass reflection points violates with  $-109 \dots 119 \mu\text{m}$  the required alignment of  $\pm 50 \mu\text{m}$ . In the simulation, the alignment requirements for the dummy test masses (DTM) in step 3 as well as the positioning of the real test masses in step 7 were implemented to be uncorrelated. As a result, the position of the reflection points is at least the sum of
  - $2 \cdot \pm 20 \mu\text{m}$  precision of DTM placement.
  - $\pm 8 \mu\text{m}$  displacement of TM2 in sensitive direction causes  $8 \mu\text{m}$  beam walk on TM2. The same effect for TM1 is a common mode effect and causes no differential displacement of the reflection points.
  - $2 \cdot \pm 22 \mu\text{m}$  precision for positioning the electrical nulls and therefore the in-flight position of both test masses.

Therefore, the differential displacement of both reflection points is at least  $\pm 92 \mu\text{m}$  and violates the requirement. The simulation result is even larger than this value, again due to the in-flight alignment procedure: the rotation of TM1

## 7. Results obtained by the LTP-OBI-Alignment Simulation

causes beam walk on TM2 and increases thereby in worst case the offset between both reflection points.

- **IAF1/IAF2  $\Delta\varphi$**  (could also be expressed as XMRF1/XMRF2  $\Delta\varphi$ ): the differential in-plane angular alignment of the test masses in flight violated with  $-120 \dots 128 \mu\text{rad}$  the requirement of  $\pm 50 \mu\text{rad}$  [ASD-3065]. Here, 28% of all generated OBI violated the requirement. As before, this is explained by two effects: the angular alignment of the dummy test masses during the bonding procedure ( $2 \cdot \pm 30 \mu\text{rad}$  and the in-flight alignment to  $\text{DWS} = 0$ ).

**Conclusion** In summary, every not-designed value violated the requirement. Main cause was in each case the in-flight alignment procedure that rotates the test masses to  $\text{DWS} = 0$  and thus imposes the misalignment of BS8 and BS10 on the respective test mass.

**Remark to the requirement specification document** All requirements stated in table 7.6 are taken from table 3-2 to 3-4 in [ASD-3020, iss 3]. This document was the most recent requirement specification document available, when the investigation was performed in 2007. Today, the latest requirement specification document is [ASD-3020, iss 6], but it is difficult to compare the results with values stated in this updated document for two reasons:

First of all, ASD changed the basic meaning of the MRF, XMRF and IAF: in issue 3 these were defined like in this thesis with respect to in-flight aligned test masses that are located in the electrical null. However, in the new issue, these coordinate frames are on ground measured coordinate frames. Especially the IAF is defined in the new issue by the as built model with placed dummy test mass. With these changes the meaning changed so rigorously, that an update to the new requirements is not feasible. Secondly, the LTP-OBI-Alignment simulation was programmed to used requirements of the older document as input (cf. step 3 and step 7 in section 6.3). When ASD updated this requirement document and changed the meaning of the coordinate frames, all requirement values were kept unchanged, except of the  $\pm 100 \mu\text{m}$  for XMRF/nominal stated in table 7.6. This value changed to  $\pm 45 \mu\text{m}$  [ASD-3020, iss 6, table 3-1].

Despite these changes, the results shown in table 7.6 still give an impression of the resulting in-flight alignment of the OBI. In particular, it stays a fact that the in-flight alignment procedure is a main contributor to the final misalignment of the test masses in science mode. Likewise the misalignment of the beam combiners BS8 and BS10 will be transformed to angular misalignment of the test masses, if the test masses are rotated to  $\text{DWS} = 0$ .

### 7.3.2. Alternative 1: DWS calibration

As discussed in the previous section, a major part of the in-flight misalignment of the test masses and reflection points result from the rotation of the test masses to  $\text{DWS} = 0$ . This procedure was planned for two reasons: On the one side, the DWS signal provides the most accurate measurement of the angular alignment of the test masses. It was expected that  $\text{DWS} = 0$  corresponds to the best achievable angular alignment of the test masses. Furthermore,  $\text{DWS} = 0$  corresponds to optimal angular

DWS calibrated		RMS	$\sigma$	Max	Min	Req	above Req
XMRF1/nominal	$\Delta x$ [ $\mu\text{m}$ ]	52	52	100	-100	$\pm 100$	
	$\Delta y$ [ $\mu\text{m}$ ]	12	12	22	-22		
	$\Delta\varphi$ [ $\mu\text{rad}$ ]	16	16	30	-30	$\pm 50$	
XMRF2/nominal	$\Delta x$ [ $\mu\text{m}$ ]	52	52	100	-100	$\pm 100$	
	$\Delta y$ [ $\mu\text{m}$ ]	11	11	22	-22		
	$\Delta\varphi$ [ $\mu\text{rad}$ ]	16	16	30	-30	$\pm 50$	
XMRF1/IAF1	$\Delta y$ [ $\mu\text{m}$ ]	17	17	45	-49	$\pm 50$	
XMRF2/IAF2	$\Delta y$ [ $\mu\text{m}$ ]	18	18	56	-57	$\pm 50$	< 1%
IAF1/IAF2	$\Delta y$ [ $\mu\text{m}$ ]	26	26	85	-89	$\pm 50$	6%
IAF1/IAF2	$\Delta\varphi$ [ $\mu\text{rad}$ ]	23	23	59	-57	$\pm 50$	< 1%

**Table 7.7.:** Same as 7.6, but before in-flight alignment procedure rotated both test masses to DWS = 0. All values are rounded to the nearest integer. This represents the static TM alignment for the science mode if the test masses are not rotated to DWS = 0 but to a previously at UGL measured DWS signal. The values highlighted in green are designed: they were used as input in the simulation.

alignment of the interfering beams on the QPD yielding maximal contrast. However, there is an alternative procedure: the offset in the DWS signals could be calibrated and the test mass tilted to the appropriate value  $\text{DWS} \neq 0$ .

The DWS signal would then be measured on ground as a function of the test mass angle. The resulting curve could be used to calibrate the DWS signal including the offset. Naturally, the calibration is not arbitrary precise. It can be assumed that the precision known for the alignment of the dummy test masses is valid for this calibration. Thus, using the calibrated DWS signal, the test masses could be rotated to their nominal angle  $\pm 30 \mu\text{rad}$ .

For a simulation, this procedure was simplified as follows. The alignment results were saved before executing step 8. It is thereby assumed that the in-flight angular correction precisely returns the test masses to the attitude the dummy test masses had. The result is listed in table 7.7. A comparison of these values with the corresponding values in table 7.6 shows precisely the impact of the in-flight alignment to an uncalibrated  $\text{DWS} = 0$ .

**Results** All values that were used directly as input to the simulation, are highlighted in green in table 7.7.

- **XMRF/nominal**  $\Delta\varphi$ : The test mass angles in flight with respect to their nominal angle (or with respect to the OB) have values between  $\pm 30 \mu\text{rad}$ . This is as designed, because the dummy test masses were placed with a CND of  $\pm 30 \mu\text{rad}$ .
- **XMRF2/IAF2**  $\Delta y$ : The shown result of  $-57 \dots 56 \mu\text{m}$  confirms the previously discussed statement, that the displacement of TM1 causes a beam walk of  $\pm 8 \mu\text{m}$  on TM2. In order to fulfill the requirement, the electrical null would need to be aligned by  $\pm(22 - 8) \mu\text{m} = \pm 14 \mu\text{m}$  with respect to nominal.

## 7. Results obtained by the LTP-OBI-Alignment Simulation

- **IAF1/IAF2  $\Delta y$ :** The offset between both reflection points is of the order of the discussed  $\pm 92 \mu\text{m}$  and does therefore not fulfill the requirement. The alignment of both reflection point in flight is almost entirely uncorrelated. Only  $8 \mu\text{m}$  of beam walk caused by the longitudinal displacement of TM1 are common mode and do not contribute to the offset between both reflection points. In order to fulfill the required  $\pm 50 \mu\text{m}$ , a correlation between the alignment of test mass 1 and 2 would therefore be needed. If the alignment of both test masses is independent as assumed here, it is likely that the requirement will be violated.
- **IAF1/IAF2  $\Delta\varphi$ :** The resulting differential angular alignment is again simply  $2 \cdot \pm 30 \mu\text{rad}$ , since the angles of both test masses were placed independently with a precision of  $\pm 30 \mu\text{rad}$ . Still this comparably small angle violates the requirement of  $\pm 50 \mu\text{rad}$ . However, this violation occurred only in roughly 1% of the investigated cases. In order to guarantee that the requirement is met, the angular precision for placing the dummy test masses would need to be reduced from  $\pm 30 \mu\text{rad}$  to  $\pm 25 \mu\text{rad}$  or a correlation between the angles would be needed.

**Conclusion** It was shown that calibration of the DWS signals results potentially in a considerably better aligned OBI. However, the alignment requirements are so tight, that even with this procedure some requirements could be violated. Even though calibrating the DWS signals might reduce the amount of misalignment of the test masses and reflection points, it is effectively an intended misalignment of the beams impinging on the photodiodes. It is not known yet what causes less noise in the interferometer channels: a well aligned jittering test mass in an interferometer with misaligned beams (calibrated case), or test masses with fairly large amount of misalignment but very well aligned beams impinging on the QPDs (conventional DWS = 0 case).

### 7.3.3. Alternative 2: Hovered BS3

The subsequent alignment strategy is a modification of the conventional OB alignment strategy. It was designed to improve the angular alignment of TM2 as well as the displacement of the reflection point in flight ( $\text{XMRF2}/\text{IAF2 } \Delta y$ ) by aligning DTM1 to DWS = 0 before aligning and bonding the x12-interferometer components. This prevents that TM2 picks up the angular misalignment of the x1 beam combiner BS8. However, it will be shown, that this can only be achieved at the cost of increasing the differential angular misalignment of the test masses.

The hovered BS3 alignment procedure and its implementation in the LTP-OBI-Alignment Simulation consists of the following steps:

**Step 1: Positioning of both dummy test masses.** DTM1 and DTM2 are set to their nominal position, assuming a precision of  $\pm 20 \mu\text{m}$  for  $x$  and  $y$  and  $\pm 30 \mu\text{rad}$  for  $\varphi$ .

**Step 2: Aligning BS1 to dummy test mass 1.** BS1 is rotated until DTM1 is hit at its centre. As in the implementation of the conventional alignment procedure, zero tolerance was assumed for this step.

**Step 3: Aligning BS8 to contrast and DWS  $\approx 0$ .** It is assumed for this step that UGL has bonded M1 and hovered, that means placed but not bonded, BS3. Now, BS8 is positioned and aligned, using both the DWS signal and the contrast to find the optimal position and angle. BS8 is bonded as precisely as possible in this position, with assumptions for the precision of  $\pm 10 \mu\text{m}$  for the position and  $\pm 65 \mu\text{rad}$  for the angle. In the simulation the optimal position is therefore computed geometrically and the DWS signal was driven to zero by rotating BS8. This defines the optimal position and angle of BS8. To account for alignment tolerances, this optimal position and angle was varied by a CND with  $\pm 10 \mu\text{m}$  and  $\pm 65 \mu\text{rad}$  respectively.

**Step 4: Rotating DTM1 to DWS  $\approx 0$ .** Now DTM1 will be rotated, while BS3 is still hovered. UGL assumed that the rotation of DTM1 has an accuracy of  $\pm 5 \mu\text{rad}$ . Since this was an assumption, a safety factor of 2 was set and  $\pm 10 \mu\text{rad}$  used. In the simulation, DTM1 was therefore rotated to DWS = 0 and the resulting optimal angle was varied again by a CND with  $\pm 10 \mu\text{rad}$  to account for the experimental precision.

**Step 5: bonding BS3.** BS3 is rotated until the measurement beam hit the centre of the reflecting surface of DTM2. This rotation of BS3 has only a negligible effect on the transmitting beam, such that the alignment of the x1-interferometer is not affected. Step 3 to 5 effectively decouple the alignment of both test masses, since the alignment to DWS = 0 is executed before the x12-interferometer is fully bonded.

**Step 6 and 7: bonding BS10 and rotating DTM2 to DWS  $\approx 0$ .** The alignment steps 3 and 4 are now repeated for BS10 and DTM2, assuming the same precissions. After these 7 steps, the OBI is fully bonded and transferred to ASD for LTP assembly.

**Step 8 and 9 assembly and in-flight alignment.** During this assembly the electrode housing is aligned to the OBI and therefore the position of the electrical null is set. This defines the in-flight position of the test mass. The precision assumed for the conventional alignment strategy (cf. step 7 in section 6.3) is also used here:  $\Delta x = \pm 100 \mu\text{m}$ ,  $\Delta y = \pm 22 \mu\text{m}$ . From the results of the conventional alignment procedure it is known, that the displacement of TM2 by  $\Delta y = \pm 22 \mu\text{m}$  results in a violation of the requirement for XMRF2/IAF2. However, it is not clear whether the needed  $\pm 14 \mu\text{m}$  are achievable during the assembly. Therefore, the conventional value was used again.

**Resulting alignment for the Hovered BS3 strategy** A run of the LTP-OBI-Alignment Simulation using the Hovered BS3 alignment strategy with 2000 generated OBI gave the results listed in Table 7.8. Obviously, the modified alignment strategy optimizes the static angle of TM2 in science mode (XMRF2/nominal). Instead of  $\pm 143 \mu\text{rad}$ , the static angle of TM2 was  $-96 \dots 105 \mu\text{rad}$  and thereby in the same order as the angle of TM1. This is in fact as designed, because rotating the dummy test mass to DWS = 0 and only afterwards aligning the x12-interferometer decouples the alignment of both test masses. However this still means, that every fourth generated OBI exceeded the required  $50 \mu\text{rad}$ .

The offset of the reflection point on TM2 with respect to the centre of the reflecting

Hovered BS3		RMS	$\sigma$	Max	Min	Req	above Req
XMRF1/nominal	$\Delta x[\mu\text{m}]$	52	52	100	-100	$\pm 100$	
	$\Delta y[\mu\text{m}]$	11	11	22	-22		
	$\Delta\varphi[\mu\text{rad}]$	41	41	104	-99	$\pm 50$	26%
XMRF2/nominal	$\Delta x[\mu\text{m}]$	52	52	99	-100	$\pm 100$	
	$\Delta y[\mu\text{m}]$	12	12	23	-23		
	$\Delta\varphi[\mu\text{rad}]$	41	41	96	-105	$\pm 50$	25%
XMRF1/IAF1	$\Delta y[\mu\text{m}]$	16	16	45	-47	$\pm 50$	
XMRF2/IAF2	$\Delta y[\mu\text{m}]$	19	19	53	-55	$\pm 50$	< 1%
IAF1/IAF2	$\Delta y[\mu\text{m}]$	27	27	85	-94	$\pm 50$	6%
IAF1/IAF2	$\Delta\varphi[\mu\text{rad}]$	58	58	173	-162	$\pm 50$	40%

**Table 7.8.:** Static misalignment of coordinate frames as a result of the modified alignment strategy. The column “req” gives the required values according to [ASD-3020, iss 3] except of the angular requirements which are taken from [ASD-3065]. These values are the result of a simulation with default settings, constant beam parameters and 2000 generated OBI setups.

surface (XMRF2/IAF2  $\Delta y$ ) has decreased from  $\pm 100 \mu\text{m}$  with the nominal OB alignment strategy to  $-55 \dots 53 \mu\text{m}$  in the modified alignment strategy. This is the same result as in the case of the calibrated DWS signal: The longitudinal displacement of TM1 by  $\pm 100 \mu\text{m}$  causes a beam walk of  $8 \mu\text{m}$  on TM2 which was not accounted for in the requirements and therefore in the settings of the simulation.

Finally, the maximal differential offset of the TM reflection points (IAF1/IAF2) has decreased from  $119 \mu\text{m}$  to  $94 \mu\text{m}$ . Again, this is an anticipated result: the alignment of the test masses is uncorrelated here, which is the idea in the hovered BS3 alignment strategy. As a consequence, the differential offset of the reflection points is the sum of the displacement of each reflection point:  $\pm(50 + 50) \mu\text{m} = \pm 100 \mu\text{m}$ . The misalignment is thus reduced, but still does not satisfy the required  $\pm 50 \mu\text{m}$ .

The prevention of the correlation in the alignment has a major effect on differential angle between both test masses. Since each test mass has an angular alignment of the order of  $\pm 100 \mu\text{rad}$ , the differential angle is expected to be of the order of  $\pm 200 \mu\text{rad}$ . Within the 2000 generated OBI, this value did not converge yet and showed a maximal differential angle of IAF1/IAF2  $\Delta\varphi = -173 \dots 162 \mu\text{rad}$ , such that 40% of the 2000 generated OBI violated the requirement. This is a major increase in comparison to the conventional alignment strategy, which showed values between  $-120 \dots 128 \mu\text{rad}$ .

### 7.3.4. Alternative 3: generating a dummy test mass cavity

The following alignment option could be applied to any of the three previously discussed alignment strategies (conventional, hovered-BS3 or DWS-calibration).

The angular misalignment of the dummy test masses results for each of these strategies in a misalignment of the test masses in science mode. So far, it was assumed that the angular misalignment of the DTMs is not correlated. If it was possible to create such a correlation, the final differential angular alignment of the TMs should improve. A possibility to create such a correlation could be to use the dummy test masses to build



DTM cavity		RMS	$\sigma$	Max	Min	Req	above Req
XMRF1/nominal	$\Delta x$ [ $\mu\text{m}$ ]	53	53	100	-100	$\pm 100$	
	$\Delta y$ [ $\mu\text{m}$ ]	11	11	23	-23		
	$\Delta\varphi$ [ $\mu\text{rad}$ ]	42	42	99	-104	$\pm 50$	26%
XMRF2/nominal	$\Delta x$ [ $\mu\text{m}$ ]	52	52	100	-100	$\pm 100$	
	$\Delta y$ [ $\mu\text{m}$ ]	12	12	24	-23		
	$\Delta\varphi$ [ $\mu\text{rad}$ ]	50	50	139	-137	$\pm 50$	34 %
XMRF1/IAF1	$\Delta y$ [ $\mu\text{m}$ ]	16	16	46	-44	$\pm 50$	
XMRF2/IAF2	$\Delta y$ [ $\mu\text{m}$ ]	34	34	97	-96	$\pm 50$	14 %
IAF1/IAF2	$\Delta y$ [ $\mu\text{m}$ ]	37	37	115	-124	$\pm 50$	20 %
IAF1/IAF2	$\Delta\varphi$ [ $\mu\text{rad}$ ]	38	38	90	-92	$\pm 50$	22 %

**Table 7.9.:** Same as Table 7.6, but using a dummy test mass cavity. These values are the result of a simulation with default settings, constant beam parameters and 2000 generated OBI setups.

a cavity. Thereby, the DTMs could be set parallel to a high precision.

In the simulation this alignment is represented by setting the angle of DTM2 to the angle of DTM1 and adding to this angle a CND with a width of 10  $\mu\text{rad}$ , accounting for cavity misalignment. This value is an assumption for general testing.

**Result** The resulting test mass alignment for the case of the use of a dummy test mass cavity in combination with the conventional alignment strategy is shown in table 7.9. As expected, all values coincide with those where no cavity is used. The only alignment that changed is the differential TM angle (IAF1/IAF2  $\Delta\varphi$ ). Instead of the  $-120 \dots 128 \mu\text{rad}$  (without cavity), this differential angle decreases to  $-92 \dots 90 \mu\text{rad}$ . One might expect a decrease of 50  $\mu\text{rad}$  here. However, “Max” and “Min” in all alignment tables are not the real worst case, but only the maximal misalignment in the 2000 or 4000 generated OBI. Especially in those cases where many statistics add up, the worst possible case lies above the max/min values given in the tables. It is anticipated that the worst case misalignment, not necessarily the maximal values, reduces by 50  $\mu\text{rad}$  when a DTM cavity is used.

### 7.3.5. Combining alternative 3 and 1

For the case of a conventional OB alignment but using a dummy test mass cavity and using DWS calibration, the test mass alignment results are listed in table 7.10. Comparing these results to the corresponding ones without DTM cavity (table 7.7) shows the following changes:

The angle of TM2 with respect to nominal (IAF2/nominal  $\Delta\varphi$ ) has increased from 30  $\mu\text{rad}$  without DTM cavity, to 39  $\mu\text{rad}$  with DTM cavity. This is anticipated, since DTM2 was set parallel to DTM1 with a precision of  $\pm 10 \mu\text{rad}$ . The maximal angular misalignment of TM2 is therefore  $\pm 40 \mu\text{rad}$ .

The important change is the differential angle (IAF1/IAF2  $\Delta\varphi$ ), which decreased from approximately  $\pm 60 \mu\text{rad}$  without DTM cavity, to  $\pm 10 \mu\text{rad}$  with DTM cavity. This value is as designed, since both test masses are rotated to exactly the angle of the DTMs (there is no error assumed here) and the dummy test masses are parallel with a

## 7. Results obtained by the LTP-OBI-Alignment Simulation

DTM cavity, DWS calib.		RMS	$\sigma$	Max	Min	Req	above Req
XMRF1/nominal	$\Delta x$ [ $\mu\text{m}$ ]	53	53	100	-100	$\pm 100$	
	$\Delta y$ [ $\mu\text{m}$ ]	11	11	22	-22		
	$\Delta\varphi$ [ $\mu\text{rad}$ ]	16	16	30	-30	$\pm 50$	
XMRF2/nominal	$\Delta x$ [ $\mu\text{m}$ ]	52	52	100	-100	$\pm 100$	
	$\Delta y$ [ $\mu\text{m}$ ]	12	12	22	-22		
	$\Delta\varphi$ [ $\mu\text{rad}$ ]	17	17	39	-39	$\pm 50$	
XMRF1/IAF1	$\Delta y$ [ $\mu\text{m}$ ]	16	16	44	-43	$\pm 50$	
XMRF2/IAF2	$\Delta y$ [ $\mu\text{m}$ ]	18	18	54	-56	$\pm 50$	<1%
IAF1/IAF2	$\Delta y$ [ $\mu\text{m}$ ]	25	25	77	-81	$\pm 50$	4 %
IAF1/IAF2	$\Delta\varphi$ [ $\mu\text{rad}$ ]	5	5	10	-10	$\pm 50$	

**Table 7.10.:** Same as Table 7.7, but using a dummy test mass cavity. These values are the result of a simulation with default settings, constant beam parameters and 2000 generated OBI setups.

precision of 10  $\mu\text{rad}$ . The differential TM angle is thereby decreased by 50  $\mu\text{rad}$ , that means IAF1/IAF2  $\Delta\varphi$  can be optimized by 60  $\mu\text{rad}$  less DTM cavity-precision, which was assumed to be  $\pm 10 \mu\text{rad}$  by using a DTM cavity.

### 7.3.6. Combining alternative 3 and 2

Combining the Hovered BS3 alignment strategy with the use of a dummy test mass cavity results in the alignment values listed in table 7.11. As before, the use of the DTM cavity changes increases slightly the angular misalignment of TM2 (XMRF2/nominal  $\Delta\varphi$ ) and decreases the differential angular misalignment. However, the differential angular misalignment (IAF1/IAF2  $\Delta\varphi$ ) is so high in the hovered BS3 case, that a reduction by at most 50  $\mu\text{rad}$  by using a DTM cavity cannot restrain the misalignment to the requirement.

### 7.3.7. Conclusions of OBI alignment in flight

With the assumptions for precision made in the conventional alignment procedure, it is expected that the requirements for the alignment of both test masses are not met in science mode (cf table 7.6). It was shown that the alignment of the test masses in science mode can be significantly improved by calibrating the DWS signal offset on ground. This calibration does however mean, that the interferometer beams are tilted with respect to each other when impinging on the QPDs of the x1 and x12-interferometer. It was not shown here and is currently unknown, what causes more noise in the pathlength signals: a larger misalignment of the test masses but well aligned interferometer beams, or vice versa.

An alternative alignment strategy was investigated, where BS3 was hovered and the angular misalignment of the x1-beam combiner was corrected by a rotation of DTM1 before aligning and bonding the x12-interferometer. This improves significantly the alignment of TM2. However, this procedure eliminates the correlation of the angular alignment of both test masses. This results on the one side in a significantly improved alignment of TM2, but on the other side in a very large differential angular misalignment

DTM cavity and hovered BS3		RMS	$\sigma$	Max	Min	Req	above Req
XMRF1/nominal	$\Delta x$ [ $\mu\text{m}$ ]	52	52	100	-100	$\pm 100$	
	$\Delta y$ [ $\mu\text{m}$ ]	11	11	22	-22		
	$\Delta\varphi$ [ $\mu\text{rad}$ ]	41	41	105	-102	$\pm 50$	26%
XMRF2/nominal	$\Delta x$ [ $\mu\text{m}$ ]	52	52	100	-100	$\pm 100$	
	$\Delta y$ [ $\mu\text{m}$ ]	12	12	23	-23		
	$\Delta\varphi$ [ $\mu\text{rad}$ ]	40	40	107	-107	$\pm 50$	24%
XMRF1/IAF1	$\Delta y$ [ $\mu\text{m}$ ]	16	16	46	-45	$\pm 50$	
XMRF2/IAF2	$\Delta y$ [ $\mu\text{m}$ ]	19	19	51	-58	$\pm 50$	< 1%
IAF1/IAF2	$\Delta y$ [ $\mu\text{m}$ ]	26	26	74	-103	$\pm 50$	6%
IAF1/IAF2	$\Delta\varphi$ [ $\mu\text{rad}$ ]	54	54	141	-142	$\pm 50$	37%

**Table 7.11.:** Same as Table 7.8, but using a dummy test mass cavity. These values are the result of a simulation with default settings, constant beam parameters and 2000 generated OBI setups.

of both test masses.

Finally it was investigated, how the alignment of both test masses in science mode would improve, if the alignment of the dummy test masses (DTM) during the bonding phase were correlated. This correlation could be generated by aligning the dummy test masses to build a cavity. This additional procedure would improve the differential angular alignment in flight (IAF1/IAF2  $\Delta\varphi$ ) by  $\pm 60 \mu\text{rad}$  less the precision for parallelism of the dummy test masses. Since this precision was estimated with  $\pm 10 \mu\text{rad}$  here, the simulations showed an improvement of  $\pm 50 \mu\text{rad}$ .

**When these results were known the cost to benefit ratio of each procedure were discussed. It was then decided to measure the calibration curve of the DWS signal on ground. A comparison of the performance of LTP with and without calibrated DWS signal is planned.** Therefore, the DWS calibration curves were measured at UGL, when the OBI were fully bonded [UGL-3039].

**The most critical components of the OBI** It was a well known fact, that the FIOS' were critical components, since any vertical beam tilt caused by misalignment of a FIOS could not be corrected by any component on the optical bench. However, the role of the FIOS' was not investigated here, since the main simulation tool OptoCad is two dimensional. In the previous sections it was shown, that the alignment of the x1 and x12 beam combiners is likewise critical, and for the same reason. The resulting angular misalignment between measurement and reference beam could not be corrected by any other component on the optical bench, since the beam combiners are the last components to be bonded. The resulting angular misalignment of the beams is then passed to the test masses, caused by the in-flight alignment procedure which rotates the test masses to DWS = 0.

Several alternative alignment procedures were investigated. However, the alignment requirements are tight and each strategy reduces the amount of misalignment of one degree of freedom at the cost of an increased misalignment in another degree of freedom.



## 8. QPDs to monitor amplitude stability

The amplitude stability of the measurement and reference beam of the OBI on LISA Pathfinder is measured by PDA1 and PDA2 respectively (cf. figure 8.3). These two photodiodes were designed to be single element photodiodes (SEPDs). Due to delivery and manufacturing problems it was necessary to replace them in the proto flight models of the OBI by spare quadrant photodiodes (QPDs) with specifications partly incompatible to those of the single element diodes. Since each single element diode had capacitance specification of less than 1500 pF [UGB-3007] the accompanying hardware and software was designed with this specification. Consequently, only photodiodes with capacitances below 1500 pF can be electrically connected to the existing hardware. Each quadrant of the spare QPDs had a capacitance of about 1000 pF [UGB-3007]. For this purpose, it was investigated whether using two or even just one quadrant of each QPD could provide a sufficiently stable power readout. It is shown in this section, that in fact aligning the beam to just one quadrant is the optimal choice to provide a low noise power readout.

### 8.1. Beam power measured by a QPD

Generally, the three configurations shown in figure 8.1 had to be compared. In configuration 1, the beam gets centered on the QPD and all four quadrants are used to measure the beam intensity. This is shown in figure 8.1(b). This option would result in the least amount of beam clipping on the outer borders of the QPD but has the critical disadvantage, that the overall capacitance violates the requirement of  $< 1500$  pF [UGB-3007].

Alternatively, the beam could get centered on one side of the QPD as shown in figure 8.1(c), such that two quadrants are used for the measurement (figure 8.1(c)). However, the planned SEPDs had a diameter of 3 mm, such that they were a factor of

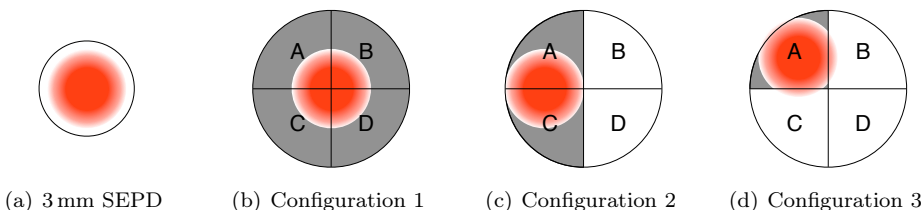


**Figure 8.1.:** Configurations of a QPD when used instead of an SEPD on the OB of LISA Pathfinder. The grey parts of the QPD indicate which segments are active and used for power measurement.

## 8. QPDs to monitor amplitude stability

Configuration	label	$x$	$y$
1	conf 1	0	0
2	conf 2, centered right	$\frac{r_{\text{QPD}}}{2}$	0
2	conf 2, centered left	$-\frac{r_{\text{QPD}}}{2}$	0
3	conf 3, centered on A	$-\frac{4r_{\text{QPD}}}{3\pi}$	$\frac{4r_{\text{QPD}}}{3\pi}$

**Table 8.1.:** Nominal position of beam center in Configuration 1 to 3 and labels used for identification. The radius of the QPD ( $r_{\text{QPD}}$ ) is 2.5 mm.

3 larger than the beam which had a spot radius of 0.5 mm (cf. section 4.6.1 on p. 47). The QPDs have a diameter of 5 mm and insensitive slits of 45  $\mu\text{m}$ . Centering the beam on one half of the QPD was therefore expected lead to beam clipping on the outer borders of the QPD.

Finally the beam could get centered on just one quadrant and this single quadrant would be used for the measurement (figure 8.1(d)). Due to the shape of the quadrant and its radius of 2.5 mm it was expected that this option would result in the largest amount of beam clipping. However, this option was technically preferable, because one single quadrant fulfilled the capacitance requirement with 1000 pF.

Beam clipping is here an important criterion, since these photodiodes are used for laser amplitude stabilization. If the beam position on the QPD was perfectly fixed, beam clipping would not be any harm, since the sensed beam power would be proportional to the incident beam power. However, there will be some residual beam jitter on PDA1 and PDA2 originating from the fiber injectors. If the beam is clipped, this beam jitter results in clipping different beam segments such that the measured beam power varies. This means, that beam pointing jitter couples into the beam power measurement, and since the measured power is used in a feed-back loop, it causes laser amplitude noise. This needs to be avoided.

In this section a two dimensional coordinate system of the type shown in figure 8.2 is used:

- center: center of the four quadrants (ABCD),
- $x$ -axis: horizontal slit of QPD (between quadrant B and quadrant D),
- $y$ -axis: vertical slit of QPD (between quadrant A and quadrant B).

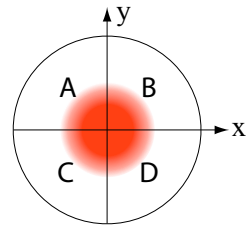


**Figure 8.2.:** coordinate system for this section.

Using this coordinate system the beam centroids in the three configurations have the coordinates listed in table 8.1, where  $r_{\text{QPD}} = 2.5$  mm is the radius of the QPD. The point  $(-\frac{4r_{\text{QPD}}}{3\pi}, \frac{4r_{\text{QPD}}}{3\pi})$  is the centroid of quadrant A.

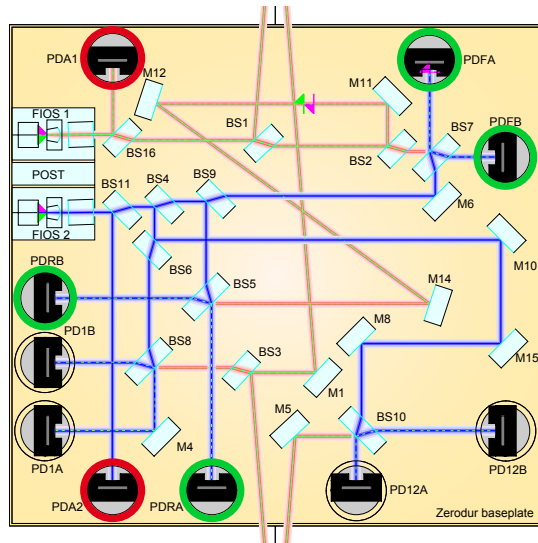


**Figure 8.3:** Position of the photodiodes of interest on the flight model design of the LTP OBI. Highlighted in red are the power monitors PDA1 and PDA2, which needed to be replaced. The photodiodes encircled in green are those used for the measurement of DC-spectra in section 8.2.3.

### 8.1.1. Methods and assumptions

For the computation of the beam power QPD.c was used (cf. section 3.2). The input parameters were taken from an OptoCad model of the flight model OBI (figure 5.4) on the surface of PDA2 and had the following values:

- $z_0 = 79.964$  cm (Rayleigh range)
- $z = 29.469$  cm (distance of PDA2 from the waist)
- $x_0 = 0$  cm (horizontal distance of beam centroid to QPD-center)
- $\alpha = 0^\circ$  (incident angle on QPD)
- $s = 14.421$  cm (total pathlength propagated from fiber output to PDA2)

All computations performed were specifically done for PDA2, since it has a larger lever arm than PDA1 as can be seen in figure 8.3. It is therefore expected that PDA2 has more pointing and thus more relative power noise than PDA1. If it can be shown, that the relative power noise of PDA2 fulfills the requirement, it is expected that the same is valid for PDA1. This will however be discussed later in more detail.

The beam parameters indicate that the beam has a waist of  $w_0 = 0.52$  mm (eq. (3.7) with  $\lambda = 1064$  nm) and a spot size of  $w = 0.55$  mm (eq. (3.6)) on the photodiode. The nominal configuration of QPD.c has rectangular quadrants even though the shape of the QPDs used for LISA Pathfinder is circular. Usually the beam size is small compared to the size of the QPD and the beam is centered to the QPD, such that the difference between circular and rectangular shaped QPDs is negligible. Here, in configuration 3 a beam with a diameter of 1.1 mm points on a QPD-segment which has a radius of 2.5 mm. Hence the shape of the QPD had to be adjusted to circular, to correctly compute the amount of beam clipping. In case of generating SEPD signals the diameter was set to 3 mm and the slits were removed.

## 8. QPDs to monitor amplitude stability

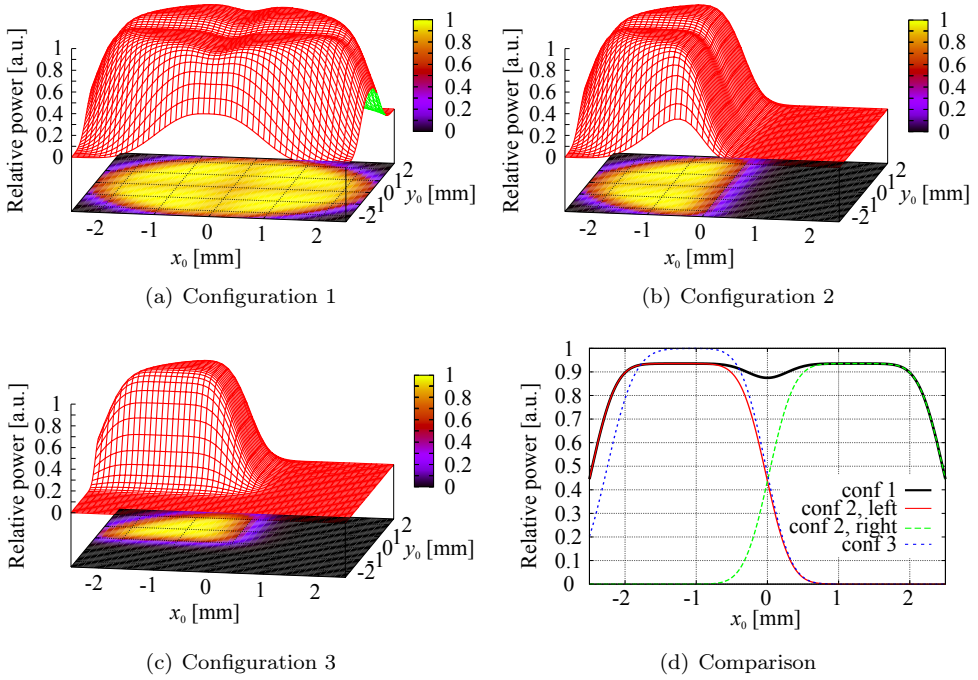


**Figure 8.4.:** Measured power in the three configurations, normalized to the incident beam power. Shown is this relative power if the incident beam is scanned over the QPD such that sensed power is plotted against the beam centroid position  $(x_0, y_0)$ . The entire scan is shown for the three configurations in (a) – (c) respectively. A direct comparison of the three configurations is shown in (d), which is an excerpt of the previous figures at  $y_0 = 0$  for configurations 1 and 2 and  $y_0 = \frac{4r_{\text{QPD}}}{3\pi}$  for configuration 3.

For simplicity it is assumed that the beam impinges orthogonally on the photodiode even though each photodiode on the optical bench of LISA Pathfinder is tilted by  $2.5^\circ \pm 0.5^\circ$  around its  $x$ -axis and by  $2^\circ \pm 0.5^\circ$  around its  $y$ -axis in order to prevent back reflection [UGB-3002]. Since QPD.c is a program that computes heterodyne signals, it expects two input beams but on both PDA1 and PDA2 only one beam impinges. Therefore, the second input beam used, was a copy of the first beam with zero amplitude. With these settings QPD.c computed the beam power on each segment and on the whole photodiode.

### 8.1.2. Result: measured power for different configurations

For a first comparison of the three configurations the power readout of each segment was computed while the beam scanned the complete surface of the QPD. The results of this computation are shown in figure 8.4(a)-8.4(c). Each of these graphs shows the overall relative power readout of all activated quadrants if the beam center points to the coordinates  $(x, y)$ . The relative power is defined as the fraction of measured power to incident beam power.



Figure 8.4(a) shows the relative power readout of configuration 1, where the whole QPD is used to measure the beam amplitude. This graph shows the effect of the insensitive slits between the 4 quadrants, which results in a local minimum in the sensed power if the beam is centered on the QPD. Furthermore, four comparably large stable areas with high power readout located between the slits and the edge of the circular shaped photodiode can be seen.

Due to the insensitive slit in the center of the QPD pointing the beam to the QPD center results in a small reduction of the measured power compared to pointing the beam to one of the four flat maxima shown in figure 8.4(a).

Figure 8.4(b) shows the relative power readout for configuration 2. Again the effect of the insensitive slit can be seen which separates two comparably large stable areas of high power readout. Hence pointing the beam directly on one of the quadrants (configuration 3) results in a slightly higher power readout than pointing it to the center of two adjacent quadrants.

Figure 8.4(c) finally shows the relative power readout of configuration 3. This graph shows that pointing the beam on the center of one quadrant results in high power readout and even allows slight misalignment of the beam on the quadrant without significant change in the power readout. This graph shows, that the amount of beam clipping at the borders of the quadrant are negligible, if the beam is centered on the local maximum, which is at the centroid of the quadrant.

A direct comparison of the three configurations is shown in figure 8.4(d). From this graph the following statements can be deduced:

- Configuration 1 has a power readout of 87.5% in its nominal position. The nominal working point of this configuration is a minimum in the power readout curve such that beam jitter couples to a very little degree into amplitude noise. Still small misalignment of the beam could shift the power readout in a linear range such that beam jitter couples into power readout noise. The flat top in the power readout of this configuration has a width of about 1.2 mm and a power readout of 93% in this range.
- Configuration 2 has a power readout of 93% in its nominal position and its flat top in the power readout has a width of approximately 1 mm.
- Configuration 3 has a power readout of 99.9% in its nominal position. The flat top has a width of 0.7 mm in  $x$ -direction.

These results are summarized in table 8.2. They indicate, that configuration 3 can be chosen for the alignment of the QPD. However, it is not known so far, whether the resulting power readout noise is sufficiently low. To estimate the amount of power readout noise, the derivative of the shown graphs is needed as well as an estimate of the beam pointing jitter. This is investigated in the subsequent section.

## 8.2. Relative power fluctuations

The two photodiodes PDA1 and PDA2 do not only measure the beam power but their signals are used in feedback loops to stabilize the power of the two laser beams. As shown in the previous section, the measured power depends on the exact position of

## 8. QPDs to monitor amplitude stability

Configuration	position of beam center $(x, y)$	power readout	width flat top
1	$(0,0)$	87.5%	
1	$(\frac{-r_{\text{QPD}}}{2}, 0)$	93%	1.2 mm
2	$(\frac{-r_{\text{QPD}}}{2}, 0)$	93%	1 mm
3	$(\frac{-4r_{\text{QPD}}}{3\pi}, \frac{-4r_{\text{QPD}}}{3\pi})$	99.9%	0.7 mm
SEP	$(0,0)$	99.99996	

**Table 8.2.:** Comparison of the three configurations according to figure 8.4(d). The radius of the QPD ( $-r_{\text{QPD}}$ ) is 2.5 mm. The width of a flat top is defined here by a power loss of 0.5 % with respect to the value of the maximum if the beam is horizontally shifted over the QPD-surface. A validation of the power readout of 87.5% in configuration 1 is described in appendix B.2 and the relative power readout of the SEPD is validated in appendix B.3.

the impinging beam on the photodiode. As a result, any beam jitter couples into the power readout and due to the feedback loops result in laser amplitude noise. Laser amplitude noise causes radiation pressure noise and therefore an acceleration of both test masses. The primary mission goal of LISA Pathfinder is to verify free floating test masses with residual acceleration noise of less than  $3 \cdot 10^{-14} \text{ m/s}^2 \text{ Hz}^{-\frac{1}{2}}$  in the measurement band of 1 mHz to 30 mHz (cf. section 5.1 and eq. (5.1)). Therefore, laser amplitude noise needs to fulfill a tight requirement which is expressed in terms of relative power fluctuation noise. The power spectrum normalized to the mean power need to be:

$$S(P)_{\text{rel}}^{\text{req}}(f) < \frac{9 \cdot 10^{-5}}{\sqrt{\text{Hz}}} \sqrt{1 + \left(\frac{f}{3 \text{ mHz}}\right)^4} \quad (8.1)$$

after power stabilization between 1 mHz and 30 mHz according to [ASD-3007, p. 17]. This is an acceleration noise type requirement, which has its minimal value of approximately  $9 \cdot 10^{-5} / \sqrt{\text{Hz}}$  at 1 mHz (cf. appendix A.2 and in particular figure A.2(b).)

In the next sections the amount of relative power fluctuation due to beam jitter is estimated and compared to the requirement.

### 8.2.1. Relation of relative power noise and beam pointing jitter

The power  $P$  measured by PDA2 is a function of the position of the beam centroid. This position is assumed to be the nominal position  $((x, y)$  set to zero for convenience) plus an offset  $(x_0, y_0)$  which accounts for initial misalignment, such that the measured power is

$$P = P(x_0, y_0) . \quad (8.2)$$

The beam will jitter around this mean position  $x_0$  with a spectrum  $S(x_0)$ . The amount of beam jitter is expected to be small since the beam is reflected only by components on the ultra stable optical bench and it is assumed that only jitter originating from the fiber injectors results in significant beam jitter on the power monitors. Thus the amount of power fluctuation due to beam jitter is linearized:

$$S(P) = \frac{\partial P(x_0)}{\partial x_0} \cdot S(x_0) . \quad (8.3)$$

Dependencies are mainly omitted in the subsequent equations in order to avoid confusing arrangements like  $S(P(x_0, y_0))(f)$ .

It is assumed that the beam jitter in  $x$ - and  $y$ -direction is uncorrelated (eq. (8.4)) and of the same amount (eq. (8.5)), such that the power sensing noise resulting from beam jitter in  $x$ - and  $y$ -direction is

$$S(P) = \sqrt{\left(\frac{\partial P(x_0, y_0)}{\partial x_0} \cdot S(x_0)\right)^2 + \left(\frac{\partial P(x_0, y_0)}{\partial y_0} \cdot S(y)\right)^2} \quad (8.4)$$

$$\approx \sqrt{2} \frac{\partial P(x_0)}{\partial x_0} \cdot S(x_0) . \quad (8.5)$$

The relative power fluctuation  $S(P)_{\text{rel}}(f, x_0)$  is the power fluctuation  $S(P)(f, x_0)$  divided by its mean value  $P(x_0)$  which needs to be smaller than the requirement:

$$S(P)_{\text{rel}} := \frac{S(P)}{P(x_0)} \quad (8.6)$$

$$\begin{aligned} &= \sqrt{2} \frac{\partial P(x_0)}{\partial x_0} \cdot S(x_0) \frac{1}{P(x_0)} \\ &= \sqrt{2} \frac{P(x_0 + \epsilon) - P(x_0)}{\epsilon \cdot P(x_0)} \cdot S(x_0) \end{aligned} \quad (8.7)$$

$$=: \sqrt{2} k_x^{P_{\text{rel}}} \cdot S(x_0) \stackrel{!}{<} S(P)_{\text{rel}}^{\text{req}} . \quad (8.8)$$

This means, that for an estimate of the relative power sensing noise  $S(P)_{\text{rel}}$  two independent values are needed: the coupling factor  $k_x^{P_{\text{rel}}}$  and an estimate of the beam pointing jitter  $S(x_0)$ . The coupling factor  $k_x^{P_{\text{rel}}}$  was computed from  $P(x_0)$  and  $P(x_0 + \epsilon)$  using the methods of section 8.1.1 and setting  $\epsilon = 1$  nm. The resulting values for the three configurations are shown as a function of the initial misalignment  $x_0$  of the impinging beam are shown in figure 8.5.

The pointing jitter  $S(x_0)$  is not known and needs to be derived separately. Two different approaches were used to compute  $S(x_0)$ :

- from a DWS-requirement
- from measured spectra of the “DC-alignment” signals on the EM of the OB.

This will be described in the subsequent sections.

### 8.2.2. Relative power noise derived from a DWS-requirement

One of the LTP mission goals is measuring the test mass angular alignment with a noise level of less than  $10 \text{ nrad}/\sqrt{\text{Hz}}$  [Heinzel2005, Steier2009]. Contributors to this noise are mainly test mass angular jitter, electronic noise and initial beam jitter which is measured by the x1 and x12-interferometer. As a worst case assumption the entire  $10 \text{ nrad}/\sqrt{\text{Hz}}$  is allocated to beam jitter, even though this single noise source is only one contributor to the noise budget. The lever arm, that means the distance from FIOS to PDA2, was then rounded to 20 cm. This led to a beam pointing jitter of less

## 8. QPDs to monitor amplitude stability

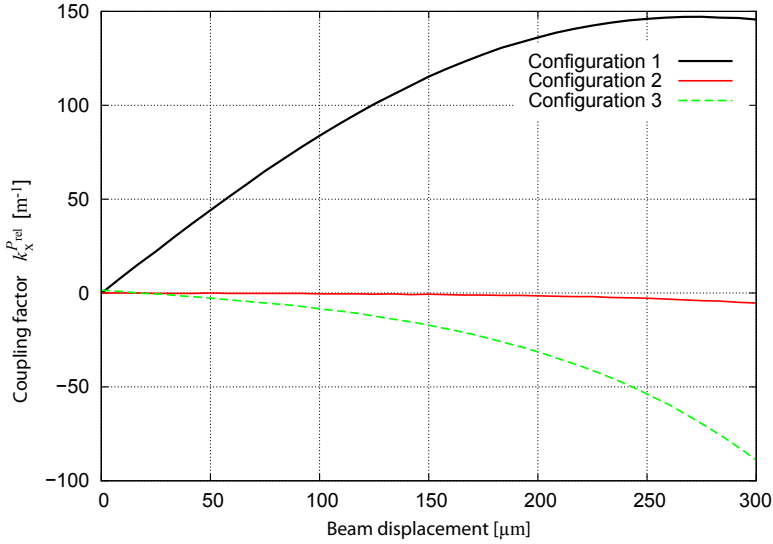


**Figure 8.5.:** Coupling factor  $k_x^{P_{rel}}$  as a function of the horizontal beam misalignment  $x_0$  computed for each of the three configurations (cf. figure 8.1).

than  $2 \text{ nm}/\sqrt{\text{Hz}}$ :

$$S(x_0)^{\text{DWS}} < \tan(10 \text{ nrad}) \cdot 20 \text{ cm} \quad (8.9)$$

$$< 2 \frac{\text{nm}}{\sqrt{\text{Hz}}} \quad (8.10)$$

The upper index “DWS” indicates that the value was derived from a DWS-requirement. The coupling factor  $k_x^{P_{rel}}$  is already known from section 8.2.1 and figure 8.5 but since this coupling factor depends on the misalignment of the beam on the photodiode and the configuration used, the misalignment on the beam displacement on the photodiode needs to be estimated. The configuration of main interest was configuration 3 and since this type of beam alignment was not performed before, an estimate of the beam misalignment was not available. However, it is known that the quadrant photodiodes in LTP are aligned to  $\pm 33 \mu\text{m}$  with respect to their optimal position. In case of configuration 3, there is no DC signal to aid the alignment procedure. Therefore, a misalignment of  $300 \mu\text{m}$  of the beam to its nominal position on the photodiode was used as a very cautious estimate and worst case assumption. The coupling factor  $k_x^{P_{rel}}$  has at this point its highest value of about  $150 \text{ /m}$  for configuration 1. According to eq. (8.8) the relative power fluctuation is thus

$$S(P)_{\text{rel}} =: \sqrt{2} \cdot k_x^{P_{rel}} \cdot S(x_0) \quad (8.8)$$

$$< \sqrt{2} \cdot 150 \text{ m}^{-1} \cdot \frac{2 \text{ nm}}{\sqrt{\text{Hz}}} \quad (8.11)$$

$$\rightarrow \boxed{S(P)_{\text{rel}} < 4.2 \cdot 10^{-7} \frac{1}{\sqrt{\text{Hz}}} \ll 9 \cdot 10^{-5} \frac{1}{\sqrt{\text{Hz}}} = S(P)_{\text{rel}}^{\text{req}}} \quad (8.12)$$

for any of the three configurations, any beam misalignment smaller than  $300\ \mu\text{m}$  and any frequency. With the assumptions made, the relative power noise safely fulfills the required  $9 \cdot 10^{-5} \frac{1}{\sqrt{\text{Hz}}}$  at 1 mHz (eq. (8.1)).

### 8.2.3. Relative power noise derived from measured DC spectra

An alternative approach to find an estimate for the beam jitter  $S(x_0)$  on PDA2 (the only photodiode investigated in this work) is an analysis of a measured DC-alignment signal. The DC-alignment signal is a measure of the beam centroid position on the QPD (cf. section 2.3 and section 4.6 for more details). A linear relation of beam position and DC signal can therefore be deduced, for instance in horizontal direction:

$$\text{DC}_h = k_x^{\text{DC}_h} \cdot x . \quad (8.13)$$

The amount of beam pointing jitter  $S(x_0)$  can then be computed from a measured DC-spectrum by:

$$S(x_0) = \frac{1}{k_x^{\text{DC}_h}} \cdot S(\text{DC}_h) . \quad (8.14)$$

Even though eq. (8.13) and eq. (8.14) might seem to be the same except of rearrangement, they are quite different. Equation (8.13) expresses that a slight shift of the beam on one photodiode causes a linear change of the DC signal. This is the method to obtain  $k_x^{\text{DC}}$  in a simulation. On the other hand eq. (8.14) indicates that the measured DC-spectrum  $S(\text{DC}_h)$  which is an average of the DC-signals measured by the redundant photodiode pair, converted by the factor  $k_x^{\text{DC}}$  to give an estimate of the pointing jitter  $S(x_0)$ . This equation implies that any noise source contributing to  $S(\text{DC}_h)$  like for instance electrical readout noise originating from photodiode and phasemeter is converted to pointing jitter. The amount of pointing jitter  $S(x_0)$  computed from eq. (8.14) is therefore understood as worst case estimate.

As input to eq. (8.14) a measured DC-spectrum on PDA2 would be optimal. However, all measurements available at the time of the investigation (November 2009) were performed with the engineering model of the OBI which was integrated in a complete breadboard model of the interferometer in Hanover. The engineering model (EM) of the OBI has single element photodiodes as power monitors (PDA1, PDA2) which obviously cannot generate DC signals. The only DC spectra available were measured for the x1-, x12-, reference - and frequency interferometer (cf. section 5.2.1 for details on these interferometers). The DC spectra of the x1- and x12-interferometer contain TM jitter noise which does not exist on PDA2. They are thus less significant than the DC spectra of the reference or frequency interferometer.

The coupling factor  $k_x^{\text{DC}}$  was therefore computed for the reference and frequency interferometer by using QPD.c in the following way:

Beam parameters on the surfaces of the PD1B, PD12B, PDRA and PDFA (cf. figure 8.3) were taken from the nominally, and thus perfectly, aligned OBI OptoCad model and given to QPD.c. The thus generated beams were vertically centered and successively shifted horizontally over the QPD while the DC-alignment signal was computed. The resulting plot of the DC-signal in dependency of the beam position  $x$  as well as their

## 8. QPDs to monitor amplitude stability

PD	$k_x^{\text{DC}_h}$ [m <sup>-1</sup> ]	$s$ (beam 2) [mm]	$s$ (beam 1) [mm]	$\bar{s}$ [mm]	scale factor [a.u.]
PDA2		144.23	-		
PDRA	-2934	197.68	556.39	377.04	2.6
PDFA	-3208	232.13	208.39	220.26	1.5

**Table 8.3.:** Coupling  $k_x^{\text{DC}}$  and lever arm needed to compute the pointing jitter  $S(x)$  on PDA2. Here, beam 1 is the measurement and beam 2 the reference beam. The factor  $k_x^{\text{DC}}$  is the slope in figure 8.6. The scaling factor was computed from the total optical path length propagated ( $s$ ) from fiber injector to the respective photodiode by using the intercept theorem. The values of  $s$  were taken from the nominal OptoCad model of the FM OBI.

linear fit is plotted in figure 8.6. The slope in the origin is the coupling factor  $k_x^{\text{DC}_h}$  which has the following values:

$$k_x^{\text{DC}_h} = -2934 \frac{1}{\text{m}} \quad \text{for PDRA} \quad (8.15)$$

$$k_x^{\text{DC}_h} = -3208 \frac{1}{\text{m}} \quad \text{for PDFA} . \quad (8.16)$$

The beam pointing jitter  $S(x_0)$  computed with eq. (8.14) from a DC-spectrum measured with the frequency or reference interferometer corresponds to pointing jitter on the surface of PDRA or PDFA respectively, not on PDA2. Assuming that all pointing noise originates from angular beam jitter at the fiber injector, the resulting pointing jitter on PDRA and PDFA can be scaled by the ratio of the corresponding lever arms. There are however, two beams impinging on PDRA and PDFA and both contribute to the local pointing jitter. Both beams propagated different lengths, and have therefore different lever arms. It is assumed that the total lever arm is the mean value of the two contributing lever arms, such that:

$$S^{\text{PDA2}}(x_0) = \frac{s_{\text{PDA2}}}{\bar{s}_{\text{PDRA}}} S^{\text{PDRA}}(x_0) \quad \text{or} \quad (8.17)$$

$$= \frac{s_{\text{PDA2}}}{\bar{s}_{\text{PDFA}}} S^{\text{PDFA}}(x_0) . \quad (8.18)$$

### Implementation

In section 8.2.2 the beam displacement on the photodiode in configuration 3 was estimated as  $x_0 = 300 \mu\text{m}$ . This was a very cautious assumption used as a worst case estimate. In order to gain an impression of the effect of alignment, a second more stringent estimate of  $x_0 = 50 \mu\text{m}$  is used. With these two assumptions for the misalignments the coupling factor were  $k_x^{\text{Prel}}$  was:

- $k_x^{\text{Prel}} \approx 3 \text{ m}^{-1}$  for configuration 3 and a beam misalignment  $x_0 = 50 \mu\text{m}$
- $k_x^{\text{Prel}} \approx 91 \text{ m}^{-1}$  for configuration 3 and a beam misalignment  $x_0 = 300 \mu\text{m}$  .

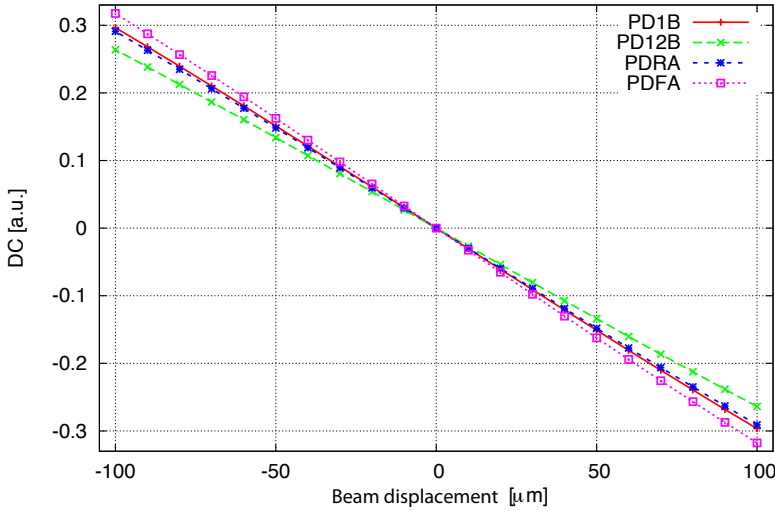


**Figure 8.6.:** DC signal computed on PD1B, PD12B, PDRA, PDFA as function of the respective beam centroid position. Each beam is vertically centered on the respective QPD and horizontally misaligned by  $x_0$ . The coupling factor  $k_x^{\text{DC}}$  is the slope of each curve and has a value of roughly  $-3000 \text{ m}^{-1}$ . Exact values are given in table 8.3.

$$S(P)_{\text{rel}}^{\text{F}} = \sqrt{2} \cdot k_x^{P_{\text{rel}}} S^{\text{PDA2}}(x) \quad (8.8a)$$

$$= \sqrt{2} \cdot k_x^{P_{\text{rel}}} \cdot \frac{\bar{s}^{\text{PDFA}}}{s_{\text{PDA2}}} S^{\text{PDFA}}(x) \quad (8.19)$$

$$= \sqrt{2} \cdot k_x^{P_{\text{rel}}} \cdot \frac{\bar{s}^{\text{PDFA}}}{s_{\text{PDA2}}} \frac{1}{k_x^{\text{DC}}} S(\text{DC}_h^{\text{PDFA}}) \quad (8.20)$$

or likewise for the reference interferometer:

$$S(P)_{\text{rel}}^{\text{R}} = \sqrt{2} \cdot k_x^{P_{\text{rel}}} \cdot \frac{\bar{s}^{\text{PDRA}}}{s_{\text{PDA2}}} \frac{1}{k_x^{\text{DC}_h}} S(\text{DC}_h^{\text{PDRA}}) \quad (8.21)$$

Inserting all values results in

$$S(P)_{\text{rel}}^{\text{F}} \approx \begin{cases} 8.7 \cdot 10^{-4} S(\text{DC}_h^{\text{PDFA}}) & \text{for } x_0 = 50 \mu\text{m} \\ 2.6 \cdot 10^{-2} S(\text{DC}_h^{\text{PDFA}}) & \text{for } x_0 = 300 \mu\text{m} \end{cases} \quad (8.22)$$

$$S(P)_{\text{rel}}^{\text{R}} \approx \begin{cases} 5.5 \cdot 10^{-4} S(\text{DC}_h^{\text{PDRA}}) & \text{for } x_0 = 50 \mu\text{m} \\ 1.7 \cdot 10^{-2} S(\text{DC}_h^{\text{PDRA}}) & \text{for } x_0 = 300 \mu\text{m} . \end{cases} \quad (8.23)$$

These factors were therefore multiplied to measured DC spectra. The used DC spectra  $S(\text{DC})_h$  result from a typical measurement carried out at the AEI in Hanover with the engineering model of the OBI which was integrated in a complete breadboard model of the interferometer at that time (May 2009).

## 8. QPDs to monitor amplitude stability

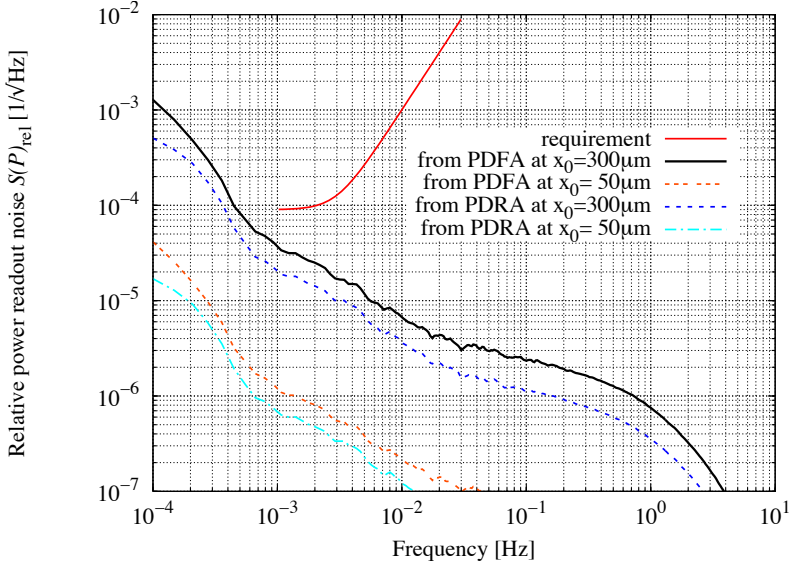


**Figure 8.7.:** Relative power fluctuation  $S(P)_{rel}$  for configuration 3 derived from typical DC spectra measured with the reference (PDRA) and frequency interferometer (PDFa) of the engineering model of the OBI at the AEI. The graphs were computed with eq. (8.22) and eq. (8.23) thus taking into account vertical and horizontal beam jitter and assuming a beam misalignment of either 50  $\mu\text{m}$  or 300  $\mu\text{m}$  on the photodiode. Any noise contributing to the DC spectra (e.g. electronic noise) was transferred by eq. (8.14) into beam jitter on the photodiode even though beam jitter is only one contributor to the DC-spectrum. Thus the shown relative power fluctuation is expected to be larger than it will be in flight.

### Result

The resulting relative power noise spectra  $S(P_{rel})$  are shown in figure 8.7 and fulfills the requirement. This is the case even though very pessimistic assumptions were made: all noise in the measured DC spectra was assumed to originate from beam jitter on the photodiode (eq. (8.14)) and the misalignment of the beam on the photodiode was set to a fairly large number of 300  $\mu\text{m}$ .

## 8.3. Conclusion

The main point of interest in this investigation was whether a QPD in configuration 3 could be used for power readout in LISA Pathfinder.

It was shown that configuration 3 has the following properties:

- It has the highest power readout of the three configurations (figure 8.4(d)), since it is not clipped at the insensitive slit (figure 8.4(a)-figure 8.4(c)).
- It has a flat top in the power readout with an  $x$ -diameter of 0.7 mm (table 8.2).
- It shows sufficiently low power readout noise, no matter whether computed from a measured DC-spectrum figure 8.7 or a DWS-stability-requirement (eq. (8.12)).



Thus from a pure optics point of view, QPDs can be used in configuration 3 to replace the single element photodiodes.

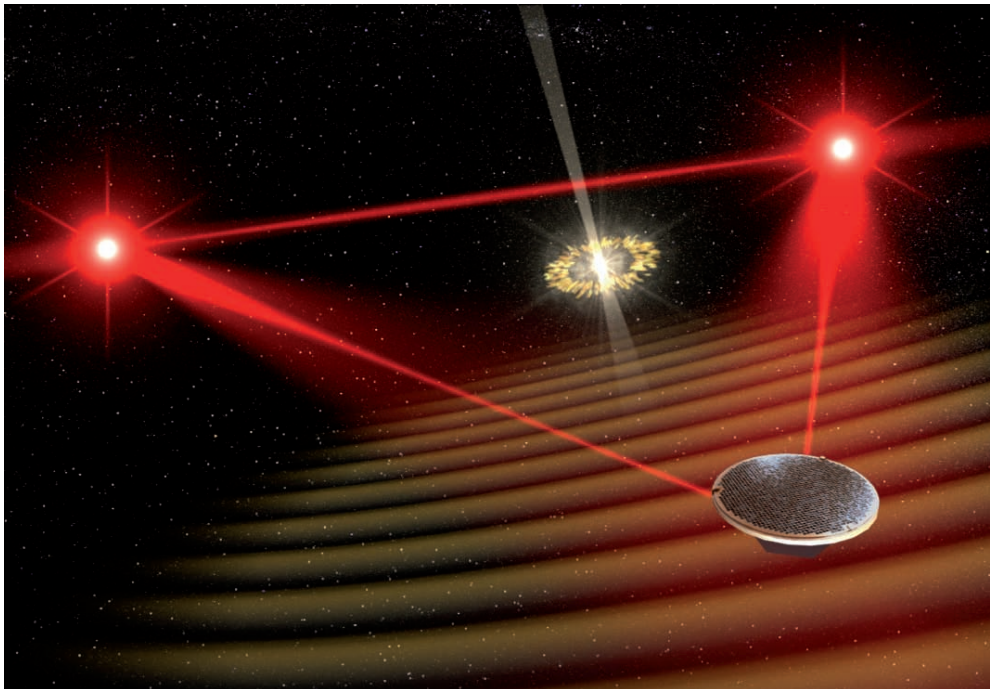
Due to the high electrical capacitance of each segment it is desirable to use as few quadrants as possible. Thus from a pure electrical point of view configuration 3 is to be preferred.

It was finally decided to use the space InGaAs-QPDs in configuration 3 to replace the single element photodiodes.



Part III.

## LISA interferometry





## 9. LISA interferometry concepts

The relevance of LISA as interferometric gravitational wave observatory, its sources and its standing among other gravitational wave detectors was already discussed in chapter 1. This chapter focuses on LISA technology and interferometer concepts. The measurement principle and the layout of the optical bench interferometer are introduced. This chapter provides the necessary background to integrate chapter 10 regarding the work performed for the test mass interferometer into the LISA mission.

### LISA technology

LISA consists of three identical spacecraft flying in triangular formation linked via laser beams. All three arms forming the equilateral triangle are technically independent, that means each arm consists of one local test mass in an inertial sensor (or gravitational reference sensor GRS), one local optical bench which hosts the interferometer, one Schiefspiegler telescope (cf. figure 9.3(a)), and exactly the same configuration on the remote spacecraft, as shown in figure 9.1. Consequently, there are two inertial sensors aboard each spacecraft, two optical benches and naturally two telescopes. One telescope, optical bench and GRS each are rigidly connected to another to form one movable optical subassemblies (MOSA, as shown in figure 9.2). The MOSA will point the laser beams towards the remote spacecraft and need to be movable, for the following reason.

The three large scale arm lengths of LISA are determined by the orbits of the three spacecraft. Each spacecraft is effectively free falling except of the small corrections performed to keep the GRS centered to the free falling test masses. During one orbital period, that means during one year, each spacecraft is subject to varying gravity, resulting from altering distances between the spacecraft and the Sun. Since the LISA triangle is tilted with respect to the ecliptic, each spacecraft is accelerated by this effect by a different amount. This results in arm length changes of the order of 1% and therefore approximately 50,000 km during a year [Xia2010, Jennrich2009]. As a consequence, the  $60^\circ$  angles between the interferometer arms will vary by  $\pm 0.8^\circ$  [Weise2008, Jennrich2009]. These changes are not linear but rather periodic, such that they are referred to as breathing effect. The MOSA are designed to account for this breathing effect and point the transmit laser beams towards the remote spacecraft.

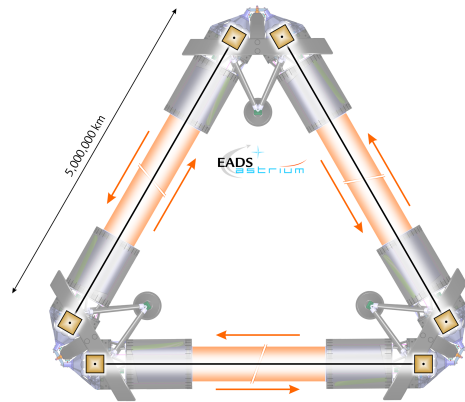


**Figure 9.1.:** LISA constellation. Credit: EADS Astrium.

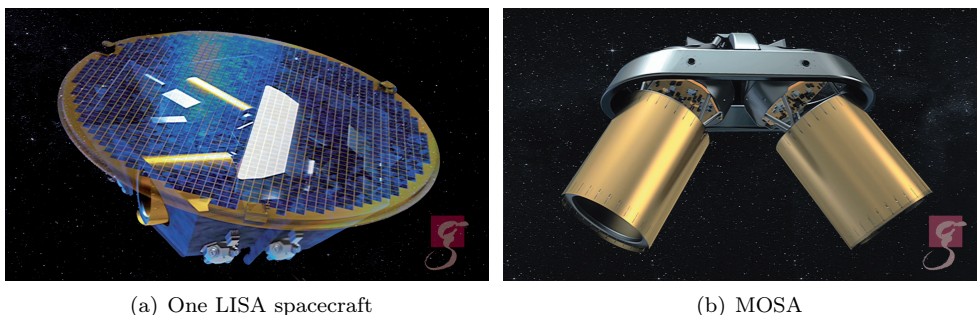


**Figure 9.2.:** (a) LISA Spacecraft with transparent solar panel revealing the movable optical sub-assembly (MOSA) in its core. (b) Two MOSA in their static frame. The pinholes in the frame indicate the MOSA pivot axes. The test masses in the inertial sensors are not visible, because of their location behind the optical benches. Credit: AEI / MildeMarketing / Exozet.

### LISA optical bench interferometry

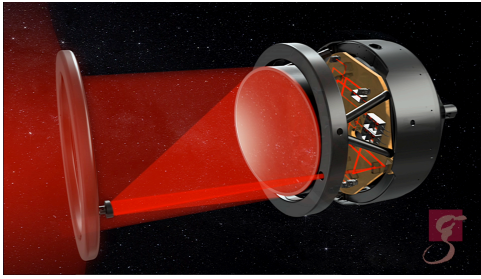
The working principle of LISA is a measurement of the distance between a test mass and its counterpart on a remote spacecraft. This arm length measurement is split into three individual measurements:

- local test mass with respect to the local optical bench, measured by the test mass interferometer (cf. figure 9.3(b) for an illustration)
- local optical bench to optical bench on a remote spacecraft, measured by the science interferometer
- relative distance between remote optical bench and corresponding remote test mass, measured by the remote test mass interferometer.

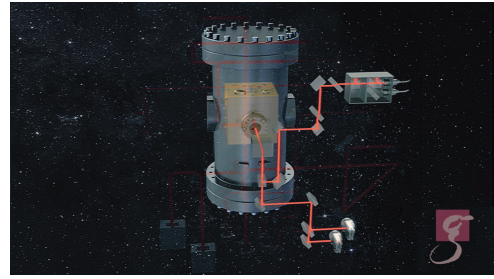
These measurements are performed by distinct interferometers whose signals are not combined on the spacecraft but rather sent to Earth. On ground, the signals of the three spacecraft are evaluated with a technique called time delay interferometry (TDI) which combines the signals of the various interferometers to imitate a variety of large-scale interferometer types, like for example a Michelson or a Sagnac interferometer. Using TDI it is possible to choose during data analysis the optimal detector type for each gravitational wave signal type.

Currently, the elegant breadboard (EBB, that means a prototype model) of the optical bench interferometer (OBI) of LISA is being designed and will be manufactured soon. The OptoCad model of the current layout is sketched in figure 9.4. Since this is a prototype of the optical bench, changes are likely and the shown arrangement is only one step in an iterative process of designing the real flight model.

The EBB of the optical bench consists of a circular shaped Zerodur baseplate with a diameter of 58 cm to which the variety of components is bonded via hydroxide-catalysis bonding. The layout shown in figure 9.4 has noticeable non-orthogonal beam paths. These result from wedged components which are used in order to separate ghost beams from the nominal beam path and thereby reduce interferometer noise. Furthermore,



(a) Schiefspiegler telescope



(b) GRS and test mass interferometer

**Figure 9.3.:** (a) Assembly of Schiefspiegler telescope and optical bench as part of one movable optical subassembly (MOSA). (b) Test mass interferometer and inertial sensor with transparent vacuum chamber revealing the electrode housing which encloses one free floating test mass. Credit: AEI / MildeMarketing / Exozet.

the interferometer uses polarizing optics which, for instance, allows the use of orthogonal incidence on the test mass. The polarizing beam splitters (PBS) are currently planned to be dielectrically coated plate beam splitters instead of the commonly used PBS cubes to avoid ghost beams that are coaligned to the main beam. Polarizing and non-polarizing beam splitters have therefore identical physical appearance. The polarizing beam splitters are therefore drawn in a different, slightly darker blue, color in figure 9.4 to identify them.

The measurement beam (red) is a local laser beam provided by two redundant fiber optical subassemblies (FIOS, labeled as Tx Beam Delivery in figure 9.4). The reference beam (blue) is in fact the Tx beam of the other OBI on the spacecraft, provided again by two redundant FIOS. It is therefore sufficient to have only one power monitor on each optical bench which is positioned in the beam path of the measurement path. This power monitor is the equivalent to PDA1 and will be used for amplitude stabilization of the measurement beam. This amplitude stabilized measurement beam is then routed to the other bench and acts there as – already stabilized – reference beam.

The current design of the OBI comprises four interferometers: a reference interferometer, a test mass interferometer, a science interferometer and a PAAM interferometer.

The reference interferometer superimposes the reference beam with the local measurement beam and does not include a reflection from a test mass. It is therefore the equivalent to the reference interferometer of LISA Pathfinder with the exception, that the two beams originate indeed from two different frequency shifted lasers.

The test mass interferometer beats the local reference beam (blue) and measurement beam (red) which reflects from the local test mass. It provides therefore the measurement of the test mass with respect to the optical bench and is the equivalent to the x1-interferometer of LISA Pathfinder. Both beams in the reference and test mass interferometer are local and therefore Gaussian laser beams.

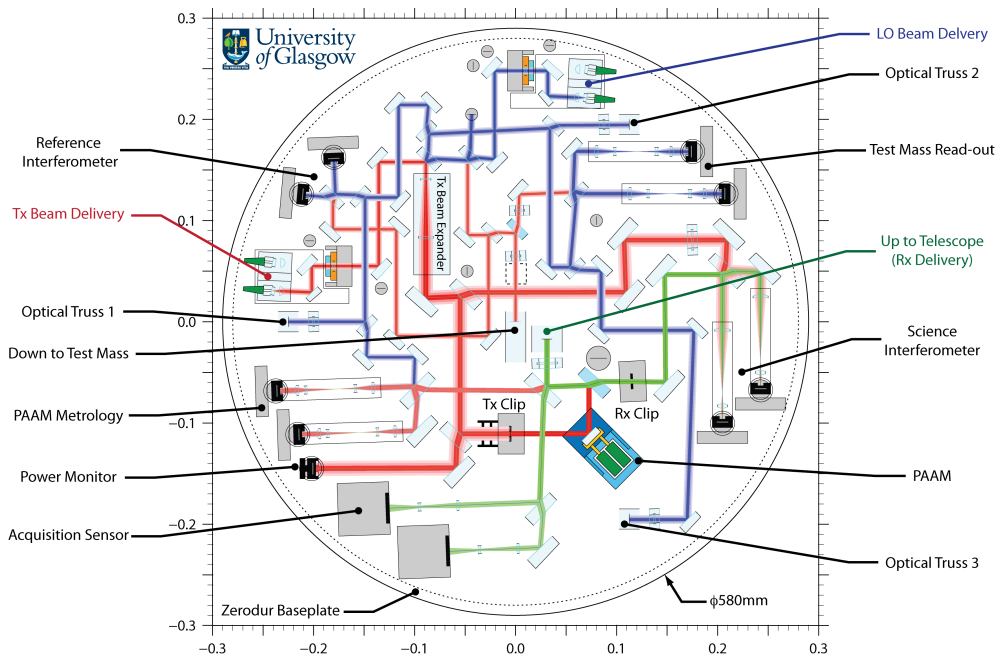


**Figure 9.4.:** OptoCad-Model of the EBB LISA OBI (status August 2010). Credit: UGL

The science interferometer superimposes the received beam (Rx beam, drawn in green) with the local reference beam. The received beam originates from a laser beam which traveled a distance of approximately 5 million kilometers through space such that it has a diameter of the order of 17 km and planar wavefronts when it reaches the local spacecraft. From this beam, 40 cm are clipped by the telescope, focussed and delivered to the optical bench. The Rx beam has therefore a top hat beam shape and very little power: approximately 200 pW at the beam combiner of the science interferometer. The local Rx beam is on the remote spacecraft the transmit or Tx beam, which is a fraction of the measurement beam that did not reflect on the remote test mass. The science interferometer superimposes therefore a beam originating from the remote optical bench with the reference beam on the local optical bench. It thereby senses pathlength changes between these two optical benches. Located in the path of the transmit beam is the TxClip which clips the Tx beam on the optical bench, rather than in the telescope in order to increase the received light power on the remote spacecraft.

The fourth interferometer on the optical bench is the PAAM interferometer which is used to sense the angle of the point ahead angle mechanism (PAAM). The PAAM is used to achieve an angular offset between receive and transmit beam. This is needed for the following reason. The large distance between two spacecraft implies a rather



long travel time for the laser beam of

$$\Delta t = \frac{L}{c_0} \approx \frac{5 \cdot 10^9 \text{ m}}{3 \cdot 10^8 \frac{\text{m}}{\text{s}}} \approx 16.7 \text{ s}, \quad (9.1)$$

where  $L$  is the distance between two spacecraft and  $c_0$  the speed of light. This travel time indicates, that pointing the beam in the direction of the received beam would result in effectively missing the remote spacecraft, because it moves out of the line of sight during the beam propagation time. The transmit beam is therefore planned to be “pointed ahead” of the current remote spacecraft position, which means an angular offset between Tx and Rx beam is needed. These angles are in the order of a few hundred micro-radian.

In the beam paths of PAAM-, science- and test mass interferometer located in front of the photodiodes are lens systems which reduce the beam size, such that they match the rather small photodiode. These beam compressors are currently being designed and investigated. This is discussed in detail in the following chapter (chapter 10).

Besides the four interferometers on the optical bench, there are three more interferometers, which sense expansions of the Schiefspiegler telescope. Therefore, the reference beam is deflected at three places, optical truss no. 1 to 3, off the optical bench to the telescope where it interferes with a clipped fraction of the transmit beam.

Finally, there are two acquisition sensors located on the optical bench acting partly as star trackers. These aid the initial alignment of the three spacecraft with respect to each other.

Since LISA Pathfinder is the technology demonstration mission for LISA, the aim is obviously to use LISA Pathfinder technology ideally unchanged. Therefore, the LISA FIOS are planned to be the LISA Pathfinder FIOS except of minor adaptations and the entire inertial sensors will preferably be copies of the LISA Pathfinder inertial sensors.



# 10. Imaging optics

*In section 7.2.4 it was shown, that test mass angular jitter cross couples into the pathlength readout of LISA Pathfinder. This cross coupling results in pathlength noise which exceeds the allocated budget such that noise subtraction is required. Even though this DWS-correction was already shown for LISA Pathfinder, it is desirable to avoid the problem in LISA by suppressing the cross coupling and thereby make DWS-correction unnecessary. Such a suppression can be achieved by a specially designed lens system, which images the test mass surface onto the photodiode.*

*In this chapter the work performed to find an appropriate lens system is discussed and tolerance analyses of found systems are shown. In section 10.2 the numerous design criteria for the imaging optics are introduced, and the primary design goal is derived. Furthermore, a comparison between geometrical optics design criteria and Gaussian optics design criteria is performed, the term pupil plane imaging system is introduced and translated to Gaussian optics. In section 10.3 it is shown for one selected example, that a lens system with pupil plane imaging property decouples the pathlength signal from test mass angular jitter. However, the investigated system does not fulfill all length constraints for the test mass interferometer and cannot be adapted to all constraints. Therefore two alternative beam compressors with pupil plane imaging property that fulfill all constraints are investigated in section 10.4. It is shown that both systems nominally show sufficient decoupling (section 10.4.1). A tolerance analysis shows, that both systems tolerate fairly large longitudinal misalignments, however vertical alignment of the QPD to sub-micron level and relative longitudinal waist displacements of only a few centimeters are required (section 10.4.2).*

*The simulation work performed for the test mass interferometer is accompanied by a corresponding experiment, which shall validate the accurateness of the simulation tools. For this experiment, an additional tolerance analyses with experimentally achieved beam parameters was performed (section 10.4.4). It was shown, that with the current uncertainty in the beam parameters, a large variety of results might occur.*

## 10.1. Objective

Since the measurement beam in the test mass interferometer has a nominal waist size of 1 mm, while the photodiodes have a radius of 0.5 mm, a lens system is needed to image the beam onto the small photodiodes. Without this imaging optics, stray light originating from the shiny outer borders of the quadrant photodiodes (QPDs) would occur, an effect which should generally be avoided. Since this imaging optics is needed anyway, it is reasonable to design it carefully and thereby reduce another noise source: the cross coupling of test mass angular jitter in pathlength readout. The primary design goal of the lens system – besides beam size reduction – is therefore decoupling of the pathlength signal from test mass angular jitter.

As shown in figure 9.4 and mentioned in section 9 imaging optics are also needed for the LISA science and PAAM interferometer. However, these interferometers superimpose non-Gaussian top hat beams. The software tools currently used at the AEI (IfoCad and OptoCad+QPD.c) do not yet include higher mode beam parameter computation. However, IfoCad is currently being upgraded such that the design and investigation of beam compressors for top hat beam interferometers will be possible soon.

## 10.2. Design criteria and constraints

There exists a high number of constraints that complicate the design of the imaging optics. These criteria are listed in table 10.1. The primary design goal C01 as well as the compression factor C06 are discussed in the subsequent paragraphs. All remaining criteria are discussed in appendix A.6.

	Criterion	Meaning	Rating
C01	Decoupling of test mass tilts into the pathlength signal, i.e. for all test mass angles $\varphi$ between $\pm 250 \mu\text{rad}$ : $k_{\varphi}^{\Delta L_e}(\varphi) \leq 3.2 \frac{\text{pm}}{\mu\text{rad}}$	primary design goal	high
C02	As stable as possible against misalignment	secondary goal	high
C03	Distance: test mass $\leftrightarrow$ first lens: 425 mm	constraint	high
C04	Overall length of imaging system in the order of 8 cm or less	constraint	high
C05	Distance: last lens $\leftrightarrow$ QPD $> 5$ mm	constraint	high
C06	Compression factor: 3:1 or 5:1		medium
C07	Existence of intermediate focus	constraint	medium
C08	Collimated beam impinging on QPD	constraint	low
C09	Beam waist position: on the test mass	constraint	low
C10	Beam waist size (on test mass): 1 mm	constraint	high
C11	QPD shape: circular	fact for pre-experiment	
C12	QPD slit: 20 $\mu\text{m}$ total width	fact for pre-experiment	
C13	QPD diameter: 1 mm	fact for pre-experiment	

**Table 10.1.:** Design criteria for imaging optics in the test mass interferometer. A discussion of these constraints is given in appendix A.6. The QPD parameters were chosen according to the laboratory QPDs used for the accompanying experiments, which are described in [PD1].

### Criterion C01: the primary design goal

According to TN 6 [LOB-06, p. 28] the overall pathlength noise allocated for the TM optical readout (ORO) is  $1.06 \text{ pm}/\sqrt{\text{Hz}}$  (white noise). There are 5 uncorrelated contributors assumed, according to p. 30 in the same document. One of these contributors is the coupling of test mass angular jitter into the pathlength readout. Therefore, the

budget for pathlength noise  $S(s)$  originating from test mass angular jitter is

$$S(s) \leq \frac{1.06 \text{ pm}}{\sqrt{5} \sqrt{\text{Hz}}} = 0.47 \frac{\text{pm}}{\sqrt{\text{Hz}}} . \quad (10.1)$$

The angular jitter  $S(\varphi)$  of the test mass is defined in requirement R<130-050> in [LOB-06] as

$$S(\varphi) \leq 150 \frac{\text{nrad}}{\sqrt{\text{Hz}}} . \quad (10.2)$$

The first derivative of the pathlength signal  $s$  by the test mass angle is the coupling factor  $k_\varphi^s$ :

$$k_\varphi^s := \frac{\partial s}{\partial \varphi} . \quad (10.3)$$

Assuming linearity, this coupling factor  $k_\varphi^s$  transfers between angular jitter  $S(\varphi)$  and resulting pathlength noise  $S(s)$  by:

$$k(\varphi) \cdot S(\varphi) = S(s) \quad (10.4)$$

$$k(\varphi) \cdot 150 \frac{\text{nrad}}{\sqrt{\text{Hz}}} \leq 0.47 \frac{\text{pm}}{\sqrt{\text{Hz}}} , \quad (10.5)$$

such that it has to fulfill the requirement:

$$k(\varphi) \leq 3.2 \frac{\text{pm}}{\mu\text{rad}} . \quad (10.6)$$

The coupling shall fulfill this requirement for the full test mass angular variation range of  $\pm 250 \mu\text{rad}$ , which was taken from requirement R<130-040> in TN 6 [LOB-06]. This requirement is valid, if DWS-correction is not to be performed. That means in particular, that the imaging optics needs to provide sufficient decoupling to reduce the residual pathlength noise to less than the allocated budget of  $0.47 \text{ pm}/\sqrt{\text{Hz}}$ . An alternative requirement for the case that DWS-correction is performed is currently being analyzed by ASD.

### Criterion C06: Investigation of an optimal compression factor

The waist of the beam on the optical bench was chosen to have a nominal radius of 1 mm [LOB-06, p. 80 R<130-090>] which is larger than the quadrant photodiodes which have a radius of 0.5 mm [LOB-06, p.71]. Both values need to be regarded as fixed (cf. appendix A.6 in the paragraphs regarding C09 – C13 for a discussion of these values). The imaging optics will reduce the size of the beam such that it suits the size of the QPD. A compression factor of 5 was originally suggested by ASD and UGL because this reduces the spot size to approximately one third of the photodiode size, the typically used size ratio as discussed in section 4.6.1 on page 47. The test mass interferometer does not superimpose low power laser beams from a remote spacecraft like the science interferometer, but solely local laser beams. It is therefore not a necessity to achieve maximal power readout. However, maximal power readout corresponds to the least amount of beam clipping. Since beam clipping affects the pathlength readout

## 10. Imaging optics

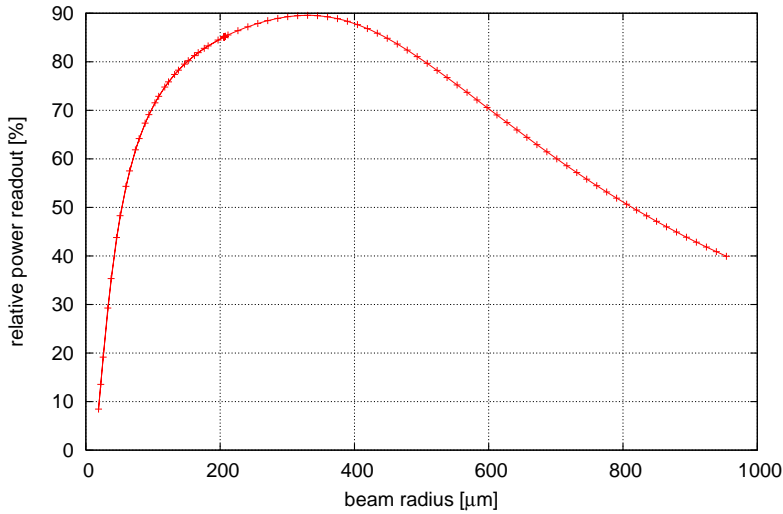


**Figure 10.1.:** Relative power readout as function of incident beam radius. A beam radius of  $330\ \mu\text{m}$  results in maximal power readout of 89.5 %.

(a fact shown in section 10.4.3), it is desirable to have as little beam clipping as possible.

In order to find an optimal compression ratio, the amount of beam clipping for a given photodiode and varying beam radii was computed. The result is shown in Figure 10.1. The maximal power readout achievable and thus least beam clipping for 1 mm QPDs with a slit size of  $20\ \mu\text{m}$  is 89.5% with a beam radius of  $330\ \mu\text{m}$ . This value gives a compromise between clipping the beam due to the limited size of the QPD (beam radii  $> 330\ \mu\text{m}$ ) and beam clipping on the insensitive slit of the QPD (beam radii  $< 330\ \mu\text{m}$ ).

**In order to achieve least amount of beam clipping, the beam compressor should have a compression ratio of 3:1.**

### Geometrical and Gaussian optics design criteria

The first beam compressor was designed by ASD using geometrical optics. The criteria used were:

- (A) little beam walk on the photodiode due to test mass rotation  $\rightarrow$  pupil plane imaging,
- (B) low aberration,
- (C) astronomical telescope design.

However, the test mass interferometer superimpose local laser beams, which will be mainly in the TEM00 mode and thus have ideally Gaussian shape, such that OptoCad and QPD.c are ideal simulation tools for this task. In order to allow joined design

efforts a translation of the classical optics design criteria to Gaussian optics was needed. This translation is discussed in the subsequent paragraphs.

### Pupil planes (criterion A)

According to classical optics, there exist two pupil planes in an imaging system: the entrance pupil and the exit pupil. These are defined as the planes of the images of the aperture stop in the object space - i.e. close to the object (entrance pupil) or in the image space (exit pupil), as shown in figure 10.2. The position of the pupil planes can

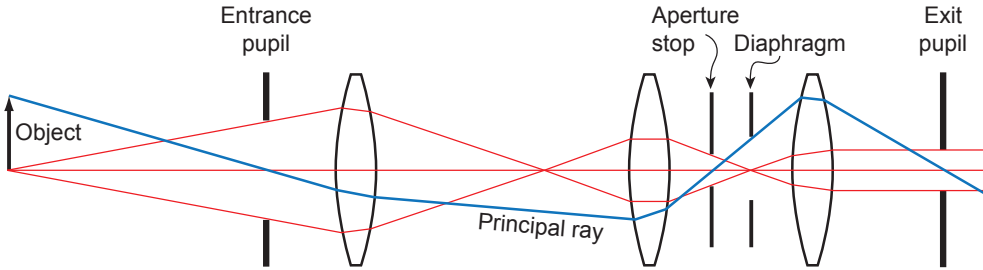


**Figure 10.2.:** Position of pupil planes in an arbitrary lens system.

be found by the following simple steps:

- Since geometrical optics operates with plane waves of infinite size, there will always be an element which limits the size of the entering beam. This element is the aperture stop.
- Define a beam with arbitrary angle through the center of the aperture stop. This beam is called principal ray.
- The position where the principal ray intersects the optical axis on the image side is the position of the exit pupil.
- The intersection point with the optical axis on the object side defines the position of the entrance pupil. If the aperture stop is located before the first lens of the system (seen in direction of beam propagation), then the entrance pupil coincides with the aperture stop position.

The uniqueness of the pupil planes is, that their position is (to first order) independent of the beam angle through the center of the aperture stop. A rotation of an on-axis-beam at e.g. the entrance pupil tilts the beam at the aperture stop and exit pupil but does not cause a beam walk on these planes. It was suggested to use this principle for the LISA test mass interferometer in the following way:

Position the test mass in the entrance pupil of the imaging system and a photodiode in the exit pupil. Test mass rotation does then not cause beam walk on the photodiode. Such a system is then called a **pupil plane imaging system**.

## 10. Imaging optics

The term ‘pupil plane imaging’ is thereby defined for geometrical optics. It is necessary to translate this term, before it can be used in a Gaussian system.

The definition of pupil planes is based on the existence of an aperture stop. Gaussian beams are in principle of infinite extent like the plane waves assumed in geometrical optics. However, their profile suggests to consider them as finite and use the spot size  $w(z)$  as a measure for the finite size. All components on the optical bench are chosen carefully to be sufficiently large in comparison to the spot size, such that clipping can be neglected. It shall thus not be assumed, that any mirror, beam splitter or lens on the optical bench acts as aperture stop. The definition of pupil plane imaging in Gaussian optics is therefore chosen by complete disregard of an aperture stop. Instead the property of a classical pupil plane imaging system is used for a definition:

A system, where a rotation of the object (test mass) does not cause beam walk on the detector (QPD) is a **(Gaussian) pupil plane imaging system**.

Since beam walk is measured by the DC signal, the defining characteristics of a pupil plane imaging system is a zero line in a DC signal versus beam tilt graph.

The primary design goal is the decoupling of test mass rotation into the pathlength signal, not into the DC signal. That pupil plane imaging systems also fulfill the primary design goal is not obvious and needs to be shown. A general proof is extensive and time-consuming. Therefore, this property was tested on a variety of systems and is shown here in section 10.3 for one selected example.

### **Aberration (criterion B)**

It is not immediately clear how aberration will be sensed in the interferometer signals. If aberration intensifies the cross coupling of test mass tilts into the pathlength readout, then aberration needs to be avoided. However, this constraint is then already included in the primary design goal. For an investigation how aberration changes the interferometer signals, a comparison of systems with aspheric lenses or achromatic lenses to spherical lenses would be needed. In neither of the available software tools for signal generation: IfoCad or OptoCad & QPD.c is a definition of these lens types implemented yet. Therefore the design of the imaging optics is done with spherical lenses only.

### **Astronomical telescope design (criterion C, C07 and C08)**

An astronomical telescope images a collimated beam onto a collimated beam and has an intermediate focus as shown in figure 10.3. It consists of two spherical lenses separated by the sum of their focal lengths. Thereby, the secondary focus ( $F1^b$ ) of the first lens coincides with the primary focal point of the second lens ( $F1^f$ ).

The intermediate focus was suggested because it allows the use of a field stop to filter stray light. Furthermore, this criterion states that the beam impinging on the photodiode shall be collimated. The advantage of collimated beams impinging on the



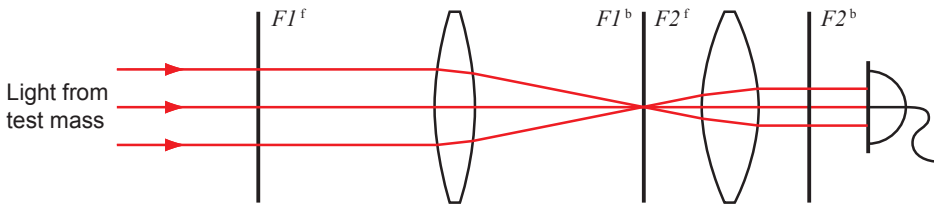


**Figure 10.3.:** Beam compressor with astronomical telescope design.

photodiode is that the beam size varies little if the photodiode is slightly misplaced further up or down the beam path. Hence having collimated beams behind the imaging optics might ease positioning the photodiode. However, the position of the photodiode is precisely defined in a pupil plane imaging system and the photodiode needs to be positioned accurately to the exit pupil. Criterion C is thus rated as inappropriate criterion for the design of the imaging optics. If a lens system can be found that has a focusing or diverging outgoing beam, but fulfills the primary design goal as well as the constraints and is sufficiently stable in performance against realistic misalignment, then this system can be used.

## 10.3. Simulating a pupil plane imaging system

In the subsequent sections it is shown for one example that a pupil plane imaging system fulfills the primary design goal: it decouples the longitudinal readout from test mass angular jitter. This system was designed as astronomical telescope, such that the distance between the lenses (defined from vertex to vertex) is the sum of the back focal length of the first lens (L1) and the front focal length of the second lens (L2):

$$d_{L1 \rightarrow L2} = f1^b + f2^f . \quad (10.7)$$

### 10.3.1. Setting lens parameters for a simulation

Originally a compression factor of  $\kappa = 5$  was suggested (cf. section 10.2, p. 133). This compression factor was chosen for the validation, that pupil plane imaging systems fulfill the primary design goal. Furthermore it was decided to use lenses with focal lengths of

$$f1 \approx 5 \text{ cm} \quad \text{and} \quad f2 \approx 1 \text{ cm} . \quad (10.8)$$

These allow a compression factor of

$$\kappa = \frac{w1_0}{w2_0} = \frac{f1}{f2} \approx \frac{5 \text{ cm}}{1 \text{ cm}} \approx 5 , \quad (10.9)$$

and a rather small beam compressor size of

$$d_{L1 \rightarrow L2} \approx f1 + f2 \approx 6 \text{ cm} , \quad (10.10)$$

where  $w1_0$  is the beam waist before L1 and  $w2_0$  the beam waist behind L2. Originally, it was planned to validate the simulation results experimentally. For this experimental

## 10. Imaging optics

Lens	Catalogue no.	$f$ [mm]	$d$ [mm]	diameter [mm]	$R$ [mm]	$f^f$ [mm]
L1	G311203000	$f1 = 55.66$	$d1 = 4.2$	10.0	49.403	54.192
L2	G311209000	$f2 = 11.39$	$d2 = 4.0$	22.4	9.5780	9.9148

**Table 10.2.:** Specification of the lenses used for testing the performance of a pupil plane imaging system. The Catalogue no. refers to the Linos Catalogue [10]. Both lenses are spherical and made of fused silica ( $n = 1.44963$ ). Parameters:  $f$ : focal length,  $d$ : thickness,  $R$ : radius of curvature,  $f^f$ : front focal length. The radii of curvature  $R1, R2$  were taken from the catalogue embedded in WinLens [19] and the front focal lengths were computed with eq. (10.12).

validation, commercial off the shelf (COTS) lenses ought to be used to reduce costs. Therefore, exact specifications were chosen according to the Linos lens catalogue [10]. The specifications of the two chosen spherical fused silica lenses are listed in table 10.2.

In order to place the test mass and photodiode in the focal points of the two thick lenses  $L1$  and  $L2$ , it is necessary to know the position of these focal points. At the time where the simulations were performed, OptoCad had no routines implemented to compute these positions. Therefore it was necessary to compute the location of these focal points.

For thin lenses the focal points are of course located a focal length away from the center of the lens, such that

$$f^f = f - \frac{d}{2} \quad (10.11)$$

where  $d$  is the thickness of the lens and  $f^f$  the front focal length (cf. figure 10.4), that means the distance of the focal point to the vertex of the lens surface. The lenses L1 and L2 are implemented in the simulations as perfectly symmetric lenses. Therefore the front focal length is identical to the so-called back focal length  $f^b$ , the distance from secondary vertex of the lens to the back focal point  $F^b$ . Both are therefore computed with the same equations.

The thin lens approximation is not sufficient for the given lenses and the equations for thick lenses need to be used. For thick lenses the focal point is positioned in the focal length measured from the principal planes (cf. figure 10.4). Since the front and back focal lengths  $f^f$  and  $f^b$  were not given by the manufacturer, they were computed according to [Hecht] and [Smith]

$$f^b \equiv f^f = f - \frac{f(n-1)d}{Rn}, \quad (10.12)$$

using the focal length  $f$ , refractive index  $n$  and radius of curvature  $R$  of the symmetric lenses: The radius of curvature of L1 and L2 was found using the catalogue information in WinLens [19]. The resulting values for  $f^f$  and  $f^b$  are listed in table 10.2.

### 10.3.2. Setting up a simulation for pupil plane imaging

Once all lens parameters were known, four setups were generated to investigate, whether a pupil plane imaging system does fulfill the primary design goal and decouples

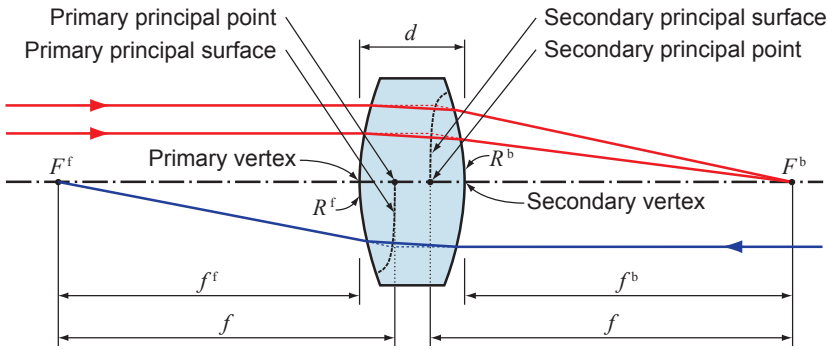


**Figure 10.4.:** Properties of a thick lens. Shown are the primary and secondary focal points, focal lengths, principal points and planes, front and back focal lengths.

the pathlength signal from test mass angular jitter. These four setups were thus implemented in the interface part of the LTP-OBI-Alignment Simulation (cf. chapter 6) and the signals for varying test mass angles were computed.

### The pupil plane imaging system: Setup D

This setup is the pupil plane imaging system and was designed according to the following set of rules:

- **DR1:** distance between L1 and L2  $d_{L1 \rightarrow L2} = f1^b + f2^f$  (cf. eq. (10.7))
- **DR2:** position of test mass: front focal point of L1 ( $F1^f$ )
- **DR3:** position of QPD: back focal point of L2 ( $F2^b$ )

and a summary of all its properties is listed in table 10.3. Design rule DR1 defines the astronomical telescope design, DR2 and DR3 in combination with DR1 result in a pupil plane imaging system. However, DR2 indicates that design criterion C03 is violated, since the distance between test mass and L1 is approximately 55 mm and not 425 mm as required. However, it is not possible to adapt Setup D to fulfill design criterion C03, as discussed briefly in section 10.3.4. However, it is not necessary that Setup D fulfills all length constraints, since it is used solely to investigate the general performance of a pupil plane imaging system.

Apart from that, setup D fulfills design criteria 4 to 13 (cf. table 10.1), such that for instance the beam waist is located on the test mass. In a perfectly aligned system, this would result in an imaged beam waist position on the QPD, as shown in appendix B.4. As shown in table 10.3, the waist of both beams is approximately 166 nm away from the photodiode. This means the lenses were sufficiently well (even though not perfectly) positioned.

In summary, Setup D is thus a pupil plane imaging system with astronomical telescope which images a waist on the TM to a waist on the QPD.

### Reference systems: Setup B and C

These two setups are reference setups and therefore not pupil plane imaging systems. Both systems have the properties DR2 and DR3 and were chosen to fulfill requirement C03 such that the distance between test mass and lens 1 was set to 425 mm. The waist was placed on the test mass and the photodiode was positioned in the imaged waist. The separation of the two lenses was approximately  $f1^b + f2^b = 64.1$  mm, the distance used for Setup D. Therefore Setup B and C have mainly the same settings as Setup D, except for the large distance between test mass and the first lens.

The main difference between Setup B and C is the slightly different distance between the two lenses and the resulting photodiode positions. In geometrical optics there exists exactly one lens separation in an astronomical telescope, which results in a collimated beam. However, this is different in Gaussian optics, since the term “collimated” is defined more broadly: In geometrical optics a collimated beam is a plane wave with focus at infinity. Gaussian beams fulfill this criterion only in one single point: the waist. However, the spreading near the waist can be neglected, such that a Gaussian beam is said to be collimated for all points within a Rayleigh range. A large Rayleigh range corresponds to small divergence, such that it can also be said, that a Gaussian beam is collimated if it has small divergency. This definition results in a margin for setting the lens separation. Setup B and C were found by varying the lens separation in finite steps and monitoring the position of the imaged waist. Setup B has approximately the minimal eye relief (criterion C05 in table 10.1), with a lens separation of 64.2 mm. Setup C was found by increasing the lens separation by another 100  $\mu\text{m}$ . Here the beam compressor size reaches the maximal value of  $64.4 + 17.7 = 82$  mm (criterion C04 in table 10.1).

### Reference Setup A

The values chosen for Setup A have historical reasons: it was used as a test setup, before the back and front focal lengths of L1 and L2 were known. However, Setup A is in fact a misaligned version of Setup B and C. Even though it is still a 5:1 relay like Setup B, C and D, the misalignment results in a diverging beam on the QPD. The beam compressor in Setup A is thus not an astronomical telescope. Furthermore, the waist is shifted off the QPD, such that Setup A is no waist imaging system. Therefore, Setup A is a reference to Setup B and C.

### 10.3.3. Results: pupil plane imaging

All results for Setup A to C are shown in figure 10.5, the results for Setup D are shown in figure 10.6. The separation into two figures results from the large difference in the results.

A comparison of figure 10.6(a) and 10.6(b) to figure 10.5(a) and 10.5(b) shows that Setup D decouples sufficiently the pathlength readout from test mass tilts, while none of the reference setups shows this property. Setup D has a residual coupling of 0.8 pm/ $\mu\text{rad}$ , which is below the required value of 3.2 pm/ $\mu\text{rad}$ . The reference systems show coupling in the order of up to 300 nm/ $\mu\text{rad}$ .

Parameter	Setup A	Setup B	Setup C	Setup D
distance TM→ L1 [mm]	425.000	425.00	425.00	$f1^f$
distance L1→ L2 [mm]	$f1 + f2$	64.2	64.3	$f1^b + f2^f$
distance L2→ PD [mm]	$f2$	5.65	17.76	$f2^b$
waist position	TM	TM, PD	TM, PD	TM, PD
compression ratio	5:1	5:1	5:1	5:1
<b>measurement beam parameter on TM</b>				
beam radius $w_M^{TM}$ [mm]	1	1	1	1
radius of waist $w_{0,M}^{TM}$ [mm]	1	1	1	1
Rayleigh range $z_{0,M}^{TM}$ [m]	2.95	2.95	2.95	2.95
distance $w_0 \rightarrow$ TM $z_M^{TM}$ [m]	0	0	0	0
<b>measurement beam parameter on PD</b>				
beam radius $w_M^{PD}$ [ $\mu$ m]	199.6	206.1	205.8	204.6
radius of waist $w_{0,M}^{PD}$ [ $\mu$ m]	71	206.1	205.8	204.6
rayleigh range $z_{0,M}^{PD}$ [mm]	14.9	125.4	125.1	123.64
distance $w_0 \rightarrow$ PD $z_M^{PD}$ [ $\mu$ m]	$-39.1 \cdot 10^3$	0	0	-0.166
<b>reference beam parameter on PD</b>				
beam radius $w_R^{PD}$ [ $\mu$ m]	199.7	206.1	205.8	204.6
radius of waist $w_{0,R}^{PD}$ [ $\mu$ m]	71	206.1	205.8	204.6
rayleigh range $z_{0,R}^{PD}$ [mm]	14.9	125.4	125.1	123.64
distance $w_0 \rightarrow$ PD $z_R^{PD}$ [ $\mu$ m]	$-39.1 \cdot 10^3$	-152	143	-0.166
<b>fulfilled design criteria</b>	3-13	3-13	3-13	4-13

**Table 10.3.:** Settings for waist to waist imaging in the simulation. For all four setups the lenses  $L1$  and  $L2$  with specifications listed in table 10.2 are used. The focal length  $f1$  and  $f2$  as well as the front and back focal length  $f1^f$ ,  $f2^f$ ,  $f1^b$  and  $f2^b$  also refer to table 10.2. The listed fulfilled design criteria refer to table 10.1. Of course it is task of the simulation to show which of the setups fulfills criterion C01 and C02. Therefore they are not listed as fulfilled here. Setup 4 does not fulfill criterion C03, the length constraint for the distance between TM and L1 of 425 mm. This is discussed in section 10.3.2.

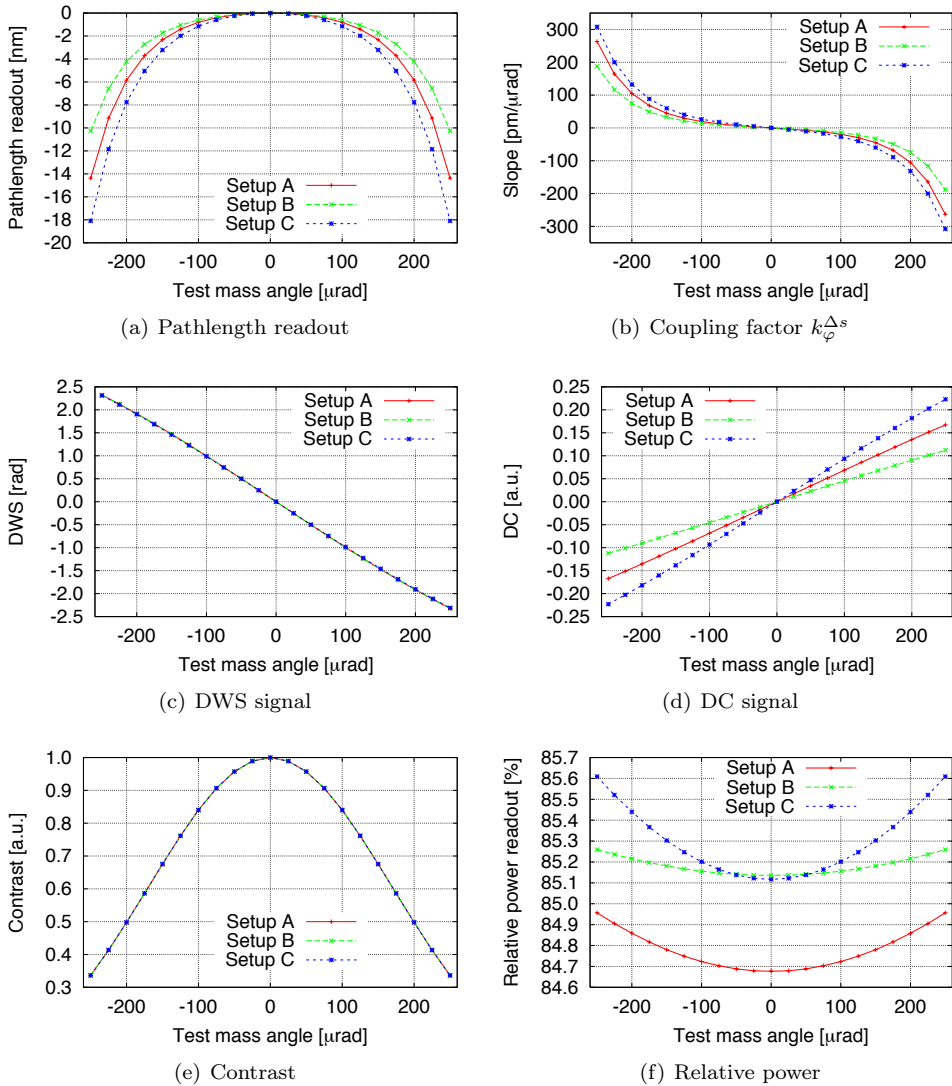


**Figure 10.5.:** Signals of Setup A - C. The pathlength signal (a) for all three setups is in the nanometer range and thus very large. The corresponding coupling factor (b) is of the order of a few hundred pm/ $\mu$ rad and exceeds thereby the required 3.2 pm/ $\mu$ rad. The DWS signal (c) is linear in the complete range and identical for all three setups. The slope (coupling factor) of  $-10^4$  rad<sup>DWS</sup>/rad is a value that provides good angular readout. The DC signal (d) shows beam walk on the QPD which can also be seen in the detected power (f). All systems show a contrast decay (e) to approximately 0.3 at the maximal test mass angle of 250  $\mu$ rad.

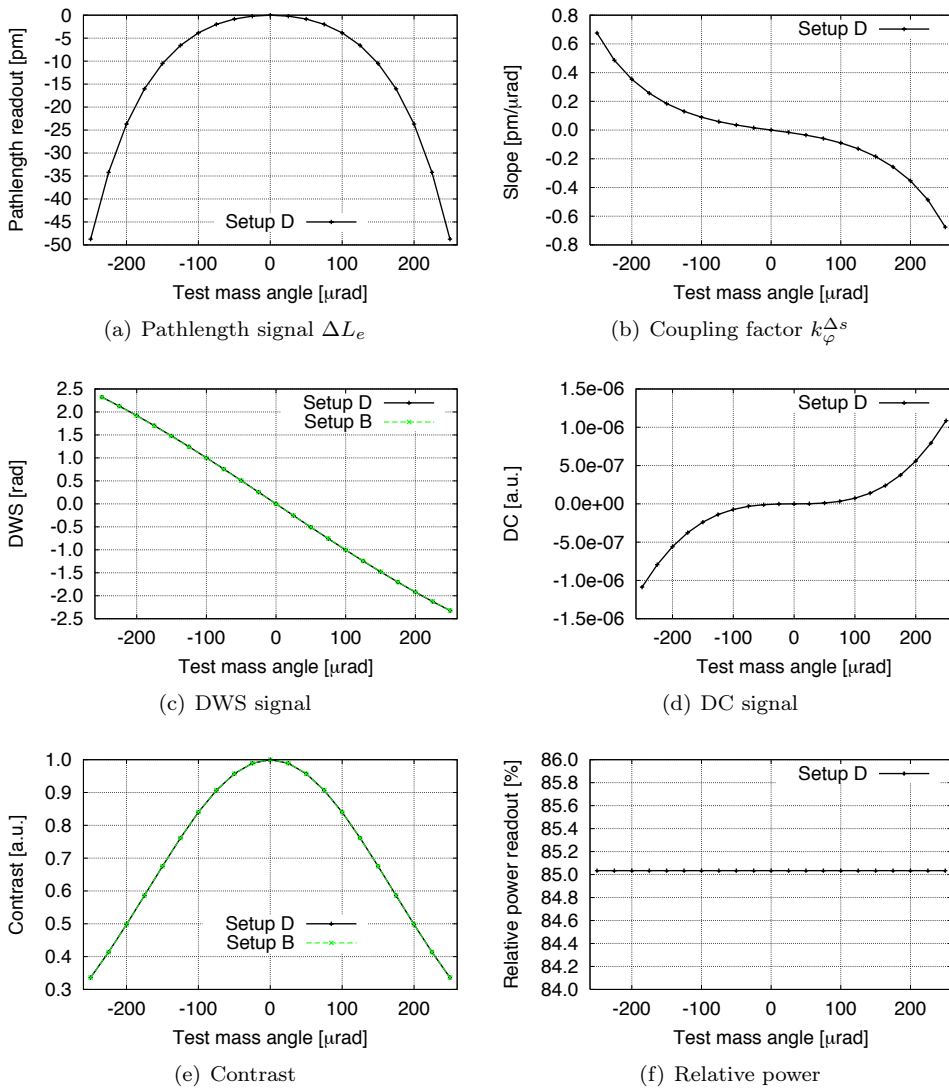


**Figure 10.6.:** Signals of Setup D. The pathlength signal (a) is in the picometer range and thus much smaller than for Setups A-C even though the same lenses were used and only distances between the components were changed. The corresponding coupling factor (b) is below  $1 \text{ pm}/\mu\text{rad}$ . Setup D fulfills thereby the slope requirement of  $3.2 \text{ pm}/\mu\text{rad}$  and provides sufficient decoupling of test mass tilt to the length measurement.

The DWS signal (c) is identical to the DWS signals of Setups A-C and thus linear in the complete range with the coupling factor of  $-10^4 \text{ rad}^{\text{DWS}}/\text{rad}$ .

The DC signal (d) shows almost no beam walk on the QPD which results in a constant detected power (f) for all test mass angles. The contrast decay (e) is the same as for Setup A-C. This is a known effect, since the same lenses were used for all four setups.

The DWS signal shown in figure 10.6(c) and 10.5(c) is identical in all four setups. It is linear in the whole range of test mass angles and has a slope of  $-10^4 \text{ rad}^{\text{DWS}}/\text{rad}$ . These properties are suitable for an angular readout.

The DC signal is a measure of the beam shift on the QPD. Figure 10.5(d) shows beam walk on the QPD which results from test mass rotation. This beam walk is just as designed, since these systems were built to be no pupil plane imaging systems. The slopes are  $689 \text{ rad}^{-1}$ ,  $454 \text{ rad}^{-1}$  and  $941 \text{ rad}^{-1}$  for Setup A, B and C respectively. Figure 10.6(d) shows a residual beam walk in Setup D which might originate from aberration. However, the amount of beam walk is very small and the curve can be regarded as zero - the system is indeed a pupil plane imaging system.

The contrast of all four setups is identical, as shown in figure 10.5(e) and 10.6(e). At the maximal TM angle of  $\pm 250 \mu\text{rad}$  the contrast drops to 0.3. In TN 6 [LOB-06] it is described, that the pointing range of  $\pm 250 \mu\text{rad}$  is limited by loss of heterodyne efficiency. That means the low contrast is an expected value. It is remarkable, that all four setups show identical contrast-functions, even though Setup A to C have beam walk (and thus lateral displacement between measurement and reference beam), while Setup D does not. However, contrast loss for larger angles is also expected for Setup D, because the measurement beam is tilted with respect to the reference beam, which causes fringes in the interference pattern and contrast loss.

Finally, figure 10.5(f) and 10.6(f) show the power sensed by the QPD normalized to the incident beam power. For Setup A to C, the sensed beam power varies with varying test mass angle. This results from the described beam walk over the insensitive slit of the QPD: if the beam is shifted off the insensitive slit, the sensed power increases. For Setup D the curve is flat, since there is only a negligible amount of beam walk due to test mass rotation. About 85% of the incident beam power is sensed by the QPD. The deviation from 100% is caused mainly by clipping at the insensitive slit. The small difference in sensed power of the four setups at nominal test mass angle results from small deviations in the beam sizes.

### 10.3.4. Adaptability of Setup D for the test mass interferometer

The shown pupil plane imaging system (Setup D) violates design criterion C03 by having a distance between TM and L1 of approximately 54 mm instead of the required 425 mm. A straight forward adaptation of Setup D to correct the distance between TM and L1 to 425 mm is using lenses with focal lengths of 425 mm and 85 mm or 140 mm for a 5:1 or 3:1 relay respectively. However, this would result in a very large beam compressor size that could not be embedded in the LISA OBI.

Alternatively, it is possible to shift the test mass further away from the first lens, the exit pupil will then move closer to L2. In case of Setup D, setting the distance between test mass and L1 to 425 mm results however in a virtual exit pupil, that means the exit pupil is located between L1 and L2 and is thereby not accessible. It is thus not possible to adapt Setup D to design criterion C03.



### 10.3.5. Conclusions on pupil plane imaging

- The pupil plane imaging system (Setup D) has small coupling of test mass rotation into pathlength noise. The coupling factor is less than  $1 \text{ pm}/\mu\text{rad}$ . It fulfills thereby the primary design criterion C01.
- The performance of Setup D originates from the property that it is a pupil plane imaging system, since none of the reference setups achieves decoupling the pathlength signal from test mass angular jitter. This means in particular, waist to waist imaging (Setup B and C) is no criterion to achieve the desired decoupling.
- The shown pupil plane imaging system (Setup D) cannot be used for the LISA optical bench, because it does not fulfill the constraint for the distance between TM and L1. It was shown, that this system cannot be adapted to fulfill this constraint. Mainly there are two options for further proceeding: either the number of lenses is increased, which reduces the size of the system but makes it more complicated, or one of the minor design criteria is relinquished. One system for each option is investigated in the subsequent sections.

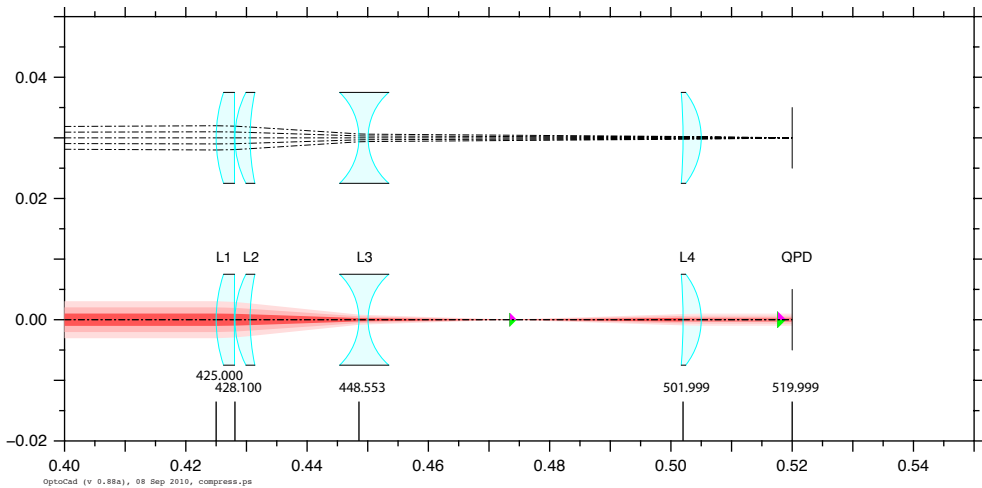
## 10.4. New beam compressors: ASD-4L and AEI-D003

When the results of the previous sections were known, new beam compressors with compression ratio of 3:1 instead of 5:1 were investigated. ASD presented a new beam compressor design in March 2010. This design is a 3:1 relay with 4 spherical lenses, an entrance pupil of 425 mm, an exit pupil of 15 mm and a length (distance first surface first lens to second surface of fourth lens) of approximately 8 cm (cf. figure 10.7(a)). The design details are listed in table C.3.

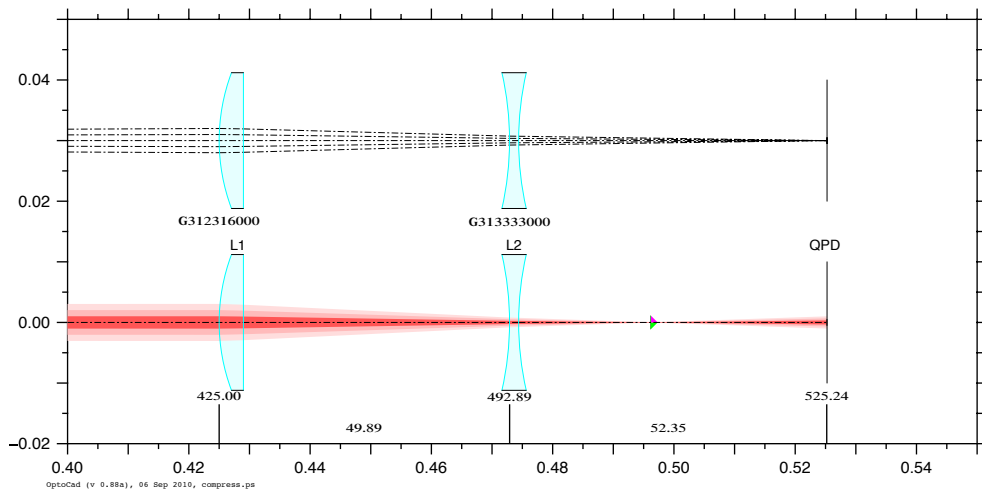
In parallel, Gerhard Heinzl searched for new beam compressors with two spherical lenses and no beam walk caused by test mass rotation (pupil plane imaging systems). The computed 3:1 relay is referred to as beam compressor D003 and shown in figure 10.7(b) as ray-tracing result with dashed black lines and Gaussian beam propagation showing a waist between L2 and the QPD indicated by the purple and green triangle. Detailed system specifications are listed in table C.4.

D003 was generated in disregard of criterion C07 and C08, such that it has diverging beams impinging on the QPD and no focus between L1 and L2. However, D003 has a focus between L2 and the QPD which still allows the use of a diaphragm to reduce stray light and there is no clear evidence for the need of collimated beams, as already discussed in section 10.2. This design was the solution with least cross coupling of test mass angular jitter into pathlength readout in an IfoCad simulation which combined any two spherical Linos COTS lenses from arbitrary material (for instance BK7 or fused silica) and shape. That means the presented solution shows least cross coupling of all combinations of two spherical Linos lenses.

## 10. Imaging optics



(a) ASD beam compressor



(b) AEI beam compressor D003

**Figure 10.7.:** ASD design of a beam compressor with four spherical lenses and AEI beam compressor design D003 with two spherical lenses. Each setup is plotted twice. The upper graph shows the ray tracing result (black dashed lines) for 5 beams starting with different angles in the origin. The lower graph shows the Gaussian beam propagation result including the waist position for the tangential (green) and sagittal (magenta) plane. All four lenses in the ASD design are custom made. Their diameter was set to 15 mm for convenience. The lenses in D003 are commercial off the shelf (COTS) lenses. The number above L1 and L2 is the Linos catalogue number of these lenses [10]. The straight line indicates the QPD position.

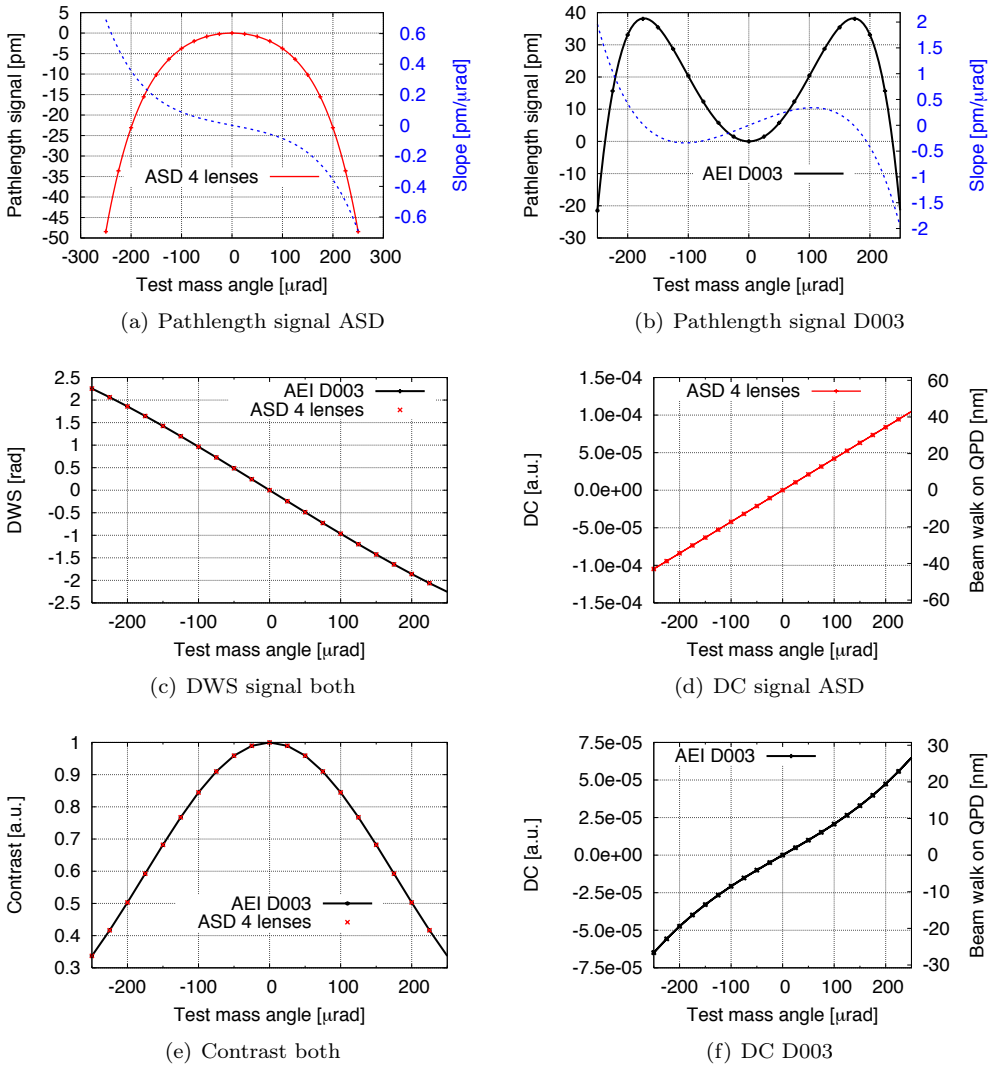


**Figure 10.8.:** Performance of the ASD beam compressor design with four spherical lenses and the AEI beam compressor D003 with two spherical lenses. Both systems fulfill the primary design goal by showing a residual coupling of angular motion to pathlength readout by less than  $3.2 \text{ pm}/\mu\text{rad}$ . Both systems have identical DWS and contrast curves. The DC signals of both beam compressors are plotted together with the causative beam walk. Both lens systems have a residual beam walk of the order of a few tens of nanometers.

### 10.4.1. Nominal signals

Both designs were analyzed with OptoCad and QPD.c. The resulting graphs are shown in figure 10.8. In this figure, all resulting graphs for the ASD four lens beam compressor are shown in red, those of the 2 lens beam compressor D003 are shown in black.

Figure 10.8(a) and 10.8(b) show the pathlength signal of both systems. The pathlength signal of the ASD-4 lens design appears to be a parabola, but is indeed a fourth order function with just one maximum. The two lens system D003 is an “M-shaped” fourth order function. Both curves were fitted and the derivative of the resulting function was computed. This derivative (shown in blue) shows the coupling of test mass angular motion into the pathlength readout. This coupling is of the order of  $0.6 \text{ pm}/\mu\text{rad}$  for the ASD beam compressor and  $2 \text{ pm}/\mu\text{rad}$  for the D003. Thereby, both beam compressors show sufficient decoupling of pathlength readout and test mass angular motion for nominal alignment.

The DWS (figure 10.8(c)) and contrast curves (figure 10.8(e)) of both lens systems coincide. This probably results from the comparable beam sizes and angles on the QPD. However, this effect is not yet fully understood.

In figure 10.8(d) and 10.8(f) the DC signal and causative beam walk are plotted. Both systems show a residual beam walk of the order of a few tens of nanometers. The coupling factor between DC and beam walk is for both setups  $-2437 \text{ m}^{-1}$ . It is known, that the DC signal depends solely on the spot size on the QPD and photodiode parameters (form, diameter and slit size). It is therefore reasonable, that this value is valid for both systems, since they have the same compression factor and therefore identical beam sizes on the QPD.

### 10.4.2. Tolerance analyses

The aim of the tolerance analyses is to investigate whether the beam compressors tolerate misalignments typical for a laboratory assembly. The main questions to be answered are therefore:

- Is it feasible to built either beam compressor and achieve the primary design goal even though the system is slightly misaligned?
- By what amount can each degree of freedom be misaligned, such that the primary design goal is still achieved?

The most simple way to answer these question is to vary one variable at a time until the coupling violates the required value of  $3.2 \text{ pm}/\mu\text{rad}$ . This was performed and the resulting maximal tolerable displacements are summarized in table 10.4. Listed are the maximal and minimal displacement of each component before the slope criterion is violated. “Lateral” is defined here as orthogonal to the direction of propagation. Since all components are rotational symmetric this value is assumed to be valid for both orthogonal directions: out of plane and in plane orthogonal to the direction of

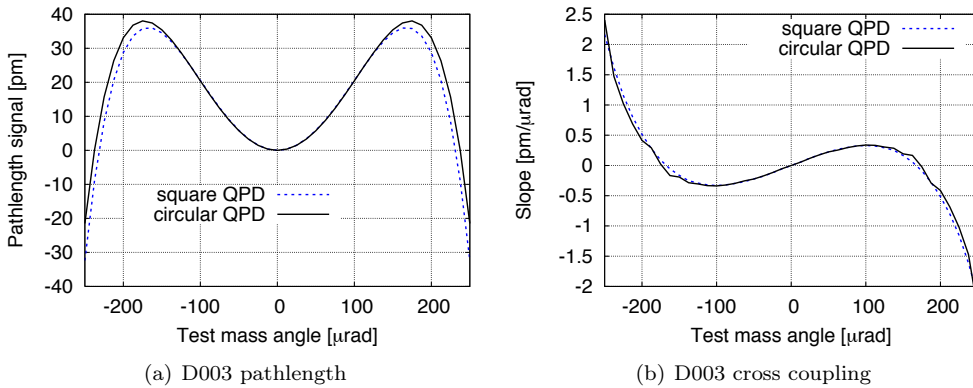


**Figure 10.9.:** Beam compressor D003: comparison of pathlength signal and numerically computed coupling of angular test mass motion into the pathlength readout. The results deviate slightly. However the numerical integrator in QPD.c converges for square QPDs in a fraction of the time it needs for circular QPDs. Furthermore numerical precision problems occur for circular QPDs. It is thus convenient to work with square QPDs.

<b>D003</b>	longitudinal shift	lateral shift	lateral realigned
L1	-73.1 ... 365.3 $\mu\text{m}$	$\pm 0.115 \mu\text{m}$	$\pm 47.0 \mu\text{m}$
L2	-485.4 ... 96.6 $\mu\text{m}$	$\pm 0.270 \mu\text{m}$	$\pm 285 \mu\text{m}$
QPD	-1293.3 ... 261 $\mu\text{m}$	$\pm 0.250 \mu\text{m}$	–
ref. beam	<b>-2.920 ... 15.10 mm</b>	$\pm 0.600 \mu\text{m}$	–
c.m. waist	-0.926 .. 1.176 m	–	$\pm 56.5 \mu\text{m}$
<b>ASD</b>			
L1	-117.5 ... 98.5 $\mu\text{m}$	$\pm 0.227 \mu\text{m}$	$\pm 42.0 \mu\text{m}$
L2	-41.5 ... 64.0 $\mu\text{m}$	$\pm 0.276 \mu\text{m}$	$\pm 150 \mu\text{m}$
L3	-47.5 ... 31 $\mu\text{m}$	$\pm 0.152 \mu\text{m}$	$\pm 28.5 \mu\text{m}$
L4	-852.4 ... 1410.8 $\mu\text{m}$	$\pm 1.252 \mu\text{m}$	$\pm 190 \mu\text{m}$
QPD	-987.2 ... 625.9 $\mu\text{m}$	$\pm 0.598 \mu\text{m}$	–
ref. beam	<b>-7 ... 11.2 mm</b>	$\pm 1.468 \mu\text{m}$	–
c.m. waist	-2.505 ... 2.502 m	–	$\pm 2.53 \text{ mm}$

**Table 10.4.:** Maximal tolerable displacement of the various components of the ASD and D003 beam compressors. The column “lateral realigned” shows the maximal tolerable displacement of each component in lateral direction, if the QPD is re-centered to the measurement beam at nominal angle. The corresponding graphs (figure D.5 and D.6) show therefore DC=0 at nominal test mass angle. The line “ref. beam” shows by how much the waist of the reference beam can be shifted, before the slope requirement is violated. The line “c.m. waist” shows the corresponding results for a simultaneous shift of both waists. The corresponding graphs are shown in figure D.1 – D.10.

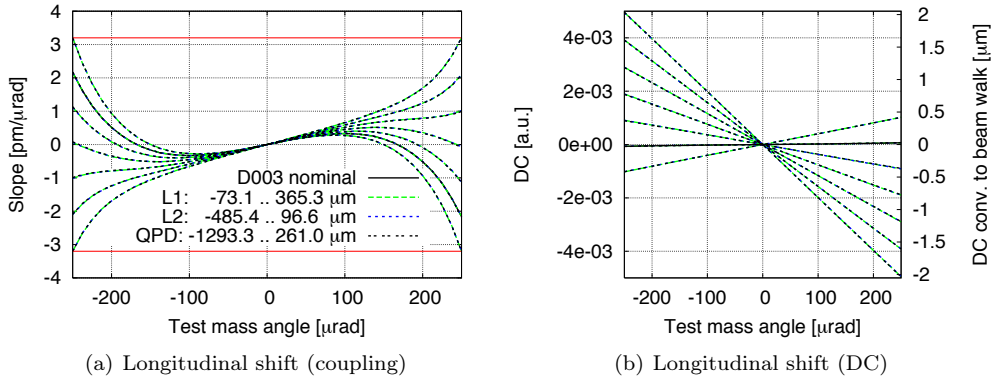


**Figure 10.10.:** Beam compressor D003 signals if one component is shifted in longitudinal direction in equidistant steps. (a) Residual coupling of test mass angular jitter into the pathlength readout shown in comparison to the slope requirement of  $3.2 \text{ pm}/\mu\text{rad}$ . (b) Corresponding DC signal, which shows that the nominal curve (solid black line) is a pupil plane imaging system even though it does not show the least amount of residual coupling.

propagation. The accompanying graphs are shown in appendix D figures D.1 – D.10. For all simulations regarding tolerances, square QPDs were used instead of circular QPDs to reduce the computer runtime. This can be done, since the deviations between the signals of square and circular QPDs are small, as shown in figure 10.9 for the nominal beam compressor D003.

### Longitudinal misalignment

Both beam compressors are sufficiently tolerable against longitudinal misalignment of the various components, as shown in table 10.4. Each lens can be displaced by at least a few tens of micrometers with respect to their nominal position. Noticeable is the asymmetry in the longitudinal displacements. This is explained by the corresponding signals shown in figure 10.10 or figure D.1 and D.2. In the D003 signals (figure 10.10(a)) one can see that the nominal signals (drawn as black solid line) is not optimal, even though this nominal setup is the actual pupil plane imaging system and does not show beam walk (cf. figure 10.10(b)). The optimal setup of beam compressor D003 has residual beam walk of the order of  $750 \text{ nm}$  at a test mass tilt angle of  $250 \mu\text{rad}$ . This setup shows a residual coupling of test mass angular motion into the pathlength signal of the order of  $0.5 \text{ pm}/\mu\text{rad}$ . It is remarkable that it is indistinguishable from the signals which component was shifted longitudinally. The optimal system can thus be found by shifting either L1, L2 or the QPD (but each by a different amount).

**ASD beam compressor: L1 longitudinal displacement** The reason, why the curves for longitudinal L1 displacement do not match all other curves is, that L1 cannot be shifted until the slope reaches the maximal value of  $3.2 \text{ pm}/\mu\text{rad}$ . The distance between L1 and L2 is nominally only  $100 \mu\text{m}$  and the slope reaches only roughly  $\pm 1.5 \text{ pm}/\mu\text{rad}$  when both lenses touch another. The curves are then equally spread between  $-3.2 \text{ pm}/\mu\text{rad}$  and  $1.5 \text{ pm}/\mu\text{rad}$ . This different distribution causes the mismatched graphs.

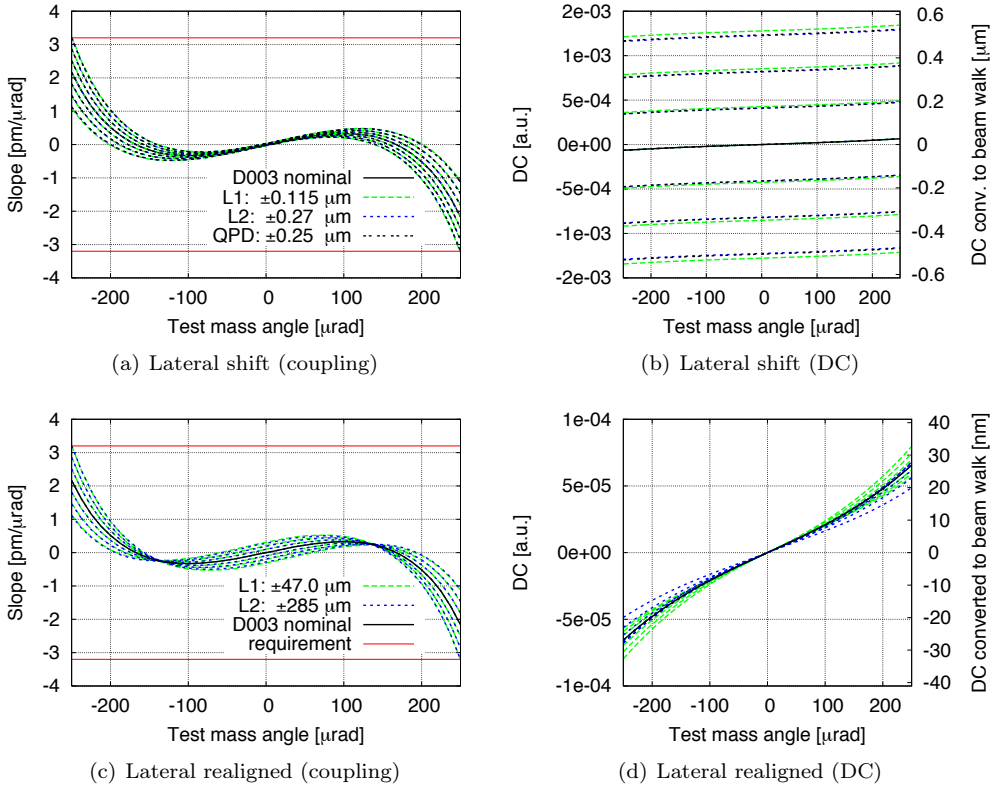


**Figure 10.11.:** Beam compressor D003: Residual coupling and DC signal for lateral displacement of either L1, L2 or the QPD. Subfigures (a) and (b): Each component was shifted in seven equidistant steps, while all other components remained untouched. Subfigures (c) and (d): After each displacement of L1 or L2, the QPD was realigned to the reference beam. The DC signal is therefore zero for normal beam incidence.

### Lateral misalignment

There are two columns for lateral misalignment shown in table 10.4: “lateral shift” with critical values and “lateral realigned” with moderate results. The column labeled “lateral shift” shows the maximal tolerable lateral displacement of each component, before the slope requirement is violated. Solely one component was shifted at a time and in particular the QPD position stayed fixed. This results in very stringent alignment requirements. Since a lens displacement orthogonal to the incident beam results in a beam displacement on the QPD, the corresponding DC-curves in figure 10.11(b) show for each lens displacement a constant offset. In an experimental realization the QPD would naturally be realigned to the beam. This realignment was also simulated and the corresponding maximal lens displacements are shown in the column labeled “lateral realigned”. These results are less critical: every lens can be displaced laterally by a few tens of micrometer. As a result of the realignment of the QPD, the corresponding DC-graphs in figure 10.11(d) (and figure D.6 for ASD-4 lens design results) show no

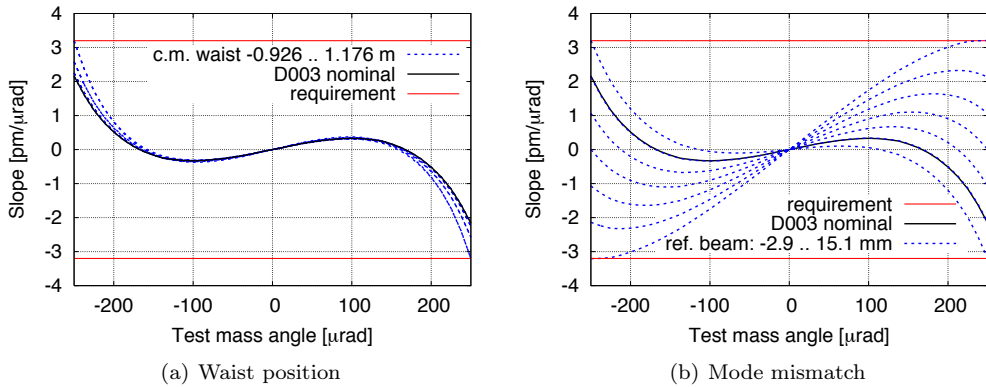


**Figure 10.12.:** Beam compressor D003: impact of waist position. (a) Both beam waists are shifted simultaneously in longitudinal direction. The system tolerates beam waist displacements in the order of one third of the Rayleigh range, which is 3 m. It is therefore not necessary to place the waist of the measurement beam on the test mass, which shows that design criterion C09 is not necessary. (b) The reference beam is shifted in longitudinal direction while the beam parameters of the reference beam remain unchanged. This causes a mode mismatch which results in an increased cross coupling.

beam walk for nominal test mass angle. The only critical item for lateral displacement is the QPD itself. It needs to be aligned to the (coaligned) beams by  $\pm 0.25 \mu\text{m}$  in D003 and roughly  $\pm 0.6 \mu\text{m}$  in the ASD four lens beam compressor. This degree of alignment is not achievable with the alignment techniques presented in section 5.3.1. If an alignment to such a high degree is required, that means if it was planned to use either of the here described beam compressors and no DWS-correction, then this alignment goal might be feasible by using piezo-mounted QPD-chips and control the QPD positions with DC signal feedback loops. However, such a delicate solution should be avoided.

**Beam parameters** For both beam compressors, the waist of the measurement beam is on the test mass and the reference beam is mode matched to the measurement beam. This was chosen according to design criterion C09 in order to provide a beam locally similar to a plane wave. This criterion was investigated by shifting the waist of both beams simultaneously away from the test mass, until the slope requirement was violated. The results are listed in table 10.4 in the line “c.m. waist” (common mode waist displacement). It was found that a shift of the order of  $\pm 1$  m (one third of the Rayleigh range) can be tolerated for D003 as shown in figure 10.12(a) and  $\pm 2.5$  m (0.83 Rayleigh range) for the ASD beam compressor. **This shows that it is not necessary to place the waist of the measurement beam on the test mass, provided that the beams are mode matched and that the beams entering the lens system are collimated.**

This is an anticipated result: both beam compressors were designed with classical optics and ray tracing. That means it is expected that the waist position of both beams (as long as they are mode matched) is initially arbitrary, given that the beam is collimated when entering the lens system.



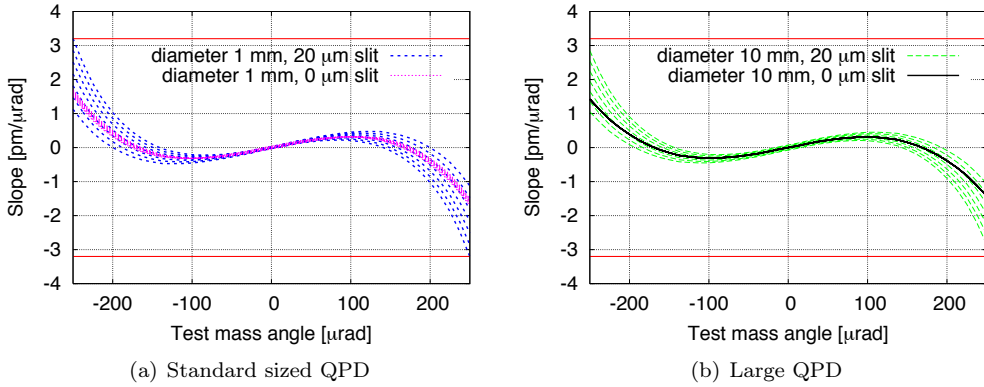


**Figure 10.13.:** Comparison of photodiode types to investigate the origin of the stringent requirement for lateral QPD alignment. Like for figure 10.11(a) the QPD was shifted orthogonal to the impinging beam until the slope requirement was violated. Subfigure (a) shows a comparison of the signals of the standard QPD which has a diameter of 1 mm and a slit size of 20 μm in comparison to a QPD of the same size that has no slit. Subfigure (b) shows the same comparison for QPDs of 10 mm diameter. It can be seen that the cross coupling mainly originates from beam clipping effects at the insensitive slit which separates the quadrants of the QPD.

Mode matched waist displacements are uncritical, however mode mismatched waist displacements are rather critical as shown in figure 10.12(b). The full set of signals is shown in the appendix in figure D.9 and D.10. It was found that the maximal tolerable longitudinal displacement of the reference beam waist w.r.t. the measurement waist is of the order of  $\pm 9$  mm in the optimal D003 and ASD beam compressor setup ( $-3 \dots 15$  mm in the nominal D003 setup and  $-7 \dots 11$  mm in the nominal ASD setup).

**Remark: “beam walk” and “DC converted to beam walk”** In several DC-graphs, a secondary  $y$ -axis was drawn to estimate the corresponding beam walk. This axis was either labeled “beam walk” or “DC converted to beam walk”. In the first case, the beam walk was directly plotted but due to distinct scaling this curve matched the DC-curve such that only one curve is visible. In the “DC converted to beam walk” cases, the DC curves were scaled by  $-2437 \text{ m}^{-1}$ , the value stated in section 10.4.1. This results exactly in the right amount of beam walk, if the beam size on the QPD is nominal. Generally, the lens shifts performed during the tolerance analysis cause slight changes in the beam size on the QPD, such that this conversion is only roughly valid.

### 10.4.3. Cause of critical QPD alignment value

It was shown, that the alignment of the QPDs in both beam compressor designs is critical. The cause of the stringent alignment requirement is beam clipping:

It is indistinguishable, whether the QPD is misaligned to the impinging beam or vice versa. Shifting therefore the beam over an infinite single element photodiode (SEPD) does however not cause a change in the pathlength signal, since the propagated pathlength does not change and the entire beam is sensed by the photodiode. Since a finite QPD is used for the readout, there is always some amount of beam clipping

at the insensitive slit separating the quadrants and at the outer borders of the QPD. The beam segments which are clipped carry some amount of pathlength information, and this value is generally different for each infinitely small segment. If the beam is then shifted over the QPD, different beam segments are clipped and therefore different pathlength information is lost. Therefore, the sensed pathlength signal varies – even though the geometrical pathlength has not changed. Shifting a beam over a QPD, or equivalently, misaligning a QPD does therefore cause a non-zero pathlength signal which is caused by beam clipping.

This beam clipping effect was further investigated, to find the actual source: does the coupling mainly result from clipping at the insensitive slit or on the outer borders of the QPD? The simulation performed for the analyses of QPD lateral alignment in D003 was therefore repeated, but the QPD parameters were varied. The QPD lateral displacement was set as before to  $\pm 250$  nm in equidistant steps. Figure 10.13 shows the corresponding results for a standard sized QPD with and without slit (figure 10.13(a)) and a large QPD with and without slit (figure 10.13(b)). It can be seen that eliminating the insensitive slit in the standard sized (1 mm) QPD reduces the amount of coupling by a reasonable amount (figure 10.13(a)). The clipping at the outer borders of the QPD play only a minor role, as can be seen in figure 10.13(b), since the large 10 mm QPD with slit shows only little reduction of the residual coupling in comparison to the small 1 mm QPD.

It was initially expected, that beam clipping causes cross coupling in the pathlength readout. For this reason, the compression ratio of the beam compressors was set to 3:1 because this results in a balance between beam clipping at the outer borders and at the insensitive slit of the QPD (cf. section 10.2 and figure 10.1). These results suggest however a reinvestigation of an optimal compression factor, since beam clipping at the insensitive slit causes the critical requirement for lateral QPD alignment of sub-micrometer level. It is therefore expected that a smaller compression factor and therefore a larger beam size on the QPD results in a less stringent requirement for QPD lateral alignment – which is of course at the cost of more stray light.

### 10.4.4. Performance of D003 with experimentally realized beam parameters

The simulation work presented in this chapter is accompanied by a corresponding experiment, which shall verify the simulation results. This is a significant experiment, since generally not all results obtained from simulations can be verified by experiments - for instance simulations regarding free floating test masses cannot be verified on ground. It is therefore important to compare any results verifiable on ground to gain sufficient evidence for the reliability of the software tools.

It is not possible to achieve perfectly mode matched beams in an experimental setup. The beam parameters of the current laboratory setup of D003 are shown in figure 10.14: the waist of the measurement beam is 47 cm behind the test mass, the waist of the reference beam is 20 cm in front of the measurement beam waist. Furthermore, the size of the reference beam waist is 0.9 mm (design value is 1 mm). The OptoCad script was updated to the measured beam parameters and the signals were recomputed. The resulting signals are plotted in figure 10.15. The measurement setup also includes a

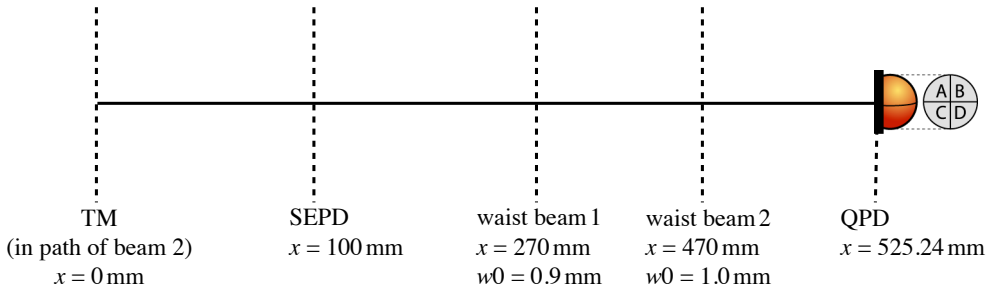


**Figure 10.14.:** Implementation of the experimental realization of D003 in OptoCad.

single element photodiode (SEPD) with a diameter of 5 mm. The signals of the SEPD were computed and are also shown in figure 10.15. The results can be summarized by:

- The slope requirement is expected to be violated by a factor of roughly 5.
- It is expected that the pathlength signals of QPD and SEPD almost match.
- The DWS signal is expected to be almost identical to the nominal D003 DWS signal. It shows a sign change if the beam compressor is taken out of the beam path. This is anticipated, since the imaging optics inverts the beam walk on the photodiode.
- The system without beam compressor shows considerably higher contrast (almost 80% at  $250 \mu\text{rad}$ ) than with beam compressor (roughly 35% at  $250 \mu\text{rad}$ ).

Nevertheless, these results need to be handled with care. The beam parameters used for these results are known only to a certain precision. A deviation of 20% for each parameter was assumed for a first comparison. A new simulation was performed where each beam parameter (waist size and position of reference and measurement beam) was **independently** varied in 7 steps by  $\pm 20\%$ . The resulting  $7^4 = 2401$  curves are shown in figure 10.16 (QPD results with beam compressor) and figure 10.17 (results for QPD with removed beam compressor). The beam compressor results show that a 20% deviation from the measured beam parameters has the following effects:

- The slope curves (coupling of TM angular motion into pathlength readout) show a large spreading, such that the residual coupling can take any value between roughly -200 and 250 pm/ $\mu\text{rad}$  at a TM angle of  $-250 \mu\text{rad}$ . It is thus possible to fulfill the required 3.2 pm/ $\mu\text{rad}$  residual coupling or just as well to violate the requirement by more than a factor of 75.
- The DWS curves show a small spreading, such that the DWS signal can take any value between approximately 1.7 and 2.5 rad at a TM angle of  $-250 \mu\text{rad}$ . It is therefore anticipated, that the DWS curves in simulation and experiment match.
- The DC curves show also a small spreading, such that it is anticipated, that the DC curves in experiment and simulation match.

- The contrast has a rather high spreading with a peak value between roughly 90 and 100% and a value of roughly 25 to 55% at a test mass angle of  $-250 \mu\text{rad}$ .

As discussed, all curves are computed for square-shaped photodiodes, to reduce the software runtime. In figure 10.16 and 10.17 nominal results with circular- and square-shaped QPDs are shown as reference. Figure 10.16 shows negligible effect of the shape of the QPD. However, the curves without lenses (figure 10.17) show a deviation of the results with circular or square-shaped QPDs. This deviation can be explained by the fact that the beam is much larger when the beam compressor is removed. As a result a large amount of the beam is clipped at the outer borders of the QPD – which are different for the two types of QPDs. However, the results give an impression of the deviation caused by a beam parameter variation of 20%.

Generally, these results show, that with the current uncertainty in the values of the beam parameters a large variety of results might be obtained, such that a significant comparison of simulation and experiment especially in the case of the pathlength signal and cross coupling is rather difficult. Since the experiment is still work in progress, a direct comparison is not shown in this thesis. However, the corresponding experiment is documented in [PD1].

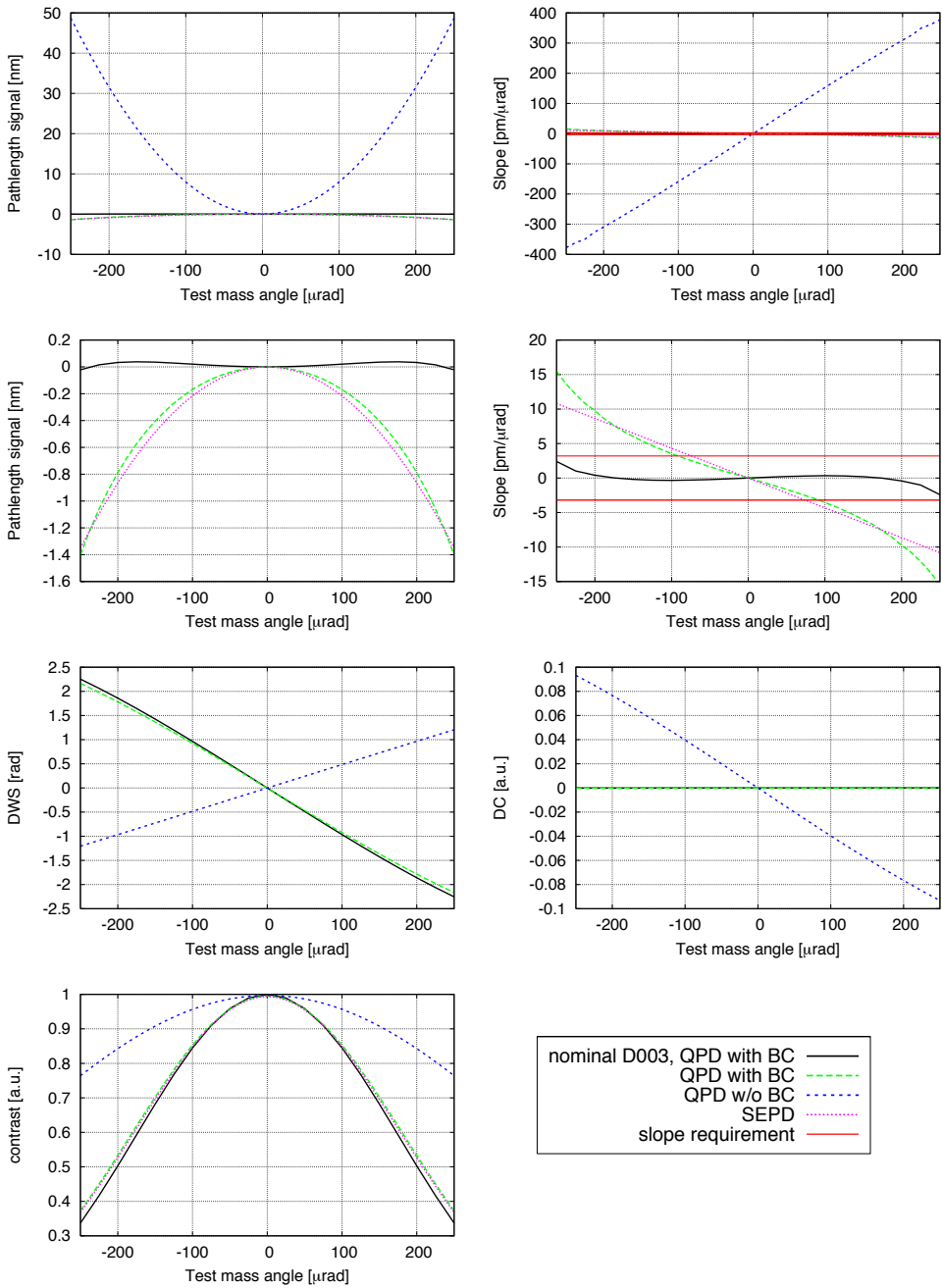
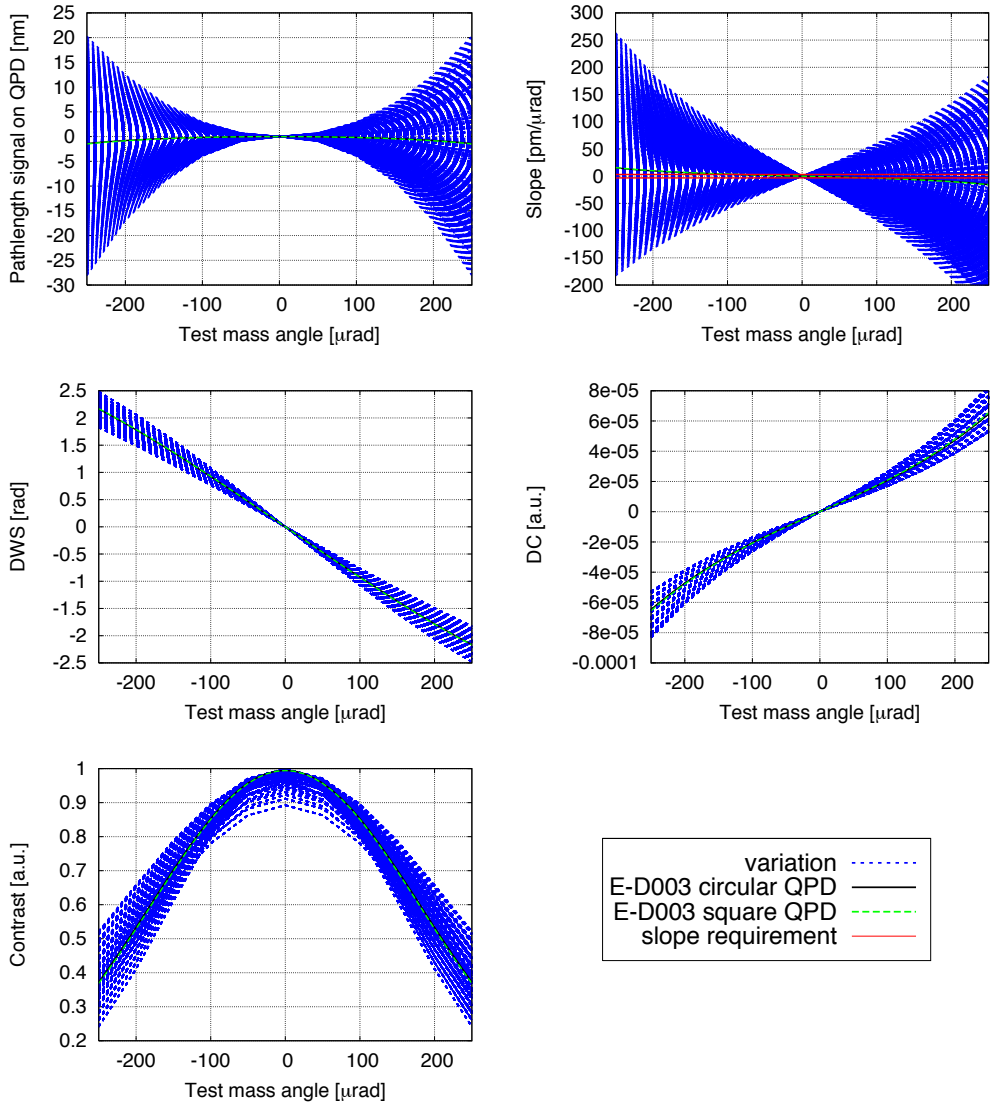
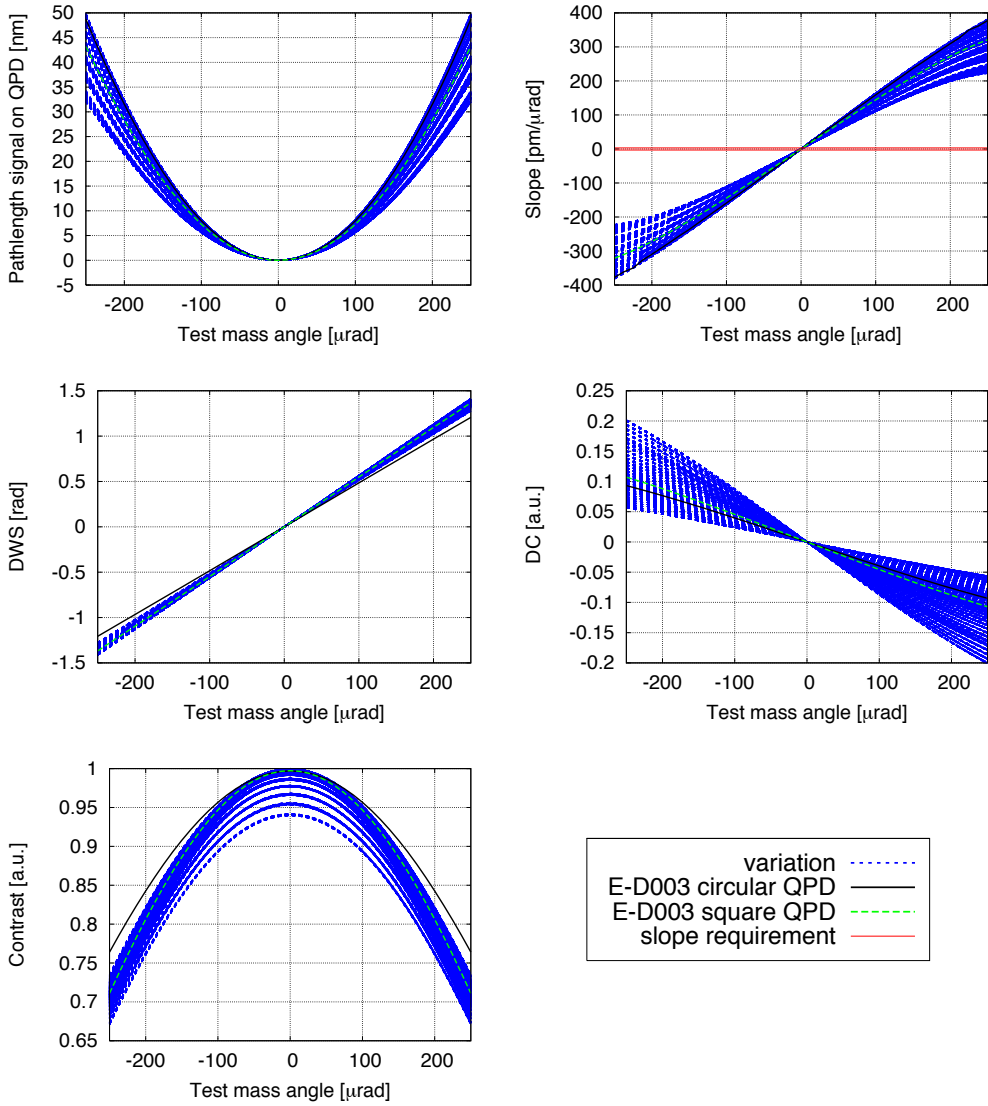


Figure 10.15.: Signals computed for E-D003: the experimental realization of D003.



**Figure 10.16.:** Experimental realization of **D003** (with lenses and computed with a QPD): all beam parameters were varied by 20% with respect to the measured (nominal) value. For the variation, square QPDs were used. The nominal curves with measured beam parameters are shown as reference, computed with circular and square QPDs.



**Figure 10.17.:** Experimental realization of **D003** QPD **without lenses**: all beam parameters were varied by 20% with respect to the measured (nominal) value. For the variation, square QPDs were used. The nominal curves with measured beam parameters are shown as reference, computed with circular and square QPDs.





# Appendix



# A. Background information

## A.1. Strain caused by gravitational waves

In section 2.1, the relation between arm length  $L$  of an interferometer and the amplitude of a gravitational wave was introduced:

$$\Delta L = \frac{h \cdot L}{2} . \quad (2.1)$$

This equation is well known in a rearranged form:

$$h = \frac{2 \Delta L}{L} , \quad (2.1a)$$

and a derivation of this equation can be found in numerous places, for instance [Heinzel1995] and [Hewitson2004]. However, there often exists unclarity, for which cases this equation is valid: only a Michelson interferometer, or also one of its arms, for round trip of the light or also for one direction? Therefore, the derivation of this equation is shown below with focus on its application. A variety of simplifications is therefore made, like the choice of the optimal polarization and the negligence of the time dependency of the gravitational wave signal. A slightly more general derivation is given in [Heinzel1995] and a general computation is shown in [Saulson, sec. 2.3].

### Derivation

In general relativity, the effect of a gravitational wave is described as a small disturbance in the otherwise flat Minkowski metric  $\eta_{\mu\nu}$ :

$$g_{\mu\nu} = \eta_{\mu\nu} + h_{\mu\nu} . \quad (A.1)$$

The perturbation  $h_{\mu\nu}$  can be expressed as two polarizations of plane waves

$$\begin{pmatrix} 0 & 0 & 0 & 0 \\ 0 & h_+ & h_\times & 0 \\ 0 & h_\times & h_+ & 0 \\ 0 & 0 & 0 & 0 \end{pmatrix} . \quad (A.2)$$

It is now assumed that the detector is optimally aligned with respect to the incident wave, such that only one polarization is needed to express the resulting effect. For convenience,  $h_+$  is chosen, such that  $h_\times$  is set to zero. As mentioned,  $h_+$  can be interpreted as plane wave, which could be for instance a harmonic oscillation:  $h_\times = h \cos \omega_{\text{h}} t + \Phi$ . Since the precise shape of the wave depends on the source and for

## A. Background information

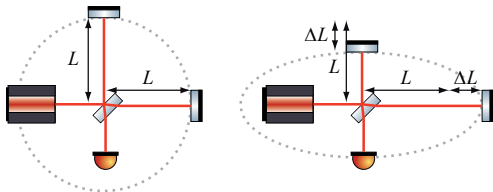


**Figure A.1:** Arm length changes in a simple Michelson interferometer if a gravitational wave transmits orthogonally to the shown plane.

convenience, the amplitude  $h$  of this wave is used as representative of the entire wave. Then, the metric gains the form

$$g_{\mu\nu} = \begin{pmatrix} -1 & 0 & 0 & 0 \\ 0 & 1+h & 0 & 0 \\ 0 & 0 & 1-h & 0 \\ 0 & 0 & 0 & 1 \end{pmatrix} \quad (\text{A.3})$$

For the photons which travel at the speed of light  $c_0$ , the following equation yields:

$$0 = (ds)^2 = -(c_0 dt)^2 + (1+h(t))(dx)^2 + (1-h(t))(dy)^2 + (dz)^2. \quad (\text{A.4})$$

### Single link one direction

Subsequently, the path of the photon traveling along one arm is computed. Here, the  $x$ -direction is chosen for convenience. It is therefore  $dy = dz = 0$ , such that

$$(c_0 dt)^2 = (1+h)(dx)^2. \quad (\text{A.5})$$

Integration of this term over the propagation time of the photon along one arm results in

$$c_0 \Delta t = \int_0^L dx \sqrt{1+h}, \quad (\text{A.6})$$

where  $L$  is the coordinate of the end mirror and simultaneously the geometrical arm length in absence of a gravitational wave. Here, due to the chosen transverse traceless (TT-) gauge, coordinates of particles are fixed while their distances are altered by the gravitational wave. If it is assumed, that the gravitational wave has a large wavelength and is thus constant over the propagation time, then eq. (A.6) can be evaluated:

$$c_0 \Delta t = \int_0^L dx \sqrt{1+h} \approx \int_0^L dx \left(1 + \frac{h}{2}\right) = L + \frac{Lh}{2}. \quad (\text{A.7})$$

By definition,  $\Delta t$  is the time the light needs to propagate along the entire arm, such that  $c\Delta t$  is the length the light propagated:

$$c_0 \Delta t = L + \Delta L. \quad (\text{A.8})$$

For one single arm, it is thus:

$$L + \Delta L = L + \frac{Lh}{2} \quad (\text{A.9})$$

which can be rearranged to the well known form

$$h = \frac{2\Delta L}{L}. \quad (2.1a)$$

### Single link round trip

The same deviation can be performed for one single arm but for one round trip (RT) of a photon. In that case, eq. (A.6) is expanded by the path from end mirror located at position  $L$  back to the origin, such that

$$c_0 \Delta t_{\text{RT}} = \int_0^L dx \sqrt{1+h} - \int_L^0 dx \sqrt{1+h}. \quad (A.6a)$$

$$= 2 \int_0^L dx \sqrt{1+h} \quad (A.10)$$

$$= 2 \left( L + \frac{Lh}{2} \right). \quad (A.7a)$$

The minus sign in eq. (A.6a) accounts for the inverse direction of propagation. Since  $\Delta t_{\text{RT}}$  is the round trip time,  $c\Delta t_{\text{RT}}$  is the entire distance traveled by the photon, that means the pathlength  $s_x$  which is

$$c_0 \Delta t_{\text{RT}} = s_x = 2(L + \Delta L). \quad (A.11)$$

Consequently, it is

$$2(L + \Delta L) = 2 \left( L + \frac{Lh}{2} \right) \quad (A.12)$$

which can again be rearranged to result in eq. (2.1a).

### Michelson interferometer

A Michelson interferometer measures the differential pathlength change:

$$\Delta s = s_x - s_y. \quad (A.13)$$

The pathlength for the second arm is computed starting from eq. (A.4) by

$$c_0 \Delta t_{\text{RT}}^y = s^y = \int_0^L dx \sqrt{1-h} - \int_L^0 dx \sqrt{1-h}. \quad (A.6b)$$

$$= 2 \int_0^L dx \sqrt{1-h} \quad (A.14)$$

$$= 2 \left( L - \frac{Lh}{2} \right), \quad (A.7b)$$

such that

$$c_0 \Delta t_{\text{RT}} = s_y = 2(L - \Delta L). \quad (A.15)$$

## A. Background information

Consequently, the differential pathlength  $\Delta s$  can be computed by

$$\Delta s = 2(L + \Delta L) - 2(L - \Delta L) = 2\left(L - \frac{Lh}{2}\right) - 2\left(L - \frac{Lh}{2}\right) \quad (\text{A.16})$$

$$4\Delta L = 2Lh. \quad (\text{A.17})$$

This too, can be rearranged to eq. (2.1a).

### Conclusion

It is therefore shown, that eq. (2.1a) is valid no matter whether a Michelson, one single arm or even one single arm with light propagation in one direction is considered. However, the equation is valid only if the gravitational wave has a wavelength sufficiently larger than the arm length  $L$  and impinges with optimal polarization orthogonal to the detector.

One further conclusion from the stated equations is, that the pathlength change in a single link in one direction  $\Delta s^{\text{SL1}}$  is

$$\Delta s^{\text{SL1}} = \Delta L = \frac{hL}{2} \quad (\text{A.18})$$

in one arm (round trip) it is

$$\Delta s^{\text{RT}} = 2\Delta L = hL \quad (\text{A.19})$$

and for a Michelson:

$$\Delta s^{\text{MI}} = 4\Delta L = 2hL. \quad (\text{A.20})$$

Consequently, it is in principle possible to detect gravitational waves with just one single arm, at the cost of a factor of 2 in sensitivity. However, it is currently not possible to build a single arm detector for the following reason:

Effectively, a single arm detector is a Michelson with very small arm length in  $y$ -direction. Since the propagation time through the two unequal arms is different, the interferometer superimposes laser light emitted at different times. As a result, laser frequency fluctuations couple intensely into the pathlength readout. This can be shown as follows:

$$\omega = 2\pi f = \frac{\delta\phi}{\delta t} \quad (\text{A.21})$$

$$(\text{A.22})$$

where  $f$  is the laser frequency,  $\delta t$  the propagation time difference for both arms

$$\delta t = \frac{\delta L_{xy}}{c_0}, \quad (\text{A.23})$$

and  $\phi$  the resulting phase change in the interferometer readout. The phase change  $\phi$  is converted to the pathlength signal using  $k$  with the mean wavelength and not taking into account the fluctuations

$$\delta s = \frac{\phi}{k}. \quad (\text{A.24})$$

As a result, the frequency fluctuations couple linearly into the pathlength readout, such that the amount of pathlength noise scales with the arm length difference  $\delta L_{xy}$ . Laser frequency stability presently achievable is not sufficient to allow large differences in the interferometer arm lengths. Gravitational wave detectors therefore need the interferometer arms to be approximately of the same length.

## A.2. Science requirements for LISA and LISA Pathfinder

The science requirements for LISA and LISA pathfinder are generally expressed as linear spectral densities of either position, pathlength or acceleration noise ( $S(x_m)$ ,  $S(\Delta s_m)$  or  $S(a_m)$  respectively). Position and pathlength noise curves appear in literature in two different forms. Either the form used in the present thesis:

$$S(\Delta s_m) \approx 2S(x_m) = 2K_x \sqrt{1 + \left(\frac{f_c}{f}\right)^4} \quad (\text{A.25})$$

or

$$S(\Delta s_m) \approx 2S(x_m) = 2K_x \left(1 + \left(\frac{f_c}{f}\right)^2\right) \quad (\text{A.26})$$

where  $K_x$  and  $K_a$  are constants. The constant  $f_c$  is the corner frequency (cf. figure A.2). Similarly, the amount of acceleration noise appears generally in two forms:

$$S(a_m) = K_a \sqrt{1 + \left(\frac{f}{f_c}\right)^4} \quad (\text{A.27})$$

or

$$S(a_m) = K_a \left(1 + \left(\frac{f}{f_c}\right)^2\right) \quad (\text{A.28})$$

These noise estimates differ only by a small amount, as shown in figure A.2. The largest deviation between both curves is a factor of  $\sqrt{2}$  at the corner frequency  $f_c$ . All these noise curves originate from the assumption that the readout in LISA and LISA Pathfinder will be dominated by constant (i.e. white) acceleration noise at low frequencies and by constant pathlength noise at high frequencies (cf. figure A.2). If it is assumed that these two limiting noise types are uncorrelated because they origin from a variety of different sources, then the total noise will be:

$$\text{total noise} = \sqrt{(\text{lim. pathlength noise})^2 + (\text{lim. interferometer noise})^2}, \quad (\text{A.29})$$

which results in eq. (A.25) and eq. (A.27). If it is contrary assumed that the noise sources are correlated, the total noise is the linear sum of the contributors:

$$\text{total noise} = \text{lim. pathlength noise} + \text{lim. interferometer noise}, \quad (\text{A.30})$$

and the noise estimates and requirements have the form of eq. (A.26) and eq. (A.28).

## A. Background information

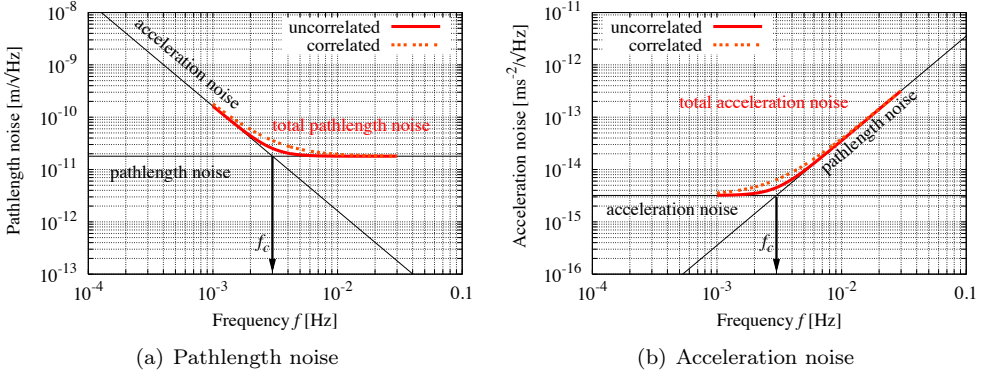


**Figure A.2.:** General composition of LTP and LISA requirements. Shown is how pathlength noise (a) is decomposed in a constant pathlength and acceleration noise, as well as the corner frequency  $f_c$ . The equivalent acceleration noise is shown in (b).

### Derivation

Acceleration and position are in frequency domain simply related by a factor of  $-\omega^2$ :

$$a(f) = \ddot{x}(f) = -\omega^2 x(f). \quad (\text{A.31})$$

Furthermore, pathlength noise  $S(\Delta s_m)$  is computed from position noise  $S(x_m)$  by the corresponding coupling factor  $k_x^{\Delta s_m}$ . This factor was shown in section 7.1.1, eq. (7.10) and eq. (7.14) to have a value of

$$k_x^{\Delta s_m} = 2 \cos(\alpha) \approx 2, \quad (\text{A.32})$$

where  $\alpha$  is the incident angle of  $4.5^\circ$  in LTP and  $0^\circ$  in LISA of the beam on the respective test mass. Assuming now a white position noise of  $K_x$  and a white acceleration noise of  $K_a$ , then the total pathlength noise  $S(\Delta s_m)$  is:

uncorrelated:

$$S(\Delta s_m) \approx 2S(x_m) = 2\sqrt{K_x^2 + \frac{K_a^2}{\omega^4}} \quad (\text{A.29}')$$

$$= 2K_x \sqrt{1 + \frac{K_a^2}{K_x^2 \omega^2}} \quad (\text{A.33})$$

$$= 2K_x \sqrt{1 + \frac{K_a^2}{(4\pi^2)^2 K_x^2 f^4}} \quad (\text{A.34})$$

$$=: 2K_x \sqrt{1 + \left(\frac{f_c}{f}\right)^4} \quad (\text{A.25})$$

correlated:

$$S(\Delta s_m) \approx 2S(x_m) = 2\left(K_x + \frac{K_a}{\omega^2}\right) \quad (\text{A.30}')$$

$$= 2K_x \left(1 + \frac{K_a}{K_x \omega^2}\right) \quad (\text{A.35})$$

$$= 2K_x \left(1 + \frac{K_a}{4\pi^2 K_x f^2}\right) \quad (\text{A.36})$$

$$=: 2K_x \left(1 + \left(\frac{f_c}{f}\right)^2\right) \quad (\text{A.26})$$



The relation between corner frequency  $f_c$ ,  $K_x$  and  $K_a$

$$f_c = \sqrt{\frac{K_a}{4\pi^2 K_x}} \quad (\text{A.37})$$

can be used to transfer in a very simple way from a requirement for position noise to one for acceleration noise or vice versa:

$$K_x = \frac{K_a}{4\pi^2 f_c^2} \leftrightarrow K_a = 4\pi^2 f_c^2 K_x. \quad (\text{A.38})$$

The total acceleration noise eq. (A.27) and eq. (A.28) can be derived in a similar way, using the same constants  $K_x, K_a$  and the same corner frequency  $f_c$ :

uncorrelated:

$$S(\Delta a) = \omega^2 \cdot S(x_m) \quad (\text{A.39})$$

$$= \sqrt{K_x^2 \omega^4 + K_a^2} \quad (\text{A.29''})$$

$$= K_a \sqrt{\frac{K_x^2 \omega^2}{K_a^2} + 1} \quad (\text{A.40})$$

$$=: K_a \sqrt{\left(\frac{f}{f_c}\right)^4 + 1} \quad (\text{A.27})$$

correlated:

$$S(\Delta a) = \omega^2 \cdot S(x_m) \quad (\text{A.41})$$

$$= (K_x \omega^2 + K_a) \quad (\text{A.30''})$$

$$= K_a \left( \frac{K_x \omega^2}{K_a} + 1 \right) \quad (\text{A.42})$$

$$=: K_a \left( \left(\frac{f}{f_c}\right)^2 + 1 \right) \quad (\text{A.28})$$

### A.3. LPF noise break down

In this section the displacement noise budget for noise originating from spacecraft jitter is derived. This break down was performed by Nico Brandt (ASD) and bases upon reference [ASD-3036]. Matrix labeling, coordinate labeling etc. are all according to this document. The resulting break down of the budget is sketched in figure A.3.

#### Derivation

Displacement noise due to space craft (S/C) acceleration is computed by:

$$\Delta x_{SC\text{only}} = \frac{1}{s^2} C_{DC,SC\text{only}} \cdot a_{SC} , \quad (\text{A.43})$$

where  $C_{DC,SC\text{only}}$  are the first six components of  $C_{\text{req}}$  [ASD-3036, p.138]

$$C_{DC,SC\text{only}} = \begin{pmatrix} 100 \cdot 10^{-6} \text{m/m} \\ 50 \cdot 10^{-6} \\ 50 \cdot 10^{-6} \\ 0 \\ 60 \cdot 10^{-6} \text{m} \\ 60 \cdot 10^{-6} \text{m} \end{pmatrix} . \quad (\text{A.44})$$

The transformation between Drag-Free axes ( $x_1, y_1, z_1, \theta_1, y_2, z_2$ ) and S/C axes ( $x, y, z, \theta, \eta, \phi$ ) is computed by:

$$a_{SC} = B_{DF}^{-1} \cdot a_{DF}$$

with

$$B_{DF}^{-1} = \begin{pmatrix} -1 & 0 & 0 & 0 & 0 & 0 \\ 0 & -\frac{1}{2} & 0 & 0 & -\frac{1}{2} & 0 \\ 0 & 0 & -\frac{1}{2} & 0 & 0 & -\frac{1}{2} \\ 0 & 0 & 0 & -1 & 0 & 0 \\ 0 & 0 & \frac{1}{2x} & 0 & 0 & -\frac{1}{2x} \\ 0 & -\frac{1}{2x} & 0 & 0 & \frac{1}{2x} & 0 \end{pmatrix} \quad (\text{A.45})$$

and  $x$  being the translation between spacecraft center of mass (CoM) and test mass CoM. It is assumed that geometrical center and center of mass coincide. The distance between the center of the optical bench and the reflecting surface of each test mass is nominally 165 mm and the diameter of each test mass is 46 mm, such that the displacement  $x$  between test mass and spacecraft CoM is

$$x = 165 \text{ mm} + \frac{46 \text{ mm}}{2} = 0.188 \text{ m} . \quad (\text{A.46})$$

Drag-Free axes acceleration requirements taken from performance budget:

$$a_{DF} = \begin{pmatrix} 2.66479 \cdot 10^{-10} \\ 4.84101 \cdot 10^{-10} \\ 4.84101 \cdot 10^{-10} \\ 0 \\ 4.84101 \cdot 10^{-10} \\ 4.84101 \cdot 10^{-10} \end{pmatrix} \frac{\text{m}}{\text{s}^2 \sqrt{\text{Hz}}} . \quad (\text{A.47})$$

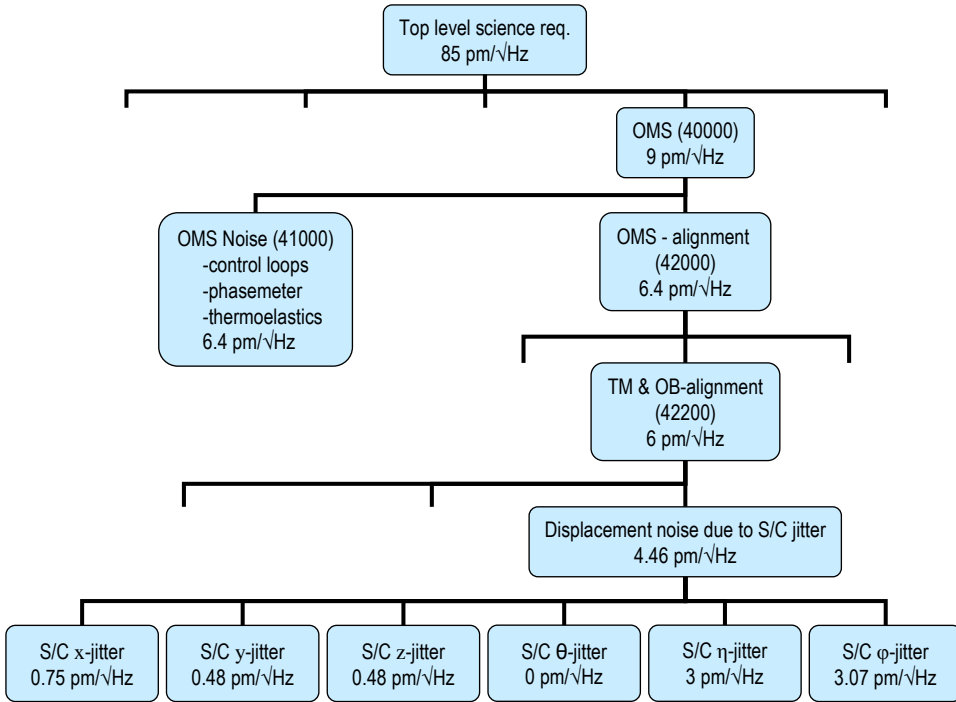


**Figure A.3.:** LTP noise break down from top level science requirement to displacement noise originating from spacecraft jitter in its various degrees of freedom. This is an extended excerpt of the organigram shown in reference [ASD-3036, p.39]. The top level requirement of 85 pm/√Hz is better known as a pathlength noise requirement of 170 pm/√Hz which corresponds to an acceleration noise of  $3 \cdot 10^{-14} \text{ m/s}^2/\sqrt{\text{Hz}}$ .

Note: These values replace the incorrect numerical values stated in [ASD-3036, p.140 R42241 ff.].

Transformation to S/C axes acceleration requirements by assuming that accelerations along DF axes are uncorrelated:

$$a_{SC} = \sqrt{(B_{DF}^{-1})^2 \cdot a_{DF}^2} \tag{A.48}$$

$$a_{SC} = \begin{pmatrix} 2.66479 \cdot 10^{-10} \\ 3.42311 \cdot 10^{-10} \\ 3.42311 \cdot 10^{-10} \\ 0 \\ 1.8208 \cdot 10^{-09} \\ 1.8208 \cdot 10^{-09} \end{pmatrix} \frac{\text{m}}{\text{s}^2 \sqrt{\text{Hz}}} \tag{A.49}$$

The individual displacement noise contributions from S/C acceleration can be computed by a component-wise multiplication:

$$a_{SC} = \frac{1}{(2\pi \cdot 30 \text{ mHz})^2} C_{DC,SC_{\text{only}}} * a_{SC} = \begin{pmatrix} 0.74999 \\ 0.481713 \\ 0.481713 \\ 0 \\ 3.07477 \\ 3.07477 \end{pmatrix} \frac{\text{pm}}{\sqrt{\text{Hz}}} . \quad (\text{A.50})$$

The total sum of displacement noise originating from S/C axes accelerations can be computed by

$$\frac{1}{(2\pi \cdot 30 \text{ mHz})^2} \sqrt{C_{DC,SC_{\text{only}}}^2 \cdot a_{sc}^2} = 4.46486 \frac{\text{pm}}{\sqrt{\text{Hz}}} . \quad (\text{A.51})$$

The squares in this equation are defined component-wise, such that in fact an uncorrelated summation of the contributing displacement noise requirements is performed. The resulting value of 4.46486 pm/ $\sqrt{\text{Hz}}$  is the apportioned displacement noise as stated in reference [ASD-3036, p.140].

## A.4. Implementation of tolerances in the LTP-OBI-Alignment Simulation

In section 6.1 the clipped normal distribution (CND) was introduced. In this section it is discussed, why this distribution was chosen for all random variables in the LTP-OBI-Alignment Simulation.

It is reasonable to assume that larger deviations from the nominal value are less likely than smaller ones. That means the angles and positions are not uniformly distributed. Furthermore, it can be assumed that the final alignment is influenced by many different parameters, which define the precision of the CMM, adjusters and CQP. Those are for instance electrical noise, calibration precision and piezo hysteresis. Finally the curing process affects the final alignment of a component. Thus, the final alignment is influenced by many independent statistics. According to the central limit theorem the alignment will thus be approximately normally distributed. However, a normal distribution gives arbitrary large deviations a finite likelihood, such that for example a mirror that should be placed at 45° could be set to 90° instead. It is clear that in manufacturing, there is always a maximal deviation. Therefore, the probability density function needs to be clipped. Due to these reasons a clipped normal distribution (CND) was chosen for the alignment simulation.

### Clipped normal distributions

The probability density function (PDF) of a normal distribution is a normalized Gaussian function with mean value  $\mu$  and standard deviation  $\sigma$ :

$$\text{ND}(x, \mu, \sigma) = \frac{1}{\sqrt{2\pi}\sigma} e^{-\frac{(x-\mu)^2}{2\sigma^2}} . \quad (\text{A.52})$$

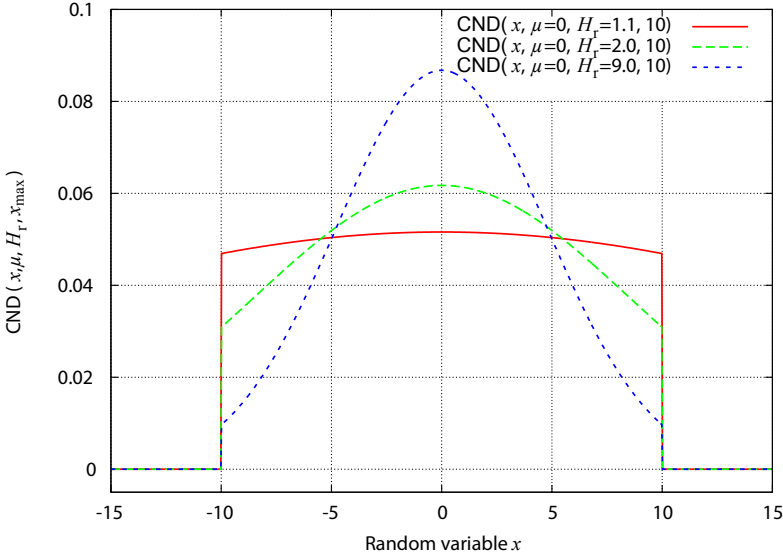


**Figure A.4.:** Probability density function of a clipped normal distribution for different relative heights  $H_r$ . It can be seen how the function flattens towards a uniform distribution as  $H_r$  goes to 1. For  $H_r \rightarrow \infty$  slowly a non clipped normal distribution evolves. In the alignment simulation  $H_r$  was set to 2 (green curve in the middle).

If the normal distribution is clipped, the overall probability needs to stay 1, i.e. the probability density function needs to stay normalized. Therefore, the clipped normal distribution has the following probability density function:

$$\text{CND}(x, \mu, \sigma, x_{\max}) = \begin{cases} \frac{e^{-\frac{(x-\mu)^2}{2\sigma^2}}}{\sqrt{2\pi}\sigma \text{erf}\left(\frac{x_{\max}}{\sqrt{2}\sigma}\right)} & \text{if } \mu - x_{\max} \leq x \leq \mu + x_{\max} \\ 0 & \text{else.} \end{cases} \quad (\text{A.53})$$

For each alignment step estimates for the mean value  $\mu$  and the clipping value  $x_{\max}$  are needed. These estimates were provided by UGL for the components of the OB, and by ASD (cf. section 6.3). However the standard deviation and thus the precise shape of the alignment statistics was not known and needed to be estimated. This shape (as shown in figure A.4) can be expressed by the relative height  $H_r$  which is the ratio of the peak value  $\text{CND}(x = \mu)$  and the edge value  $\text{CND}(x = \mu + x_{\max})$  of the PDF:

$$H_r := \frac{\text{CND}(x = \mu)}{\text{CND}(x = \mu + x_{\max})} \quad (\text{A.54})$$

$$= \exp\left(\frac{x_{\max}^2}{2\sigma^2}\right). \quad (\text{A.55})$$

The relative height  $H_r$  allows a direct judgment of the curve shape:  $H_r \rightarrow 1$  corresponds to a uniform distribution while  $H_r \rightarrow \infty$  corresponds to a normal distribution with negligible clipping (see figure A.4 for an illustration). For the alignment simulation a

## A. Background information

relative height of 2 was chosen:

$$H_r = 2. \quad (\text{A.56})$$

It is convenient to substitute the standard deviation by the relative height:

$$\sigma = \frac{x_{\max}}{\sqrt{2 \ln(H_r)}} \quad (\text{A.57})$$

such that the PDF of the clipped normal distribution obtains the form

$$\text{CND}(x, \mu, H_r, x_{\max}) = \frac{H_r \frac{-(x-\mu)^2}{x_{\max}^2} \sqrt{\ln H_r}}{x_{\max} \sqrt{\pi} \operatorname{erf}(\sqrt{\ln H_r})} \quad (\text{A.58})$$

$$= \frac{2 \frac{-(x-\mu)^2}{x_{\max}^2} \sqrt{\ln 2}}{x_{\max} \sqrt{\pi} \operatorname{erf}(\sqrt{\ln 2})}, \quad (\text{A.59})$$

which was used to generate figure A.4.

## A.5. Labeling of QPD-quadrants in LTP

A beam tilt or angular jitter at the fiber output results in beam walk on the various quadrant photodiodes. However, the direction of the beam walk depends on the number of reflections, as shown in figure A.5 for the engineering model (EM) of the OBI. To counteract this effect, the QPD labeling was adapted. Further information can be found in [ASD-3018].

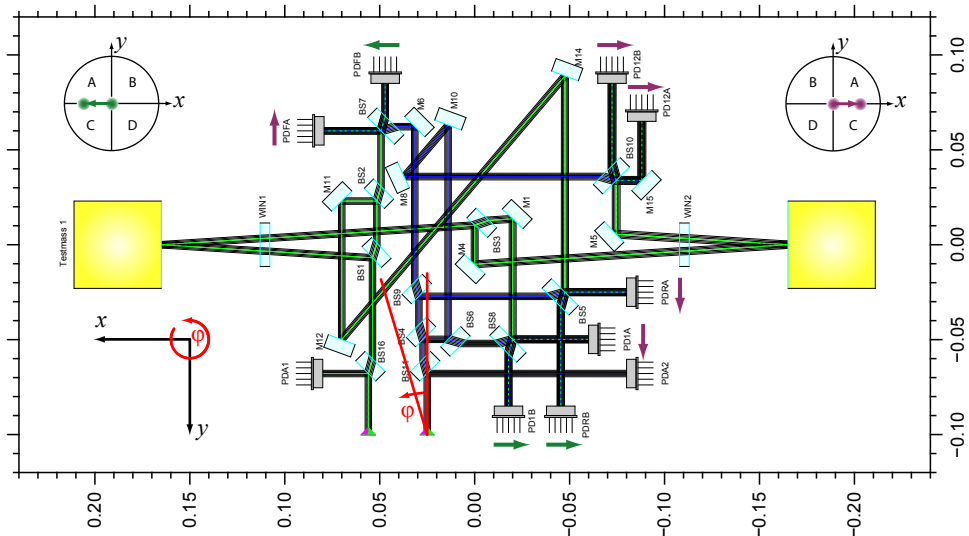


**Figure A.5.:** Beam walk caused by beam tilt at the fiber end of the reference beam, shown here for the engineering model (EM) of the LISA Pathfinder optical bench.

## A.6. Design Criteria for the LISA OB

### Location of the imaging optics

First it has to be decided where the lens system will be located on the optical bench. It could be placed before the beam combiner, so in the beam path between test mass and beam combiner. Alternatively, it could be positioned between beam combiner and photodiode. Positioning the imaging optics before the beam combiner has the advantage of having more space and a smaller distance between test mass and the first lens. The importance of this fact is shown in section 10.3.4. Nevertheless, the large disadvantage of this location is that two imaging optics would be needed for each interferometer, one in the path of the measurement beam, but another one in the path of the reference beam. Since the alignment of a lens system is generally difficult and affects the beam parameters, the resulting mode mismatch between the two beams is expected to be rather high. Thus the imaging optics is planned to be located behind the beam combiner.

### Primary design goal: C01

Please see section 10.2 for a derivation of this design criterion.

### Tolerances: C02

The imaging optics shall be as insensitive to misalignment as possible, that means in particular: the interferometer performance shall not be lost by misalignment of the lenses in the order of ten micrometers, beam waist position shifts in the order of roughly a tenth of a Rayleigh range or waist size deviations in the order of 10%. These are not fixed requirements but estimates.

### Dimensions: C03-C05

The location of the imaging optics between beam combiner and photodiode leaves very little space, such that the optics optimally including the photodiode should be in the order of 8 cm or less. Furthermore, the distance between test mass and the first lens cannot be smaller than 42.5 cm due to lacking space on the optical bench. Finally, the distance between the last surface of the lens system and the chip on the QPD (the so called eye relief) needs to be larger than 5 mm for alignment feasibility reasons.

### Compression factor: C06

Please see section 10.2 for a discussion of the optimal compression factor.

### Secondary constraints including C07

Of course the lens system designed should be as simple as possible. Thus a system with just two spherical lenses is the design goal. Furthermore, it was suggested to have an intermediate focus. A field stop could then be placed at the position of the intermediate focus which would result in a reduction of stray light. Nevertheless such a field stop cannot filter ghost beams which was in the experience gained with LISA

## A. Background information

Pathfinder critical stray light.

Finally, it was suggested to have a collimated beam behind the beam compressor. It was assumed that this would ease alignment issues.

### **Beam properties including C09, C10**

A beam radius at the waist of 1 mm was defined by ASD [LOB-06, p. 80 R<130-090>]. This value is a compromise between having beams as large as possible in order to have small divergence and having small beams to reduce the size of the optical components and thus the overall weight of the OBI. The beam waist of the measurement beam was suggested to be on the test mass in order to have zero beam curvature there, such that the beam has locally the properties of a plane wave. This allows the use of geometric optics design tools and criteria, which are described in section 10.2. However, it is shown in section 10.4.2 and figure 10.12(a) that this design criterion is not necessary, provided that both beams are collimated when entering the beam compressor.

### **Quadrant photodiodes: C11-C13**

The LISA science interferometer operates with approximately 100 pW of laser light power impinging on each photodiode. Therefore photodiodes are required which have high quantum efficiency, that means a high ratio of photo electrons to impinging photons. Therefore InGaAs-photodiodes were chosen to be used which provide a high quantum efficiency in the order of 80%. For simplicity these photodiodes shall be used for all interferometers on the optical bench.

The largest InGaAs-photodiodes available with the required frequency bandwidth has a diameter of 1 mm. The photodiodes procured for pre-experiments regarding LISA imaging optics were circular shaped InGaAs-photodiodes with 1 mm diameter and a 20  $\mu\text{m}$  slit. These specifications are used for the simulations presented in chapter 10.



## B. Proofs and validations

### B.1. Equivalent representations of the electric field

In this section the equivalence of the two generally used representations of the electric fields  $E^q \equiv E^R$  will be shown:

$$E^q(r, z) = E_0 \frac{w_0}{w(z)} \exp\left(-\frac{ikr^2}{2q(z)} + i\zeta(z) - ikz\right) \quad (3.13)$$

$$E^R(r, z) = E_0 \frac{w_0}{w(z)} \exp\left(\frac{-r^2}{w(z)^2}\right) \cdot \exp\left(-\frac{ikr^2}{2R(z)} + i\zeta(z) - ikz\right). \quad (3.14)$$

Both equations are obviously identical except of the following part:

$$\frac{-ikr^2}{2q(z)} \stackrel{?}{=} \frac{-ikr^2}{2R(z)} - \frac{r^2}{w^2(z)} \quad (B.1)$$

This can be shown by a transformation of  $1/q$  starting by its definition (eq. (3.10)):

$$\frac{1}{q} := \frac{1}{z + iz_0} = \frac{z - iz_0}{z^2 + z_0^2} \quad (B.2)$$

$$= \frac{z}{z^2 + z_0^2} - \frac{iz_0}{z^2 + z_0^2} = \frac{1}{z\left(1 + \frac{z_0^2}{z^2}\right)} - \frac{i}{z_0\left(1 + \frac{z_0^2}{z^2}\right)} \quad (B.3)$$

$$= \frac{1}{R(z)} - \frac{iw_0^2}{z_0w^2(z)} = \frac{1}{R(z)} - \frac{i\lambda}{\pi w^2(z)} \quad (B.4)$$

where the definitions of the complex beam parameter  $q(z)$ , the radius of curvature  $R(z)$ , the beam radius at the waist  $w_0$  and the beam radius  $w(z)$  at position  $z$  were used:

$$w(z) = w_0 \sqrt{1 + \left(\frac{z}{z_0}\right)^2} \quad \text{with} \quad w_0 = \sqrt{\frac{z_0 \cdot \lambda}{\pi}}, \quad (3.6, 3.7)$$

$$R(z) = z \left[1 + \left(\frac{z_0}{z}\right)^2\right]. \quad (3.8)$$

The left hand side of eq. (B.1) can be rearranged:

$$\frac{-ikr^2}{2q} = \frac{-ikr^2}{2} \left(\frac{1}{R(z)} - \frac{i\lambda}{\pi w^2(z)}\right) \quad (B.5)$$

$$= \frac{-ikr^2}{2R(z)} - \frac{\lambda kr^2}{2\pi w^2(z)} \quad (B.6)$$

Using the identity

$$k = \frac{2\pi}{\lambda} \quad (\text{B.7})$$

leads to eq. (B.1) and the equivalence of the two representations of the electric field is shown.

→ Back to page 28.

## B.2. Confirmation of power loss due to the insensitive slit

In chapter 8, the power sensed by a QPD was computed to be 0.875 W, as shown in table 8.2. This value can be validated by the subsequent set of simple equations.

The power readout for a 1 Watt input beam with configuration 1 is 0.875 W according to table 8.2 . The loss of 0.125 W results from beam clipping at the insensitive slit of the QPD. It is assumed that the beam intensity is constant over the surface of the QPD. In that case the power is proportional to the illuminated area and the relative power can be expressed as:

$$P_{\text{rel}} = \frac{P_{\text{measured}}}{P_{\text{b}}} \quad (\text{B.8})$$

$$= \frac{I \cdot A_{\text{sensitive}}}{I \cdot A_{\text{overall}}} \quad (\text{B.9})$$

$$= \frac{A_{\text{beam}} - A_{\text{slit}}}{A_{\text{beam}}}, \quad (\text{B.10})$$

where  $I$  is the local intensity,  $A$  indicates an area and  $P_{\text{b}}$  is the total beam power (1 Watt). A rough estimate of the illuminated area is

$$A_{\text{beam}} = \pi r^2 \quad (\text{B.11})$$

$$= \pi(0.55462 \text{ mm})^2, \quad (\text{B.12})$$

while the area of the slit illuminated by the beam (the clipped area) is

$$A_{\text{slit}} = 2 \cdot (\text{slit-size} \cdot \text{beam-diameter}) - \text{slit-size}^2 \quad (\text{B.13})$$

$$= 2 \cdot 45 \mu\text{m} \cdot 2 \cdot 0.55462 \text{ mm} - (45 \mu\text{m})^2. \quad (\text{B.14})$$

Evaluating eq. (B.10) with these values yields

$$P_{\text{rel}} = 0.899, \quad (\text{B.15})$$

which is a reasonable agreement with the 0.875 computed by QPD.c. Of course 0.875 is more accurate as QPD.c takes into account the gaussian beam shape.

→ Back to section 8.1.2.

## B.3. Confirmation of computed power for a 3 mm SEPD

In section 8.1.2, the power sensed by a for a single element photodiode (SEPD) of 3 mm diameter and a 1 W beam with a radius of 0.55462 mm was computed with QPD.c to 0.9999996 W (cf. table 8.2). This might seem to be a high power readout, since the radius of the SEPD is less than three times the beam radius. But the value can be confirmed by one simple equation:

$$P_{\text{SEPD}} = \int_0^{1.5} dr \frac{4r}{0.55462^2} \exp\left(\frac{-2r^2}{0.55462^2}\right) \quad (\text{B.16})$$

$$= 0.9999996 . \quad (\text{B.17})$$

### Derivation

As shown in section 4.6.1 an electrical field  $E$  propagating in  $z$  direction can be expressed in the following form

$$E(r, z) = \sqrt{\frac{2P_b}{\pi w(z)^2}} \exp\left(\frac{-r^2}{w(z)^2}\right) \cdot \exp\left[-\frac{ikr^2}{2R(z)} + i\zeta(z) - iks\right], \quad (\text{3.14a})$$

where  $w(z)$  is the spot size on the photodiode and  $P_b$  the beam power of 1 W. The local intensity of this electrical field is the square magnitude of  $E(r, z)$  which has a simple form:

$$I(r, z) = \left\| \sqrt{\frac{2P_b}{\pi w(z)^2}} \exp\left(\frac{-r^2}{w(z)^2}\right) \right\|^2 . \quad (\text{B.18})$$

The beam power on a circular (photodiode) surface of radius  $R_{\text{SEPD}}$  can be computed by the following integral:

$$P_s(z) = \int_0^{R_{\text{SEPD}}} dr 2\pi r \cdot I(r, z) \quad (\text{B.19})$$

$$= \int_0^{R_{\text{SEPD}}} dr \frac{4P_b r}{w(z)^2} \exp\left(\frac{-2r^2}{w(z)^2}\right) . \quad (\text{B.20})$$

Using a 1 Watt input beam with a radius of  $w(z) = 0.55462$  mm and a photodiode radius  $R_{\text{SEPD}} = 1.5$  mm leads to eq. (B.16).

→ Back to section 8.1.2.

## B.4. Imaged waist position

In general the waist of a gaussian beam is not located in the focal point of a lens. Its distance  $x'$  from the focal point and size  $w'_0$  after passing a lens can be computed from the original waist size  $w_0$  and the original distance to the primary focal point according to [Smith] by:

$$x' = \frac{-xf^2}{x^2 + \left(\frac{\pi w_0^2}{\lambda}\right)^2} \quad (\text{B.21})$$

$$w_0'^2 = \frac{f^2 w_0^2}{x^2 + \left(\frac{\pi w_0^2}{\lambda}\right)^2} \quad (\text{B.22})$$

$$= w_0^2 \left(\frac{-x'}{x}\right) \quad (\text{B.23})$$

- $w_0$ : waist size (radius) of the original beam
- $w'_0$ : waist size (radius) of the beam imaged by the lens or lens system
- $x$ : distance of waist of initial beam waist to first focal point of the lens
- $x'$ : distance of imaged beam waist to second focal point of the lens
- $\lambda$ : wavelength of the beam
- $f$ : focal length of the lens or lens system

In section 10.3.2 it was stated that if the lens system setup D was perfectly aligned, it would image the beam waist onto the photodiode. It was described, that the beam waste in placed on the test mass which is located in this setup in the focal point of the first lens. According to eq. (B.21), the distance  $x$  is therefore zero, which results in  $x' = 0$ , such that the imaged waist is located in the secondary focal point of the first lens. This point conveniently is also the primary focal point of the second lens, such that the waist is imaged again to the secondary focal point of the second lens, which is the location of the photodiode. Therefore, if setup D is perfectly aligned, it images the beam waist from the test mass to the photodiode. This property was used as a simple test to see, whether the system was implemented correctly.

→ Back to section 10.3.2.

## C. Settings of the various simulations

parameter	label	value
Rayleigh range	$z_0$	250 mm
wave length	$\lambda$	1064 nm
position of beam waist	$z_{w_0}$	0
position of QPD	$z_{\text{QPD}}$	$+z_0 = 250$ mm
position of pivot, e.g. test mass	$z_{\text{TM}}$	$-z_0 = -250$ mm
full width of slit of QPD	$d_{\text{Slit}}$	20 $\mu\text{m}$
full width of a square shaped QPD	$r_{\text{QPD}}$	1 mm

**Table C.1.:** Settings used to compute the signals shown in figure 4.7 and figure 4.10

parameter	label	value
Rayleigh range	$z_0$	250 mm
wave length	$\lambda$	1064 nm
position of beam waist	$z_{w_0}$	0
position of QPD	$z_{\text{QPD}}$	$-z_0 = -250$ mm
position of pivot, e.g. test mass	$z_{\text{TM}}$	$-3z_0 = -750$ mm
full width of slit of QPD	$d_{\text{Slit}}$	20 $\mu\text{m}$
full width of a square shaped QPD	$r_{\text{QPD}}$	1 mm

**Table C.2.:** Settings used to compute the signals shown in figure 4.4 and figure 4.5

C. Settings of the various simulations

Lens specification	L1	L2	L3	L4
position [mm]	425	428.1	448.553049	501.999947
refractive index	1.44063	1.44063	1.44063	1.44063
diameter [mm]	15	15	15	15
thickness [mm]	3	2.5	1.5	3
R1 [mm]	23.55296	16.39397	-10.41632	-94.79141
R2 [mm]	802.72893	36.14198	9.91442	-12.28514
QPD specification				
eye relief [mm]	14.998781			
position QPD [mm]	519.998728			

**Table C.3.:** Specification of the the ASD four lens beam compressor. The sign convention for the radii of curvature follow the ZEMAX definition, please cf. figure 10.7(a) for an illustration. The beams were defined as listed in table C.4 for the AEI beam compressor.

initial beams	Value	
starting point	$x = 0$	
wave length ( $\lambda$ ) [nm]	1064	
waist (radius)	1.00799 mm	
waist position	$x = 0$	
angle measurement beam	$-500 \dots 500 \mu\text{rad}$	representing a TM rotation of $-250 \dots 250 \mu\text{rad}$
lens specifications	L1	L2
LINOS catalogue number	G312316000	G313333000
position [mm]	425	472.82
refractive index	1.50669	1.44963
diameter [mm]	22.4	22.4
thickness [mm]	4.0	1.0
focal length [mm]	-62.86	-55.89
QPD		
position [mm]	525.24	
diameter [mm]	1	
slit width [ $\mu\text{m}$ ]	20	

**Table C.4.:** Properties of AEI beam compressor setup D003. These properties were used to generate the result shown in figure 10.8. All lens positions stated are those of the center of the primary surface.

## D. Coupling factors and figures accompanying section 10.4.2

In this section, the complete summary of the computed LTP OBI coupling factors is shown. Table 7.1, table 7.2 and table 7.3 in section 7.1 are excerpts of the here shown tables (D.1, D.2 and D.3).

Furthermore, the signals accompanying the tolerance analysis performed in section 10.4.2 for the investigated beam compressor designs for the LISA test mass interferometer are shown in figure D.1–figure D.10.

	RMS	$\sigma$	Max	Min
$k_{x_{OB}}^{\Delta s1} \left[ \frac{\mu\text{m}}{\mu\text{m}} \right]$	<b>1.99382</b>	$17.5035 \times 10^{-6}$	1.99387	1.99377
$k_{y_{OB}}^{\Delta s1} \left[ \frac{\text{pm}}{\mu\text{m}} \right]$	84.3175	84.3257	200.792	−207.392
$k_{\varphi_{OB}}^{\Delta s1} \left[ \frac{\text{pm}}{\mu\text{rad}} \right]$	33.6534	33.6559	95.9569	−89.265
$k_{x_{OB}}^{\text{DWS1}} \left[ \frac{\mu\text{rad}}{\mu\text{m}} \right]$	180.998	$360.711 \times 10^{-3}$	−180.02	−182.547
$k_{y_{OB}}^{\text{DWS1}} \left[ \frac{\mu\text{rad}}{\mu\text{m}} \right]$	$7.65591 \times 10^{-3}$	$7.65671 \times 10^{-3}$	$18.9881 \times 10^{-3}$	$−18.1765 \times 10^{-3}$
$k_{\varphi_{OB}}^{\text{DWS1}} \left[ \frac{\mu\text{rad}}{\mu\text{rad}} \right]$	<b>4903.6</b>	3.80308	−4900.02	−4925.39
$k_{x_{OB}}^{\text{DC1}} \left[ \frac{1}{\text{m}} \right]$	237.592	1.83135	−225.325	−239.937
$k_{y_{OB}}^{\text{DC1}} \left[ \frac{1}{\text{m}} \right]$	$10.0142 \times 10^{-3}$	$10.0153 \times 10^{-3}$	$23.935 \times 10^{-3}$	$−23.894 \times 10^{-3}$
$k_{\varphi_{OB}}^{\text{DC1}} \left[ \frac{1}{\text{rad}} \right]$	<b>901.506</b>	6.85116	907.278	856.94
$k_{x_{OB}}^{\Delta s12} \left[ \frac{\text{pm}}{\mu\text{m}} \right]$	<b>63.4768</b>	63.4723	175.64	−173.743
$k_{y_{OB}}^{\Delta s12} \left[ \frac{\text{pm}}{\mu\text{m}} \right]$	87.5974	87.6023	254.288	−239.332
$k_{\varphi_{OB}}^{\Delta s12} \left[ \frac{\text{pm}}{\mu\text{rad}} \right]$	54.6531	54.6496	187.47	−198.037
$k_{x_{OB}}^{\text{DWS12}} \left[ \frac{\mu\text{rad}}{\mu\text{m}} \right]$	1.44595	1.44581	3.98461	−3.98607
$k_{y_{OB}}^{\text{DWS12}} \left[ \frac{\mu\text{rad}}{\mu\text{m}} \right]$	$12.3973 \times 10^{-3}$	$12.3981 \times 10^{-3}$	$36.132 \times 10^{-3}$	$−33.8938 \times 10^{-3}$
$k_{\varphi_{OB}}^{\text{DWS12}} \left[ \frac{\mu\text{rad}}{\mu\text{rad}} \right]$	<b>1264.19</b>	1239.55	−1262.17	−1272.30
$k_{x_{OB}}^{\text{DC12}} \left[ \frac{1}{\text{m}} \right]$	1.0736	1.07349	2.88811	−2.97966
$k_{y_{OB}}^{\text{DC12}} \left[ \frac{1}{\text{m}} \right]$	$9.18701 \times 10^{-3}$	$9.18759 \times 10^{-3}$	$25.8485 \times 10^{-3}$	$−25.3153 \times 10^{-3}$
$k_{\varphi_{OB}}^{\text{DC12}} \left[ \frac{1}{\text{rad}} \right]$	<b>939.375</b>	10.1018	−871.841	−947.71

**Table D.1.:** Coupling factors for the flight model of the LTP optical bench. These values are the result of a simulation with the settings described in section 6.3, constant beam parameters and more than 4000 generated OBI setups. An excerpt of this table is discussed in section 7.1.

D. Coupling factors and figures accompanying section 10.4.2

	RMS	$\sigma$	Max	Min
$k_{x_1}^{\Delta s1} \left[ \frac{\text{m}}{\text{m}} \right]$	<b>1.99382</b>	$17.0891 \times 10^{-6}$	-1.99377	-1.99387
$k_{y_1}^{\Delta s1} \left[ \frac{\mu\text{m}}{\text{m}} \right]$	83.9195	83.9342	215.218	-203.812
$k_{\varphi_1}^{\Delta s1} \left[ \frac{\mu\text{m}}{\text{rad}} \right]$	37.5765	37.5758	120.03	-101.613
$k_{x_1}^{\text{DWS1}} \left[ \frac{\text{rad}}{\text{m}} \right]$	184.528	30.2806	276.082	110.724
$k_{y_1}^{\text{DWS1}} \left[ \frac{\text{mrad}}{\text{m}} \right]$	7.81339	7.8157	22.6499	-25.3636
$k_{\varphi_1}^{\text{DWS1}} \left[ \frac{\text{rad}}{\text{rad}} \right]$	<b>4890.52</b>	244.254	-4167.26	-5459.87
$k_{x_1}^{\text{DC1}} \left[ k^1 \text{m} \right]$	237.881	12.8461	282.832	208.607
$k_{y_1}^{\text{DC1}} \left[ \frac{1}{\text{m}} \right]$	$10.016 \times 10^{-3}$	$10.0182 \times 10^{-3}$	$26.096 \times 10^{-3}$	$-25.3897 \times 10^{-3}$
$k_{\varphi_1}^{\text{DC1}} \left[ \frac{1}{\text{rad}} \right]$	<b>902.64</b>	48.7365	$1.07242 \times 10^3$	790.834
$k_{x_1}^{\Delta s12} \left[ \frac{\text{m}}{\text{m}} \right]$	<b>1.99382</b>	$16.9015 \times 10^{-6}$	-1.99377	-1.99387
$k_{y_1}^{\Delta s12} \left[ \frac{\mu\text{m}}{\text{m}} \right]$	83.9194	83.9341	215.215	-203.815
$k_{\varphi_1}^{\Delta s12} \left[ \frac{\mu\text{m}}{\text{rad}} \right]$	40.3412	40.3388	115.066	-97.7352
$k_{x_2}^{\Delta s12} \left[ \frac{\text{m}}{\text{m}} \right]$	<b>1.99382</b>	$47.5934 \times 10^{-6}$	1.99393	1.99367
$k_{y_2}^{\Delta s12} \left[ \frac{\mu\text{m}}{\text{m}} \right]$	97.8159	97.8545	271.433	-254.337
$k_{\varphi_2}^{\Delta s12} \left[ \frac{\mu\text{m}}{\text{rad}} \right]$	45.6448	45.64	111.229	-136.463
$k_{x_1}^{\text{DWS12}} \left[ \frac{\text{rad}}{\text{m}} \right]$	285.675	34.2492	-204.554	-381.517
$k_{y_1}^{\text{DWS12}} \left[ \frac{\text{mrad}}{\text{m}} \right]$	12.0983	12.1014	35.6987	-32.0623
$k_{\varphi_1}^{\text{DWS12}} \left[ \frac{\text{rad}}{\text{rad}} \right]$	<b>4352.72</b>	301.593	5006.73	3361.20
$k_{x_2}^{\text{DWS12}} \left[ \frac{\text{rad}}{\text{m}} \right]$	285.694	34.2424	379.467	205.247
$k_{y_2}^{\text{DWS12}} \left[ \frac{\text{mrad}}{\text{m}} \right]$	13.9771	13.9836	37.3037	-40.4021
$k_{\varphi_2}^{\text{DWS12}} \left[ \frac{\text{rad}}{\text{rad}} \right]$	<b>5616.14</b>	183.881	-4994.62	-6105.50
$k_{x_1}^{\text{DC12}} \left[ \frac{1}{\text{m}} \right]$	209.547	8.81168	-189.026	-236.895
$k_{y_1}^{\text{DC12}} \left[ \frac{1}{\text{m}} \right]$	$8.79848 \times 10^{-3}$	$8.80017 \times 10^{-3}$	$21.6877 \times 10^{-3}$	$-22.2967 \times 10^{-3}$
$k_{\varphi_1}^{\text{DC12}} \left[ \frac{1}{\text{rad}} \right]$	<b>1405.10</b>	59.0319	-1269.20	-1588.09
$k_{x_2}^{\text{DC12}} \left[ \frac{1}{\text{m}} \right]$	209.563	8.8142	236.275	190.242
$k_{y_2}^{\text{DC12}} \left[ \frac{1}{\text{m}} \right]$	$10.2452 \times 10^{-3}$	$10.2492 \times 10^{-3}$	$26.7303 \times 10^{-3}$	$-25.9168 \times 10^{-3}$
$k_{\varphi_2}^{\text{DC12}} \left[ \frac{1}{\text{rad}} \right]$	<b>466.139</b>	19.5801	526.961	421.176

**Table D.2.:** Coupling factors of flight model of the LTP optical bench, computed from 1000 generated OBI setups and default settings. Beam parameters were varied. The numbers with bold font are the main coupling factors needed for calibration. An excerpt of this table is discussed in section 7.1. The simulation used for the computation is introduced in chapter 6, its details and settings are discussed in section 6.3.



	RMS	$\sigma$	Max	Min
$k_{x_1}^{\Delta s1} \left[ \frac{\text{m}}{\text{m}} \right]$	<b>1.99382</b>	$17.3391 \times 10^{-6}$	-1.99377	-1.99386
$k_{y_1}^{\Delta s1} \left[ \frac{\mu\text{m}}{\text{m}} \right]$	81.6692	81.7001	193.487	-184.057
$k_{\varphi_1}^{\Delta s1} \left[ \frac{\mu\text{m}}{\text{rad}} \right]$	37.8894	37.907	103.094	-116.889
$k_{x_1}^{\text{DWS1}} \left[ \frac{\text{rad}}{\text{m}} \right]$	181.002	$361.251 \times 10^{-3}$	182.306	180.078
$k_{y_1}^{\text{DWS1}} \left[ \frac{\text{mrad}}{\text{m}} \right]$	7.41585	7.41854	16.6513	-17.6336
$k_{\varphi_1}^{\text{DWS1}} \left[ \frac{\text{rad}}{\text{rad}} \right]$	<b>4903.45</b>	3.56021	-4900.14	-4923.18
$k_{x_1}^{\text{DC1}} \left[ \frac{1}{\text{m}} \right]$	237.663	1.71199	239.75	228.426
$k_{y_1}^{\text{DC1}} \left[ \frac{1}{\text{m}} \right]$	$9.70399 \times 10^{-3}$	$9.70769 \times 10^{-3}$	$21.9338 \times 10^{-3}$	$-22.9835 \times 10^{-3}$
$k_{\varphi_1}^{\text{DC1}} \left[ \frac{1}{\text{rad}} \right]$	<b>901.804</b>	6.41945	907.255	868.046
$k_{x_1}^{\Delta s12} \left[ \frac{\text{m}}{\text{m}} \right]$	<b>1.99382</b>	$17.2227 \times 10^{-6}$	-1.99377	-1.99386
$k_{y_1}^{\Delta s12} \left[ \frac{\mu\text{m}}{\text{m}} \right]$	81.6692	81.7001	193.488	-184.061
$k_{\varphi_1}^{\Delta s12} \left[ \frac{\mu\text{m}}{\text{rad}} \right]$	39.8225	39.8383	104.998	-123.212
$k_{x_2}^{\Delta s12} \left[ \frac{\text{m}}{\text{m}} \right]$	<b>1.99382</b>	$47.5447 \times 10^{-6}$	1.99393	1.99367
$k_{y_2}^{\Delta s12} \left[ \frac{\mu\text{m}}{\text{m}} \right]$	96.3695	96.4162	255.698	-265.907
$k_{\varphi_2}^{\Delta s12} \left[ \frac{\mu\text{m}}{\text{rad}} \right]$	44.1821	44.1722	121.07	-155.049
$k_{x_1}^{\text{DWS12}} \left[ \frac{\text{rad}}{\text{m}} \right]$	282.125	$499.793 \times 10^{-3}$	-280.84	-284.515
$k_{y_1}^{\text{DWS12}} \left[ \frac{\text{mrad}}{\text{m}} \right]$	11.5601	11.5644	27.4577	-25.9741
$k_{\varphi_1}^{\text{DWS12}} \left[ \frac{\text{rad}}{\text{rad}} \right]$	<b>4358.21</b>	3.95939	4383.24	4354.17
$k_{x_2}^{\text{DWS12}} \left[ \frac{\text{rad}}{\text{m}} \right]$	282.133	1.14338	285.407	279.272
$k_{y_2}^{\text{DWS12}} \left[ \frac{\text{mrad}}{\text{m}} \right]$	13.6363	13.6429	36.1472	-37.6806
$k_{\varphi_2}^{\text{DWS12}} \left[ \frac{\text{rad}}{\text{rad}} \right]$	<b>5622.33</b>	5.07279	-5618.11	-5655.24
$k_{x_1}^{\text{DC12}} \left[ \frac{1}{\text{m}} \right]$	209.796	2.1027	-197.476	-212.065
$k_{y_1}^{\text{DC12}} \left[ \frac{1}{\text{m}} \right]$	$8.55263 \times 10^{-3}$	$8.55589 \times 10^{-3}$	$19.9072 \times 10^{-3}$	$-19.3189 \times 10^{-3}$
$k_{\varphi_1}^{\text{DC12}} \left[ \frac{1}{\text{rad}} \right]$	<b>1406.73</b>	14.0027	-1323.18	-1418.12
$k_{x_2}^{\text{DC12}} \left[ \frac{1}{\text{m}} \right]$	209.802	2.2475	213.255	196.786
$k_{y_2}^{\text{DC12}} \left[ \frac{1}{\text{m}} \right]$	$10.1486 \times 10^{-3}$	$10.1535 \times 10^{-3}$	$27.0582 \times 10^{-3}$	$-28.253 \times 10^{-3}$
$k_{\varphi_2}^{\text{DC12}} \left[ \frac{1}{\text{rad}} \right]$	<b>466.671</b>	4.64693	470.669	438.953

**Table D.3.:** Same as table D.2 but with constant beam parameters. That means, 1000 OBI were generated but step 2 in the LTP-OBI-Alignment simulation was not executed (cf. section 6.3).

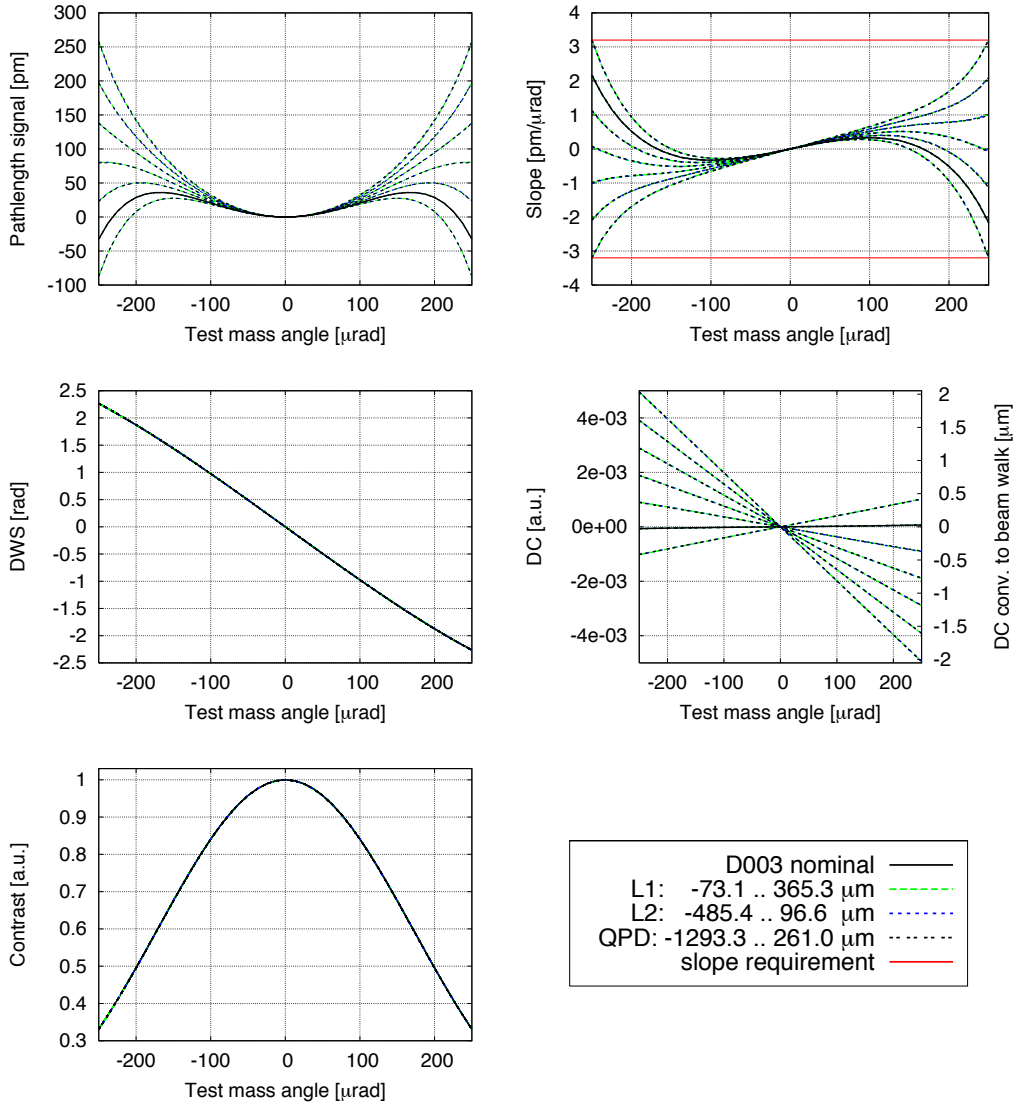


**Figure D.1.:** Beam compressor **D003**: longitudinal displacement in equidistant steps. One component was shifted in longitudinal direction until the slope reached the maximal value of 3.2 pm/μrad. The plotted curves are for equidistant displacements between the maximal displacements. Only one component was shifted at a time, all other components remained untouched.

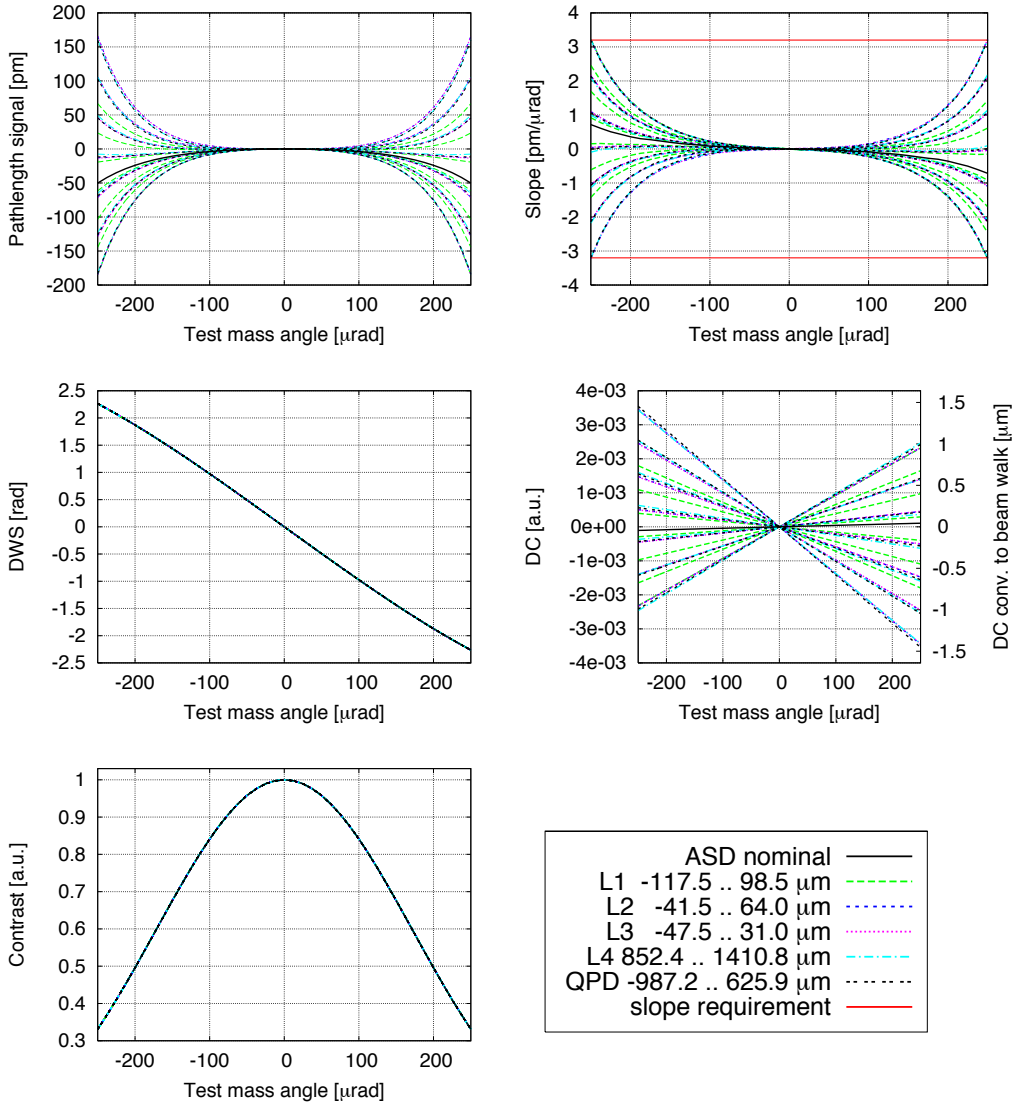


**Figure D.2.:** ASD four lens beam compressor: longitudinal displacements in equidistant steps while all other components remained untouched. The curves for L1-shifts do not match because L1 touches L2 before the maximal slope is reached. The distribution of the L1-curves is thus different from those of the other components.

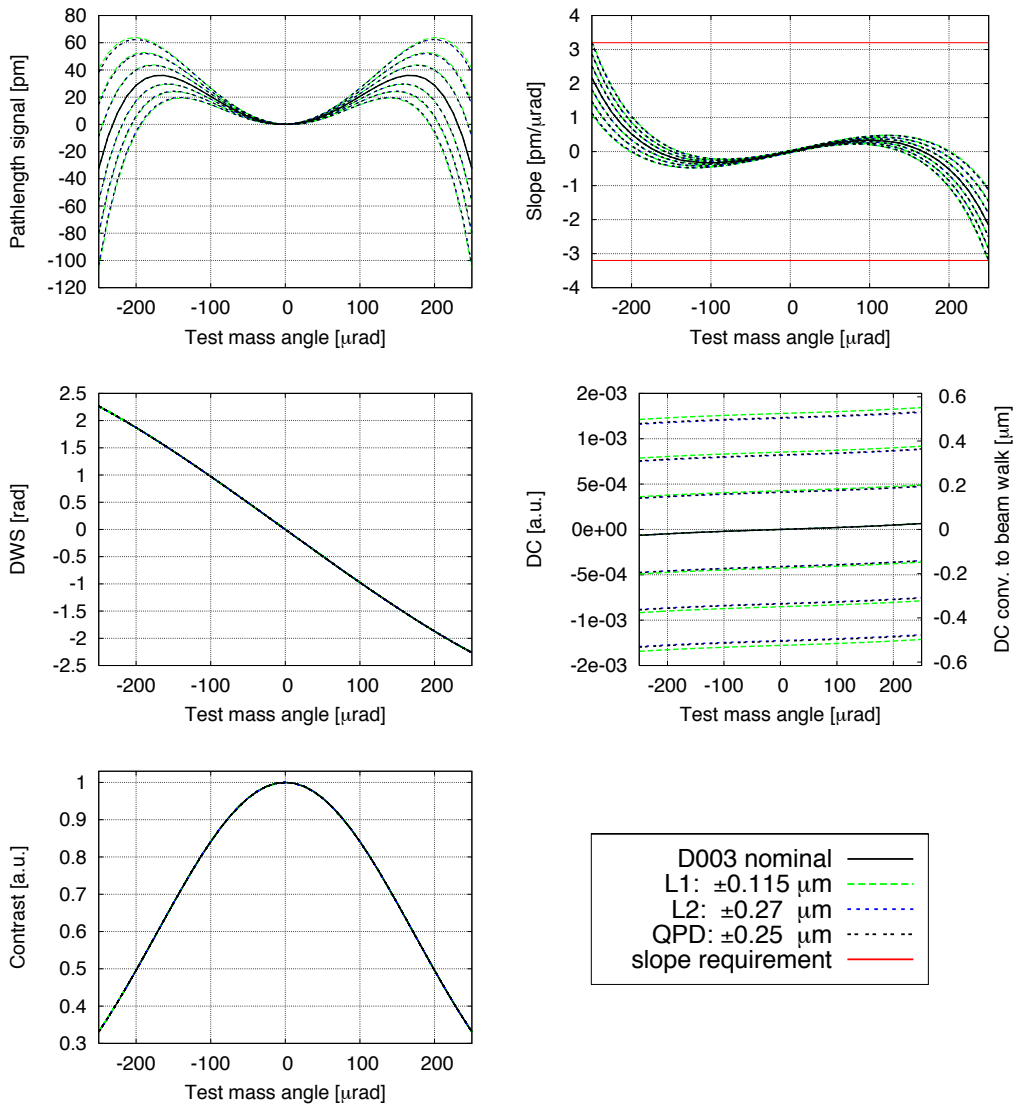


**Figure D.3.:** Beam compressor **D003**: Influence of **lateral** displacement of either L1, L2 or the QPD. Each component was shifted in 7 equidistant steps, while all other components remained untouched.

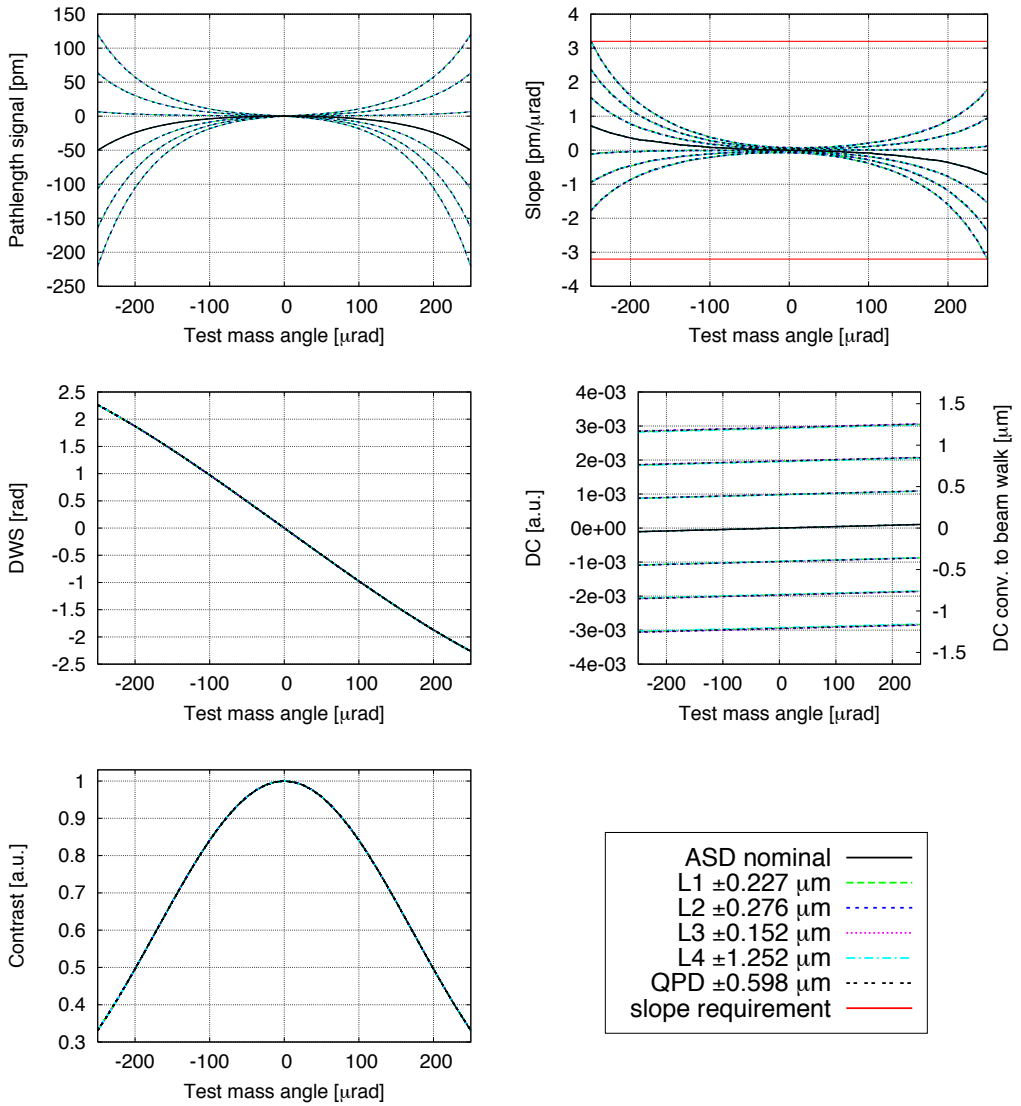


**Figure D.4:** ASD four lens beam compressor: lateral displacements in equidistant steps while all other components remained untouched.

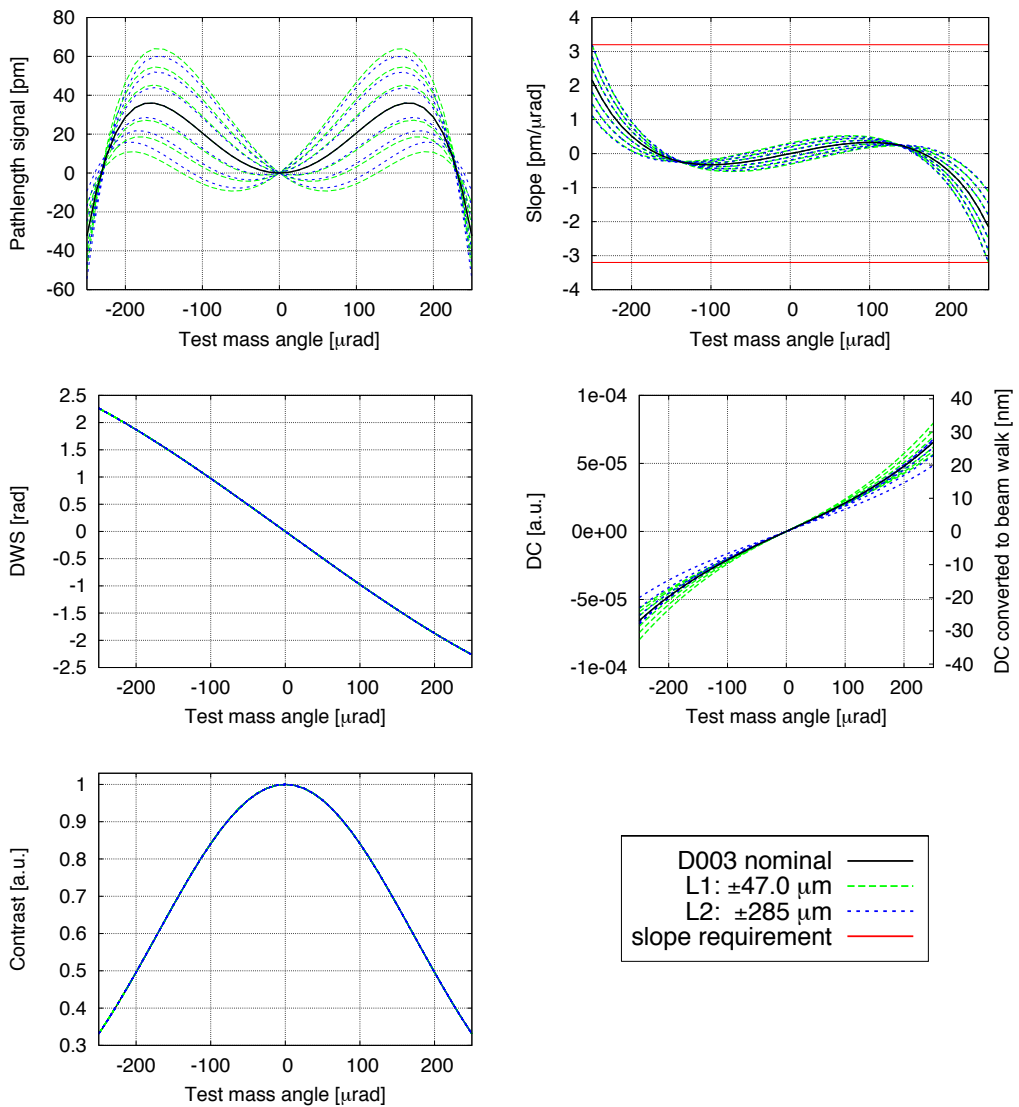


**Figure D.5.: D003 beam compressor: lateral displacements in equidistant steps.** After each displacement, the QPD was **realigned** to the reference beam. This causes the zero DC-signal for nominal test mass angle.

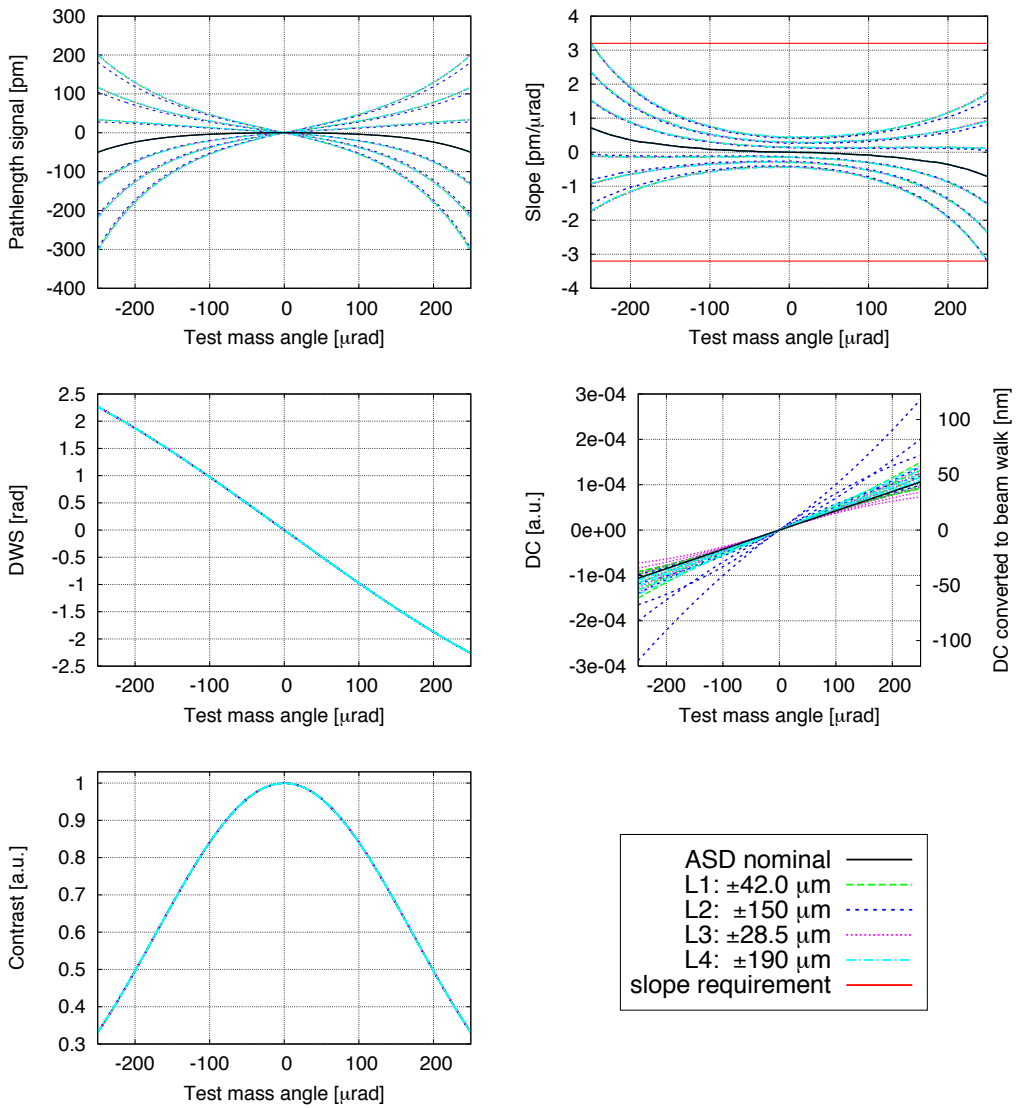


**Figure D.6.:** ASD four lens beam compressor: **lateral** displacements in equidistant steps with realigned QPDs.

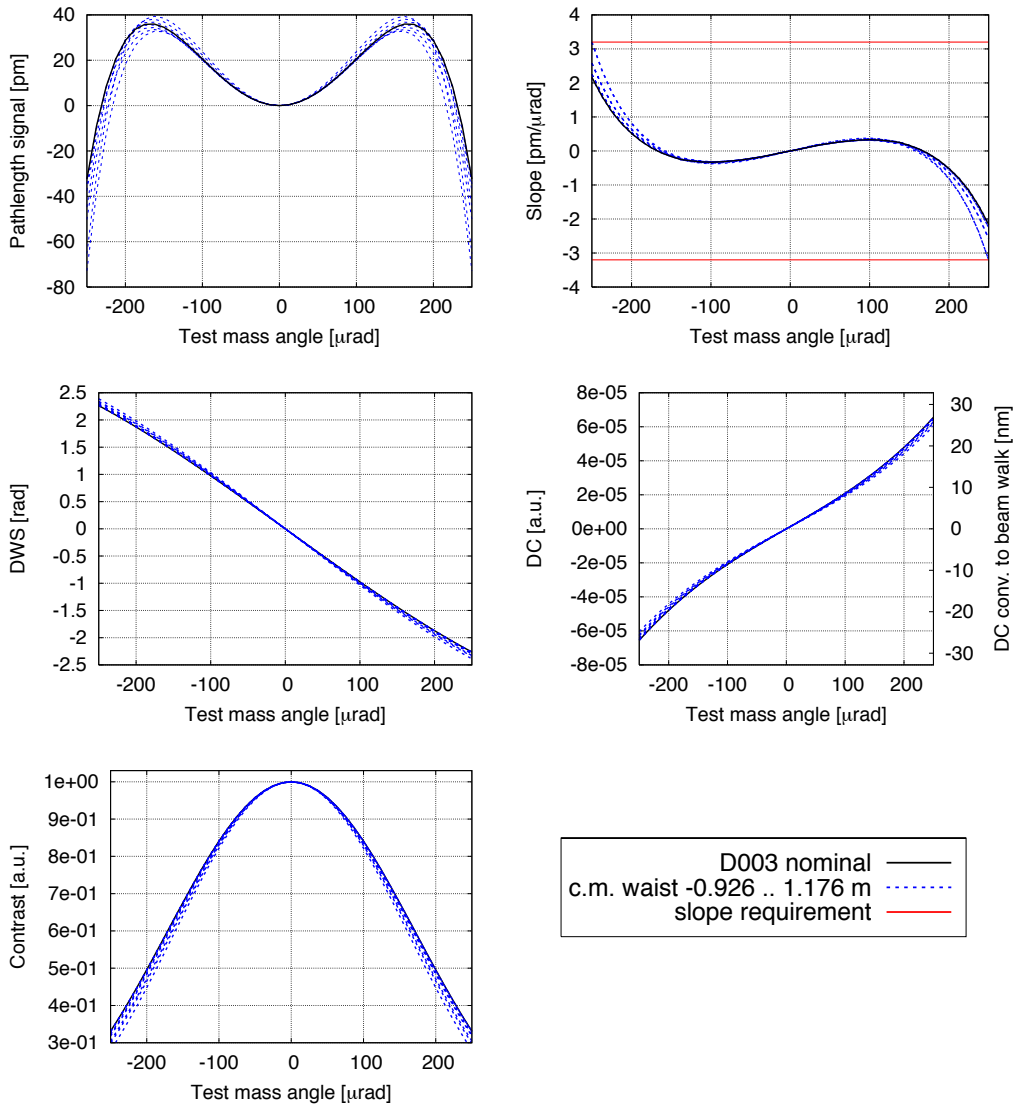


**Figure D.7.:** Beam compressor **D003: common mode waist displacement**. These graphs show that the waist can be shifted by roughly  $\pm 1$  m away from the test mass before the slope requirement is violated. It is thus not necessary to place the waist on the test mass in the first place, provided that collimated mode matched beams enter the imaging optics.



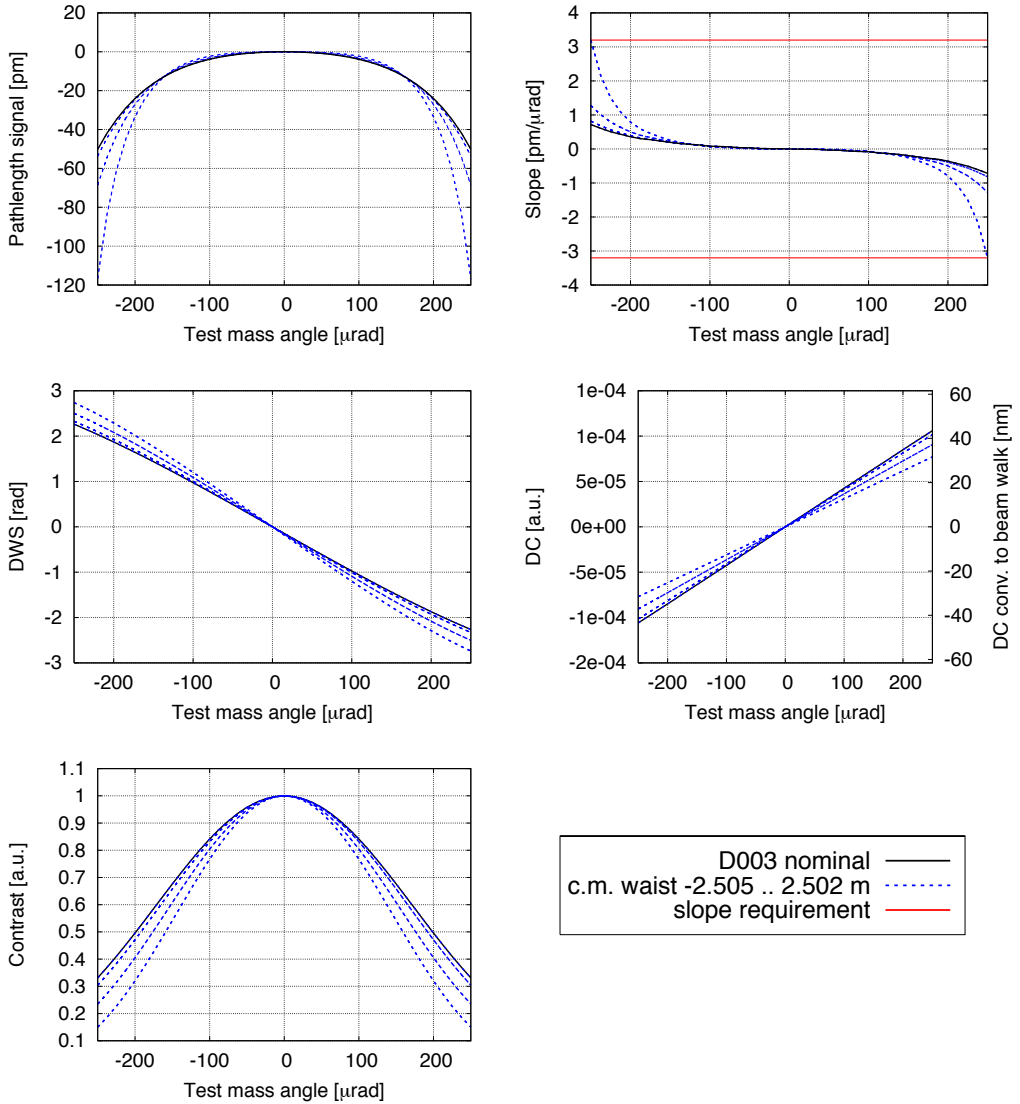


**Figure D.8.: Beam compressor ASD: common mode waist displacement.** These graphs show that the waist can be shifted by roughly  $\pm 2.5$  m away from the test mass before the slope requirement is violated. It is thus not necessary to place the waist on the test mass in the first place, provided that collimated mode matched beams enter the imaging optics.

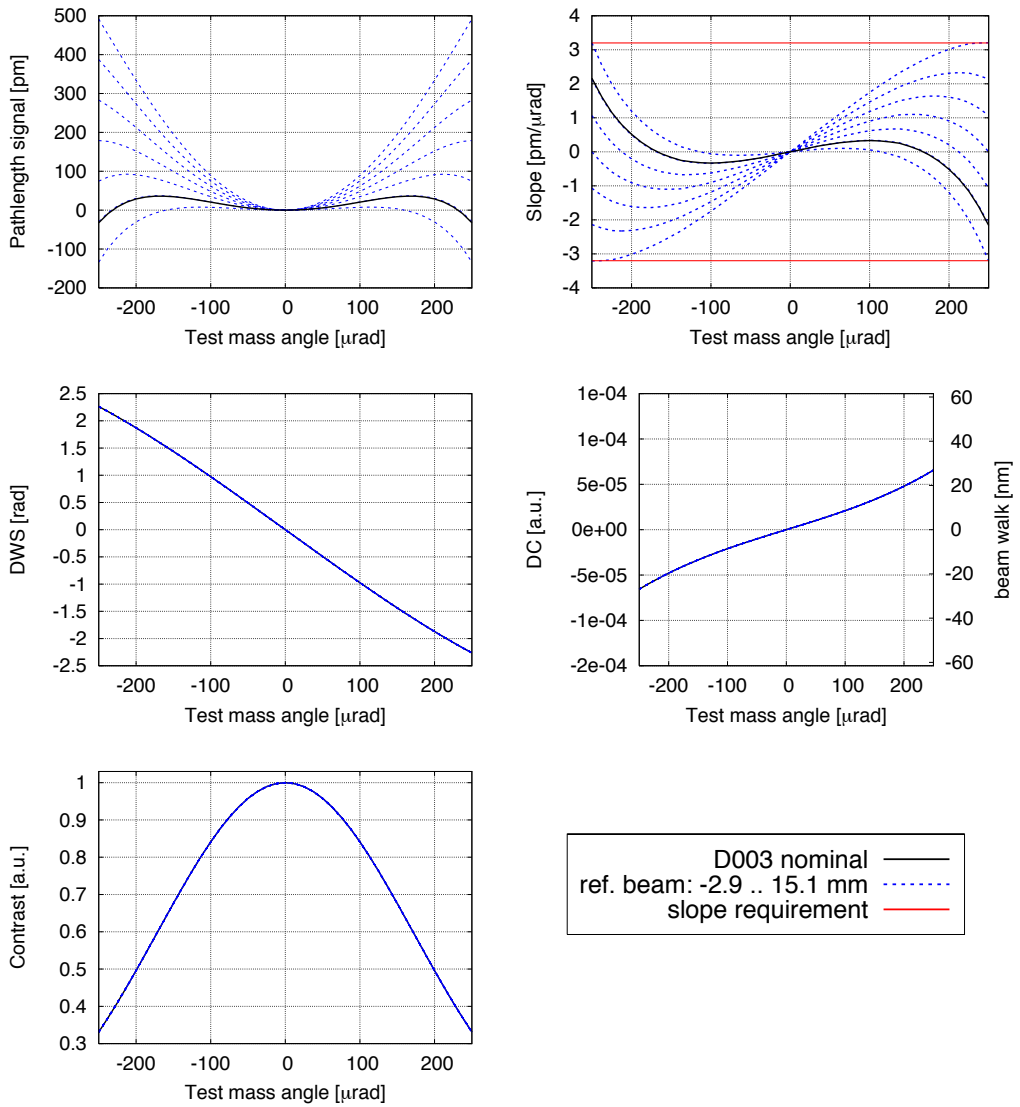
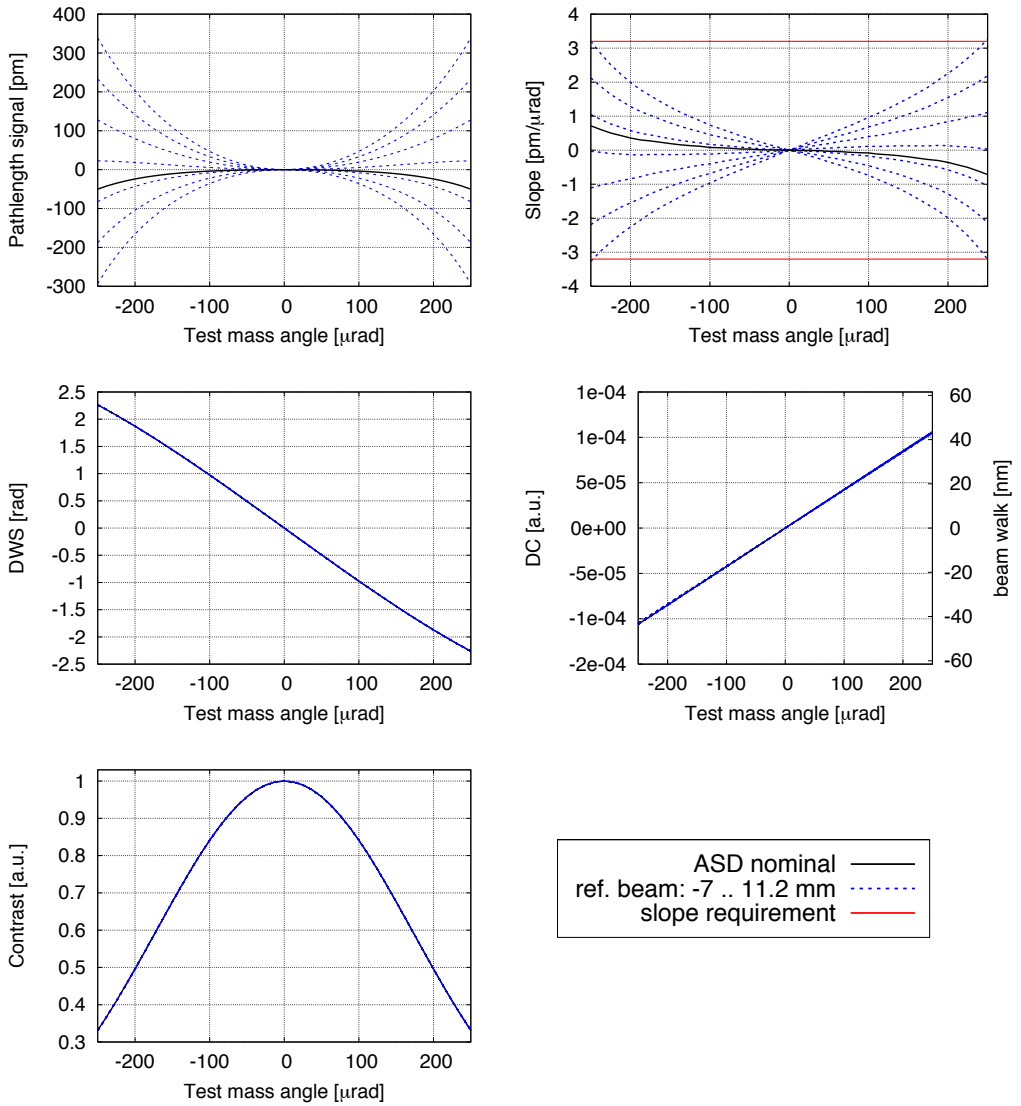


Figure D.9.: Beam compressor D003: Influence of mode mismatch.



**Figure D.10.:** ASD four lens beam compressor: **mode mismatch** in equidistant steps while all other components remained untouched.



# Glossary

**aberration**, short for “optical aberration” which is a generic term for imperfections in image formation by an optical system. The main types of aberration are Spherical aberration (which occurs when light rays strike a lens or mirror near its edge), Chromatic aberration (caused by differences in the refractive index for different wavelengths of light) and Defocus aberration (which occurs when a system is out of focus). (p. 134)

**achromatic lens**, a lens which brings beams of (typically two specific) different wavelengths into the same focus. (p. 136)

**ADC**, analog to digital converter, a device which transforms an input voltage into a proportional digital number. (p. 23)

**adjustable bonding**, or adjuster aided bonding, the alignment technique used during a bonding procedure of critical components. The components are positioned by two probes called adjusters, which are in direct contact to the component that is to be aligned (cf. section 5.3.1). (p. 62)

**AEI**, Albert Einstein Institute, name of the Max Planck Institute for Gravitational Physics (p. 24, 66, 119, 132)

**AIGO**, Australian international gravitational wave observatory, a planned interferometric gravitational wave detector which shall be located 80 km north of Perth in western Australia. This location in the southern hemisphere makes AIGO important. Adding a detector on the southern hemisphere to the currently

operating array of gravitational wave detectors will increase the sky coverage and improve the angular resolution for gravitational wave detection [Barriga2010]. Technically, AIGO will be similar to advanced LIGO: it is planned to have an arm length of 4 km, Fabry-Pérot cavities and dual recycling. Therefore, the expected sensitivity is the sensitivity of advanced LIGO. (p. 2)

**amplitude spectral density**,  $S(\cdot)$ , referred to throughout this work as “spectrum”, also called linear spectral density. An amplitude spectral density is the square root of a power spectral density (PSD). Generally, a PSD is computed by the absolute square of the Fourier transformation divided by the frequency resolution (which is the inverse of the measurement time). Furthermore, a window function is used in order to avoid aliasing effects. A PSD gives the frequency composition of a measurement variable (e.g. the measured arm length in an interferometer) per frequency. Due to the normalization, PSDs of measurements performed with different measurement times show the same amplitude. As a result of the normalization, PSDs have the unit “(basic unit)<sup>2</sup>/Hz”, e.g. V<sup>2</sup>/Hz. Consequently, the linear spectral density has the generic unit “basic unit/ $\sqrt{\text{Hz}}$ ”, e.g. m/ $\sqrt{\text{Hz}}$ . Detailed information about amplitude and power spectral densities can be found in [Heinzel2002]. The software LPSD to compute these spectra is described in [Tröbs2006, Tröbs2009]. (p. 53, 91)

**AOM**, acousto-optic modulator. An AOM consists of a solid body or crystal in which acoustic waves are generated. Transmitting laser beams are diffracted and frequency shifted by the created grating. AOMs are used in this context to generate the frequency shift between the two interfering beams in a heterodyne interferometer. (p. 13, 35)

**aperture stop**, component in an optical imaging system that limits the size of a ray beam. Usually the aperture stop is a diaphragm but it can also be the edges of a lens, mirror or a photodiode in the system. Its size influences brightness, sharpness and contrast of the image. (p. 135)

**arm length**,  $L$ , distance between remote test masses (LISA and LISA Pathfinder) or distance between the central beam splitter and an end mirror in a Michelson interferometer. In LISA Pathfinder, the arm length is approximately 35 cm, in LISA about 5 million kilometer with a variation of roughly 1% over a year. The LISA arm length was chosen as a trade-off between having a value as large as possible to increase the sensitivity of the detector (eq. (2.1)) and keeping the arm length short enough to receive sufficient amount of beam power on the remote spacecraft. With 5 million kilometer arm length the spot diameter on the remote spacecraft is approximately 17 km. From this large beam only a small fraction is collected by the telescope such that from approximately 720 mW transmitted beam power only 230 pW are received on the remote optical bench [LOB-06]. The received beam is then split, such that only 100 pW impinge on the redundant photodiodes of the science interferometer. (p. 12, 6)

**ASD**, EADS Astrium GmbH Deutschland, an industry partner involved in LISA and LISA Pathfinder. (p. 56, 66, 96, 134, 170, 176)

**aspheric lens**, a lens with a rotational symmetric surface that cannot be expressed by the surface of a sphere but typically a conic section, for instance a hyperbola or parabola. These lenses have to be expressed by a set of parameters that characterize their curvature. By matching the curvature of the lens to the beam curvature, aberration effects can be reduced. In particular spherical aberration, which is unavoidable for spherical lenses, can be fully eliminated. (p. 136, 76)

**astronomical telescope**, A system consisting of two convex lenses positioned in the sum of their focal lengths (cf. figure 10.3). The focal length of an astronomical telescope is infinite, such that it images collimated beams to collimated beams. Key parameters are a comparably large size and an intermediate focus. An astronomical telescope design was suggested and investigated for use as a beam compressor on the LISA optical bench. (p. 136, 134)

**AU**, astronomical unit, defined as the mean distance between the Earth and the Sun over one Earth orbit.  $1 \text{ AU} = 149.6 \cdot 10^6 \text{ km} = 4.8481 \cdot 10^{-6} \text{ pc}$ . (p. 5)

**back focal length**,  $f^b$  distance between the secondary refracting surface of a lens or lens system and the secondary focal point (cf. figure 10.4). The back focal length is computed from the (effective) focal length  $f$ , thickness  $d$ , radius of curvature of the primary surface  $R_1$  and the refractive index  $n$  of the material by:  $f^b = f - \frac{f(n-1)d}{R_1 n}$  [Hecht][Smith]. Throughout this thesis, back and front focal length of all lenses used are assumed to be equal. (p. 138)

**baseplate**, for LISA Pathfinder, the  $200 \times 212 \times 45 \text{ mm}$  Zerodur slab to which the optical components (10 mirrors, 12 beam splitters) and 10 photodiodes are attached. The baseplate has four triangular pockets on its underside to reduce its

weight. Furthermore, the baseplate has 4 mounting holes on each side which are needed to mount the baseplate within the LCA. The form and size of the LISA baseplate is not yet finally decided. For the EBB design, a massive 580 mm diameter  $\times$  80 mm high circular baseplate without any light-weighting is planned. (p. 72, 58, 68)

**BB**, breadboard which is effectively a prototype. According to ECSS: ‘Breadboard models are used to demonstrate key aspects of a design are feasible and understood. They should be manufactured during the early stages of a project such that maximum benefit can be derived. They need not be flight representative in respect of the materials used but are functionally representative of the key aspects to be proven.’ [ECSS2000] (p. 202)

**BBO**, Big Bang Observer, a planned gravitational wave detector in space that might launch in a few decades. Its aim is to measure gravitational waves that originate from the inflation in the very early universe. Key parameters are according to references [Harms2008, Cutler2006] 12 spacecraft flying in the formation shown in figure 1.6 where each interferometer arm has a length of  $5 \cdot 10^7$  m. Aboard each spacecraft will be mirrors of 3.5 m diameter with residual acceleration noise of less than  $3 \cdot 10^{-17} \frac{\text{m}}{(\text{s}^2\sqrt{\text{Hz}})}$  whose attitude will be measured by lasers with a wavelength of 500 nm and an initial power of 300 W. For comparison: The nominal initial laser power in LISA is 1.5 W and LISA will demonstrate free floating test masses with a residual acceleration noise of  $3 \cdot 10^{-15} \frac{\text{m}}{(\text{s}^2\sqrt{\text{Hz}})}$  at 0.1 mHz. (p. 2)

**beam combiner**, in a Michelson interferometer there is one beam splitter which first splits the beam into two and recombines them later on. In a Mach Zehnder interferometer, two semi transparent mirrors are needed. The first one splits the

beam into a measurement and a reference beam. The second beam splitter is the beam combiner, which recombines these two beams. (cf. for instance figure 2.2). On the LTP OBI beam combiners have dimensions of  $20 \times 20 \times 7$  mm (H $\times$ W $\times$ T) with a precision of  $\pm 0.4$  mm in height and width, and  $\pm 0.1$  mm in thickness. [UGL-3001, req. LTP-PFM-OBI-4301] Thereby they are slightly larger than all other mirrors and beam splitters on the optical bench, which have a dimension of  $20 \times 15 \times 7$  mm. In section 7.3 it is shown that the beam combiners are critical components, since any angular misalignment causes an offset in the DWS calibration function. Without calibration, the test masses would thereby pick up the angular misalignment of the beam combiners which causes additional angular misalignment in the order of  $\pm 70$   $\mu\text{rad}$  for test mass 1 and  $\pm 140$   $\mu\text{rad}$  for test mass 2. (p. 14, 35, 128)

**beam parameters**, here, a set of parameter that fully describes a Gaussian beam in particular one that impinges on a quadrant photodiode (QPD). These parameters are needed for two beams as input to QPD.c in order to compute heterodyne signals. Beam parameters are the Rayleigh range  $z_0$ , the distance  $z$  of the position of interest measured from the waist, the horizontal distance of the beam centroid to the detector, the horizontal distance  $x_0$  of the beam centroid to the center of the QPD, the in plane incident angle  $\alpha$  of the beam with respect to the normal on the QPD surface, and the total pathlength  $s$  propagated from beam definition to the QPD. Here, the out of plane displacement  $y_0$  and angle are neglected, because these values cannot be computed from the two dimensional software OptoCad, which was used for all computations throughout this thesis. (p. 31, 72, 76, 111)

**beat frequency**, frequency shift be-

tween two slightly different frequencies. Throughout this work, this beat frequency is called heterodyne frequency ( $f_{\text{het}}$  or if angular  $\omega_{\text{het}}$ ), since the frequency differences of interest occur in heterodyne interferometers. (p. 14)

**BH**, black hole (p. 3)

**bonded**, used throughout this work as an abbreviation for bonded with  $\rightarrow$  hydroxide-catalysis bonding. (p. 61, 35, 58)

**BS**, beam splitter. See  $\rightarrow$  beam combiner for more information. (p. 58)

**capacitive sensor**, generally a device that measures positions, displacements etc. by sensing changes of capacitances. They have a wide range of application today, like in touch screens, laptop trackpads, MP3 players and many more. Capacitive sensors are used in the LTP and LISA inertial sensors to measure the position and displacement of the enclosed test masses. (p. 66)

**central limit theorem**, a theorem in probability theory which states that a random number which depends on the statistics of a large variety of independent random numbers with finite mean and variance, is approximately normally distributed. (p. 172)

**CLIO**, Cryogenic Laser Interferometer Observatory, an interferometric gravitational wave detector with cryogenic mirrors which is situated in the Kamioka mine in Japan. CLIO has an arm length of 100 m, and reached in 2006 a strain sensitivity of  $6 \cdot 10^{-21} / \sqrt{\text{Hz}}$  at 300 K [Yamamoto2008]. CLIO is used to experimentally test cryogenic mirrors for LCGT. (p. 2, 4)

**CMM**, coordinate measurement machine (p. 61)

**CND**, clipped normal distribution, the type of distribution used for all random variables in the LTP-OBI-Alignment simulation. Please see section A.4 for further details. (p. 172, 73)

**collimated**, in geometrical optics a beam is said to be collimated if its focus is at infinity, that means the beam is a plane wave describable by parallel rays. Gaussian beams fulfill this definition solely in one point: their waist. They are called collimated for all points within a Rayleigh range  $z_R$  since the spot size enlarges in this range only by a factor of  $\sqrt{2}$ . (p. 176, 136, 140)

**CoM**, center of mass (p. 82)

**compression factor**, ratio between beam size before and after a lens system. In fact the compression factor is the magnification of the lens system. (p. 133, 132, 137, 148)

**contrast**, one of the heterodyne signals defined as  $c := \frac{P_{\text{max}} - P_{\text{min}}}{P_{\text{max}} + P_{\text{min}}}$ . However, the computation of the contrast is in LTP and QPD.c not done by using this equation but by the equations described in section 2.3. (p. 17, 12, 34)

**COTS**, commercial off the shelf - in contrast to custom made. Custom made lenses are generally expensive, since each coating run has a high fixed cost. It was therefore decided to use COTS lenses for the LISA OBI pre-experiments. (p. 138, 146, 145)

**CQP**, calibrated quadrant photodiode pair. A CQP is a device which measures the angle and position of a beam to high accuracy. It was developed by UGL [Fitzsimons2010] for the precision bonding needed for the LTP OBI. The working principle is illustrated in figure 5.10: a beam is split on a beam splitter. One beam segment is propagated over a short distance to one QPD, the other beam segment over a larger distance to the second QPD. If the QPDs are calibrated, a beam impinging on the center of one QPD will only hit the center of the other QPD, if the beam angle is optimally aligned to the CQP. This device was used at UGL during the bonding procedure of the LTP OBI. It achieves precisions in



the order of  $\pm 2.5 \mu\text{m}$  and  $\pm 30 \mu\text{rad}$  according to [Bogenstahl2010]. Currently a CQP is being built at AEI with a slightly different layout than the UGL CQP. A photograph of the UGL CQP is shown in figure 5.11. (p. 61, 64)

**coupling factor**, ( $k_{\text{DoF}}^{\text{Signal}}$ ) first derivative of a heterodyne signal by a degree of freedom of the interferometer at a specific working point. Its inverse is  $\frac{1}{k_{\text{DoF}}^{\text{Signal}}} = k_{\text{Signal}}^{\text{DoF}}$ . The coupling factor of test mass 1 (TM1) longitudinal shift into the pathlength signal is for instance  $k_{x_1}^{\Delta L_m} = 1.99382$  for LISA Pathfinder. This value is computed by setting up a realistic OBI and then shifting TM1 by  $\pm \epsilon$  in direction of TM2 and computing the numerical derivative  $k_{x_1}^{\Delta L_m} = \frac{\Delta L_m(x_1 + \epsilon) - \Delta L_m(x_1 - \epsilon)}{2\epsilon}$ . (p. 43, 20, 74, 81, 83, 87, 168)

**DC signal**, DC originates from “direct current”. Throughout this work a DC signal is an alignment signal, which effectively measures the position of the beam centroid on a quadrant photodiode (QPD). The horizontal DC signal  $\text{DC}_h$  is defined as the difference of the measured beam power on the left and right hand side of a QPD divided by the overall measured power  $\text{DC}_h := \frac{P_{\text{left}} - P_{\text{right}}}{P_{\text{left}} + P_{\text{right}}}$ . The vertical DC signal is defined likewise as  $\text{DC}_v := \frac{P_{\text{top}} - P_{\text{bottom}}}{P_{\text{top}} + P_{\text{bottom}}}$ . Throughout this work, generally the horizontal DC signal was computed such that the index  $h$  could be omitted. An analytical computation of the DC signal is given in section 4.6. (p. 20, 34, 43, 62, 144)

**DC-spectrum**, As shown in section 4.6, the DC signal is in a certain range proportional to beam displacement on the QPD. The DC signal senses therefore beam displacements, such that pointing jitter is equivalently sensed as noise in the DC signal. This noise can be represented in form of an amplitude spectral density, which is then referred to as DC-spectrum.

In section 8.2.3 measured DC-spectra are used to estimate the amount of pointing jitter on the power monitor PDA2 and compute the resulting relative power readout noise of this photodiode. (p. 117, 20)

**DECIGO**, “Deci-hertz Interferometer Gravitational Wave Observatory”, a spaceborne interferometric gravitational wave detector to be launched by Japan’s national aerospace agency (JAXA) in 2024. DECIGO consists of 12 satellites in the BBO-formation. Key elements are Fabry-Pérot arm cavities, mirror diameters of 1 m corresponding to mirror masses of 100 kg and 10 W laser beams. DECIGO will be most sensitive in the range of 0.1 Hz to 100 Hz and thus bridges between LISA and the terrestrial detectors. Further information can be found in [Sato2009]. (p. 2)

**DECIGO Pathfinder**, (DPF) The precursor mission of DECIGO and similar to LISA Pathfinder: DPF will carry an interferometer with approximately 30 cm arm length, use a comparable caging mechanism as in LPF and drag free control. Major differences to LISA Pathfinder are arm cavities, polarizing optics and the use of Yb:YAG lasers (1030 nm) [2]. Furthermore DPF will carry another payload to measure the gravity field of the earth. Therefore, DPF will be launched to a low earth orbit. The earliest possible launch is currently estimated to be in 2015 [13]. (p. 2)

**DFACS**, the drag free attitude control system which controls the actuators and the spacecraft according to a chosen mode. In LTP science mode, for example, the DFACS sends commands to the micro-Newton thrusters such that the test mass 1 (TM1) remains drag free. Furthermore, it commands the actuators of TM2 in order to keep the distance between both test masses constant (without affecting the differential measurement in

the measurement band). (p. **55**, 66, 79, 81)

**divergence**,  $\theta_{\text{div}}$ , the radius of a Gaussian beam  $w(z)$  approaches a straight line for distances that are large with respect to the Rayleigh range. The angle between this tangent and the beams central axis is the divergence  $\theta_{\text{div}}$  (cf. figure 3.3). It is computed by  $\theta_{\text{div}} = \arctan(\frac{w_0}{z_0}) = \arctan(\frac{\lambda}{\pi w_0})$ . This shows that the better a beam is focussed, that means the smaller  $w_0$ , the faster it spreads out. Thus, a Gaussian beam can only be reasonably collimated, if it has a large waist. (p. **140**)

**DMU**, data management unit. As part of the ‘data and diagnostic subsystem’, the DMU performs acquisition and processing of phasemeter data for example for test mass attitude and position readout, optical pathlength difference stabilization and laser frequency stabilization. More information can for instance be found in [ASD-3008]. (p. **23**)

**DoF**, degree of freedom. (p. **43**, 82)

**DPF**, acronym for →DECIGO Pathfinder (p. **6**)

**DRS**, disturbance reduction system, the second instrument besides LTP aboard LISA Pathfinder. Originally DRS and LTP were comparable instruments and DRS contained its own test masses which were meant to be monitored by a homodyne interferometer. However, DRS was descope and consists by today mainly of colloidal thrusters, a control mechanism for the spacecraft and will make use of the optical metrology system (OMS) of LTP. (p. **53**, 5)

**DTM**, dummy test mass, a mirror used as a replacement for the test masses during the alignment procedure of the OBI and any performance test of an OBI on ground. In section 7.3 it is shown that the alignment of the dummy test masses during the bonding procedure of the OBI affects the alignment of the real

test masses in science mode. (p. **65**, 77, 99)

**DWS signal**, differential wavefront sensing signal. One of the heterodyne signals which is in a certain range proportional the relative angle between two interfering beams impinging on a photodiode. The DWS signals of the LTP x1- and x12-interferometer are used for the angular readout and control of test masses and spacecraft. DWS signals are generated by comparing the phase signals of the various quadrants of a QPD, for instance the horizontal DWS signal is computed by  $DWS_h = \phi_{\text{left}} - \phi_{\text{right}}$ . The technique is based on [Morrison1994-1] and [Morrison1994-2]. (p. **20**, 33, 63, 144)

**EBB**, elegant breadboard. By definition, an EBB is a breadboard (BB, that means a prototype) which is representative in form, fit and function to an engineering model (EM). (p. **126**)

**ECSS**, European Cooperation for Space Standardization (p. **199**)

**electrical null**, the position of the test mass in flight, when the signals of the capacitive sensors are balanced. The electrical null is thus close to, but not necessarily identical to the geometrical center of the electrode housing. (p. **66**, 69, 78)

**EM**, engineering model, defined by the European Cooperation for Space Standardization (ECSS) as ‘a model which is flight representative in form, fit and function, without full redundancy and hi-rel parts. The engineering models are used for functional qualification, except redundancy verification, failure survival demonstration and parameter drift checking.’ [ECSS1998] (p. **58**, 63, 74, 117, 174, 202)

**entrance pupil**, in geometrical optics, image of the aperture stop in the object space - i.e. close to the object. The location of the entrance pupil is the in-

tersection point of the principal ray and the optical axis (cf. figure 10.2). If the aperture stop is located between object and first lens, then the location of the entrance pupil is the position of the aperture stop. See for example [Hecht, sec 5.3.2] or [Smith, sec 6.2]. (p. 135)

**error function**,  $\text{erf}(x)$ , defined as  $\text{erf}(x) := \frac{2}{\sqrt{\pi}} \int_0^x dt e^{-t^2}$  (p. 44)

**ESA**, European Space Agency. LISA and LISA Pathfinder are joint missions of ESA and NASA, that means for instance, that both agencies provide money for the industrial development of needed technology. Mission Control of LISA Pathfinder will be from ESA's ESOC, the European Space Operations Centre in Darmstadt. (p. 2)

**ET**, Einstein Telescope, a European gravitational wave detector which is currently in its design study phase. At present, arm length of 10 kms, an underground site and squeezed light input and a Sagnac shape are under discussion. See [6] for more information. (p. 2)

**exit pupil**, in geometrical optics, image of the aperture stop in the image space, i.e. close to the image, see figure 10.2 for an illustration. It is shown in section 10.3 that positioning a QPD in the exit pupil of a lens system decouples the pathlength readout from the angular jitter of a component in the entrance pupil of the lens system. A description of how the position of the exit pupil can be constructed is given in section 10.2. (p. 135, 137, 144, 145)

**eye relief**, distance between the last surface of a lens system and the exit pupil in classical geometrical optics. Its name originates from the fact that the human eye is usually set in the position of the exit pupil of an optic (for instance a telescope) in order to achieve a clear image. The eye relief is then the distance between the last surface of the optics

and eye. For this reason, the term eye relief is used here directly for the distance between last surface of the lens system and detector (QPD). (p. 175)

**field stop**, a diaphragm that does not limit the beam size in an imaging optics. It can be used to filter stray light. (p. 175)

**FIOS**, Fiber injector optical subassembly. For LISA Pathfinder, there is one FIOS for the measurement and one for the reference beam, that means there is no redundant counterpart. The experience gained at LISA Pathfinder is, that a FIOS is a critical system, such that it was decided to place redundant counterparts on the LISA optical bench. (p. 58, 64, 87, 107, 127, 129)

**FM**, flight model. According to ECSS [ECSS2000]: 'The flight model is the realized design delivered for flight. The flight model is subject to acceptance testing to demonstrate the actual build performs as required and is free from manufacturing defects.' (p. 58, 63, 74)

**focal length**, distance from the principal plane of a lens to the focal point. The focal length of a thick lens can be computed from the radii of curvature  $R_1$  and  $R_2$ , the refractive index  $n$  of the material and the thickness  $d$  of the lens by  $\frac{1}{f} = (n - 1) \left[ \frac{1}{R_1} - \frac{1}{R_2} + \frac{(n-1)d}{nR_1R_2} \right]$ . (p. 138)

**focal point**, the focal point of a lens is the point where parallel light rays transmitting through the lens intersect. The focal point is generally not the position of the waist of a Gaussian beam. Only if the beam waist of the initial beam was located in the primary focal point of the lens, the waist of the beam segment that passed the lens will also be in the focal point, cf. eq. (B.21). (p. 138)

**front focal length**,  $f^f$ , distance between primary focal point of a lens or lens system and the vertex of its primary

refracting surface. For thick lenses the front focal length is computed from the focal length  $f$ , thickness  $d$ , radius of curvature of the secondary surface  $R_2$  and the refractive index  $n$  of the material by:  $f^f = f - \frac{f(n-1)d}{R_2 n}$  [Hecht][Smith]. (p. 138, 198)

**GEO600**, an interferometric gravitational wave detector located near Hanover (Germany). GEO600 is a project in collaboration of Germany and the UK. It has a geometrical arm length of 600 m, and an effective arm length of 1200 m due to folding. Even though GEO600 has shorter arms than LIGO or VIRGO, its key techniques like dual recycling or quasi-monolithic fused silica suspensions of the test masses that allow a reduction in thermal noise give GEO600 high sensitivity and let it take an important role in the international collaboration. The upgrades planned for 2010 and 2011 are described in reference [Lück2010]. (p. 2, 11)

**ghost beam**, a specific type of stray light, generated by back reflection from secondary surfaces of mirrors, beam splitters or lenses. Ghost beams are phase shifted and parallel to the main beam in case of beam splitters with non-normal incidence. In case of normal incidence they perfectly coincide with the main beam e.g. in polarizing beam splitter cubes. Ghost beams impinging on photodiodes are a major noise source in case of LISA and LISA Pathfinder and usually need to have a power less than about 1 pW in order to fulfill the requirements. (p. 126, 175)

**Gouy phase**, ( $\zeta(z) = \arctan(z/z_0)$ ). An additional phase accumulated by a Gaussian beam during a propagation along  $z$ . The Gouy phase is zero in the waist and goes to  $\pm\pi/2$  as  $z$  goes to  $\pm$  infinity. The shape of the Gouy phase is plotted in figure 3.4(b). Con-

text: Gaussian beams accumulate a phase of  $\phi$  that splits into three parts:  $\phi = -kz + \frac{kr^2}{2R(z)} + \zeta(z)$  where the first term is the longitudinal phase, the second considers the curvature of the phase front of the Gaussian beam and the resulting additional phase at off axis points and the third term finally is the Gouy phase. (p. 27)

**gravity gradient noise**, noise in earth-bound gravitational wave detectors which originates from changes in the gravitational field of the Earth. These changes are for example caused by seismic waves passing the ground under the detector. For further information see for example [Hughes1998]. (p. 4)

**GRS**, gravitational reference sensor,  $\rightarrow$  inertial sensor. (p. 54, 125)

**heterodyne**, an interferometer is called heterodyne if the superimposing beams have different frequencies. (p. 13)

**heterodyne frequency**,  $f_{\text{het}}$  the frequency offset between the superimposing beams of a heterodyne interferometer. In case of LISA Pathfinder, the heterodyne frequency is approximately  $f_{\text{het}} \approx 1$  kHz, and between 2 and 20 MHz in LISA. The angular heterodyne frequency is defined as  $\omega_{\text{het}} = 2\pi f_{\text{het}}$ . (p. 14)

**heterodyne signals**, generic term for the pathlength signal, DWS and DC signals, contrast and power readout. The term “heterodyne signals” is commonly used in the LISA Pathfinder community to differ the signals of the heterodyne interferometer from the variety of signals LISA Pathfinder generates, like the signals of the capacitive sensors, temperature sensors, charge sensors and magnetometer, star trackers and many more. (p. 18, 72)

**homodyne**, an interferometer is said to be homodyne if the interfering beams have the same frequency. (p. 12, 13)

**hydroxide-catalysis bonding**, a tech-

nique to induce crystal growth between two highly polished typically silicate-based materials like fused silica, ULE or Zerodur such that one quasi-monolithic composite is formed. This is achieved by polishing the respective surfaces, applying a bonding fluid and bringing the surfaces into contact. The bonding fluid can in principal be plain water, however to increase the quality special bonding fluids like sodium hydroxide (NaOH), potassium hydroxide (KOH) and sodium silicate ( $\text{Na}_2\text{SiO}_3$ ) dissolved in water are used [Veggel2007]. The working principle is that the  $\text{OH}^-$  ions etch both surfaces which results in chemical reactions that finally lead to siloxane chains:  $(\text{HO})_3\text{SiOSi}(\text{OH})_3$  that rigidly connect the two materials. Once a bond is fully cured, it is impossible to break it again. Attempts to break the bond generally result in breaking the material at its weakest location, which is typically not the bonding surface. This technique was first described in reference [Elife2005], which also contains a description of the chemistry involved. (p. 61, 35, 126)

**IAF**, interferometer axis frame. A coordinate frame in LISA Pathfinder which has its origin in the reflection point on the free-floating test mass 1 (IAF1) or 2 (IAF2). The IAF is used to state requirements for the in flight alignment of the test masses in LISA Pathfinder. See figure 5.13(b) for an illustration and page 69 for more information. Requirements for the alignment of the IAF are given e.g. in [ASD-3020, iss 6]. (p. 69, 79)

**IfoCad**, a script based three dimensional ray tracing tool written by G. Heinzl that also computes heterodyne signals for Gaussian beams and optimizes interferometer setups. It is currently being upgraded to include computations for top hat beams. (p. 26, 132, 145)

**in plane**, in the plane of the OBI (p. 91,

148)

**in-flight alignment**, The procedure after decaging, where both test masses are successively aligned to contrast, DC signal and finally DWS-signal, as described in section 5.3.3. In section 7.3.1 it is shown that an in-flight alignment to  $\text{DWS}=0$  as originally planned results in misalignments violating several requirements. It was therefore suggested and is currently planned for LTP, to align the test masses to a previously measured offset in order to improve the alignment. (p. 67, 99, 99, 100, 107)

**inertial sensor**, (IS), lately also referred to as Gravitational Reference Sensor (GRS). Generally, inertial sensors are units that measure the orientation, velocity and acceleration of a craft. In LISA and LISA Pathfinder, the ISS (inertial sensor subsystem) is divided into the actual inertial sensors or inertial sensor heads and the caging mechanism. One inertial sensor head consists mainly of the inertial sensor housing (vacuum valve, optical window, getter assembly,...), one test mass and its electrode housing. The main function of the inertial sensors is to measure test mass displacement and apply forces through the capacitive sensors to generate a low frequency suspension of the test masses. A detailed description of the assembly of the inertial sensor subsystem and a brief introduction to the functionality of the components is e.g. given in reference [ASD-3008] or [Dolesi2003]. (p. 54, 66, 125, 129, 204)

**InGaAs-photodiodes**, photodiodes that use the semiconductor material indium gallium arsenide. There exist InGaAs-photodiodes available with a high quantum efficiency of 80%. This high quantum efficiency is needed in LISA's science interferometer, where the measurement beam impinging on a QPD has a nominal power of 100 pW. This was the main reason why InGaAs-



photodiodes were chosen for the pre-experiments regarding the test of interferometry concepts for LISA. One part of these pre-experiments is the imaging optics experiment, for which the simulations described in chapter 10 were performed. (p. 176, 59, 78)

**intermediate focus**, A focus located inside a lens system, e.g. between the first and second lens of a 2-lens beam compressor. Such an intermediate focus is the optimal position to place a field stop to reduce the amount of stray light in the system. (p. 175, 136, 198)

**JAXA**, **Japan Aerospace Exploration Agency**, the Japanese analogue to ESA and NASA. (p. 2, 201)

**Lagrangian point L1**, one of five locations, a small free floating body like a satellite can have relative to two massive objects like Sun and Earth without being pulled into either of them. The L1 point is located on the connecting line between the two massive objects, which is in case of LISA Pathfinder between Sun and Earth. (p. 5)

**LCA**, LTP core assembly, central part of LTP consisting of the OBI, two vacuum chambers each containing a caging mechanism, a test mass and support structure. (cf. figure on p. 51 and figure 5.2(a)) (p. 54, 55, 66, 89)

**LCGT**, Large Scale Cryogenic Gravitational Wave Telescope, a planned interferometric gravitational wave detector with cryogenic mirrors which shall be located in the Kamioka mine in Japan (just like CLIO). The underground location will provide low seismic noise, while the use of cryogenic mirrors reduces thermal noise, which is a major noise source in all ground detectors. LCGT is designed to have an arm length of 3 km and shall reach  $3 \cdot 10^{-24} / \sqrt{\text{Hz}}$  strain sensitivity around 100 Hz[9]. This will allow detection of signals from up to 250 Mpc and thus observation of the coalescence

of one binary neutron star every other month [Kuroda2010]. (p. 2, 4, 200)

**LIGO**, Laser Interferometer Gravitational Wave Observatory. LIGO runs three interferometers at two sites in the USA: the main detectors in Hanford and Livingston have each an arm length of 4 km and are thus the largest earth-bound gravitational wave detectors. An additional 2 km detector is situated in Hanford. This additional interferometer is now planned to be taken offline, shipped to Australia and operated there under the new name LIGO-Australia. (p. 2, 11, 197)

**Linos**, a manufacturer of lenses [10] (p. 138, 145)

**LISA**, Laser Interferometer Space Antenna. A spaceborne gravitational wave detector to be launched around 2019. This launch date is determined by funding reasons and not technical readiness. LISA consists of three sciencecraft that form an equilateral triangle with an arm length of 5 million km, trailing Earth by  $20^\circ$  in its orbit around the Sun. LISA has 1 W Nd:YAG lasers at 1064 nm, 1.96 kg cubic gold platinum alloy test masses and a data volume of 60 GB per 5 years mission time. Its gravitational wave sources are compact galactic binaries, massive black hole binaries, extreme-mass-ratio (EMRI) inspirals, the stochastic background and bursts[11]. See chapter 9 for further information and chapter 10 for the work performed specifically for LISA. (p. 4)

**LISA Pathfinder**, (LPF) the technology demonstration mission for LISA, consisting of one sciencecraft to be launched in 2013 by a VEGA rocket from Kourou, French Guiana. LISA Pathfinder will carry two instruments, the European ‘LISA technology package’ (LTP) and the US ‘disturbance reduction system’ (DRS). LISA Pathfinder will prove technology readiness for LISA, in particular

laser interferometry with a position resolution of approximately a factor of 10 relaxed wrt. the LISA requirements and drag-free attitude control (→ DFACS) of a spacecraft with two test masses including micro-Newton electric propulsion. See chapter 3 for information regarding phase demodulation in LISA Pathfinder, chapter 5 for more information about the mission, and chapter 6-8 for the work performed specifically for LISA Pathfinder. (p. 5)

**local oscillator**, a term often used for the reference beam of an interferometer. (p. 29)

**locked**, a physical quantity is locked, when a feed-back loop controls the system such that the quantity stays constant. Here, the system is locked to a desired operation point. (p. 13)

**LPF**, → LISA Pathfinder (p. 5)

**LPSPD**, a program by M. Tröbs and G. Heinzel which computes amplitude or power spectral densities (PSD) from given time series.[Tröbs2006][Tröbs2009]. See also → amplitude spectral density. (p. 92, 197)

**LTP**, LISA Technology Package, one of the two instruments aboard LISA Pathfinder. LTP comprises two inertial sensors, consisting each of a test mass in an electrode housing, a caging mechanism which will secure the test mass during launch from damaging the surrounding electrode housing and a vacuum chamber which provides a clean environment mainly during assembly and launch. Furthermore, LTP contains the optical metrology system (OMS) which provides the interferometric readout of the test mass attitude and position, a data and diagnostics system, some auxiliary equipment like support structure and harness as well as some ground support equipment - and its propulsion system: the FEEP micro-Newton thrusters. The composition of the various elements

of LISA Pathfinder can be seen best in product trees, for instance in reference [ASD-3008], but general information can also be found for example in [Gerndt2007]. (p. 53, 5, 71, 202)

**LTP-OBI-Alignment Simulation**, the simulation introduced in chapter 6 which was used for all computations shown in this thesis except of section 8 where only QPD.c was used. This simulation consists of an interface between OptoCad and QPD.c and a logical part which imitates of the OBI bonding and in-flight alignment procedure of the LTP. For further details, see chapter 6. (p. 71, 67, 75, 81, 91, 93, 97, 102, 139)

**LTPDA**, a MATLAB toolbox for reproducible data analysis. See [12, Hewitson2009] for more information. (p. 90, 93, 93, 94)

**luminiferous ether**, up until the late 19th century it was believed that light could not propagate without a medium. Hence it was postulated that a medium called luminiferous aether existed everywhere in the universe and that the Earth moved through the aether when orbiting the sun. (p. 12)

**Mach Zehnder interferometer**, an interferometer of the type shown in figure 2.2: a laser beam is split by a semitransparent mirror (beam splitter). The resulting two beams propagate on different paths which can be of different length, before they are recombined at a second semitransparent mirror called beam combiner. This interferometer type is named after Ludwig Mach and Ludwig Zehnder who independently developed this interferometer in 1892 and 1891 respectively [Mach1892, Zehnder1891]. All four interferometers on the LTP optical bench are of this type. (p. 13, 58, 199)

**measurement band**, in LTP the frequency band of 1 mHz to 30 mHz. In LISA the frequency band of 0.1 to 100 mHz. Sometimes a frequency band

between 0.03 mHz and 1 Hz is stated for LISA, which is a goal, not a requirement for LISA. However, the top level requirement for LISA is formulated as a list of strain sensitivities at specific frequencies, such that it is sometimes said that LISA has no measurement band. Reference [ASD-5001] shows the relation of the strain sensitivity requirements at specific frequencies and the acceleration noise budget for one test mass, eq. (5.2). (p. 53, 55, 114)

**measurement beam**, the beam which reflects off the test mass, usually drawn in red. (p. 29)

**Michelson interferometer**, The interferometer type shown in figure 2.1. One property of the Michelson interferometer is, that the beam paths do not span an area. This property can be used to differ it against other interferometer types. All gravitational wave detectors on ground are today large scale, highly advanced Michelson interferometers. (p. 12, 11, 13)

**micro-Newton thrusters**, LPF will have micro-Newton thrusters as sole propulsion mechanism, a procedure never performed before. These micro-Newton thrusters will align the spacecraft with respect to one test mass (by default TM1), such that this test mass remains drag free. Each instrument aboard LISA Pathfinder operates its own type of micro-Newton thrusters: LTP uses field emission electrical propulsion (FEEP) thrusters, while DRS will operate colloid thrusters. (p. 55, 207)

**mode mismatch**, here: discrepancy in the Gaussian beam parameters of reference and measurement beam. (p. 175)

**MOSA**, movable optical subassembly, shown in figure 9.2(b) on p. 126. The MOSA accomplishes line of sight steering by rotating a rigid assembly of telescope, optical bench, and inertial sensor (GRS). It thereby accounts for the breathing

effect of the LISA arms (cf. chapter 9). (p. 125)

**Mpc**, megaparsec. Astronomical length unit. The name parsec is an abbreviation of **parallax** of one **arcsecond**. Symbol: pc.  $1\text{pc} = 3.26\text{lightyears} = 30.857\text{km}$ . The unit ‘parsec’ is mainly used for distances within the universe, in contrast to distances in our solar system. For example, the closest dwarf galaxies are the Magellanic Clouds which are approximately 48 (small Magellanic Cloud) and 64 kpc away from our solar system. (p. 3, 206)

**NASA**, National Aeronautics and Space Administration of the USA (p. 2)

**Nd:YAG laser**, a solid-state laser that uses Nd:YAG as active medium and has a wavelength of 1064 nm. Nd:YAG stands for Neodymium-doped Yttrium Aluminium Garnet;  $\text{Nd:Y}_3\text{Al}_5\text{O}_{12}$ . (p. 14)

**NS**, neutron star, a remnant of a supernova. A typical neutron star has a mass of approximately 1.35 to 2.1 solar masses and a diameter of about 20 km. The closest neutron star yet discovered is RX J1856-3754, which has an estimated distance of about 400 light-years. (p. 3)

**OB**, optical bench, in case of LISA Pathfinder the 200x212x45 mm Zerodur baseplate to which the FIOS, 12 beam splitters, 10 mirrors, and 10 photodiodes that form the OBI are bonded. In case of LISA the baseplate is circular and has dimensions of 80 mm height  $\times$  580 mm diameter which results in a weight of 54 kg. Since the optical bench is placed perpendicular to the telescope, and due to the large diameter of the base plate, the size of the optical bench is currently determining the height of the LISA spacecraft. (p. 54, 60, 66)

**OBF**, optical bench frame, a coordinate frame defined by the geometry of the optical bench. Throughout this work the OBF is identical to a 90° rotated OCF. The OBF is the coordinate frame natu-



rally used by UGL for the bonding procedure of the LTP OBI. See figure 5.13(b) for an illustration and p. 68 for a more detailed explanation. (p. 68)

**OBI**, optical bench interferometer, which comprises one baseplate and four heterodyne interferometers, consisting of two FIOS, the optical components (10 mirrors, 12 beam splitters) and 10 photodiodes. The OBI requires two input beams, which are produced by the laser assembly (LA), frequency shifted by acousto-optical modulators, and provided by optical fibers. The OBI is one major part of the OMS which provides the heterodyne readout of the test mass attitude. (p. 58, 53, 96, 111, 126)

**OCF**, OptoCad frame, the coordinate frame used in OptoCad to define the LTP OBI. The OCF is the natural coordinate frame for all simulations performed with the LTP-OBI-Alignment Simulation for LISA Pathfinder. Nevertheless coordinates are generally stated in the OBF since this is a more commonly used coordinate frame in the LPF community. (p. 67)

**OMS**, optical metrology system. The OMS consists of the laser assembly, OBI including photodiodes, phasemeter and phasemeter back-end (the algorithms in the DMU that compute the heterodyne signals). Therefore the OMS provides the heterodyne signals that monitor the attitude and alignment of both test masses. In particular the OMS measures the displacement between both test masses (TMs) along the sensitive axis, the motion of TM1 with respect to the space craft, and the angular motion of both test masses [ASD-2046, ASD-3001, ASD-3008]. (p. 54, 58, 71, 81, 202, 207)

**OPD**, optical pathlength difference. For example the frequency interferometer of LTP has an OPD of approximately 38 cm. (p. 60)

**OptoCad**, a mainly two dimensional For-

tran program written by Roland Schilling which traces Gaussian beams through arbitrary optical setups and computes Gaussian beam parameters on specified surfaces. All optical components can be defined in a plane only, however, the beam parameters are computed for both the tangential and sagittal plane, such that the third dimension is included for the beam parameters. [15] (p. 26, 30, 33, 37, 40, 71, 107, 111, 132, 207)

**PAAM interferometer**, one of the interferometers on the LISA optical bench. See p. 128 for more information and figure 9.4 for an illustration. (p. 128)

**pathlength noise**, here: amplitude spectral density of a pathlength signal that does not originate from longitudinal displacements of a test mass. (p. 55, 58, 81, 89, 90, 93, 94, 95, 131, 132, 167)

**pathlength signal**, or pathlength readout,  $\Delta s_m$ , the phase signal of a QPD (and phasemeter) converted to length. See section 2.3 and chapter 3 for detailed information. (p. 19, 60)

**PBS**, polarizing beam splitters. (p. 127)

**PDF**, probability density function. For a continuous variable, the likelihood for one precise value is zero. Therefore, a probability density function is defined, from which the probability for continuous variables to be within a specific interval can be derived by integration:

$P_X(a < x < b) = \int_a^b dx f(x)$  where  $f(x)$  is the probability density function and  $P_X(a < x < b)$  is the likelihood for  $x$  to have a value between  $a$  and  $b$ . Probability density functions are therefore normalized:

$P_X(-\infty < x < \infty) = \int_{-\infty}^{\infty} dx f(x) = 1$ , which guarantees the overall likelihood to be 1. (p. 172)

**phase demodulation**, extraction of the phase  $\phi$  from a photocurrent. The phase demodulation scheme of LISA Pathfinder

is described in section 2.3 (p. 18, 11, 13, 23)

**phasemeter**, a measuring device for the phase difference between two alternating (photo-) currents. The phasemeters used in LISA and LISA Pathfinder are specially developed for these missions. The working principle of the LISA Pathfinder phasemeter is given in section 3.1, details can for example be found in [Wand2007, Heinzl2004]. The LISA phasemeter is currently under development. (p. 18, 23, 54, 202)

**photocurrent**, here, current generated by a laser beam impinging on a photodiode. The photocurrent is (in a certain range) proportional to the incident beam power. (p. 29, 18, 19, 23, 26, 31)

**PM3**, phasemeter no.3, an AEI phasemeter used for LTP related experiments. The phase demodulation implemented in this phasemeter is the one described in section 3.1, a photograph is shown in figure 3.2, further details can be found in [Wand2007, Heinzl2004]. (p. 24)

**pointing jitter**,  $S(x_0)$ , also pointing jitter noise. Beam displacement noise on a photodiode originating from angular jitter. The pointing noise can be computed from a DC signal by  $S(x_0) = k_{DC_h}^{x_0} \cdot S(DC_h)$  (cf. eq. (8.14)), where  $x_0$  is the displacement on the photodiode (not to be mixed with the longitudinal displacement  $x$  of a test mass). (p. 117, 110, 113, 115, 115, 118)

**position noise**,  $S(x_m)$ , pathlength noise converted to an equivalent test mass longitudinal jitter noise by applying the corresponding coupling factor:  $S(x_m) = k_{\Delta L_m}^x \cdot \Delta L_m$ . In LTP this coupling factor is  $1/[2 \cos(4.5^\circ)] \approx 0.5$ , such that in LTP position noise is half the amount of pathlength noise. (p. 56, 168)

**principal planes**, two hypothetical planes which can be used to describe the refraction of any lens. It is assumed that the refraction happens entirely on

these two planes. A ray parallel to the optical axis is then refracted on the principal plane on the image side and intersects the optical axis in the focal point. A ray coming from the object that intersects the focal point on the object side is refracted on the object sided principal plane and propagates then parallel to the optical axis. This is illustrated in figure 10.4. The (effective) focal lengths of thick lenses are defined with respect to their principal planes. (p. 138)

**principal ray**, a beam with arbitrary angle which intersects the optical axis at the aperture stop, entrance and exit pupil. (p. 135, 203)

**proof mass**, (PM), a term mainly used in the USA and in the LISA project for a  $\rightarrow$  test mass. (p. 213)

**PSD**, power spectral density with unit “(basic unit)<sup>2</sup>/Hz”. See amplitude spectral density for more information. (p. 197, 207)

**pulsar**, a highly magnetized spinning neutron star, that emits focussed electromagnetic radiation. The radiation can be received on Earth only if the beam points in the direction of Earth which happens periodically, due to the spin of the pulsar. Pulsars are therefore often described as stellar light houses. (p. 1, 2, 2)

**pupil plane**, please see  $\rightarrow$  entrance and  $\rightarrow$  exit pupil of an imaging system. Further information can be found in [Smith, chapter 6] and [Hecht, section 5.3.2]. (p. 135)

**QPD**, quadrant photodiode, essentially four photodiodes brought together in one housing, forming thereby one photodiode consisting of four segments (quadrants). The gap between the four segments is called the insensitive slit. In case of LISA Pathfinder, the QPDs are circular shaped InGaAs-photodiodes with a diameter of 5 mm and a slit size of 45  $\mu\text{m}$ . For LISA these photodiodes cannot be

used due to the higher heterodyne frequency. Generally the readout frequency depends on the capacitance and thus the size of the photodiode. The largest photodiodes found for LISA that fulfill all requirements have a diameter of 1 mm. The QPDs chosen for the LISA OB pre-experiments are currently circular shaped InGaAs-photodiodes with 1 mm diameter and a 20  $\mu\text{m}$  slit. (p. 19, 109)

**QPD.c**, a C program written by Gerhard Heinzl. QPD.c computes the heterodyne signals described in section 2.3 for two given Gaussian beams in two steps. In a first step the photocurrent of the QPD is derived (see section 3.2.2 for Details). In a second step QPD.c imitates the signal processing in the LISA Pathfinder phasemeter and DMU (see section 3.2.3). QPD.c takes into account the finite size of a QPD and the insensitive slits that separate the quadrants of a QPD. (p. 26, 30, 33, 37, 71, 111, 132, 179, 207)

**radiation pressure noise**, a quantum noise originating from the statistical distribution of the number of photons impinging on a test mass. For coherent light, the number of photons impinging on a detector per time interval is subject to a Poisson distribution. During reflection, twice the photon impulse is transferred to the test mass, such that the changing number of impinging photons results in a fluctuating pressure on the test mass. Consequently, the test mass is subject to acceleration noise. (p. 114)

**radius of curvature**,  $R(z)$ , one of the beam parameters used to describe Gaussian beams. The wavefront of a Gaussian beam can be locally described by a sphere whose radius is the radius of curvature of the Gaussian beam. It can be computed from the Rayleigh range  $z_0$  and distance  $z$  from the beam waist by  $R(z) = z \left[ 1 + \left( \frac{z_0}{z} \right)^2 \right]$ . See figure 3.4(a) for an illustration. (p. 27, 41, 76, 138)

**Rayleigh range**,  $z_0$ , for Gaussian beams measured in direction of propagation: the distance between the waist and the position where the spot size doubled its area. That means at a Rayleigh range, the beam radius increased by  $\sqrt{2}$ :

$w(z_0) = \sqrt{2} w_0$ . The Rayleigh range can be computed from the waist size  $w_0$  and wavelength  $\lambda$  by and  $z_0 = \frac{\pi w_0^2}{\lambda}$ . (p. 26, 41, 43, 111, 152)

**redundant**, redundancy is the principle of duplicating critical components in order to secure reliability. In space missions any critical component has either a cold or hot redundant counter part. Cold redundant items are nominally switched off and are only activated in case of failure of the primary component. Hot redundant items are always active. The photodiodes on the optical benches of LISA and LISA Pathfinder are examples of hot redundant items. They are active through the whole mission time and the signals of the main and redundant diodes are averaged to reduce the amount of noise. (p. 25, 59)

**reference interferometer**, in LISA Pathfinder and LISA, the interferometer on the optical bench which has approximately identical arm lengths and does not reflect off a test mass. It measures displacements mainly originating from the modulation bench and the optical fibers and its phase signal is subtracted from the measurement interferometers. Thereby, the common mode phase noise is canceled from the measurement interferometers. See section 5.2.1 for more information about the LPF and chapter 9 for the LISA reference interferometer. (p. 59, 65, 127)

**refractive index**,  $n$ , for example  $n_{\text{fused silica}} = 1.44963$ ,  $n_{\text{SF6}} = 1.77367$  at  $\lambda = 1064 \text{ nm}$ . Since the refractive index depends on the wavelength of the beam which transmits the material, one

can often find a set of six coefficients - the Sellmeier coefficients - instead of the value of the refractive index. From these coefficients the refractive index  $n$  can be computed by:

$$n = \sqrt{1 + \frac{\lambda^2 B_1}{\lambda^2 - C_1} + \frac{\lambda^2 B_2}{\lambda^2 - C_2} + \frac{\lambda^2 B_3}{\lambda^2 - C_3}}$$

(p. **138**)

**RMS**, root mean square. The RMS of a data set consisting of  $N$  values is computed by  $x_{\text{RMS}} = \sqrt{\frac{x_1^2 + x_2^2 + \dots + x_N^2}{n}}$ . The RMS of a set equals its standard deviation, if the set has zero mean. (p. **83**, 87, 93)

**Rx beam**, received beam on a LISA optical bench, that means a beam originating from a remote spacecraft. The Rx beam has top hat beam shape, because it expands while propagating along the arm length of 5 million km, such that it has effectively planar wavefronts when it clipped by the telescope. (p. **128**)

**sagittal**, The sagittal plane contains the direction of propagation of the beam and is orthogonal to the tangential plane, which contains the beam axis as well as the optical axis. Since all simulations performed for this thesis are 2-dimensional, the tangential plane is the plane shown in all OptoCad figures (containing all beams). The waist in sagittal plane is indicated in all OptoCad figures by a magenta triangle, the tangential waist by a green triangle. If these waists are not at the same location, the optical system is astigmatic. (p. **146**, 209)

**SBDFT**, single-bin discrete Fourier transform, the working principle of LISA Pathfinder phase demodulation. See section 2.3 for more information. (p. **19**, 23)

**S/C**, spacecraft, term for an (artificial) satellite that is not yet in orbit or will not be placed in an Earth orbit. The instruments on the spacecraft that are used for experiments form the so called payload. See  $\rightarrow$  sciencecraft for more

information. (p. **55**, 89, 94, 170)

**Schnupp modulation**, a phase demodulation technique for homodyne interferometers which was first proposed by L. Schnupp [[Schnupp1988](#)]. It consists of a phase modulation before the laser beam is split into the two interferometer arms and a detuning of the interferometer arms by  $\Delta L$ . As a result the interferometer signal is proportional to  $\sin(\varphi) \cdot \sin(\frac{\omega_m \Delta L}{c_0})$  where  $\omega_m$  is the modulation frequency. A detailed description of Schnupp modulation is given for instance in [[Heinzl1999](#)]. (p. **13**)

**science interferometer**, one of the LISA interferometers, which measures the relative displacement between local and remote optical bench. The measurement beam of this interferometer has a nominal power of only 100 pW impinging on a photodiode, due to the 5 million km arm length of this interferometer. See chapter 9 for more information. (p. **128**, 198)

**sciencecraft**, a term often used for LISA and LISA Pathfinder spacecraft. Unlike in most other space missions, spacecraft and payload interact in LISA and LISA Pathfinder, such that they cannot be perfectly distinguished anymore. Therefore, the generic term sciencecraft was introduced. Each LISA sciencecraft is currently planned to be a 2.9 m diameter  $\times$  0.93 m high spacecraft of 643 kg [[11](#)]. (p. **55**, 206, 206)

**sensitive direction**, in LTP, the axis connecting test mass 1 and 2, also referred to as longitudinal direction. (p. **97**, 99)

**SEPD**, single element photodiode. In case of LISA Pathfinder 3 mm circular InGaAs-photodiodes which were planned to be used as power monitors (PDA1 and PDA2). See chapter 8 for more information about these power monitors. (p. **19**, 60, 109, 179)

**SMBH**, super massive black hole which

is typically a black hole in the center of a galaxy with a mass between  $10^4$  and  $10^7$  solar masses. (p. 4)

**spectrum**, short term used throughout this thesis for an  $\rightarrow$  amplitude spectral density. (p. 6, 91, 92, 94, 114, 114)

**spot size**,  $w(z)$ , the radius at which the field amplitude of a Gaussian beam drops to  $1/e$  of the axial value. It is computed from the Rayleigh range  $z_0$ , the distance  $z$  from the waist and the beam waist  $w_0$  by  $w(z) = w_0 \sqrt{1 + \left(\frac{z_0}{z}\right)^2}$ . (p. 26, 88, 111, 133, 148, 179)

**standard deviation**,  $\sigma$ , a measure for the variation of a set of values from its average value. For a discrete set of  $N$  values the standard deviation is computed by  $\sigma = \sqrt{\frac{1}{N} \sum_{i=1}^N (x_i - \bar{x})^2}$ . (p. 83, 86, 87, 172, 173)

**TAMA300**, the interferometric gravitational wave detector at the Mitaka campus in Japan. TAMA300 is a Fabry-Pérot Michelson Interferometer, has an arm length of 300 m and reaches a sensitivity of  $10^{-21} \text{ Hz}^{-1/2}$  at 1 kHz. This sensitivity allows for detection of gravitational waves of coalescing neutron-star binaries in our galaxy, however this corresponds to an event rate of 1 per 300 000 years. (p. 2)

**TDI**, time delay interferometry, a technique to remove laser frequency noise by combining time shifted signals of the interferometers on remote spacecraft. Thereby, a variety of large scale interferometer types like Sagnac or Michelson can be synthesized. Since this technique is applied during data analyses on ground, the interferometer type can be chosen in dependency of the wave form to be observed. (p. 126)

**test mass interferometer**, one of the four interferometers on each LISA optical bench. The test mass interferometer reflects a local laser beam from the test mass and measures thereby the distance

between test mass and optical bench. It is the equivalent to the LISA Pathfinder x1-interferometer. Chapter 10 investigates the use of an imaging system to suppress the coupling of test mass angular jitter into the pathlength readout of the test mass interferometer. (p. 127, 125, 126, 131, 183)

**thick lens**, a lens with non negligible thickness  $d$  compared to its focal length  $f$ . All lenses used throughout this thesis are thick lenses. (p. 138, 204)

**thin lens**, a lens with negligible thickness  $d$  in comparison to its focal length  $f$ , such that  $d \rightarrow 0$  can be used. For instance, the focal length of a thin lens is computed by  $\frac{1}{f} = (n - 1) \left[ \frac{1}{R_1} + \frac{1}{R_2} \right]$ . (p. 138)

**TM**, test mass, also called proof mass. Like a test charge is defined as a small charge used to probe an electrical field without disturbing it, a test mass is a test particle to probe a gravitational field without changing its properties. In case of GEO600 and initial LIGO the test masses used are fused-silica mirrors with a diameter of 25 cm and a weight of 11 kg. Advanced LIGO will use 40 kg sapphire mirrors with a diameter of 32 cm [1, 7]. For LISA and LISA Pathfinder the test masses are massive gold-platinum-cubes with an edge length of 46 mm and a weight of 1.96 kg (see figure 5.2(b) for an illustration). In analogy to the appearance of the LISA and LISA Pathfinder test masses, all test masses are drawn as yellow cubes throughout this work. For on ground experiments piezoelectric driven mirrors are used as a substitute and called (dummy) test mass for convenience. (p. 11, 58)

**top hat beam**, also called ‘flat top beam’, a beam shape generated by clipping a plane wave by an aperture stop, e.g. light from remote stars that is detected and thereby clipped by a telescope.

In LISA, the laser light from a remote spacecraft has a diameter of approximately 17 km and is thus to high order a plain wave which is then clipped by the telescope. The measurement beam in the LISA science interferometer is therefore a top hat beam. (p. **128**, 132, 205, 212) **top level science requirement**, the requirement, from which all other requirements of a mission are derived. In case of LISA Pathfinder:

$$S(a)^{\text{LPF}} \leq 3 \cdot 10^{-14} \frac{\text{ms}^{-2}}{\sqrt{\text{Hz}}} \sqrt{1 + \left(\frac{f}{3 \text{ mHz}}\right)^2},$$

which is a factor of 10 below the LISA top level science requirement. This relaxation of 10 in frequency and acceleration noise was chosen not for feasibility but for the generally used cost to benefit ratio. Nonetheless, current estimates show that LPF will do better than its requirement and aims for the LISA stability goal. Furthermore, if LISA would fly ‘only’ with the LPF residual acceleration noise there would still be guaranteed sources of gravitational waves. Further information about requirements is given in appendix A.2. (p. **53**)

**transimpedance amplifier**, an amplifier that converts an input current into a proportional voltage. The constant of proportionality  $k_{I_{\text{in}}}^{V_{\text{out}}}$  is called the transimpedance. (p. **23**)

**Tx beam**, transmit beam of the LISA optical bench, that means the local laser beam which is directed to the Schiefspiegler telescope to propagate to a remote spacecraft. (p. **128**)

**UGL**, University of Glasgow, used as a synonym for the Institute of Gravitational Research at the University of Glasgow. The LISA group at UGL was responsible for manufacturing and thus the alignment of the OBI of LISA Pathfinder, and will manufacture the EBB model of the LISA OBI. UGL is part of the GEO collaboration and played a key role in the establishment of GEO 600.

Further research topics at the IGR are mirror suspensions for LIGO and thermal noise investigations, gratings and three mirror cavities as well as data analysis within the LIGO Scientific Collaboration. (p. **74**, 6, 64, 76, 87, 173, 200)

**VEGA**, a small expandable launch system currently designed by ESA. It is designed to carry small satellites between 300 and 2000 kg[5] and will be launched for the first time in 2011. LISA Pathfinder is currently planned to be the third mission launched by a VEGA rocket. (p. **53**)

**VIRGO**, the Italian/French interferometric gravitational wave detector located near Pisa (Italy). It has an arm length of 3 km, a frequency range of 10 to 6000 Hz [18] and reached in 2009 a sensitivity of  $S(h) < 10^{-22}/\sqrt{\text{Hz}}$  between 100 and 1000 Hz which corresponds to a sky coverage of approximately 9 Mpc for NS-NS coalescences [Accadia2010]. (p. **2**)

**waist**, ( $w_0$ ) minimal radius of a Gaussian beam, where the radius is defined by a field amplitude drop to  $1/e$  of the axial value. It can be computed from a given Rayleigh Range  $z_0$  and wavelength  $\lambda$  by:  $w_0 = \sqrt{\frac{z_0 \lambda}{\pi}}$ . If the beam passes a lens, the waist is generally not located in the focal point of the lens, but at a distance  $x' = \frac{-x f_L^2}{x^2 + \left(\frac{\pi w_0^2}{\lambda}\right)^2}$ , where  $f_L$  is

the focal length of the lens and  $x$  the distance of the initial waist to the first focal point of the lens. Its size is then given by  $w_0'^2 = w_0^2 \cdot \frac{-x'}{x}$ . The spot size  $w(z)$  along the optical axes ( $z$ -axes) is given by  $w(z) = w_0 \sqrt{1 + \left(\frac{z_0}{z}\right)^2}$ . (p. **26**, 13, 27, 43, 111)

**wavefront**, all points of a Gaussian beam that have zero phase difference with respect to each other. Locally, the wavefront of a Gaussian beam resembles a sphere that is fully described by its



radius  $R(z)$ : the radius of curvature of the Gaussian beam. (p. 27, 20, 20, 37, 128)

**wavenumber**,  $k$ , the magnitude of the wave vector  $\vec{k}$ . It is related to the wavelength  $\lambda$ , vacuum speed of light  $c_0$  and the angular laser frequency  $\omega_0$  by:  $k := \frac{2\pi}{\lambda} = \frac{\omega_0}{c_0}$ . The important application of  $k$  is the conversion between phase and pathlength:  $\phi = k \cdot \Delta s$ , eq. (2.5). (p. 27)

**white dwarf**, the final evolutionary state of stars that are too small to end in a supernova. It is expected that 97% of all stars in our galaxy will end as white dwarfs [Fontaine2001]. White dwarfs have a typical mass in the order of half a solar mass but planetary size, such that they are very dense. Many white dwarf binaries emit gravitational waves in the frequency band of LISA. These gravitational waves are guaranteed signals for LISA and could still be measured if LISA would perform “only” with LISA Pathfinder sensitivity. (p. 4)

**x1-interferometer**, one of the two LTP measurement interferometers. The x1-interferometer measures the relative distance between test mass 1 and optical bench. It is the equivalent to the LISA test mass interferometer. See section 5.2.1 for more information. (p. 58)

**x12-interferometer**, the interferometer on the LISA Pathfinder optical bench, which measures the relative distance between the two free floating test masses. See section 5.2.1 for more information. (p. 59)

**XMRF**, coordinate frame which has its origin at the center of the reflective sur-

face of an in-flight aligned test mass, that means it is centered on the electrical null. See figure 5.13(b) for an illustration and p. 69 for a more detailed explanation. XMRF is an acronym form “X-surface mass reference frame”, where “X-surface” is the surface orthogonal to the x-axis and thus the surface of a test mass. The XMRF is used by ASD to define requirements for the TM and interferometer alignment (cf. [ASD-3020, iss 6]). (p. 69, 79, 97)

**ZEMAX**, a commercial optical design software running on Windows machines solely. Zemax performs ray tracing through arbitrary objects (including aspheric lenses or any complicated optical structure). It can be used to investigate aberration and stray light. For the application in interferometry ZEMAX shows a main disadvantage: most analyses tools work only in sequential mode, which cannot be used to investigate interferometers. (p. 182)

**Zerodur**, a registered name of a glass ceramic of Schott Glass Technologies. It is similar to ULE and has the following characteristics: very low thermal expansion coefficient (available in qualities of  $\pm 10^{-7} \text{K}^{-1}$  to  $\pm 10^{-8} \text{K}^{-1}$  at 0-50° C)[17], high homogeneity, chemical stability, non porousness and polishable to a high quality. These properties together with usual glass ceramic properties as non magnetic and no electric conductivity make it an optimal substrate for optical components for space-missions. (p. 58, 61, 126, 198, 205)

---

## Variables with greek letters

---

$\alpha$	in-plane angle of incidence of a beam on a photodiode or of the measurement beam on a test mass, measured with respect to the surface normal. For LTP the incident angle $\alpha$ on each test mass is nominally $4.5^\circ$ , while LISA has normal incidence: $\alpha = 0$ (cf. figure 3.5 and figure 7.1).
$\epsilon$	small number needed for numerical derivatives (cf. section 7.1).
$\zeta$	Gouy phase, defined as $\zeta(z) := \arctan(z/z_0)$ where $z$ is the distance from the waist and $z_0$ the Rayleigh range (cf. section 3.2.1).
$\eta$	for LISA Pathfinder: angle of a rotation around the insensitive $y$ -axis as shown in figure 5.13(a).
$\Theta$	full opening angle of a Gaussian beam and thus twice the divergency: $\Theta = 2\theta_{\text{div}}$ as shown in figure 3.3.
$\theta_{\text{div}}$	divergence of a Gaussian beam.
$\vartheta$	for LISA Pathfinder: angle of a rotation around the sensitive $x$ -axis. This type of rotation is measured by the inertial sensors but cannot be sensed by the OMS. For an illustration see figure 5.13(a).
$\kappa$	compression factor of a lens system (cf. chapter 10).
$\lambda$	wavelength of the used laser beam. Throughout this thesis, it is $\lambda = 1064 \text{ nm}$ , since Nd:YAG lasers will be used in both LISA and LISA Pathfinder (cf. section 2.1).
$\mu$	mean value of a distribution (cf. appendix A.4).
$\pi$	ratio between a circle's circumference and its diameter: $\pi \approx 3.1415926535897932384626433832795028841971693993751\dots$ The first $2 \cdot 10^8$ digits of it can be found in [16].
$\sigma$	standard deviation, i.e. square root of a variance $\sigma^2$ (cf. chapter 7).
$\Phi$	phase of an intensity (cf. p. 15).
$\phi$	phase of a measured power in a homodyne or heterodyne interferometer (cf section 2.1).
$\varphi, \varphi_{\text{beam}}, \varphi_{\text{TM}}$	in plane angle of a test mass or beam (cf. section 4.1).
$\varphi_1, \varphi_2$	in plane angle of LISA Pathfinder test mass 1 or 2 respectively
$\omega$	angular frequency, $\omega = 2\pi f$
$\omega_{\text{het}}$	angular heterodyne frequency: $2\pi f_{\text{het}}$ (cf. section 3.2.2).



## Variables with capital letters

$A_{\text{beam}}, A_{\text{slit}}$	areas, e.g. the area of the insensitive slit of a QPD eq. (B.13).
$A_m, A_r$	amplitude of the electric field of a measurement or reference beam respectively (cf. section 2.2.1 and 3.2.1).
$A, B, C, D$	quadrants of a QPD (cf. figure 3.6).
$C_1$	factor of proportionality between photovoltage and beam power (cf. section 4.1).
$E, E_m, E_r$	Electrical field in general or of a measurement or reference beam, respectively (cf. section 3.2.1).
$F$	focal point of a lens
$F^b, F1^b, F2^b$	secondary or back focal point in front of a general lens or lens L1, L2,... respectively (cf. chapter 10).
$F^f, F1^f, F2^f$	primary or front focal point of a general lens L or lens L1, L2,... respectively (cf. chapter 10).
$H_r$	relative height in a clipped normal distribution (cf. section A.4).
$I$	Intensity of a laser beam. Unit: $\text{W}/\text{m}^2$ .
$K_1, K_2, K_3$	general constants (cf. appendix A.2).
$L$	arm length of an interferometer e.g. $L_{\text{LISA}} = 5 \times 10^9 \text{ m}$ , $L_{\text{LIGO}} = 4 \text{ km}$ , $L_{\text{GEO600}} = 600 \text{ m}$ , $L_{\text{LTP}} \approx 35 \text{ cm}$ .
$\Delta L$	length change in an interferometer arm caused e.g. by a gravitational wave - or a passing train, air plane or the surge of the ocean (cf. section 2.1).
$\Delta L_m$	measured arm length change of the interferometer. In general the measured length change is not equal to, but roughly the same as the physical arm length change: $\Delta L_m \neq \Delta L$ (cf. section 2.1).
$P$	detected power of a general beam. The power of a beam is its intensity integrated over a surface $S$ : $P = \int_S I$ . The surface $S$ is usually the detectors active surface, that means the chip of a QPD or SEPD (cf. section 2.2.1).
$P_b, P_M, P_R$	total power of a general beam or measurement or reference beam, respectively (cf. section 3.2.1 and 3.2.2).
$P_{\text{rel}}$	relative power, i.e. measured power $P$ divided by total beam power $P_b$ , (cf. section 8.2).
$R(z)$	radius of curvature of a Gaussian beam at a distance $z$ from the waist; $R(z) = z \left[ 1 + \left( \frac{z_0}{z} \right)^2 \right]$ (cf. section 3.2.1).
$S$	surface of a detector or detector segment, e.g. a photodiode or a quadrant of a QPD (cf. section 3.2.2).
$S(..)$	amplitude spectral density, e.g. of an acceleration $S(a)$ with the unit $\text{m s}^{-2}/\sqrt{\text{Hz}}$ (cf. section 5.1).
$V_n^i$	voltage on a quadrant $i$ of a QPD at a discrete time $t = n/f_{\text{samp}}$ (cf. section 3.1).

---

## Variables with lower case letters

---

$a$	acceleration, used mainly in acceleration noise requirements $S(a)$ (cf. section 5.1).
$c$	contrast, used here for the contrast of the measured power in a heterodyne interferometer, defined as $c = \frac{P_{\max} - P_{\min}}{P_{\max} + P_{\min}}$ (cf. eq. (2.30)).
$c_0$	speed of light in a vacuum: $c_0 = 299,792,458 \frac{\text{m}}{\text{s}} \approx 3 \cdot 10^8 \frac{\text{m}}{\text{s}}$ (for instance in eq. (2.12)).
$c_I$	contrast of an intensity in a heterodyne interferometer (cf. eq. (2.21)).
$d$	thickness of lens (cf. section A.2).
$d_{\text{Slit}}$	full width of the slit which divides the quadrants of a QPD (cf. section 4.6.1).
$e$	Euler's number: $e = 2.718281828459045235360287471352662497757\dots$ . The first 1 million digits can be found in [8] or up to 10 million digits but currently not checked between 2 and 10 million in [14].
$f$	frequency measured in Hertz. For electromagnetic waves traveling through vacuum: $f = \frac{c_0}{\lambda}$
$f_1, f_2, \dots$	(effective) focal length of lens L1, L2, ... (cf. chapter 10)
$f_c$	corner frequency in a noise estimate. (cf. section A.2)
$f_{\text{het}}$	heterodyne frequency, the frequency difference between the beams in the arms of an heterodyne interferometer. The heterodyne frequency in LISA Pathfinder is approximately 1 kHz (cf. page 14) and between 2 MHz and 20 MHz in LISA.
$f^f$	front focal length: distance from the front focal point of the lens to the vertex of the first optical surface (cf. figure 10.4).
$h$	amplitude of a gravitational wave, which causes a strain of $h = \frac{2 \Delta L}{L}$ (cf. section 2.1 and appendix A.1).
$i$	imaginary unit: $i^2 = -1$ .
$k$	wavenumber, i.e. magnitude of the wave vector $\vec{k}$ : $k = \frac{2\pi}{\lambda}$ (cf. section 2.1).
$k_b^a$	coupling factor between two variables $a$ and $b$ : $k_b^a := \frac{\partial a}{\partial b}$ such that a linearization of $a$ can be expressed as $a = k_b^a \cdot b$ (cf. section 4.5).
$n$	refractive index of a material, e.g. $n_{\text{fused silica}} = 1.44963$ (cf. section 10.3.1).
$\bar{n}_p$	number of periods that are averaged in a phasemeter during the phase demodulation (cf. eq. (3.2)).
$o_1, o_\Delta$	scaled length readout at LISA Pathfinder (cf. eq. (7.33)).
$q(z)$	complex beam parameter defined as $z + iz_0$ (cf. eq. (3.10)).
$q_1, q_2, q_3, q_4$	quadrants of a QPD, arranged as shown in figure 3.6(a).
$r$	radial distance in cylinder coordinates: $r = \sqrt{x^2 + y^2}$ (cf. section 3.2).
$r_{\text{QPD}}$	radius of a circular QPD or half width of a square QPD (cf. section 4.6.1).
$s$	pathlength of a laser beam, corresponding to an arm length $L$ (cf. section 2.1) or total pathlength propagated by a laser beam (cf. section 3.2.2).

$\Delta s_m$	measured pathlength change, corresponding to a measured arm length change of $\Delta L_m$ (cf. section 2.1).
$t$	time, for instance in (section 3.12).
$w_0$	beam radius at the waist: $w_0 = \sqrt{\frac{z_0 \lambda}{\pi}}$ (section 3.2.1).
$w(z)$	spot size of a Gaussian beam, i.e. beam radius at distance $z$ from the waist. $w(z) = w_0 \sqrt{1 + \left(\frac{z}{z_0}\right)^2}$ (cf. section 3.2.1).
$x_0$	horizontal distance of beam centroid to the center of a photodiode, where horizontal refers to the plane of the optical bench or baseplate as shown in figure 3.5.
$y_0$	vertical displacement of a beam centroid on a photodiode, i.e. orthogonal to the plane of the optical bench or baseplate (cf. section 8.2.1).
$z$	Gaussian beam parameter: distance from the waist in direction of propagation, i.e. the beam diverges for positive values of $z$ as shown in figure 3.3.
$z_0$	Rayleigh range $z_0 = \frac{\pi w_0^2}{\lambda}$ (cf. section 3.2.1).

---

### List of symbols

---

$\approx$	approximately, e.g. $\pi \approx 3.14$
$\equiv$	definition of term on the right hand side
$\stackrel{!}{=}$	definition of term on the left hand side
$<$	the term on the left is demanded to be smaller than the term on the right hand side
$\stackrel{?}{=}$	an equivalence that needs to be proven
$\stackrel{nom.}{=}$	nominally the same, e.g. two coupling factors are the same if the nominal and thus perfectly aligned OB is used for the computation
$\equiv$	equivalence of two functions. For example $E^q(r, z) \equiv E^R(q, z)$ means that $E^q(r, z)$ is identical to $E^R(r, z)$ for any value of $r$ and $z$ .
$\ \cdot\ $	Absolute value. For example the absolute value of a complex value $c$ with real part $a$ and imaginary part $b$ : $\ c\  = \ a + ib\  = \sqrt{(a + ib)(a - ib)} = \sqrt{a^2 + b^2}$
$c^*$	complex conjugate. If $c$ is a complex number with real part $a$ and imaginary part $b$ such that $c = a + ib$ , then $c^* = a - ib$
$\bar{P}$	time average, for example: mean power $\bar{P}$ and mean intensity $\bar{I}$
$\Re$	real part of a complex number
$\Im$	imaginary part of a complex number



# Bibliography

- [Abadie2010] J. Abadie et al.: **Predictions for the rates of compact binary coalescences observable by ground-based gravitational-wave detectors** *Class. Quantum Grav.* 27 (2010) 173001 (25pp) [p. 3]
- [Accadia2010] T. Accadia et al.: **Status and perspectives of the Virgo gravitational wave detector** *Journal of Physics: Conference Series* 203 (2010) 012074 [p. 214] [http://iopscience.iop.org/1742-6596/203/1/012074/pdf/1742-6596\\_203\\_1\\_012074.pdf](http://iopscience.iop.org/1742-6596/203/1/012074/pdf/1742-6596_203_1_012074.pdf)
- [Conti2004] L. Conti: **The AURIGA second scientific run and the dual detector of gravitational waves** *Nuclear Instruments and Methods in Physics Research A* 518 pp. 236–239 (2004) [p. 2] [http://www.lnl.infn.it/~auriga/auriga/papers\\_src/NIM\\_2004.pdf](http://www.lnl.infn.it/~auriga/auriga/papers_src/NIM_2004.pdf)
- [Barriga2010] P. Barriga et al.: **AIGO: a southern hemisphere detector for the worldwide array of ground-based interferometric gravitational wave detectors** *Class. Quantum Grav.* 27 (2010) 084005 (12pp) [p. 197]
- [Berntsen1991] J. Berntsen, T. Espelid and A. Genz: **Algorithm 698 DCUHRE: an adaptive multidimensional integration routine for a vector of integrals** *ACM Transactions on Mathematical Software (TOMS)*, Volume 17, 452 - 456 (1991) [p. 32]
- [Bogenstahl2010] J. Bogenstahl: **Interferometry for the space mission LISA Pathfinder** *PhD thesis presented in the University of Glasgow* (Feb 26, 2010) [p. 61, 62, 88, 201]
- [Cutler2006] C. Cutler and J. Harms: **Big Bang Observer and the neutron-star-binary subtraction problem** *Phys. Rev. D* 73, (Feb 2006) 042001 [p. 5, 199]
- [Danzmann1993] K. Danzmann, A. Rüdiger, R. Schilling, W. Winkler, J. Hough et al.: **LISA (Laser Interferometer Space Antenna). Proposal for a Laser-Interferometric Gravitational Wave Detector in Space.** *Report MPQ 177* (1993) [p. 4]
- [Dolesi2003] R. Dolesi, D. Bortoluzzi, P. Bosetti, L. Carbone, A. Cavalleri, I. Cristofolini, M. DaLio, G. Fontana, V. Fontanari, B. Foulon, C. D. Hoyle, M. Hueller, F. Nappo, P. Sarra, D. N. A. Shaul, T. Sumner, W. J. Weber and S. Vitale **Gravitational sensor for LISA and its technology demonstration mission** *Class. Quantum Grav.* 20 (2003) pp. 99–108 [p. 205]
- [ECSS2000] European Cooperation for Space Standardization (ECSS): "Space engineering Mechanical — Part 3: Mechanisms" ECSS-E-30 Part 3A (Apr 25, 2000) [p. 199, 203]

- [ECSS1998] European Cooperation for Space Standardization (ECSS): "Space Engineering Verification" ECSS-E-10-02A (Nov 17, 1998) [p. 202]
- [Ellife2005] E. J. Ellife, J. Bogenstahl, A. Deshpande, J. Hough, C. Killow, S. Reid, D. Robertson, S. Rowan, H. Ward, , and G. Cagnoli: **Hydroxide-catalysis bonding for stable optical systems for space** *Class. Quantum Grav.* 22 (2005) pp. 257-267 [p. 61, 205] <http://iopscience.iop.org/0264-9381/22/10/018/>
- [Fitzsimons2010] E. D. Fitzsimons: Techniques for Precision Interferometry in Space PhD thesis presented in the University of Glasgow (Sep 14, 2010) [p. 61, 62, 200]
- [Fontaine2001] G. Fontaine, P. Brassard, and P. Bergeron: **The Potential of White Dwarf Cosmochronology**, *Publications of the Astronomical Society of the Pacific* 113, 782 (April 2001), pp. 409-435 [p. 215] <http://adsabs.harvard.edu/abs/2001PASP...113..409F>
- [Gerndt2007] R. Gerndt for the entire LTP Team: **LTP – LISA Technology Package: Development Challenges of a Spaceborne Fundamental Physics Experiment** *Journal of Physics: Conference Series* 154 (2009) 012007 [p. 207]
- [Haehnelt1998] M. G. Haehnelt: **Supermassive black holes as sources for LISA** *AIP Conf. Proc.* 456, 45 (1998) [p. 4] <http://link.aip.org/link/?APCPCS/456/45/1>
- [Harms2008] J. Harms, C. Mahrtdt, M. Otto, M. Priess: **Subtraction-noise projection in gravitational-wave detector networks** *Phys.Rev.D* 77:123010 (2008) <http://arxiv.org/abs/0803.0226v2> [p. 5, 199]
- [Heinzel2005] G. Heinzel, et al.: **Successful testing of the LISA Technology Package (LTP) interferometer engineering model** *Class. Quantum Grav.* 22 (2005) pp. 149-154 [p. 115]
- [Heinzel2004] G. Heinzel, V. Wand, A. Garcíá, O. Jennrich, C. Braxmaier, D. Robertson, K. Middleton, D. Hoyland, A. Rüdiger, R. Schilling, U. Johann and K. Danzmann: **The LTP interferometer and phasemeter** *Class. Quant. Grav.* 21 (2004), pp. 581-587 [p. 23, 25, 210]
- [Heinzel2002] G. Heinzel, A. Rüdiger, R. Schilling: **Spectrum and spectral density estimation by the Discrete Fourier transform (DFT), including a comprehensive list of window functions and some new flat-top windows.** *Max Planck Institute paper* [p. 197] <http://pubman.mpg.de/pubman/item/escidoc:152164:1>
- [Heinzel1999] G. Heinzel: **Advanced optical techniques for laser-interferometric gravitational-wave detectors** *PhD thesis* (Feb. 1999) [p. 13, 212]
- [Heinzel1995] G. Heinzel: **Resonant Sideband Extraction – Neuartige Interferometrie für Gravitationswellendetektoren** *Diplomarbeit* Angefertigt am Max-Planck-Institut für Quantenoptik, Garching, (Nov. 1995) [p. 163]

- [Hewitson2009] M. Hewitson et al.: **Data analysis for the LISA Technology Package** *Class. Quant. Grav.* 26:094003 (2009) [p. 90, 207]
- [Hewitson2004] M. Hewitson: **On aspects of characterising and calibrating the interferometric gravitational wave detector, GEO 600** *PhD thesis presented in the University of Glasgow* (May 6, 2004) [p. 163]
- [Hughes2007] S. A. Hughes: **LISA sources and science** *arXiv:0711.0188v1 [gr-qc]* (Nov 1, 2007) [p. 4]
- [Hughes1998] S. A. Hughes, K. S. Thorne: **Seismic gravity-gradient noise in interferometric gravitational-wave detectors** *Phys.Rev.D*, 58:122002 (1998) <http://authors.library.caltech.edu/2041/> [p. 204]
- [Jennrich2009] O. Jennrich: **LISA technology and instrumentation** *Class. Quantum Grav.* 26 (2009) [p. 53]
- [Kuroda2010] K. Kuroda: **Status of LCGT** *Class. Quantum Grav.* 27:084004 (2010) [p. 206] <http://iopscience.iop.org/0264-9381/27/8/084004>
- [Leonor2009] I. Leonor, P. J. Sutton, R. Frey, G. Jones, S. Márka and Z. Márka: **Estimating detection rates for the LIGO-Virgo search for gravitational-wave burst counterparts to gamma-ray bursts using inferred local GRB rates** *Class. Quant. Grav.* 26:204017 (2009) [p. 3]
- [Lück2010] H. Lück: **The upgrade of GEO 600** *Proceedings of the Twelfth Marcel Grossmann Meeting on General Relativity* (2010) <http://pubman.mpg.de/pubman/item/escidoc:458065:2> [p. 204]
- [Mach1892] L. Mach: **Über einen Interferenzrefraktor** *Zeitschrift für Instrumentenkunde* Volume 12, p. 89–93 (1892) [p. 207]
- [Marin2007] A. F. García Marín: **Minimisation of optical pathlength noise for the detection of gravitational waves with the spaceborne laser interferometer LISA and LISA Pathfinder** *genehmigte Dissertation* (2007) [p 59, 67]
- [Marin2006] A. F. García Marín, V. Wand, F. Steier, F. Gumán Cervantes, J. Bogenstahl, O. Jennrich, G. Heinzl and K. Danzmann **On-orbit alignment and diagnostics for the LISA Technology Package** *Class. Quantum Grav.* 23 (2006) pp 133–140 [p. 67] <http://iopscience.iop.org/0264-9381/23/8/S18/>
- [Morrison1994-1] E. Morrison, B. J. Meers, D. I. Robertson and H. Ward: “Automatic alignment of optical interferometers” *Applied Optics*, Volume 33, No. 22, 5037 - 5040 (Aug 1994) [p. 21, 202]
- [Morrison1994-2] E. Morrison, B. J. Meers, D. I. Robertson and H. Ward: “Experimental demonstration of an automatic alignment system for optical interferometers” *Applied Optics*, Volume 33, No. 22, 5041 - 5049 (Aug 1994) [p. 21, 202]

- [Punturo2010] M. Punturo and H. Lück, **Toward a third generation of gravitational wave observatories**, *General Relativity and Gravitation*, (2010) <http://dx.doi.org/10.1007/s10714-010-1010-8> [p. 3]
- [Sato2009] S. Sato et al. **DECIGO : The Japanese space gravitational wave antenna** *Journal of Physics: Conference Series* 154 (2009) 012040 [p. 201, ??]
- [Schnupp1988] L. Schnupp: **Presentation at european collaboration meeting on interferometric detection of gravitational waves**, (Sorrent, Italy, Oct 1988), (1988). [p. 13, 212]
- [Steier2009] F. Steier, F. Guzmán Cervantes, A. F. García Marín, D. Gerardi, G. Heinzl and K. Danzmann: **The end-to-end testbed of the optical metrology system on-board LISA Pathfinder** *Class. Quantum Grav.* 26 (2009) 094010 (10pp) [p. 115]
- [Steier2008] F. Steier: **Interferometry techniques for spaceborne gravitational wave detectors** *vorgelegte Dissertation* (Okt. 2008) [p. 25]
- [Surrel2000] Y. Surrel: **Fringe Analysis** *Topics In Applied Physics* 77: 55-102, (2000) [p. 32]
- [Tröbs2009] M. Tröbs and G. Heinzl: **Corrigendum to “Improved spectrum estimation from digitized time series on a logarithmic frequency axis” [Measurement 39 (2006) 120-129]** *Measurement* 42 (2009) p. 170 [p. 92, 207, 197]
- [Tröbs2006] M. Tröbs and G. Heinzl: **Improved spectrum estimation from digitized time series on a logarithmic frequency axis** *Measurement* 39, (2006) pp. 120-129 [p. 92, 197, 207]
- [Veggel2007] A. A. Veggel, D. van den Ende, J. Bogenstahl, S. Rowan, W. Cunningham, G. H. M. Gubbels, H. Nijmeijer: **Hydroxide catalysis bonding of silicon carbide** *Journal of the European Ceramic Society* 28, (2008) pp. 303–310 [p. 205]
- [Wand2007] V. Wand: **Interferometry at low frequencies: Optical phase measurement for LISA and LISA Pathfinder** *vorgelegte Dissertation* (Apr 2007) [p. 23, 25, 210]
- [Weise2008] D. Weise, P. Marenaci, P. Weimer, M. Berger, H. R. Schulte, P. Gath, and U. Johann: **Opto-mechanical architecture of the LISA instrument** ICSO conference series 2008 <http://www.icsconference2008.com/cd/pdf/S11%20-%20LISA%20-%20Weise.pdf> [p. 125]
- [Xia2010] Xia Y, Li G. Y ,G. Heinzl, A. Rüdiger and Luo Y.: **Orbit design for the Laser Interferometer Space Antenna (LISA)** *SCIENCE CHINA Physics, Mechanics & Astronomy* 53 (2010) pp. 179-186 [p. 125]
- [Yamamoto2008] K. Yamamoto et al. **Current status of the CLIO project** *Journal of Physics: Conference Series* 122 (2008) [p. 200]
- [Zehnder1891] L Zehnder: **Ein neuer Interferenzrefraktor** *Zeitschrift für Instrumentenkunde* Volume 11, p. 275–285 (1891) [p. 207]



---

## Project documents

---

- [AEI-3017] G. Heinzel, V. Wand and A. Garcia: **Lisa Pathfinder Optical Bench Engineering model: functional and performance tests – Test Report** *LTP project document* S2-AEI-TN-3017 (Jun 4, 2004) [p. 74]
- [AEI-3034] G. Heinzel: **Generation of Random time series with prescribed spectra** *LTP project document* S2-AEI-TN-3034, Issue 0.2 (Sep 18, 2006) [p. 92]
- [ASD-2003] A. Schleicher, M. Schlotterer and W. Fichter **DFACS Science Mode 1 Design and Analysis (M3)** *LTP project document* S2-ASD-TN-2003, Issue 2.1 (Jan 9, 2006) [p. 90, 92]
- [ASD-2046] D. Gerardi: **Interferometer initial acquisition: design and analysis** *LTP project document* S2-ASD-TN-2046, Issue 1 (May 6, 2008) [p. 209]
- [ASD-3001] LTP team, R. Gerndt, H. U. Maier, U. Johann: **LTP Experiment Interface Document - Part B** *LTP project document* S2-ASD-EID-3001, Issue 3, (Jul 20, 2007) [p. 209]
- [ASD-3007] M. Bode, R. Gerndt, H. U. Maier, D. Kolbe: S2-ASD-RS-3007 *LTP project document* Laser Modulator Requirements Specification, Issue 2, (Jul 12, 2007) [p. 114]
- [ASD-3008] H. Grünert, R. Gerndt, H. U. Maeier, D. Kolbe: **LTP FMECA Report** *LTP project document* S2-ASD-RP-3008, Issue 1 (Aug 31, 2007) [p. 202, 205, 207, 209]
- [ASD-3018] U. Denskat, R. Gerndt, G. Link, U. Johann: **Phasemeter processing & laser control** *LTP project document* S2-ASD-RS-3018, Issue 3.0 (Oct 31, 2008) [p. 174]
- [ASD-3020, iss 6] I. Köker, N. Brandt, K. Eckert: **LTP Alignment Budget** *LTP project document* S2-ASD-TN-3020, Issue 6 (Feb 6, 2008) [p. 67, 100, 205]
- [ASD-3020, iss 3] I. Köker, N. Brandt, K. Eckert: **LTP Alignment Budget** *LTP project document* S2-ASD-TN-3020, Issue 3, (Aug 3, 2007) [p. 77, 79, 97, 97]
- [ASD-3036] N. Brandt, T. Ziegler, R. Schubert, H. Hirth, W. Fichter, D. Wealthy, R. Gerndt and N. Dunbar: **Experimental performance budget (M3, FEFP)** *LTP project document* S2-ASD-RP-3036, Issue 2.4 (Apr 9, 2010) [p. 56, 91, 91, 96, 170]
- [ASD-3065] N. Brandt, K. Ergenzinger, K. Eckert et al.: **LTP Science Mode Alignment Requirements** *LTP project document* S2-ASD-TN-3065, Issue 1, (Jan 30, 2008) [p. 97, 100, 104]
- [ASD-5001] P. Gath, H.-R. Schulte, D. Weise, U. Johann: **Requirement Breakdown** *LISA project document* LISA-ASD-TN-5001, Issue 2.0 (May 27, 2007) [p. 208]

- [EST-5007] S. Vitale, K. Danzmann, P. McNamara, M. Armano, R. Dolesi, C. Dunn, A. García Marín, G. Heinzel, M. Hueller, W. Weber: **LISA Pathfinder Experiments Master Plan** *LTP project document* S2-EST-PL-5007, Issue 1, (Oct 10, 2006) [p. 53, 67]  
[http://www.rssd.esa.int/SP/LISAPATHFINDER/docs/Top\\_level\\_documents/LPF\\_EMP.pdf](http://www.rssd.esa.int/SP/LISAPATHFINDER/docs/Top_level_documents/LPF_EMP.pdf)
- [LISA-LPF-0002] P. McNamara and G. Racca: **Introduction to LISA Pathfinder** *LPF project document* LISA-LPF-RP-0002, Rev. 1, Issue 1 (Mar 30, 2009) [p. 53]  
<http://sci.esa.int/science-e/www/object/index.cfm?fobjectid=45819#>
- [LOB-06] D. Weise **OB Requirements Specification and Justification** *LISA project document* LOB-ASD-TN-006-02, Issue 2.0, (Jul 29, 2010) [p. 132, 133, 144, 176, 198]
- [UGB-3002] G. Dixon, A. M. Cruise: **Photo-Diode and Mount - Requirement Specifications** *LTP project document* S2-UGB-RS-3002, Issue 5 (Mar 9, 2009) [p. 112]
- [UGB-3007] G. Dixon, D. Hoyland: **Photo-Diode - Use of QPD in the place of SEPD** *LTP project document* S2-UGB-TN-3007, Issue 1 (Sep 30, 2009) [p. 109]
- [UGL-3001] D. Robertson, H. Ward: **Optical Bench Interferometer Requirements Specification** *LTP project document* S2-UGL-RS-3001 Issue 2.4 (Dec 18, 2009) [p. 65, 66, 88]
- [UGL-3002] C. Killow, D. Robertson **OBI Alignment Plan** *LTP project document* S2-UGL-PL-3002, Issue 1.9 (Nov 6, 2008) [p. 64, 64]
- [UGL-3009] C. Killow, D. Robertson **Alibnment Precision** *LTP project document* S2-UGL-TN-3009, Issue 2.1 (Nov 5, 2008) [p. 61, 63, 78, 98]
- [UGL-3019] H. Ward: **OBI Numerical Optical Modelling** *LTP project document* S2-UGL-TN-3019 Issue 1.3 (Aug 15, 2007) [p. 75, 78]
- [UGL-3039] E. Fitzsimons and D. Robertson: **Optical characterisation of 3OB** *LTP project document* S2-UGL-TN-3039, Issue 1.2 (Jul 11, 2010) [p. 58, 75, 87, 88, 107]

---

## Books

---

- [Bronstein] Bronstein, Semendjajew, Musiol, Mühlig: **Taschenbuch der Mathematik** *Verlag Harri Deutsch, Thun und Frankfurt am Main, 2000* 5., überarbeitete und erweiterte Auflage 2000, S84 [p. 17]
- [Hecht] E. Hecht: **Optik**, 3. vollständig überarbeitete Auflage *Oldenburg Verlag München Wien*, (2001) [p. 138, 198, 203, 204, 210]
- [Saleh] B. E. A. Saleh, M. C. Teich: **Fundamentals of photonics** *Wiley Series in Pure and Applied Optics*, (1991) [p. 28]

- [Saulson] P. A. Saulson: **Fundamentals of interferometric gravitational wave detectors** *World Scientific*, (1994) [p. 163]
- [Smith] Warren J. Smith: **Modern Optical Engineering, The Design of Optical Systems**, Third Edition *McGraw-Hill*, (2000) [p. 138, 180, 198, 203, 204, 210]
- [Yariv] A. Yariv: **Quantum Electronics**, Third Edition Ch. 6.6 eq.(6.6-14) *John Wiley & Sons*, (1989) [p. 28]

---

## Web-pages

---

- [1] Caltech page on Advanced LIGO:  
[http://www.ligo.caltech.edu/advLIGO/scripts/ref\\_des.shtml](http://www.ligo.caltech.edu/advLIGO/scripts/ref_des.shtml) [p. 213]
- [2] M. Ando: *LISA Symposium 2010 talk*  
[http://www.stanford.edu/group/lisasymposium/LISA8\\_Ando.pdf](http://www.stanford.edu/group/lisasymposium/LISA8_Ando.pdf) [p. 201]
- [3] Official ESA websites of the LISA Pathfinder project:  
<http://sci.esa.int/science-e/www/area/index.cfm?fareaid=40> [p. 5]
- [4] Official ESA websites of the LISA Pathfinder project:  
[http://www.esa.int/esaSC/120397\\_index\\_0\\_m.html](http://www.esa.int/esaSC/120397_index_0_m.html) [p. 53]
- [5] ESA launch vehicles: VEGA [http://www.esa.int/SPECIALS/Launchers\\_Access\\_to\\_Space/ASEKMUOTCNC\\_0.html](http://www.esa.int/SPECIALS/Launchers_Access_to_Space/ASEKMUOTCNC_0.html) [p. 214]
- [6] The Einstein Telescope design study (FP7-Capacities, Grant Agreement 211743):  
<http://www.et-gw.eu/> [p. 203]
- [7] Specifications of GEO600 on the GEO600 Homepage:  
<http://www.geo600.org/general-information/technical-principles/specifications> [p. 213]
- [8] J. Bonnell and R. Nemirow: **The Number “e”**  
<http://www.gutenberg.org/etext/127> [p. 218]
- [9] Official website of LCGT: <http://gw.icrr.u-tokyo.ac.jp/lcgt/> [p. 206]
- [10] Linos web page  
[http://www.linos.com/pages/no\\_cache/home/shop-optic/singlelenses/symmetric-convex-lenses/](http://www.linos.com/pages/no_cache/home/shop-optic/singlelenses/symmetric-convex-lenses/) [p. 138, 138]
- [11] NASA quick facts for LISA  
[http://lisa.nasa.gov/quick\\_facts/index.html](http://lisa.nasa.gov/quick_facts/index.html) [p. 206, 212]
- [12] Official homepage of LTPDA <http://www.lisa.aei-hannover.de/ltpda/> [p. 90, 207]
- [13] Y. Michimura: *LISA Symposium 2010* [http://www.stanford.edu/group/lisasymposium/LISA8\\_michimura.pdf](http://www.stanford.edu/group/lisasymposium/LISA8_michimura.pdf) [p. 201]

- [14] R. Nemiroff and J. Bonnell: **RJN's More Digits of Irrational Numbers Page**  
[http://antwrp.gsfc.nasa.gov/htmltest/rjn\\_dig.html](http://antwrp.gsfc.nasa.gov/htmltest/rjn_dig.html) [p. 218]
- [15] OptoCad homepage:  
<http://www.rzg.mpg.de/~ros/OptoCad/> [p. 209]
- [16] The first  $2 \cdot 10^8$  digits of  $\pi$ : <http://pi.is.online.fr/> [p. 216]
- [17] Schott AG home page:  
[http://www.schott.com/lithotec/english/products/Zerodur/Zerodur.html?highlighted\\_text=Zerodur](http://www.schott.com/lithotec/english/products/Zerodur/Zerodur.html?highlighted_text=Zerodur) [p. 215]
- [18] Virgo home page:  
<http://www.virgo.infn.it/central.html> [p. 214]
- [19] Optical Design Software Package WinLens <http://www.winlens.de> [p. 138]

# Complete list of publications

- [P1] F. Antonucci ... **G. Wanner** ... P. Zweifel: **The LISA Pathfinder interferometry - hardware and system testing** *submitted to Class. Quantum Grav.*, (2010).
- [P2] L. d’Arcio, J. Bogenstahl, M. Dehne, C. Diekmann, E. D. Fitzsimons, R. Fledermann, E. Granova, G. Heinzel, H. Hogenhuis, C. J. Killow, M. Perreux-Lloyd, J. Pijenburg, D. I. Robertson, A. Shoda, A. Sohmer, A. Taylor, M. Tröbs, **G. Wanner**, H. Ward, and D. Weise: **Optical bench development for LISA** *ICSO conference series*, (2010).
- [P3] M. Hewitson ... **G. Wanner** ... P. Zweifel: **Data analysis for the LISA Technology Package**, *Class. Quantum Grav.*, 26 (2009).
- [P4] M. Armano ... **G. Wanner** ... P. Zweifel: **LISA Pathfinder: the experiment and the route to LISA**, *Class. Quantum Grav.*, 26 (2009).
- [P5] A. Monsky ... **G. Wanner** ... P. Zweifel: **The first mock data challenge for LISA Pathfinder**, *Class. Quantum Grav.*, 26 (2009).
- [P6] M. Hirth, W. Fichter, N. Brandt, A. Schleicher, D. Gerardi and **G. Wanner**: **Optical metrology alignment and impact on the measurement performance of the LISA Technology Package** *Journal of Physics: Conference Series* 154 (2009) 012003
- [P7] F. Guzmán Cervantes, F. Steier, **G. Wanner**, G. Heinzel and K. Danzmann: **Subtraction of test mass angular noise in the LISA technology package interferometer**, *Appl. Phys. B* 90, 395-400 (2008).
- [P8] B. Abbott ... **G. Diederichs** ... J. Zweizig (LIGO Scientific Collaboration): **Implications for the origin of the GRB 070201 from LIGO observations** *The Astrophysical Journal* 681, 1419-1430 (Jul 10, 2008).
- [P9] B. Abbott ... **G. Diederichs** ... J. Zweizig (LIGO Scientific Collaboration): **A joint search for gravitational wave bursts with AURIGA and LIGO** *Class. Quantum Grav.* 25 095004 (2008).
- [P10] B. Abbott ... **G. Diederichs** ... J. Zweizig (LIGO Scientific Collaboration): **Search of S3 LIGO data for gravitational wave signals from spinning black hole and neutron star binary inspirals** *Phys. Rev. D* 78, 042002 (2008).
- [P11] B. Abbott ... **G. Diederichs** ... J. Zweizig (LIGO Scientific Collaboration): **Search for gravitational waves from binary inspirals in S3 and S4 LIGO data** *Phys. Rev. D* 77, 062002 (2008).

- [P12] B. Abbott ... G. Diederichs ... J. Zweizig (LIGO Scientific Collaboration): **Search for gravitational waves associated with 39 gamma-ray bursts using data from the second, third, and fourth LIGO runs** *Phys. Rev. D* 77, 062004 (2008).
- [P13] B. Abbott,... G. Diederichs ... J. Zweizig (LIGO Scientific Collaboration): **Erratum: All-sky search for periodic gravitational waves in LIGO S4 data** *Phys. Rev. D* 80, 129904(E) (2009).
- [P14] B. Abbott ... G. Diederichs ... J. Zweizig (LIGO Scientific Collaboration): **All-sky search for periodic gravitational waves in LIGO S4 data** *Phys. Rev. D* 77, 022001 (2008).
- [P15] B. Abbott ... G. Diederichs ... J. Zweizig (LIGO Scientific Collaboration): **Searching for a stochastic background of gravitational waves with the laser interferometer gravitational-wave observatory** *The Astrophysical Journal* 659, 918 - 930 (Apr 20, 2007).
- [P16] B. Abbott ... G. Diederichs ... J. Zweizig (LIGO Scientific Collaboration): **Search for gravitational-wave bursts in LIGO data from the fourth science run** *Class. Quantum Grav.* 24, 5343–5369 (2007).
- [P17] B. Abbott ... G. Diederichs ... J. Zweizig (LIGO Scientific Collaboration): **Upper limit map of a background of gravitational waves** *Phys. Rev. D* 76, 082003 (2007).
- [P18] B. Abbott ... G. Diederichs ... J. Zweizig (LIGO Scientific Collaboration): **Searches for periodic gravitational waves from unknown isolated sources and Scorpius X-1: Results from the second LIGO science run** *Phys. Rev. D* 76, 082001 (2007).
- [P19] B. Abbott ... G. Diederichs ... J. Zweizig (LIGO Scientific Collaboration): **Search for gravitational wave radiation associated with the pulsating tail of the SGR 1806 – 20 hyperflare of 27 December 2004 using LIGO** *Phys. Rev. D* 76, 062003 (2007).
- [P20] B. Abbott ... G. Diederichs ... J. Zweizig (LIGO Scientific Collaboration): **Upper limits on gravitational wave emission from 78 radio pulsars** *Phys. Rev. D* 76, 042001 (2007).
- [P21] B. Abbott ... G. Diederichs ... J. Zweizig (LIGO Scientific Collaboration): **First cross-correlation analysis of interferometric and resonant-bar gravitational-wave data for stochastic backgrounds** *Phys. Rev. D* 76, 022001 (2007).

# Project Documents

- [PD1] M. Tröbs, J. Bogenstahl, M. Dehne, C. Diekmann, E. Granova, A. Shoda, **G. Wanner**, G. Heinzel: **Test of interferometry concept**, LOB-AEI-TN-5.1 Issue 1.1 (Sep 13, 2010) [p. 132, 156]
- [PD2] M. Tröbs, M. Dehne, C. Diekmann, **G. Wanner**, G. Heinzel: **Test of interferometry concept**, LOB-AEI-TN-5.1 (Feb 07, 2010)
- [PD3] **G. Wanner**, A. García Marín, G. Heinzel: **Brief comparison of three configurations for QPDs used instead of SEPs on the OB of LISA Pathfinder**, S2-AEI-TN-3067 Issue 2 (Nov 30, 2009) and Issue 1 (Nov 02, 2009)
- [PD4] **G. Wanner**, F. Steier, D. Robertson: **Calibration of the DWS-Signals on LTP**, S2-AEI-TN-3061, (Jun 03, 2009) [p. 87]
- [PD5] M. Nofrarias, J. Sanjuan, **G. Wanner**: **Thermal experiments on board the LTP**, S2-IEC-TN-3042, (Jan 26, 2009) [p. 89]
- [PD6] **G. Wanner**, G. Heinzel: **LTP-OBI-Alignment Simulation**, S2-AEI-TN-3051 Issue 2, (Mar 20, 2008) and Issue 1 (Nov 16, 2007)
- [PD7] **G. Diederichs**, G. Heinzel: **LTP-OBI-Alignment Simulation**, S2-AEI-TN-3042, (May 12, 2007) [p. 82]
- [PD8] N. Brandt, **G. Diederichs**, S. Lucarelli: **Influence of thermo-elastic effects, optical modelling & manufacturing tolerance on the OMS read-out**, S2-ASD-TN-3040, (Mar 03, 2007)
- [PD9] **G. Diederichs**, G. Heinzel: **Optical Bench Alignment Simulation**, S2-AEI-TN-3033, (Jul 25, 2006)





# Acknowledgements

First - and not because it is polite and tradition - my gratitude goes to Karsten Danzmann. He probably read hundreds of acknowledgments and I will not be able to state something new or different. But it is an honor, a pleasure and also fun to be part of the LISA working group at the AEI. And yes: KD is a role model, no matter if it is for infecting an audience with passion about a presented topic, knowing names and work of 200 employees, taking exams from 9 am to 6 pm without any break and still smiling to and joking with the 6 pm candidate to calm the students nervousness.

Secondly, I would like to thank Gerhard Heinzel. His programming and computer skills paired with laboratory expertise and a seemingly all-encompassing knowledge about LISA, LISA Pathfinder and interferometer techniques are incredible, even scary to a fresh starting student. But even more than that, I admire and respect his focusing on content, physics and simple, clear information rather than appearance of a work.

Thanks Nico, for introducing me to Linux, the Terminal and Vim (how was I ever able to work without these...), for helping me with my never ending programming questions and the fruitful discussions about e.g. Schopf-Tintlinge.

I would like to thank

- Andreas Freise, for being my Korreferent - which meant reading this entire 245 page-work and coming all the way from Birmingham for the disputation
- Roland Schilling for always being there for OptoCad related problems and for solving them in an incredible pace, whether it was a simple user mistake or a new feature to be implemented in OptoCad,
- Dave Robertson and Harry Ward, my supervisors in Glasgow, for always having an open door to discuss work or chat about the whereabouts in Glasgow and the loveliness of Scotland,
- the entire UGL LISA working group for the countless discussions about alignment precisions and techniques,
- Johanna Bogenstahl, for safely bringing us to the top of our first Munro - and back again,
- and simply everyone at the AEI for the valuable discussions and the great time.

Finally, my acknowledgments go to the diligent proof readers in random order: Alexander Wanner, Markus Otto, Christoph Mahrtdt, Evgenia Granova, Anneke Monsky, Ben Sheard, Miquel Nofrarias, Michael Tröbs, Martin Hewitson and Gerhard Heinzel. All of you helped to improve this work. Thank you! And of course: any remaining mistakes are my own responsibility.



# CURRICULUM VITAE

## PARTICULARS

---

Name: Gudrun Wanner, née Diederichs

Nationality: German

Date of birth: 20/01/1981

Place of birth: Dresden, Germany

Family status: married, one child (07/2008)

## SCHOOL

---

09/1987 - 07/1990	Oberschule Hermann Matern, Dresden
08/1990 - 06/1991	Grundschule Neuenmarkt-Wirsberg, Kreis Kulmbach
07/1991 - 04/1992	Markgraf-Georg-Friedrich-Gymnasium, Kulmbach
04/1992 - 08/1994	Walram-Gymnasium, Menden
08/1994 - 06/2000	Gymnasium Berenbostel, Garbsen <i>Graduated with Abitur</i>
07/1997 - 10/1997	study visit in Richmond, Michigan, USA

## UNIVERSITY

---

10/2000 - 07/2005	Studies of physics at the Universität Hannover <i>Graduate with Diploma</i>
07/2005 - 12/2010	Ph.D. student at the Albert-Einstein-Institute in Hannover
02/2009 - 07/2009	Ph.D. student at the University of Glasgow, UK